London South Bank University
EST 1892

The Digitisation of the Sputter Deposition Process of Transparent Conductive Oxides by Implementing Artificial Intelligence

A thesis submitted in partial fulfillment of the requirements of London South Bank University for the degree of Doctor of Philosophy

by

MD ABUL HASNATH

https://orcid.org/0000-0002-9170-8797

1st Supervisor: Professor Hari Upadhyaya

2nd Supervisor: Dr Ali Salimian

Dedication

I dedicate this thesis to the memory of my beloved mother, the late Rohima Begum who faced extreme hardship before her passing in September 2017.

Abstract

Plasma-based sputtering is extensively employed to fabricating thin film Transparent Conductive Oxides (TCOs), a category of semiconducting material used for a wide variety application from flat panel display to energy harvesting devices. Methods of evaluating the plasma i.e. glow discharge has been greatly studied requiring complex theoretical physics which is not viable for applied/materials scientist who frequently use this method of deposition at an operational level.

The aim of the project was to explore new methods of characterizing the plasma sputtering process to evaluate the possibility of simplifying the monitoring and assessment of the sputtering process. The first method involved monitoring the RF-based plasma sputtering process through optical spectroscopy and characterizing the discharge based on its specific colour. The 2nd method involved implementing Artificial intelligence/Machine learning and feeding the emission spectrum of the plasma extracted from an array of depositions to a deep learning model to evaluate the accuracy of predicting not only the properties of the deposited TCO film but also the growth process conditions. Implementation of such methods pave the way for the design of a digital shadow for plasma-based deposition in the material engineering industry.

Spectral data from the plasma was obtained by placing an in-vacuum collimator optic probe (Plasus) which featured a unique honeycomb structure capturing photons whilst simultaneously trapping sputtering particles and preventing gradual coating of the collimator's quartz window. The spectrometer was programmed to calculate the area under the peak of the spectral range based on predesignated segments of the spectrum. In addition to this, the light collected from the plasma was also guided to a 2nd spectrometer (Jeti) that calculates the chromaticity index of the light.

The colour of the plasma source was deduced based on conventional chromaticity index analysis and it was compared to the direct spectral data plots of the emission peaks to investigate the possibility of characterizing the plasma based on its specific colour. This technique was demonstrated to be a viable potential for evaluating the plasma in terms of providing information regarding the stability of the plasma, chamber pressure and plasma power. A linear relationship between the colour functions and the plasma power was observed, while the stability of the sputtering plasma can be assessed based on the plasma colour functions. The colour functions also follow a unique pattern when the working gas pressure is increased.

The spectral properties and colour functions of a radio frequency (RF)-based sputtering plasma source was also monitored during consecutive sputter deposition of Indium doped zinc oxide (IZO) thin films under argon and argon/hydrogen mix. The effect of target exposure to the hydrogen gas on charge density/mobility and spectral transmittance of the deposited films was investigated. Consecutive exposure to the hydrogen gas during the deposition process progressively affects the properties of thin films with a certain degree of continuous improvement in electrical conductivity while demonstrating that reverting to only argon from argon/hydrogen mix follows a complex pathway. Preparation of highly conductive zinc oxide thin films without indium presence was exhibited eliminating the need for the expensive indium addition.

The complexity of the reactive sputtering of highly conductive zinc oxide thin films in the presence of hydrogen at room temperature was investigated. A hypothesis was put forward regarding importance

of precise geometric positioning of the substrate with respect to the magnetron to achieve maximum conductivity. The electrical properties of the deposited zinc oxide thins films based on their position on the substrate holder relative to the magnetron were examined.

Machine Learning/Deep learning models were incorporated to examine the accuracy of predicting a single feature (sheet resistance) of thin films of indium-doped zinc oxide deposited via plasma sputter deposition by feeding the spectral data of the plasma to the deep learning models. It was shown that Artificial Neural networks could be implemented as a model that could predict the sheet resistance of the thin films as they were deposited, taking in only the spectral emission of the plasma as an input.

The spectral emission data from the plasma glow of various sputtering targets containing indium oxide, zinc oxide, and tin oxide were obtained. These spectral data were then converted into two-dimensional arrays by implementing a basic array-reshaping technique and a more complex procedure utilizing an unsupervised deep-learning technique, known as the self-organizing-maps method. The two-dimensional images obtained from each single-emission spectrum of the plasma mimic an image that can then be used to train a convolutional neural network model capable of predicting certain plasma features, such as impurity levels in the sputtering target, working gas composition, plasma power, and chamber pressure during the machine operation. It was demonstrated that that the single-array-to-2D-array conversion technique, coupled with deep-learning techniques and computer vision, can achieve high predictive accuracy and can, therefore, be fundamental to the construction of a sputtering system's digital twin.

Acknowledgements

I would like to thank God first and foremost for allowing me to complete this thesis.

I would like to express my deepest gratitude, appreciation and thanks to my supervisors, Professor Hari Upadhyaya and Dr Ali Salimian for their continuous guidance and support throughout this journey. I would have struggled to complete the doctorate if it were not for them. I would like to thank Ali specifically for his mentorship, getting me involved in his research projects and sharing his knowledge and technical expertise. I would also like to thank my fellow colleague, Miss Cova Pardo Sanchez for her endless support & friendship over the years. The labs and equipment would still be in a right mess were it not for her.

I would also like to thank my former supervisors Dr Jeremy Ball and Professor Hari Reehal for accepting me as a PhD student to take on this PhD (though it has taken many twists and turns from the initial aim) and introducing me to the world of thin film semiconducting materials and vacuum-based technology.

Last but not least, many thanks goes to my father for constantly motivating me and sharing words of encouragement in times of difficulty throughout the process.

Abbreviations

AC	Alternating Current
AI	Artificial Intelligence
ANN	Artificial Neural Network
AZO	Aluminium Doped Zinc Oxide
BM	Burnstein Moss Shift
CBM	Conduction Band Minimum
CIE XYZ	Commission on Illumination XYZ colour space
CIGS	Copper Indium Gallium Sulphide
CNN	Convolutional Neural Network
CVD	Chemical Vapour Deposition
CZTS	Copper Zinc Tin Sulphide
DBD	Dielectric Barrier Discharge
DC	Direct Current
DFT	Density Functional Theory
DNN	Deep Neural Network
E_A	Electron Affinity
EBSD	Electron Backscattered Diffraction
ECR	Electron Cyclotron Resonance
EDAX	Energy-dispersive X-ray spectroscopy
E_F	Fermi Level
E_I	Ionisation Energy
EM	Electromagnetic
FEG SEM	Field Emission Gun SEM
FWHM	Full Width Half Maximum
GPIB	General Purpose Interface Bus
GZO	Gallium Doped Zinc Oxide
HIPIMS	High-Power Impulse Magnetron Sputtering
IR	Infrared

ITO	Indium Doped Tin oxide
IZO	Indium Doped Zinc Oxide
LTE	Local Thermal Equilibrium
MES	Mean Squared Error
MO	Metal Oxide
MS	Magnetron Sputtering
N_D	Electron Density
N_{H}, N_{Ar}	Degrees of Dissociation of Hydrogen & Argon
NIR	Near Infrared
NIST	National Institute of Standards and Technology
OES	Optical Emission Spectroscopy
PCA	Principal Component Analysis
PECVD	Plasma Enhanced CVD
PLD	Pulsed Laser Deposition
PVD	Physical Vapour Deposition
RF	Radio Frequency
R_s	Sheet resistance
SEM	Scanning Electron Microscopy
SOM	Self Organising Map
SVD	Singular Value Decomposition
SVM	Support Vector Machines
SVS	Scientific Vacuum System Ltd
TCO	Transparent Conductive Oxides
UV	Ultraviolet
VBM	Valence Band Maximum
V_H	Hall Voltage
VIS	Visible Light
WF	Work Function

Table of Contents

Chapter 1 Introduction ... ***1***

1.1 Overview ... **1**

1.2 Aims & Objectives ... **2**

1.3 Structure of thesis ... **3**

Chapter 2 Literature Review ... ***4***

2.1 Transparent Conductive Oxides ... **4**

2.1.1 Introduction ... 4
2.1.2 Electrical Conductivity ... 4
2.1.3 Optical Transparency ... 10
2.1.4 Hydrogen Doping ... 15
2.1.5 Fabrication methods ... 16
2.1.6 Conclusion ... 17

2.2 The Glow Discharge ... **18**

2.2.1 Brief History ... 18
2.2.2 Introduction to glow discharge and applications ... 19
2.2.3 DC glow discharge ... 21
2.2.4 Radio Frequency Discharges ... 24
2.2.5 RF Magnetron Sputtering ... 27
2.2.6 Sputtering Efficiency ... 32
2.2.7 Summary ... 34

2.3 Characterisation and Modelling of Plasma ... **35**

2.3.1 Introduction ... 35
2.3.2 Novel approach to characterising the plasma ... 37
2.3.3 Modelling Background ... 40
2.3.4 Modelling plasma with artificial neural networks. ... 42
2.3.5 Summary ... 44

Chapter 3 Experimental Methods and Characterisation Techniques ... ***45***

3.1 Experimental set-up ... **45**

3.1.1 Experiments for the optical analysis of the Glow Discharge via colour characterisation ... 46
3.1.2 Experiments for the synthesis of Highly conductive Zinc Oxide films ... 47
3.1.3 Experiments for investigating the effect of substrate position relative to plasma ... 48
3.1.4 Experiments for implementing Machine Learning concepts to the sputter deposition process ... 50

3.2 Characterisation Techniques ... **62**

3.2.1 Four point probe ... 62
3.2.2 Hall Effect ... 63
3.2.3 Spectrophotometry ... 66
3.2.4 Stylus Profilometer ... 67
3.2.5 Scanning Electron Microscopy (SEM) ... 67
3.2.6 EDS ... 68

3.3 Summary ... **69**

Chapter 4 Optical Analysis of RF Sputtering Plasma through Colour Characterization *71*

4.1 Results **71**

4.1.1 Chromaticity of the Plasma Emissions 71

4.1.2 Optical Emission Spectroscopy of the Plasma Emissions 78

4.2 Discussion **83**

4.3 Conclusion **85**

Chapter 5 Highly Conductive Zinc Oxide Films Prepared Using RF Plasma Sputtering Under Reducing Atmosphere *86*

5.1 Results and Discussion **86**

5.1.1 Film Morphology, Composition and Crystallinity Characteristics 87

5.1.2 Electrical Properties 89

5.1.3 UV-Vis Spectroscopy 94

5.1.4 Spectral and Colour Function Analysis of the Plasma 96

5.2 Conclusion **99**

Chapter 6 Investigation on substrate position relative to Plasma during the sputter deposition of Hydrogen Doped Zinc Oxide *101*

6.1 Results and Discussion **101**

6.1.1 Electrical Properties 101

6.1.2 Film Thickness and Optical Properties 105

6.1.3 Analysis of the Plasma Emissions 107

6.2 Conclusion **112**

Chapter 7 Implementation of Machine Learning/Deep learning concepts: A step towards the digitisation of the sputter deposition process *113*

7.1 Results and Discussion **113**

7.1.1 Artificial Neural Networks to predict sheet resistance of IZO thin films deposited via Plasma deposition 113

7.1.2 Implementing Supervised and Unsupervised Deep-Learning Methods to Predict Sputtering Plasma Features 123

7.2 Conclusion **130**

Chapter 8 Summary, Highlights and Future Work *132*

8.1 Summary **132**

8.2 Highlights of the Research **133**

8.3 Future work **134**

References *135*

Chapter 1 Introduction

1.1 Overview

Transparent Conductive Oxides (TCO) are such type of semiconductors, which have attracted a significant amount of attention due to their vast application areas. They are an essential part of various optoelectronic devices, such as light emitting diodes (LEDs), thin-film solar cell modules, flat panel displays and flexible electronics. Physical vapor deposition (sputtering) under vacuum is one of the proven industrial methods of depositing thin films of these materials. During the sputter deposition of materials, the sputtering conditions dictate the arrangement of the atoms on the substrate and will ultimately define relevant functional parameters of the as deposited material such as bandgap. Researchers who apply this technique for TCO preparation usually report their findings by stating the growth condition of the sputtering process, such as chamber pressure, plasma power and the gas composition of the chamber during deposition. However, the properties of TCO coatings will vary from one sputter system to another depending on the dimensions of the chamber, size of the targets and a few other design related issues, even if the sputtering conditions are maintained, according to an earlier report. As a result, several trial-and-error experimental runs will most likely be carried out to refine a particular machine to produce a specific desired thin film coating with certain features and functionality. This means that, to fully digitize the sputter deposition process, significant constrains will arise. This project focused on studying the spectral emissions of the plasma, using them to predict the properties of the thin films deposited as well as its corresponding process parameters. Surely the plasma in the sputtering procedure is the core of the reaction and fundamental to the deposition of the thin film. The diagnosis of laboratory plasma is typically performed by optical emission spectroscopy (OES), through which a number of analytical techniques are established to determine certain plasma properties, such as electron density, plasma temperature, element recognition and qualification of elements present in the plasma. Such fundamental plasma physics-related investigations are complex; extensive expertise, as well as time and effort, are required to assess them.

One tool that can be exploited to digitize the sputter deposition process is Artificial intelligence/Machine Learning. This has great potential to generate huge business value in the semiconductor industry at all levels, from research & chip design to production through sales. The rise of computers alongside Artificial Intelligence (AI) in recent years has had a major impact on science and technology and ultimately changing lives and society. The latest advancement of computer technology has resulted in the production of high speed computers with high performance graphics cards and improved storage, bandwidth and data transaction speed; these have provided the tools and platforms to develop, test and implement intelligent systems. A number of AI techniques have evolved over the past decade to model the cognitive aspects of human behaviour; these include perception, reasoning, communication and learning. The development of more advance technique including Artificial Neural Networks (ANNs) and Evolutionary Algorithms (EA), which drew inspiration from the complex functions of the brain and the evolution of biological life. Artificial intelligence techniques have significant potential applications in various fields; including disaster recover, traffic control, space exploration, business management and computer games. The ultimate goal of Artificial Intelligence is to bring about automation that are capable of acting reliably on behalf of humans. Such systems would have great advantages in

domains where human intervention/errors needs to be minimised. **Figure 1.1** shows the significant traction gained in Artificial Intelligence in terms of publications and patents since its inception. The number of patents in the AI field increased at an exponential rate, surging by an average of 28% a year between 2012 and 2017 [1].

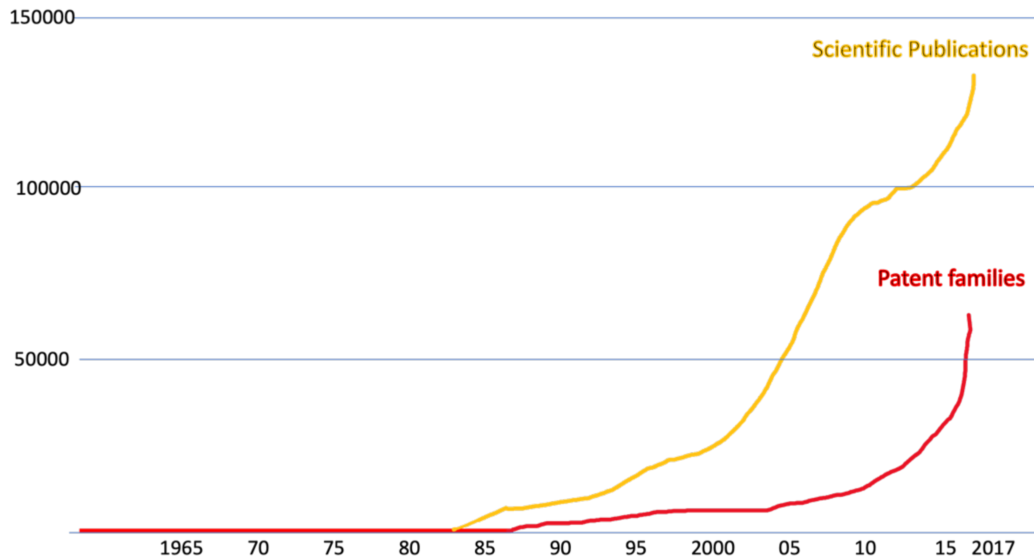

Figure 1.1. Growth of AI patent families and scientific publications.

1.2 Aims & Objectives

The aim of the project was to explore new methods of characterizing the plasma sputtering process to evaluate the possibility of simplifying the monitoring and assessment of the sputtering process. The first method involved monitoring the RF-based plasma sputtering process through optical spectroscopy and characterizing the discharge based on its specific colour. The 2nd method of evaluation involved employing an array of Machine Learning/Deep learning models to accurately predict certain characteristics of thin film TCOs deposited via plasma-based sputtering and ultimately create a digital shadow for the system. This project aimed to explore implementing an alternative approach in plasma diagnostics during the sputter deposition process to assess the qualitative parameters of thin films as they were deposited.

The objective is as follows:

- Collection of the emission spectra generated from a large number of plasma-based sputter depositions
- Electrical and optical characterization of the resultant TCOs films which includes measuring the sheet resistance, resistivity & transmittance.
- Employing several supervised and unsupervised Machine learning models created by Python within a TensorFlow framework library which includes ANN, CNN and SOM.
- Using the spectral data associated with a deposition and its corresponding characterization data (i.e. sheet resistance and resistivity) to train the array of machine learning models

- Quantify the predictions of the electrical properties and growth conditions outputted by deep learning models (not only for regressions but also classification analysis) by implementing various loss functions.

1.3 Structure of thesis

Chapter 1 is the introduction to the thesis in which discusses the motivation, aim and objectives of the research conducted. Chapter 2 provides a literature review & overview of the working principles/key mechanisms of Transparent Conductive Oxides; it also presents some historical methods of characterising & modelling the glow discharge. Furthermore, a novel and simple approach to characterising the discharge was put forward. Following on from this, Chapter 2 presents a brief introduction of artificial intelligence and key working principles associated with machine learning and more specifically deep learning techniques and it can be implemented to simplify the evaluation of the glow discharge. Chapter 3 discusses the experimental set-up that was utilised for the fabrication of various TCOs for this research project and the array of optical and electrical characterisation techniques used to characterise the thin film samples. Chapter 4 explores deeper into the study of the characteristics of plasma in vacuum-based deposition systems from a unique perspective; its colour. the stability of the emission characteristics of an RF plasma via various statistical analysis methods is investigated. Chapter 5 presents the preparation of highly conductive zinc oxide thin films without indium or aluminium doping and as such eliminating the need for the expensive indium addition. Chapter 6 investigates the complexity of the reactive sputtering of highly conductive zinc oxide thin films in the presence of hydrogen at room temperature. This chapter reports on the importance of precise geometric positioning of the substrate with respect to the magnetron to achieve maximum conductivity. Chapter 7 demonstrates the implementation of deep learning models to examine the accuracy of predicting a single feature viz. sheet resistance of thin films of indium-doped zinc oxide deposited via plasma sputter deposition by feeding the spectral data of the plasma to the deep learning models. Chapter 7 also looks at the conversion of the spectral emission data from the plasma glow of various sputtering targets containing Indium Oxide, Zinc Oxide and Tin Oxide into two dimensional arrays; this is achieved by implementing basic array reshaping technique and a more complex procedure of utilizing an unsupervised deep learning technique. Chapter 8 concludes the research project and summarises the findings in each set of experiments and also presents the work currently being carried out on the implementation of deep learning techniques on further deposition processes such as plasma-based sputtering of indium doped tin oxide (ITO) to further demonstrate the power of artificial intelligence.

Chapter 2 Literature Review

2.1 Transparent Conductive Oxides

2.1.1 Introduction

As mentioned, Transparent conducting oxide (TCO) thin films are applied in various optoelectronic devices, mobile phone screens, flat panel displays, light emitting diodes and most importantly in the fabrication of thin film-based solar cell devices, and plasma sputter deposition is one of the main established methods of applying these coatings as reported in various studies [2-8]. The nature of these materials brings about adjustments of dual functionality parameters viz. conductivity and transparency, which requires complex efforts and understanding for the optimization of various sputtering conditions. However, these characteristics are directly related to the complex electronic band configuration of these materials and have been a subject of great attention worldwide [9]. A band gap of above 3.3 eV and electrical conductivity in the range of 10^4 S·cm^{-1} (Siemens per centimetre) are the fundamental aspects of such materials. Various oxides behave as TCOs among which indium tin oxide (ITO) is the dominant commercial type [10]. Another TCO material of choice is indium zinc oxide (IZO), with applications such as transparent electrodes in heterojunction thin film solar cell structures [11-15]. One of the TCO materials that has recently gained interest is zinc doped indium oxide (IZO) due to the robust nature of its resistance against moisture. The parasitic absorption in TCOs as the front window electrode in solar cell configurations such as silicon heterojunctions is a leading factor in undermining cell efficiency. This can be resolved by the application of TCO materials that demonstrate high mobility irrespective of their charge density [2]. Due to the presence of multiple layers in solar cell designs such as CIGS (Copper Indium Gallium di-Selenide, $CuInGaSe_2$) and perovskite devices [3,4], which are sensitive to ambient moisture and temperature, deposition of TCO materials at low temperatures is highly desirable, and hence, IZO stands as a potential TCO material for these applications.

2.1.2 Electrical Conductivity

To gain a grasp of the conductivities of the TCOs, a comparison between some of the materials in terms of carrier concentration and mobility. The electrical conductivity is a product of carrier concentration *n*, elementary electric charge *e*, and mobility μ :

$$\sigma = \eta e \mu \tag{2.1}$$

A typical metal such as Ag possesses a high electrical conductivity because of the high carrier concentration in the order ~10^{23} cm^{-3} but interestingly the mobility does not stand out among the conductors like p-doped Si despite the low carrier concentration of the latter. Even if Si is doped heavily with carrier concentrations upwards of 10^{19} cm^{-3}, the conductivity won't be as high has an Ag metal because of the reduction in mobility by carrier scattering. ITO displays conductivity that is roughly 1/10th of that of Ag because of its relatively smaller carrier concentration despite possessing similar carrier mobilities [16]. **Figure 2.1** shows a plot of various conducting materials and how their carrier concentrations and mobilities differ from one another. Metals as a whole are found in the top left region indicating extremely high carrier concentrations but relatively low mobilities. In contrast, typical doped

semiconductors are plotted in the bottom right area due to its low carrier concentration and high mobility. It can be seen that TCOs lie somewhere in between metals and doped semiconductors as their mobilities is not too dissimilar from those of typical metals such as Ag. TCOs are essentially metals with a small carrier concentration and this type of material can be described as degenerate semiconductor. These types of materials are independent of temperatures for the generation of charge carriers i.e. the thermal activation energy is not necessary [16]. Degeneracy of a semiconductors simply implies that there's is an overlap of energy bands and the Fermi energy is close to the edge of the conduction band.

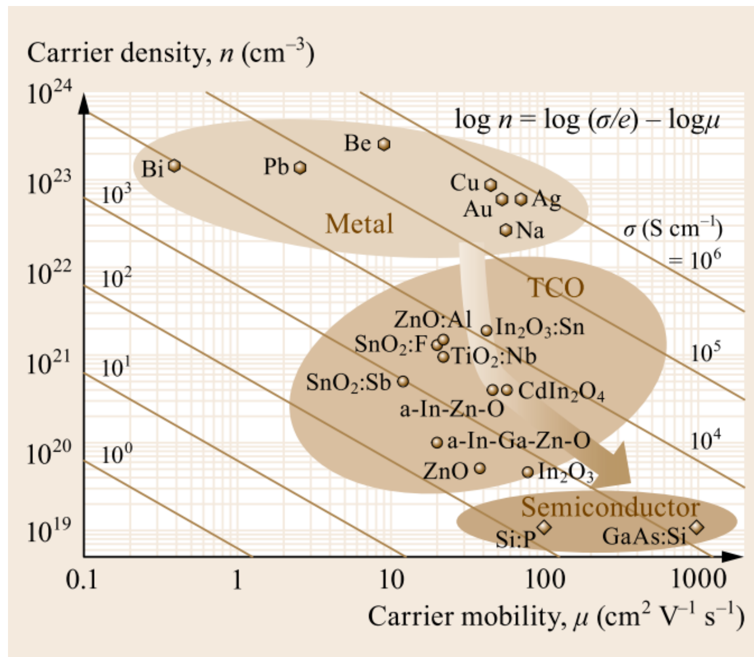

Figure 2.1. Carrier density and mobility for some metals, semiconductors and TCOs [16]

Doping of a material increases the number of charge carriers and in turn the conductivity. This can be achieved by substitutional doping i.e. creating vacancies and implanting interstitial. Though an enhancement in the mobility can boost the conductivity, it depends on intrinsic scattering mechanism which act as a limitation as the carrier density increases, thus mobility it is an important parameter that has an influence on the total conductivity.

Figure 2.2 shows the typical electronic structure of metal oxide (MO) illustrated in the form of molecular orbitals and energy bands. An essential feature of TCOs is the low absorption in the visible range; this can be attributed to the minimum bandgap of 3.0 eV. The top of the valence band mostly comprised of oxygen 2p bands; the bottom of the conduction band is occupied by a single and highly dispersed metal band. The conduction band possess antibonding features and the bottom of the valence band has bonding features as counterpart. As seen in the figure, top of the valence band possess non-bonding features as the non-bonding oxygen 2p orbitals possess low energy and remain without changing the energies thus a large bandgap can be obtained in oxides.

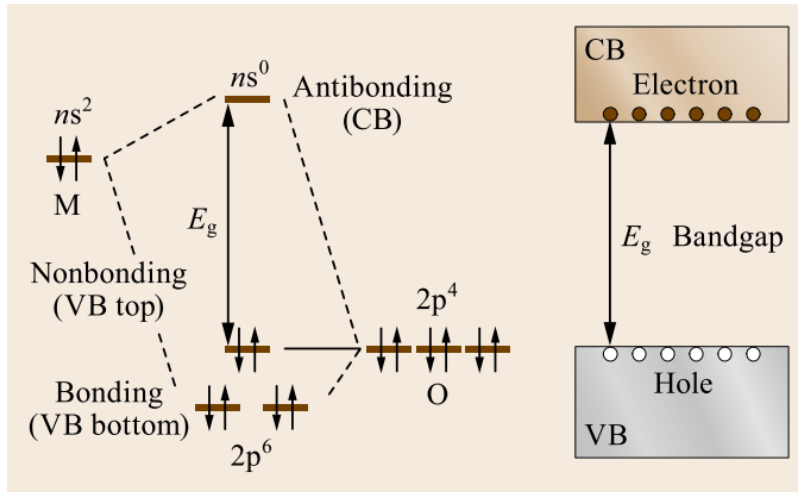

Figure 2.2 Schematic molecular orbital diagram and band structure of oxides [16]

In intrinsic stoichiometric oxides, it cannot exhibit high level of conductivity as well as transparency. However, Substitutional doping via cationic donors or anion vacancies lead to the generation of charge carriers altering the electronic band structure of the material. To improve the donor density, the donor states combine with the conduction band at the critical density which can be determined by Mott's criterion as expressed by Eq. 2.2 [17]:

$$n_c^{-1/3} < c a_0^* \tag{2.2}$$

Where a_0^* is the effective Bohr radius and c is a constant. The value of c is ≈ 0.25. If this criterion is satisfied (i.e., if the density of electrons is sufficiently high) the material becomes conductive and free electron behaviour is observed and the material is said to be degenerate. The Fermi Energy E_f is then determined by the high occupied state in the conduction band and can be expressed as:

$$E_F = \frac{\hbar^2 k^2}{2m_c^*} \tag{2.3}$$

The band structure of Tin oxide can be calculated by the parabolic functions of k in the near the edges of the bandgap. **Figure 2.3** shows the schematic diagram of the band structure for most wide bandgap metal oxide semiconductors. These types of materials can be described as direct band semiconductors as the valence band maximum and conduction band minimum can both be found at k=0.

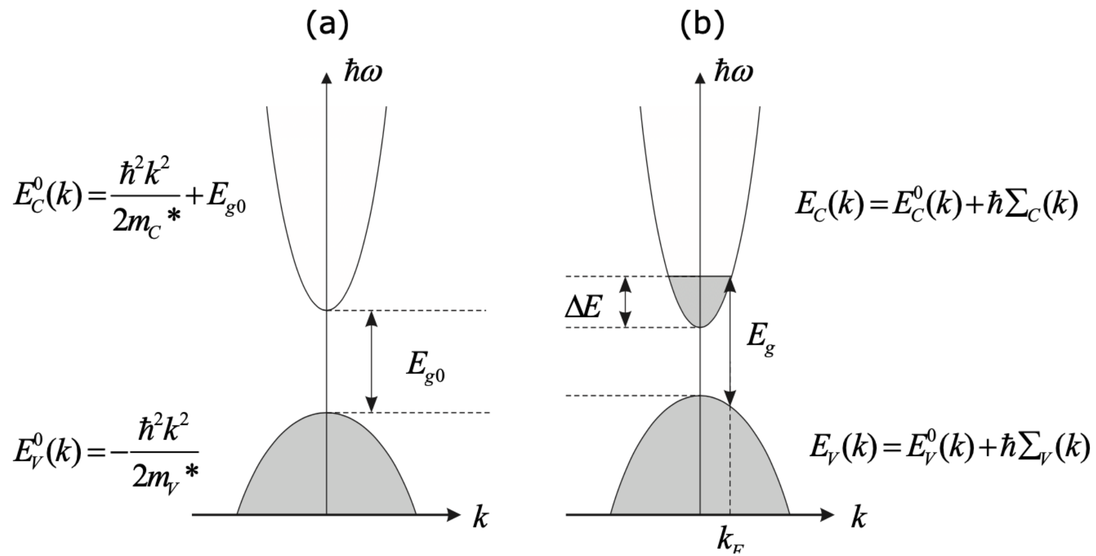

Figure 2.3. Schematic diagram of the band structure of (a) undoped and (b) doped wide band gap metal oxide semiconductor near the top of the valence band and bottom of the conduction band. Grey area represents occupied states [18]

Doping introduces states in the bandgap either just below the conduction band or above the valence band. This is depicted in **figure 2.4** whereby the band structure, density of states, fermi distribution of electron energy levels and concentration of majority charge carriers for intrinsic, n and p type materials are shown. At 0 ^oK, the Fermi level of an intrinsic material is found in the middle of the bandgap (**figure 2.4a**). There is high probability of finding an electron in the states of the valence band; in contrast the chance of finding an electron in the conduction band states is 0. There is 50% chance of finding an electron at the Fermi level. For doped semiconductors, there will be a shift in the Fermi level as doping will have an impact on the loss or gain of electrons. For n type materials (**figure 2.4b**), the impurity introduces donor levels just below the conduction band whereby electrons are the majority carriers. For p-type, impurities possess energy levels just above the valence band whereby electrons are thermally excited into these acceptor levels leaving behind positively charge vacancies in the lattices thus the majority carriers in this situation will be holes. Upon exposure to light, the generated charge carriers trigger a shift in free energy and thus perturbating the equilibrium in the semiconductor.

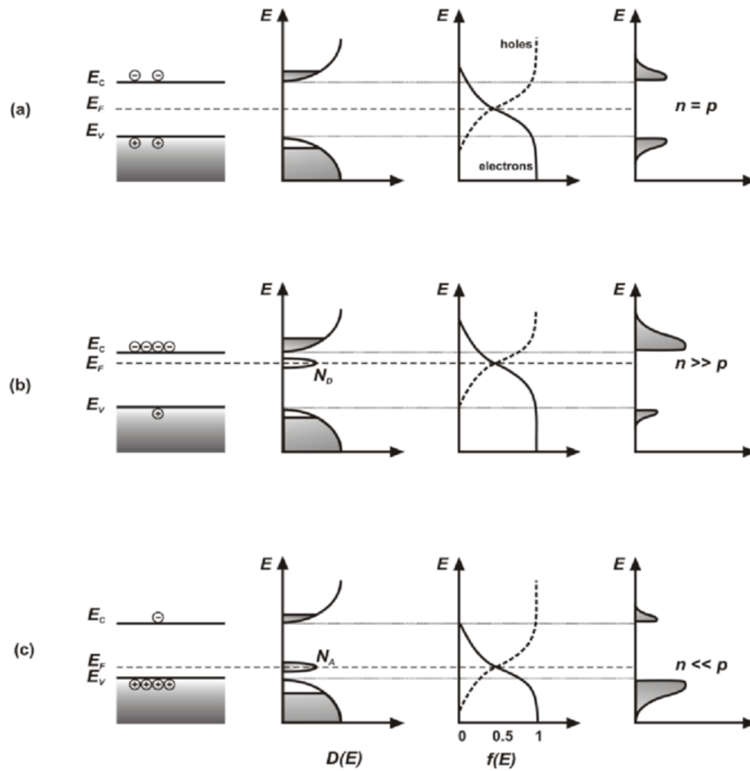

Figure 2.4. Schematics depicting the band structure, density of states, Fermi-Dirac distribution of energy levels (for a non-zero temperature), and the charge carrier concentrations for (a) intrinsic, (b) n-type, and (c) p-type semiconductors. [19]

Defects will also have an impact on the conductivity. Both defects and doping have the same effect on transparent insulators such as SnO_2, CdO, In_2O_3 and ZnO. In addition to doping, the addition of vacant oxygen sites also contribute towards the conductivity of these materials. **Figure 2.5a** shows the doping sites occupied by tin (Sn) in an indium oxide (In_2O_3) lattice [20]. The occupation of the interstitial site by an Sn atom results in donating an electron widening the bandgap and ultimately resulting in the synthesis of Indium Tin Oxide (ITO). The bandgap structure of undoped and Sn doped Indium Oxide is illustrated in **figure 2.5b**. Occupied states are just below the conduction band typically found in an n-type semiconductors. The free electrons in the conduction band come from the oxygen vacancies [20]. Thus, ITO are highly degenerate n-type semiconductors.

In the band model proposed by Fan [21] (i.e., the reference model used to date) the Indium oxide possesses a direct wide bandgap, leading to the prevention of inter-band transitions in the visible range allowing for high transparency. As mentioned previously, conduction band stems mainly from Indium 5s orbitals and the valence band from the oxygen 2p electrons. Due to the n-type doping of the Tin impurities, the Fermi energy is located a few eV below the conduction band [22]. For low doping density, the formation of donor states occur just below the conduction band and the Fermi energy lies between the donor level and the conduction band minimum. For high doping levels there is an increase in donor density [23], and the donor states merges with the conduction band at the previously mentioned critical density n_c; for ITO this is ~$3.43 \times 10^{19} cm^{-3}$.

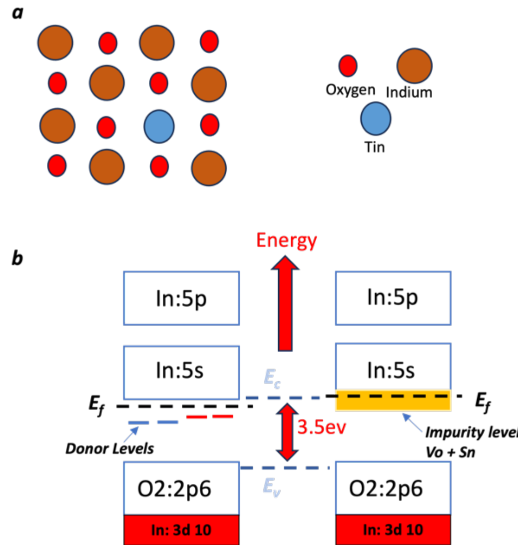

Figure 2.5. (a) Sn doping sites in an In_2O_3 lattice. (b) Schematic energy-band model for tin doped indium oxide, where E_f, E_V and E_C is the Fermi energy, the valence band energy and the conduction band energy respectively. Left: low doping level, right: high doping level.

Scattering mechanisms

Mobility can be thought of as the ease in which charge carriers move through the material. It is defined in terms of the average scattering time (τ) and the carrier effective mass (m^*) as:

$$\mu = \frac{e\tau}{m^*} \tag{2.4}$$

Equation 2.4 shows that the mobility increases with decreasing scattering time and/or a reduction in effective mass. In general, the inhibition of the carrier movement will result in a reduction in mobility and conductivity. In crystalline TCOs, there are a number of scattering mechanisms that take place. According to Matthiessen's rule [24], resistivity arises from independent scattering processes which are additive, such as scattering due to impurities, defects, and grain boundaries which is expressed in **equation 2.5** :

$$\frac{1}{\mu_{total}} = \frac{1}{\mu_{impurity}} \frac{1}{\mu_{defect}} + \frac{1}{\mu_{gb}} + \cdots \tag{2.5}$$

Ionised impurity scattering has the most impact on these structures. TCOs deposited at lower temperatures exhibit lower crystallinity and high doping concentrations results in the formation of neutral complexes. In such cases, grain boundary scattering and neutral impurity scattering should also be accounted for.

At high conducting electron density, the carrier transport is limited mainly by In ionised impurity scattering. i.e., the interaction between the ionised impurities and free electrons is said to be coulombic which provide an intrinsic source of scattering to the doped structure. With increasing dopant concentration, the resistivity reaches a lower limit it is not able to surpass whereas the optical window

gets narrower. The mobility and hence the resistivity of TCOs (ITO, SnO_2, ZnO) are limited by ionised impurity scattering for carrier concentrations above $10^{20}cm^{-3}$ [25]. Above the critical Mott density threshold, the conduction band is inhabited by impurities and associated electrons leading to the formation of degenerate electron gas which in turn increases the ionized-impurity scattering and ultimately lowering the mobility [23]. As discussed, the scattering that arises from the homogenous distribution of the ionised dopant atoms is one of the possible effects that reduce mobility.

In grain boundary scattering, there is a presence of atomic layers of disordered atoms creating a large number of defects. This leads to the entrapment of charge carriers i.e., immobilisation. The traps become electrically charged which leads to the formulation of a potential energy barrier thus reducing the mobility of free carriers from moving one crystallite to another. The potential barrier for electrons is determined by its height. [26].

Resistivity well

As mentioned, Introduction of defect sites in solids also allow for the scattering of electrons; thus one needs to find a balance between the increased in conduction and scattering by defect sites. As a result there is a conductivity maximum or a resistivity minimum for TCOs; this 'resistivity well'.It has been reported that there is a correlation between the apparent as-deposited colour of ITO films and the film resistivity and O_2 and Sn doping concentration [23]. For low doping concentrations, the resistivity is high due to the low carrier concentrations and low for high doping due to scattering from oxygen vacancies which reduces the mobility. This resistivity well trend was also observed as function of the sputtering power density. Increase in the power density generates ionised impurity centres inducing the scattering of free electron carriers and leading to reduction of mobility. The gradual increase in carrier concentration between power density of 1 and 3 W/cm^3 is due to the increase in the quantity of substituted Sn ions in the lattice. Further rise in sputtering power results in the carrier concentration plateauing which is due to the uptake of Sn ion substitution and reduction oxygen vacancies from the ITO film crystallinity.

Many studies have reported that there is a strong correlation between resistivity and annealing/deposition temperatures displaying similar curve trends as that of the power density which can also be explained by the same mechanism and as such undergoes similar physical transformation. In addition, varying the oxygen flow also presents the resistivity well effect; with relatively low oxygen content, high carrier densities are observed and vice versa, high mobility is observed with increasing oxygen content due to the enhanced crystallisation. Since both mechanisms oppose one another in terms effects, a minimum resistivity can be seen with varying levels of oxygen flow. To summarise, the resistivity and physical appearance of the ITO films displays trends as a function of a number of parameters such as doping content, deposition power, substrate temperature and oxygen flow.

2.1.3 Optical Transparency

There are some metal oxides that are electrically insulating but optically transparent in the 380 to 780nm wavelength range more specifically in the visible region; MgO and Al_2O_3 are such examples. Thus, this property makes them ideal for fulfilling the role of a window in optical applications. The optical transparent range of various materials can be seen in **figure 2.7**.

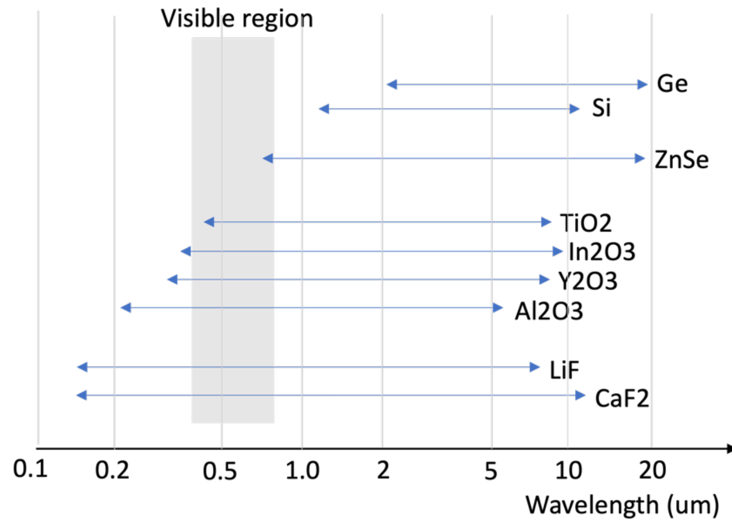

Figure 2.7. Optical transparent regions in a rage of materials [16]

Typical oxide-based compounds exhibit high level of transparency in the 300nm to 1200nm wavelength range which includes the visible region. Fluorides such as LiF and CaF_2 possess a significantly larger window range than oxide particularly in the deep ultraviolet region. In Contrast, the window range of conventional semiconductors such as Si and Ge can only be found in the IR region. Therefore, it is expected for TCOs to exhibit transparent properties in the visible range. **Figure 2.8** illustrates typical transmission spectrum of a single crystal oxide.

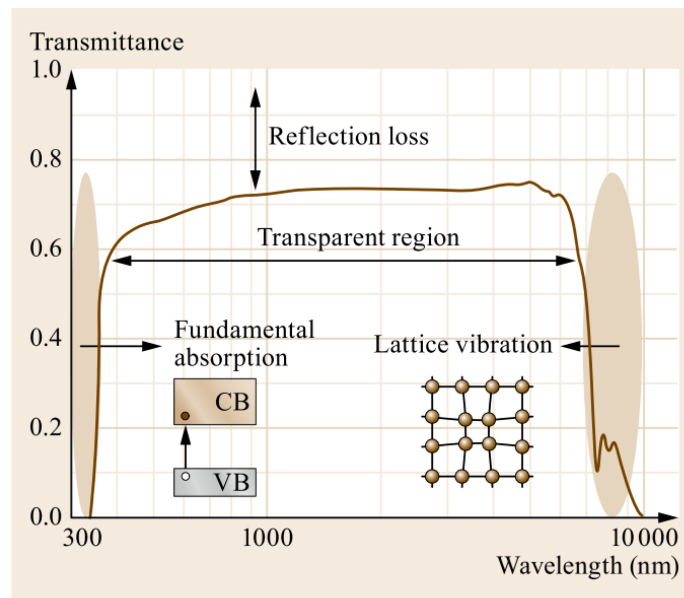

Figure 2.8. Transmission spectrum of a typical oxide [16]

As can be seen in **figure 2.8**, the absorption edge is dictated by the vibration in the lattice in the IR region; Furthermore, the electron excitation from the valence band to the conduction band results in the

fundamental absorption in the ultraviolet region. Optical absorption and reflection are impacted by introduction of new carriers into the parent material of TCOs. The collective motion of the carriers exhibit plasma-like properties in conductors. Upon the irradiation of an electromagnetic wave, the carriers oscillate at the frequency of the light which is referred to as plasma oscillation; this leads to light being reflected at the surface of the conductors. However, upon exposure to light at higher frequency, the charge carriers cannot match the fast electric field oscillation of the light and as a result, leads to the transmission of light through the conductors without causing plasma oscillation/reflection at the surface. The maximum threshold frequency that permits the oscillation of the plasma is known as the plasma frequency, ω_p and can be expressed by equation 2.6 [27]. The plasma frequency then can be converted the wavelength as shown in equation 2.7:

$$\omega_p = \frac{ne^2}{\varepsilon_0 m} \tag{2.6}$$

$$\lambda_p = \frac{2\pi c}{e}\sqrt{\frac{\varepsilon_0 m}{n}} \tag{2.7}$$

Where n, m and ε_0 and c represents the carrier concentration, electron rest mass, permittivity, and speed of light in a vacuum respectively. For a metal with high carrier concentration such as Al (>10^{22} cm^{-3}), the threshold wavelength can be found in the vacuum ultraviolet region and the reflection of visible light takes place at the surface [28]. On the other hand, the carrier concentration of ITO is one order of magnitude small than Al metal, the threshold wavelength shifts to the IR region of the spectrum, which leads to transparency in the visible region as ITO possesses a large enough bandgap (>3.5eV) to exhibit such behavior. As the carriers make the optical window of oxides narrower in the IR region, the maximum carrier of TCOs should be less than $10^{21}cm^{-3}$. Furthermore, the carriers also have an influence of the optical window in the ultraviolet region as well. As illustrated in **figure 2.10**, the bandgap can be calculated by plotting $(h\nu a)^2$ against the energy in eV whereby, *h*, *v*, and *a* are Plank's constant, frequency and absorption co-efficient respectively. With increasing carrier concentration, there is a shift of absorption edges towards the higher side of energy, and a subsequent increase the bandgap ultimately widening the optical window in the UV region. This is associated with the occupation of the conduction band by the carrier electrons as displayed in the schematic inset in **figure 2.10**.

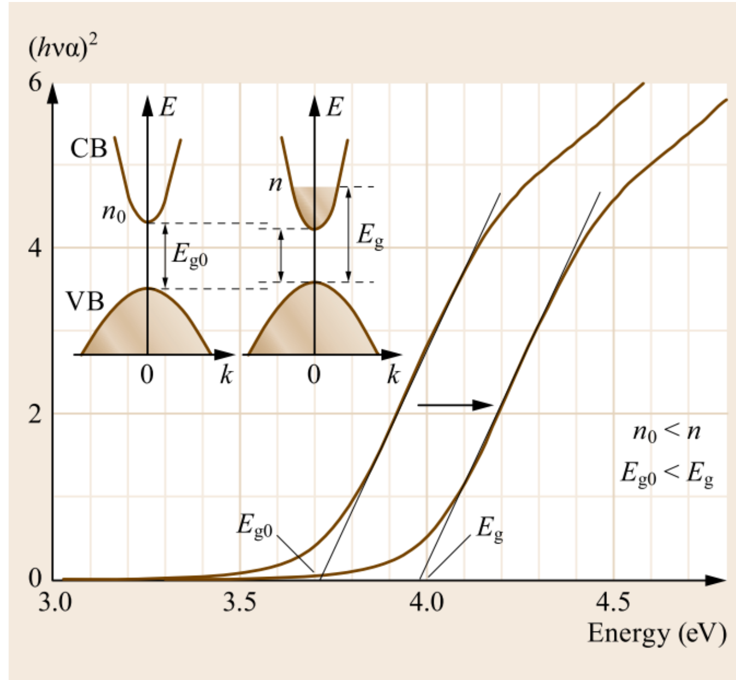

Figure 2.10: Blue shift of fundamental absorption by band filling [16]

Burnstein-Moss shift

To discuss, develop and engineer the making of these materials it is vital that the mechanism by which these materials demonstrate transparency and conductivity is well-understood and can be repeated during experimental trials. In n-type TCOs, the bandgap for the optical transition from the valence to the unoccupied conduction band becomes bigger than the original bandgap E_g due to carrier electrons occupying the bottom of the latter. This phenomenon is known as the Bernstein moss (BM shift) as illustrated in **figure 2.11** which in simple terms refers to widening the optical bandgap of the material

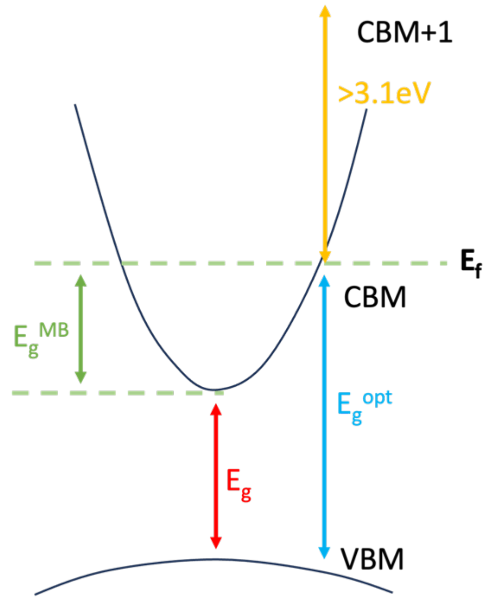

Figure 2.11. Optical widening by the effect of the Moss-burstein shift

The Fermi level, work function (WF), ionization energy (IE), energy gap (E_g), and electron affinity (EA) are fundamental parameters that need to be addressed when discussing TCOs [29-30]. These parameters define the electronic interface between the TCO surface and other materials and control the charge exchange and transport across these materials. **Figure 2.12** illustrates a simple energy diagram of a semiconductor exhibiting the above-mentioned parameters.

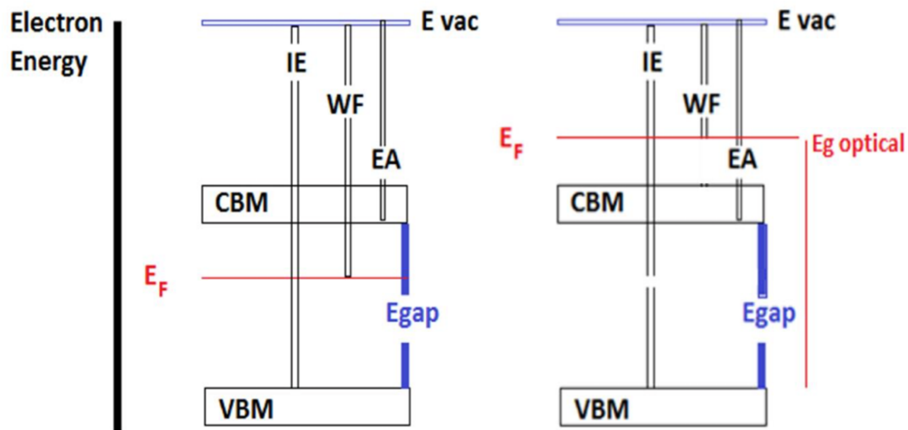

Figure 2.12. (**a**) A simple flat band representation of the energy band at the surface of a semiconductor (**b**) the schematic diagram showing the optical widening of the TCO bandgap using the Moss-Burstein shift, E_g^{MB}.

As electrons are naturally bound to the solid, they are prevented from escaping outside of the material into the vacuum via an energy barrier that culminates at the vacuum level (E_{vac}). Thus, E_{vac} is the

energy level of an electron resting within close vicinity outside the solid. At this vicinity, the electron is experiencing the full impact of the surface dipole. To get an electron from the *VBM i*nto the E_{vac} region, a certain amount of energy is required, and this is referred to as the ionization energy, IE hence when thinking of n-type doping of a TCO material or a semiconductor, the ideal doping material should have low E_I. If an electron drops from the E_{vac} region into the *CBM* level, it will release some energy, and this is referred to as the electron affinity (E_A) of the material [30]. The work function (Φ) is defined as the energy required to take an electron from the Fermi level and place it in the E_{vac} region. In a semiconductor, the Φ is dependable on the E_{vac}, and the Fermi level (E_F) is governed by the doping concentration, density of states, carrier density and temperature.

The parameters discussed in this section fundamentally depend on the technique by which the material is produced and prepared. It is ultimately the arrangements of the atoms next to each other that defines the final material's composition and properties. Hence, the preparation technique and operation method of arranging the constituting atoms of a TCO will govern the quality of the produced transparent conductive film.

2.1.4 Hydrogen Doping

While ITO is the most widely used TCOs, Zinc Oxide and related compositions are an alternative and, in some cases, the preferred materials. A big proponent of the deployment AZO is that it combats the global shortage of Indium. AZO is extensively being employed as TCOs in thin film solar cells such as CIGS and CZTS, in addition to its use as electrical contacts for laser diodes and LEDs. The n-type semiconductor possesses a direct bandgap of 3.37 at room temperature. The high conductivity of the thin film material was initially debated to be due to the oxygen vacancies and/or Zn interstitials [31], however it has been proposed that the unintentional substitutional Hydrogen impurities are the primary driving factor for the high conductivity [32]. ZnO films are usually doped with Al (AZO), Gd (GZO), excess Zn, or In to obtain highly conductive and transparent compounds [33,34]. This material is also often alloyed with other TCO materials and can be a potential alternative as it has the cheapest and most abundant atomic constituents with no significant toxicity associated with elements such as cadmium or lead. However, pure zinc oxide does not possess the required electrical properties to match those of IZO or ITO. Doping zinc oxide with hydrogen is a cheaper option that can significantly improve the conductivity of this material, and this was initially observed in 1950s [35,36].

The mechanism by which hydrogen incorporation into the zinc oxide lattice promotes n-type conductivity was theoretically investigated by van de Walle by first principal calculations based on density functional theory (DFT) [37]. The behaviour of interstitial hydrogen in zinc oxide was studied by van de Walle, and the formation energy of H^+, H^-, H^0 and H_2 states in bonding centre and anti-bonding locations were evaluated, where H^+ demonstrated the lowest formation energy. The study showed that with incorporation of the hydrogen, an O–H bond forms along the direction of the original O–Zn bond. The strength of the O–H bond is the main driving force for stabilisation of the low energy H^+ configuration. van de Walle concluded that H^+ is the stable charge state for all Fermi level positions in ZnO and acts as a donor [38]. The formation energy of the H^+ was shown to be low enough to allow for large solubility of hydrogen in ZnO. It is interesting to note that hydrogen is amphoteric in other semiconductors, although not in ZnO. This difference is due to the strong O–H bond, which lowers the formation energy of H^+. Parallel to this, a complex consisting of an oxygen vacancy and a hydrogen atom acts as a shallow donor.

Such vacancies are low energy defects [38] and neutral, but the hydrogen turns them into a shallow donor, and as such, a hydrogen located close to the centre of such oxygen vacancies acts as a substitutional impurity [37]. These theoretical observations were then verified by electron nuclear double resonance and Muon spin spectroscopy [39,40]. The Fermi energy level where the positive and negative charge states are equal in energy occurs above the conduction band minimum in ZnO [41]. Thus, overall it can be seen that in a ZnO system, hydrogen acts as donor atom as H^+, providing the lattice with an extra electron as a charge carrier, which in turn makes ZnO an n-type material and influences the conductivity of the material.

However, apart from carrier density, the mobility of the charge carriers is an even more important feature of a potential conductor. Mobility is the measure of the velocity of carriers under an electric field and is inversely proportional to the effective mass of the charge carrier. The effective mass is inversely proportional to the second derivative of energy with respect to the k-vector in an E–k plot indicating how the electron states are spaced in k-space. E-k plot is the curvature of the energy band in a way that the larger curvature of the energy band translates to a smaller effective mass of the charge carrier [42]. The energy value computed in the E–k plot is governed by the orbital overlap of adjacent atoms, where the larger the orbital overlap is, the larger will be the drift of the charge carrier.

Parallel to the electrical properties of hydrogen-doped zinc oxide, several reported studies indicate doping of ZnO with hydrogen gives ferromagnetic properties to ZnO [43-45].

Hydrogenated ZnO nanoparticles are reported to demonstrate ferromagnetism because due to low formation energies, the formation of Zn vacancies and OH bonding by hydrogen is favoured in the hydrogenation process, leading to a magnetic moment of ~0.57 μB (Bohr magneton), and the origin of ferromagnetism is explained through the hydrogenation of the ZnO polar surface [46,47].

There are some experimental reports on electrical conductivity improvements achieved in the ZnO system with the addition of hydrogen with respect to TCO materials. However, such reports only exist at the research state, and no commercial TCO based on pure ZnO doped with hydrogen is present in the market as far as literature is concerned. This work was on enhancing the electrical properties of IZO and ZnO systems by repeated exposure of the sputtering target to an argon/hydrogen mixture as the working gas [48] which will be presented in chapter 6. In one of the set of experiments interesting complexities associated with reactive hydrogen/argon sputtering of un-doped ZnO targets was obersved, which is believed to be associated with the reported magnetic properties of hydrogenated ZnO particles, and this report outlines the mentioned observations.

2.1.5 Fabrication methods

In order to optimize the performance and the cost-effectiveness of TCO films, a wide array of synthesis techniques have been developed over the years. Among these are chemical vapor deposition (CVD), sputtering techniques (DC, RF, magnetron), evaporation (reactive, thermal or e-beam), spray pyrolysis and pulsed laser deposition (PLD). Certain synthetic routes are chosen for TCO manufacturing due to their thickness uniformity, low production costs or high throughput. Each fabrication technique can have an influence on the intrinsic behaviour differently including structure morphology and composition of the thin film which in turn dictates the electrical and optical properties. Physical Vapor Deposition (PVD) techniques, such as Magnetron Sputtering (MS) or Pulsed Laser Deposition (PLD) allow

for the synthesis of TCOs with extremely low resistivity and sheet resistance (i.e. specific resistivity per unit thickness) in the most common TCOs. Sputter deposition has been favoured over other techniques in certain instances as it's able to meet industrial requirements such as fast deposition and high throughput. Other advantages are the low complications in the growth of films, possibility of growing films on relatively large substrates, and reproducibility [49,50]. In the case of ITO, the best available sputtered thin films commonly have resistivities slightly lower than 10^{-4} Ω cm, with sheet resistances typically smaller than 10 Ω/ square [50]. With PLD even lower resistivity values can be obtained (down to $7 \cdot 10\ \Omega^{-5}$ cm [52]) with the drawback of decreasing the deposited area [53].

2.1.6 Conclusion

In summary, the possibility of a semiconductor being both transparent and conductive is due its large bandgap so that it can avoid absorbing visible light (~3eV). The gap is located between parabolic oxygen 2p and metal *s* bands, resulting in the formation of the valence and conduction band respectively. Free charge carriers are generated by introducing dopants which are responsible for the conductivity. Electron densities are generally in the order of 10^{20}cm^{-3} for n-type TCOs yielding degenerate electron systems. Scattering mechanisms dominate the electrical conductivity which are strongly related to the electron concentrations. The mobility is influenced by the total contribution of all electron scattering which deterring the upper limit of conductivity. The ionised impurity scattering is considered to have the biggest impact for single crystalline materials. Conversely, as the structural nature of the thin film decreases, scattering via grain boundaries become more significant in polycrystalline films. The transparency window for TCOs is exhibited in the UV and near IR region. The bandgap determines the window in the short wavelength region and the plasma frequency dictates the window in the long wavelength region. Both values depend on the electron concentration and thus can be tuned to use in specific applications. The electrical conductivity of typical n-type TCOs is around 10^4 whilst display transmission as high as 90% in the visible region. The conductivity of TCOs of a p-type nature is generally lower than the n-type counterpart by at least a factor of 1000. Although the figure of merit is a measure of the TCO's electrical and optical performance, the thin film TCOs are engineered to possess properties tailored for specific applications. There are a wide variety of deposition techniques for these types of materials, sputtering being widely utilised to yield highly transparent and conductive thin film TCOs. Each type of growth will have its own unique influence on the intrinsic properties as thin film structure and composition. It is these properties (not the deposition method itself) that will have an emphasis on the electrical and optical performance of TCOs.

Plasma sputter deposition technique does not behave like a standard chemical reaction or a process with defined steps. For example, researchers who apply this technique for TCO preparation usually report their findings by stating the condition of the sputtering process, such as chamber pressure, plasma power and the gas composition of the chamber during deposition. However, from one sputter machine to another, depending on the dimensions of the chamber, the size of the targets, and a few other design related issues, TCO coatings with different properties are obtained, even if the sputtering conditions are maintained according to an earlier report. The sputter deposition process will be discussed in greater detail in the next section (2.2) from the constituents of a plasma discharge to the different types of discharge used to power the plasma.

2.2 The Glow Discharge

2.2.1 Brief History

The term ‘plasma’ was first introduced by Irving Langmuir in the 1920s [54]. Many physicists studied the behaviour of DC electrical discharges in gasses at low pressure during the 19th century [55]. Various experiments concerning tubes under vacuum were conducted to portray the strange behaviour of the plasma.

Applying an electric or magnetic field to the plasma leads to the preferential hearing of charged particles such as electrons and ions keeping the neutral gas atoms at low temperatures. Electrons with low mass in particular are easily accelerated to ionisation energies of the gaseous atoms; the kinetic energies of these electrons range from 1-10eV (equivalent to ~10^4-10^5 K). Due to the low gas temperatures of the plasma discharge, it is often called cold plasma. Plasmas of this nature are not in thermal equilibrium since [56]:

$$T_e \gg T_{gas} \,\&\, T_e > T_i > T_g \tag{2.8}$$

Whereby T_e, T_g and T_i are temperatures of the electrons, neutral gaseous atoms and ions respectively.

DC and RF glow discharges are two of the most common types of electrically induced plasma where the electric field of the latter is coupled with either capacitively or inductively to the electrons of the discharge. [56]

The scientific evaluation of plasma discharges was explored in the latter half of the 19th century which paved the way for the advancement made in vacuum technology. It was observed that when air was pumped out of glass vessels in an high potential environment, the high voltage electric spark between two electrodes created a variety of colourful ribbon like discharges as the gas pressure was lowered in a progressive manner. In 1994, Faraday discovered the formation of a dark space near the anode of the discharge tube as the gas pressure of was reduced demonstrating the presence of dark discharge of electricity in gases [55].

Technological advances in quartz/glass tube construction and progression of electrode material played a vital part in the investigation of the various types of the glow discharges [56]. In mid 19th century, Geissler came up with a technique for the assembly of glass discharge tubes with metal electrodes and introducing a mercury pump. Plucker noticed that effect of phosphoresce in the glass with the reduction of gas pressure. As a result, multiple investigations were conducted to identify the root cause of this effect. The use of X-ray was explored, furthermore the measurement of the electron charge to mass ratio was made operating discharge tubes at low gas pressures (10^{-2} to 10^{-3}mmHg). J.J. Thomson and F.W Aston discovered that the ‘Positively charged rays’ could be passed from a glow discharge through a hole in the cathode which led to the development of the mass spectrometry of ions [55]. The in-depth research work conducted on plasma glow discharges played a pivotal role in the development of modern physics [56].

2.2.2 Introduction to glow discharge and applications

The term 'glow discharge' is derived from the plasma's luminosity. This is produced because electron surpass the threshold energy and density threshold to generate a visible light via recombination and excitation collisions [55]. Glow discharges can be found in a wide variety of applications such as gas fluorescence lamps, neon lights and flat panel plasma screen displays. Aside from the light industry, its use can be found in the microelectronic industry and the material processing technology. Such use include treatment and etching of surfaces (for the fabrication of integrated circuits (IC) etc), modification of polymer and the deposition of thin film coatings. Other forms of glow discharge such as DC parallel plate plasma reactors, electron bombardment plasma source, are also employed in industrial applications.

The glow discharge is fundamentally produced by applying a potential difference (ranging from 1V to few kV) between two electrodes in vessel or chamber filled win an inert gas under reduced pressure (from a few mTorr to atmospheric pressure) [57]. The electrons are then accelerated away from the cathode and the collision with the gas atoms and electrons goes up as a result of the potential difference. The collisions may lead to processes such as excitation, ionisation and dissociation. Excited species generated from collisions can get demoted to lower energy levels by the emissions of light which is responsible for the 'glow' in the discharge. Secondary electrons are released when ions accelerate towards the cathode and bombarde its surface. These types of electrons are then accelerated away from the cathode surface giving rise to more ionisation collisions and subsequently yielding ion-electron pairs; the ion-electron multiplication process enables the plasma discharge to sustain itself [57].

Different types of glow discharge.

There are a range of glow discharges the most basic type being the direct current (DC) glow discharge. A constant current is produced by applying a potential different between the cathode and anode. This could lead to issues if one of the electrodes in non-conducting such as a build up of charge and resulting burn-out of the glow discharge [57]. A capacitively coupled radio-frequency (cc rf) can be applied to overcome by this issue i.e. applying an alternating voltage between the two electrodes. The accumulation of the charge during one half cycle is neutralised by the opposite charge accumulated during other half cycle giving rise to an alternating current glow discharge. This can be described as short discharges being struck consecutively whereby the cathode and anode constantly change roles. An important feature of alternating current (AC) glow discharge operating at atmospheric pressure is the dielectric barrier discharge (DBD) i.e. the electrodes are typically coated by a dielectric barrier [57].

Another type of glow discharge is one that is sourced with a pulsed current. The pulsed glow discharge consists of intermittent glow discharges (in the milli/microsecond range) which is then followed by an afterglow which is typically characterised by a lengthy time period in comparison. This type of discharge is advantageous because a high peak electrical power can be attained for a low average power; this results in high peak efficiencies for various applications [57].

The magnetron discharge is a well-known type of discharge in which a magnetic field is applied whereby the electrons are subjected to helical circulation around the magnetic field lines resulting in more

ionisation. This type of discharge is typically generated in low pressure high current environments in comparison to conventional discharges.

Several new types of glow discharge have emerged whereby they are characterised by low pressure and high plasma densities. The key difference lies in the application of the electrical power; it is applied by electromagnetic induction and not by applying a potential difference between two electrodes that's found in the conventional glow discharges. This is known as inductively coupled discharge whereby, as the name suggests, there is an inductive coupling between the RF power and plasma. The other type of plasma discharge is struck with microwave power whereby the microwave discharge and magnetic field gives rise to ECR conditions [55], the operating principle of which will be briefly touched on.

Plasma sheath

Deposition system used in this project confine the plasma within a vacuum system resulting in the plasma species interacting with elements contained in the system. As electrons have higher thermal velocities than ions [59], their interaction with the walls occur faster than that of the ions. This leads to the development of a negative bias at the chamber walls attracting ions that give rise to a potential difference; this phenomena is known as plasma sheath (**figure 2.13**)

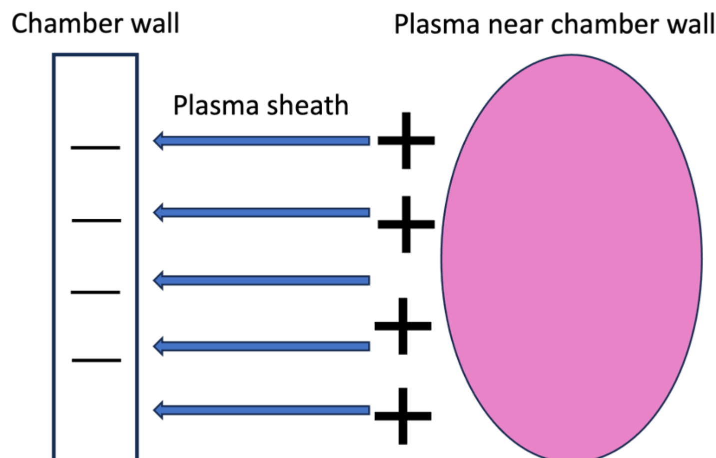

Figure 2.13 Interactions of charged particles with chamber wall giving rise to a plasma sheath

The sheath is in a dynamic balance; recombination of ions at the chamber surface occur as well as further surface recombination by electrons possessing high enough energy to overcome the energy barrier of the plasma sheath. Debye shielding prevents the potential to be distributed throughout the plasma, so the sheath confines the more mobile species within the plasma [60]. The potential difference of the sheath region can be calculated via the following equation 2.9:

$$V_{sh} = V_p - V_f \tag{2.9}$$

Where V_{sh} is the potential of the sheath, V_p is the plasma potential which oscillates with the waveform for RF and/or microwave plasmas. V_f is the floating potential which is the value held by an isolated substrate within the plasma. Bombardment of the substrate by the ionised growth species and carrier gas electrons take place at the sheath potential. This is due to the potential of the substrate attaining a dynamic equilibrium with equal flux of both positive and negative species as a result of its isolation. There

is a presence of sheath conditions in all surfaces of a plasma system. While the surfaces will be grounded (i.e. 0V potential difference), it is possible to floating potential across desired components of the system such as the sample holder, a technique which was not explored in this project.

2.2.3 DC glow discharge

The glow discharge via DC has been historically paramount to the evaluation of the properties of the plasma medium and application. The typical setup consisted of a long glass cylinder with an anode and cathode electrode on either side with an operating pressure ranging from 10mTorr to 10 Torr; a typical voltage of a few hundred volts was found between the two electrodes maintain the discharge. A summary of the range of parameters used for the glow discharge can be found in table.

Figure 2.14. illustrates the I-V characteristics of the DC low pressure electrical discharge tube. It can be seen that the current across the Townsend discharge region soars up with an increase in voltage through the dark discharge regions. When the breakdown voltage at point E is reached, the gas will breakdown at voltage V_b provided that the internal resistance of the power supply is relatively low. The discharge will then transition into the normal glow discharge.

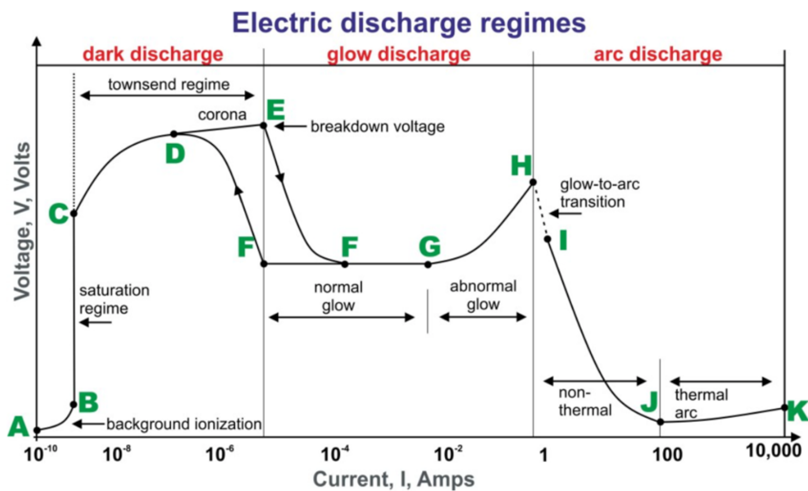

Figure 2.14: Typical V/I plot of a glow discharge including key characteristics such as breakdown voltage, the voltage current characteristic and the structure of the discharge depend on the geometry of the electrodes, the gas used, the pressure and the electrode material [58]

The normal glow discharge region is between F and G whereby the voltage is somewhat independent of the total current passing through the discharge tube; the current density approaching the electrode neither depends on the total current. This essentially means that in the normal glow discharge area, there is only small point of constant between the plasma and the cathode surface at low current. As the current increases, the total cross section of the cathode is occupied by the plasma-surface contact; this occurs until point G, the boundary of the abnormal glow discharge is reached whereby the plasma fully covers

the cathode surface, to deliver the total amount of current required at a constant current density. As the total current increases, the voltage also rises so that the cathode current density it above its setpoint and provide the required current. At point H, due to the heating of the electrodes, there is a thermionic emission of electrons from the cathode. This is then followed by a glow-to-arc transition if the DC power supply's internal resistance is relatively low [57].

The qualitative characteristics of a normal glow discharge

Figure 2.15 shows a classical electrical discharge in the normal glow region. Michael Faraday made the first observation of the glow discharge characteristics in the 1830s thus these have been named after their respective investigators [55]. The appearance of the glow discharge can be categorized as follows:

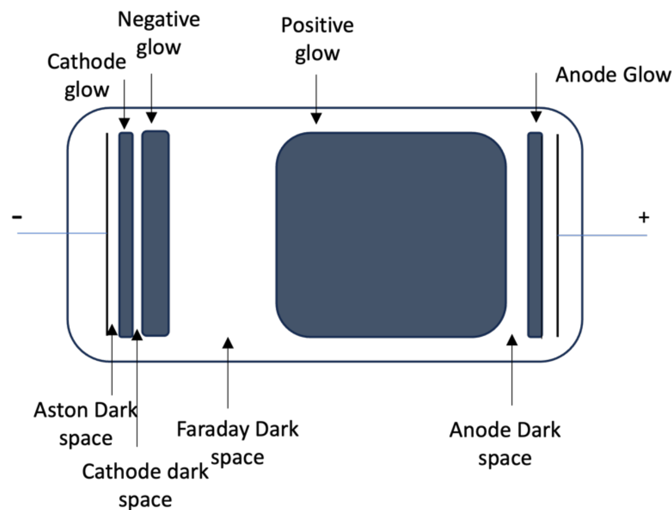

Figure 2.15: Typical characteristics of a normal glow discharge

- The cathode

The emission of secondary electrons at the surface of the cathode is pivotal for glow discharge to sustain itself. The Townsend theory of gas discharge takes into account the bombardment of ions at the cathode surface as a secondary source of electrons [61]; it defines the coefficient of secondary electron emission as the number of electrons emitted from the cathode per ion bombardment thus the current density is defined by:

-Aston dark space

The Aston dark space is essentially a thin region near the cathode with a strong presence of electric field and negative space charge. It is occupied by slow electrons which will be accelerated from the cathode. The density and energy of these electrons are too low to excite the gas hence the presence of dark space. The initial stray electrons and secondary electrons overcome the ions in this region due to the negative space charge [55].

-Cathode glow

The region next to the cathode flow contains a relatively high density of ions known as the cathode glow. The electrons in this region possess sufficient amount of energy for collision with the neutral atoms to occur and excite them. It often illuminates orange/reddish due to the emission excited atoms and/or incoming positions ions approaching the cathode and being sputter off the surface. The axial length of this region is dependant upon the type of gas and pressure. The cathode glow can from time to time conceal the Aston dark space by clinging onto the cathode.

-Crookes (or Hittorf) darkspace / Cathode Fall

This Crookes dark space is region in which there is a presence of a moderate electric field and where a good portion of voltage drop happens. It contains a positive space charge and relatively high ion density [55]

-Negative Glow

The intensity in this region is the brightest in the entire discharge. The negative glow is most intense near the cathode side with a low electric field in comparison. It is longer than the cathode with the electrons carrying the entire current in this region. The bright light output is owed to the electrons being accelerated towards the cathode resulting in ionisation and intense excitation. These electrons eventually slow down and no longer provide energy for excitation as they approach the faraday dark space. The electron number density in the negative glow region is approximately 10^{16} electrons/m^3 [55]

-Faraday Dark Space

In this region the energy and density of the electrons is low as a result of recombination and diffusion to the walls. In addition to the small net space charge, the axial electric field is also relatively minute [55]

-Positive Column

The positive column is defined as a quasi neutral region with a relatively low electric field, in the range of 1 V/cm and is just about sufficient enough to maintain the required degree of ionisation near the cathode end. The length of this region varies with the distance between the electrodes at a constant pressure and constant voltage drop as opposed the lengths of the other regions which maintained and unaffected by this. The electron number density in this region ranges from 10^{15} to 10^{16} electrons/m^3 with electron kinetic temperature of 1 to 2 eV. A long uniform glow is observed in the positive column; other phenomena seen include moving striations which are spontaneously triggered and ionisation waves which are a caused by disturbance. A glow discharge in the positive column illuminates a pinkish to blue colour [55].

-Anode Glow and Dark space

This brightness in this region is marginally more intense than the positive column. It is a the end of the positive column and is not always present. This is the boundary of the anode sheath and can be found on the right end of the positive column; however, its presence may not always be observed. The anode dark space lies in between the anode glow and the anode itself. Electrons travelling for the positive column to the anode gives the anode sheath a negative space charge. Furthermore, the electric field in

the anode space is more profound than the positive column. Positive ions accelerate away from the anode leaving a negative charge density which subsequently results in a voltage drop [55].

2.2.4 Radio Frequency Discharges

DC electrical discharges discussed above extract 'true current' from the power supplier via the flow of ions and electrons to the electrodes. Physical processes in such discharges are dominated by axial DC electric field. One of the most ground-breaking developments made in this space is the introduction of radio frequency to power the glow discharge. When the applied frequency becomes high enough, the oscillation period will be relatively similar to the time it takes charged particles to move across the sheath between the plasma and electrode. Whilst it is very similar to DC glow discharge in many ways, the differentiating factor between the two is that the rf counterpart can be applied to nonconductive insulating samples and is not just limited to electrically conductive materials. In addition to this, there are other more subtle differences between the two such as number densities, energy distributions of charged particles which can affect the efficiencies of important physical processes such as excitation and ionisation.

While DC discharges are relatively cheaper to operate, the RF glow discharge is superior as it provide several advantages such as a wider range of operating parameters, more stable plasma, less prone to surface oxidation and more enhanced sputtering depths [62]. Glow discharge processes use for treating insulating materials are often powered by a high frequency in the MHz range. For an AC discharge, conventional frequency of roughly 50Hz was not found to be an effective for processing insulators; this is due to the mismatch in the insulator charge up time and the periodicity of the AC supply leading to short-lived discharges with electrodes successively changing polarities. [63]

RF Plasma Interaction

Radio Frequency power coupled to the plasma through either oscillating magnetic, electric fields or both. The extent of the interaction between the oscillating fields and the plasma depends on a number of parameters such as the frequency of the oscillation, electron plasma frequency and electron collision frequency in the plasma.

The electron plasma frequency is a function of the electron number and the critical density given by:

$$\omega_{pe} = 2\pi v_{pe} = \sqrt{\frac{n_e e^2}{\varepsilon_0 m_e}} \tag{2.10}$$

If the incident electro-magnetic (EM) frequency is below this, the inertia of the electrons is low enough such that they illicit a response to the electric field in the incident EM wave and therefore the electrons are able to absorb the energy from it. The absorption of this energy may convert to heat via collisions, or be re-radiated in the from the reflective EM wave from the surface of the plasma.

If the frequency of the incident EM radiation is higher than the electron plasma frequency, then the electron is not fully able to respond to the incident EM wave as its inertia is too low. This leads to the propagation of the EM wave through the plasma as a quasi-optical dielectric medium, whereby the interaction between the incident EM radiation and the individual electrons is relatively insignificant [64].

The RF plasma discharge is highly utilised in the sputtering of a wide range of thin film semiconducting materials. The principle operation of this technique involves the bombardment of a source material with energetic ions, typically inert gas ions, such as Argon (Ar^+). The forceful collision of these gas ions results in the ejection of surface atoms from the target material under an RF plasma condition generated at a frequency of 13.56MHz. This results in the deposition a thin film of the target material onto the substrate.

The RF frequency is coupled to the target material via an impedance matching network and blocking capacitor as shown in fig 2.16. The blocking capacitor makes sure that the time average net current to each electrode equates to 0. As RF power is applied, there is an oscillation of electrons between the two electrodes resonating with the frequency of the rf power.

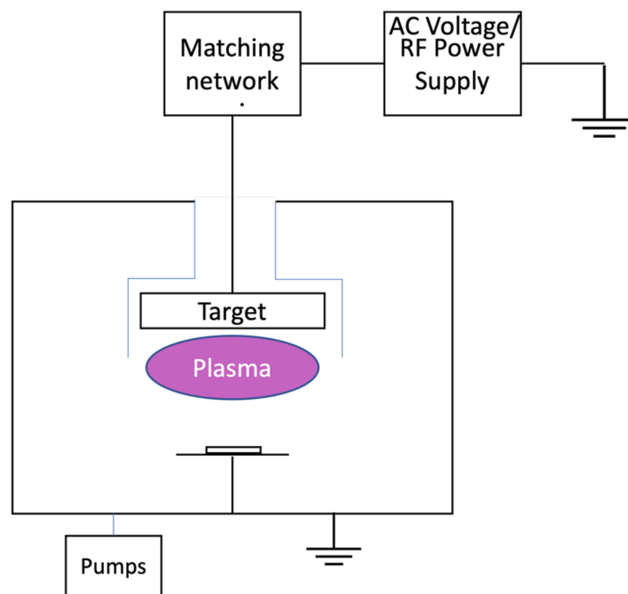

Figure 2.16 Schematic diagram of an RF sputtering system

The AC voltage/RF power supply in sputtering oscillate at a frequency that is adequate. Too low a frequency leads to the neutralisation of the target by the positive ions during the negative half-cycle and electrons neutralising during the positive half. In this case, sputtering does not occur as a result of the lack of ion sheath. Because electrons have a smaller effective mass than ions, they respond to the change in target polarity more rapidly than ions [65]. At the typical industrial radio frequency of 13.56MHz, the ion mobility is too low for it to oscillate and therefore most ions can be essentially found in the central region of the plasma [64]. During the positive half of the cycle, the target will attract many electrodes acting as an ion; conversely the counter-electrode will not acquire as many ions the negative half of the cycle. This will lead to both electrodes possessing a positive bias with respect to the plasma [64]. At some point, the target will no longer capture as many electrons due to its negative bias curing the positive half cycle. It will start acquiring enough ions to negate the gain in electrons during the negative half cycle. The target has a net negative DC bias drawing in the process gaseous ions and generating an ion sheath which leads

to the sputtering and deposition of the target material [66]. **Figure 2.17** shows the voltages in RF sputtering, with the target potential shown in green.

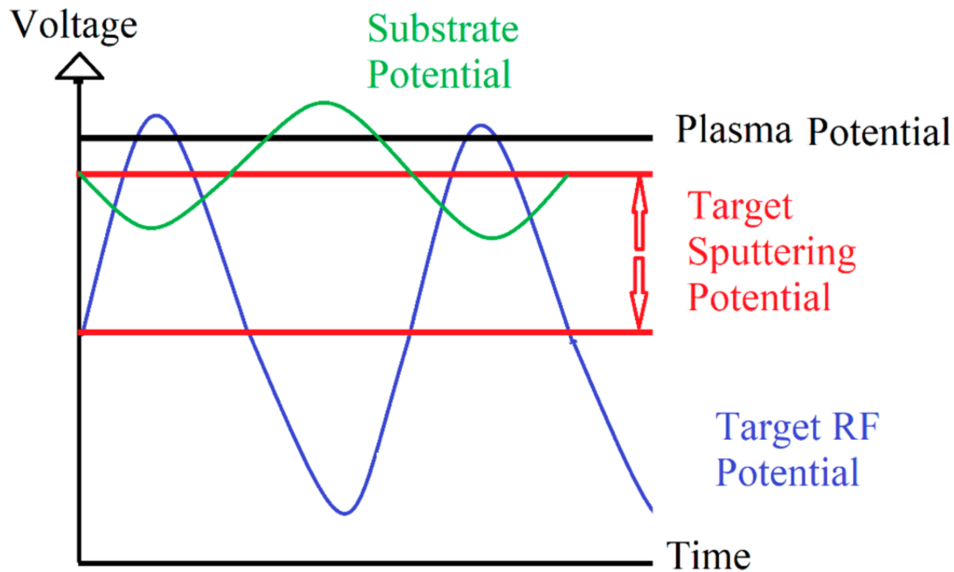

Figure 2.17: Voltages in RF sputtering [66]

It is important to mention the symmetry of the process; if the target and substrate are of the same size and magnitude then there will be complete symmetry, and neither will acquire a DC negative bias relative to each other. Conversely in an arrangement whereby the cathode and anode are not symmetrical, the chamber, in addition to the substrate, can also play the role of the anode.

$$\frac{V_t}{V_s} = \left(\frac{A_s}{A_t}\right)^n \tag{2.11}$$

The ratio of the voltages, with respect to the plasma, measured at the target, V_t, and substrate, V_s, are proportional to the that of the area of the substrate and target area whereby *n* ranges from 1.5-4 and is dependent upon the experimental set-up [67,68]. Therefore, an increased substrate/anode/chamber area raises the relative target potential. The sputtering of the anode and chamber walls will be insignificant If the area ratio is high enough.

One of the major concerns with these earlier sputtering processes was the non-uniformity in the plasma density which subsequently lead to non-uniform film deposition/thickness. Such processes are not acceptable for the deposition of uniform films in the ever growing electronic and optical coating industries.

2.2.5 RF Magnetron Sputtering.

One of the most notable advancements made in sputtering is the addition of magnetrons and it has been regarded as the one of the most effect processes for the synthesis of an array of thin film materials. By applying a magnetic field during the glow discharge sputter deposition process the electrons are trapped within the discharge for a longer period of time yielding the generation of more ions for the same electron density. The probability of ionising a gas atom during their displacement from the cathode to anode increases as the electron trajectory i.e. the mean free path is elongated. Reducing the discharge pressure and the cathode sheath. By this manner, ions can reach the cathode with almost maximal discharge voltage and the sputtered atoms can reach the substrate with minimal collision. A more stable high-density discharge is achieved thus enhancing the sputtering process efficiency. Historically the process was limited by low deposition rates, high substrate heating and low ionization efficiencies. However, in recent times, these limitations have been overcome by the development of magnetron sputtering system.

The process entails generating a strong magnetic field in the vicinity of the target area causing the traversing electrons to spiral along the magnetic flux lines near the target. This environment limits the plasma to the target area without damaging the thin film layer being deposited onto the substrate, whilst maintaining its stoichiometry and uniformity. Adding the magnets behind the target results in the ejection of electrons at an angle that is non-normal to the incidence to the target to orbit the magnetic field. This allows for retention of the electrons within the plasma sheath as opposed to losing them to grounded chamber surfaces which increases the ion generation rate and subsequently the sputter yield. **Figure 2.18** shows the schematic diagram of a basic R.F. magnetron sputtering system and the basic components involved. Ionised Ar atoms bombard a sputtering target which leads to ejection of molecules/atoms from the target forming thin layers onto a substrate.

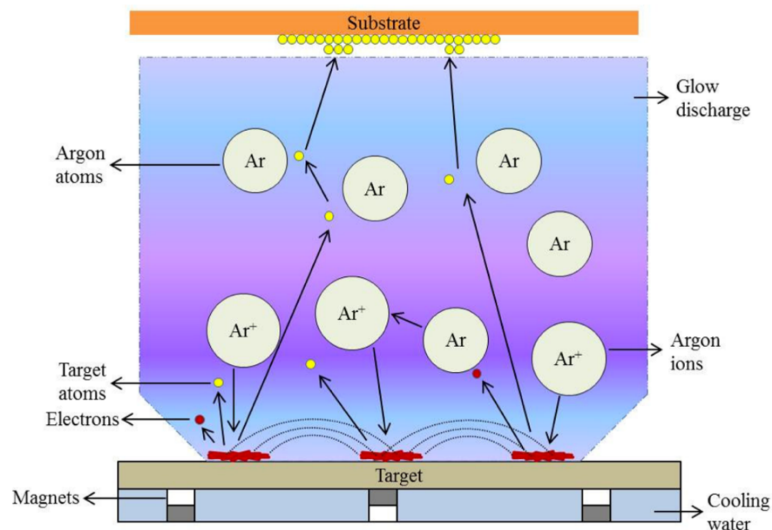

Figure 2.18. Schematic diagram of RF Magnetron Sputtering [69]

Magnetron Types

The magnets can come in various forms, one such example is the post magnetrons; a uniform magnetic B runs parallel to the surface of the cylindrical target. The most widely used type of magnets are planar magnets. As mentioned, the presence of the magnetic field influences the trajectory of the emitted electrons from the target forcing them to orbit in circular motion and bringing them back to the cathode shown in **figure 2.19.** This can be described by the Lorentz equation which is as follows:

$$\vec{F} = q\,(\vec{E} + \vec{v} \times \vec{B}) \tag{2.11}$$

with q the negative charge of the electron, E the electric field over the dark region, B the magnetic field, and $\vec{v}$ the velocity of the electron.

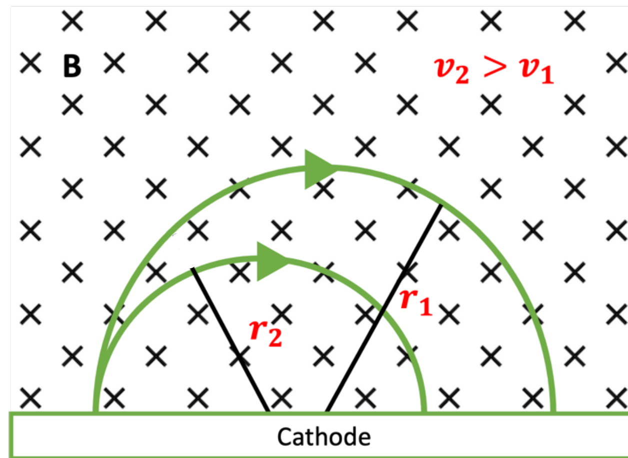

Figure 2.19 Electrons in the presence of a uniform magnetic field follow a circular motion according to the Lorentz force. Magnetic field points into the page

The Lorentz force on the electron depends on its velocity and magnetic field strength and is orthogonal to both their directions. The first component of the electron motion is the movement pattern with respect to the magnetic field lines. A 2nd component is the gyration of the electrons around the magnetic field lines with Larmor radius, r_l; this is the distance between the central point and charged particle i.e. electron and is defined as:

$$r_l = \frac{mv_{\perp}}{|q|\mathbf{B}} \tag{2.12}$$

Where m is the mass of the charged particles, v is the velocity perpendicular to the magnetic field **B** and q is the electrical charge unit.

A third component that is accounted for with respect to the electron trajectory is the **E x B** Hall drift which occurs around the post in a helical motion and is perpendicular to the electric and magnetic fields.

When an electric field is applied to the charged particles, which are already under the influence of a magnetic field, the movement of the particles will alter slightly from the circular motion around the central

point. The electric field will cause the particles to deviate and thus inducing drift in a more helical fashion perpendicular to the electric field and the magnetic field. This is the third component that is accounted for with respect to the electron trajectory known as the Hall drift i.e. **E x B**. This drift component is independent of m, v and p. The electric field E increases with v in one half of its orbit cycle while acting against it in the second phase. This is illustrated in **figure 2.20:**

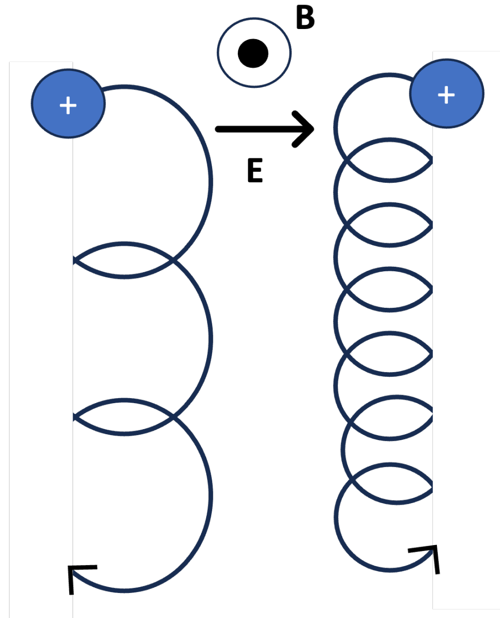

Figure 2.20: Movement of charged particles in a constant electric field

In summary, electrons are moving continuously in one direction around the target and a constantly subjected to acceleration and deceleration close to the surface of the target.

Planar magnets are the most widely used type of magnets. The easy ability to design air-to-air systems for flat substrates make the planer magnets very convenient. The permanent magnets are typically placed behind the target in which there is a central disc magnetic pole and an annular pole allowing for a circular symmetry with respect to the magnetic field lines as shown in **figure 2.21:**

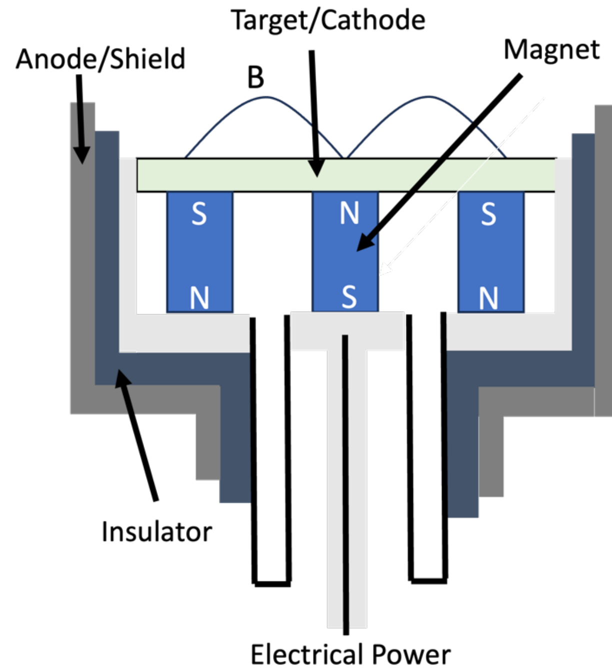

Figure 2.21: Schematic diagram of a Planar magnetron

The magnetic field oriented radially and direct above the cathode surface while the electric field decreases away from the surface. Similar to post magnetron set-up, the resulting effect is cycloid orbits above the cathode surface. The presence of a vertical component of the magnetic field forces the electron to move towards the central region of the magnets. For a circular planar magnetron, the **E x B** drift will be parallel to the target resulting in electrons following a circular path around the target resulting in a high plasma density along this path. **Figure 2.22** shows 2 common planar magnetron arrangements. The configuration of the magnet yields maximum ionisation in the region between the magnets thus most of the ions will be formed at this position. This uniformity leads to a preferential sputtering of the target around a circular region known as 'racetrack' [65] and as a results typical target utilisation is less than 50% even with an optimised magnet design as shown in **figure 2.23**. The placement of permanent magnets behind the sputter target as shown in results in the **B** field lines creating a tunnel in front of the target.

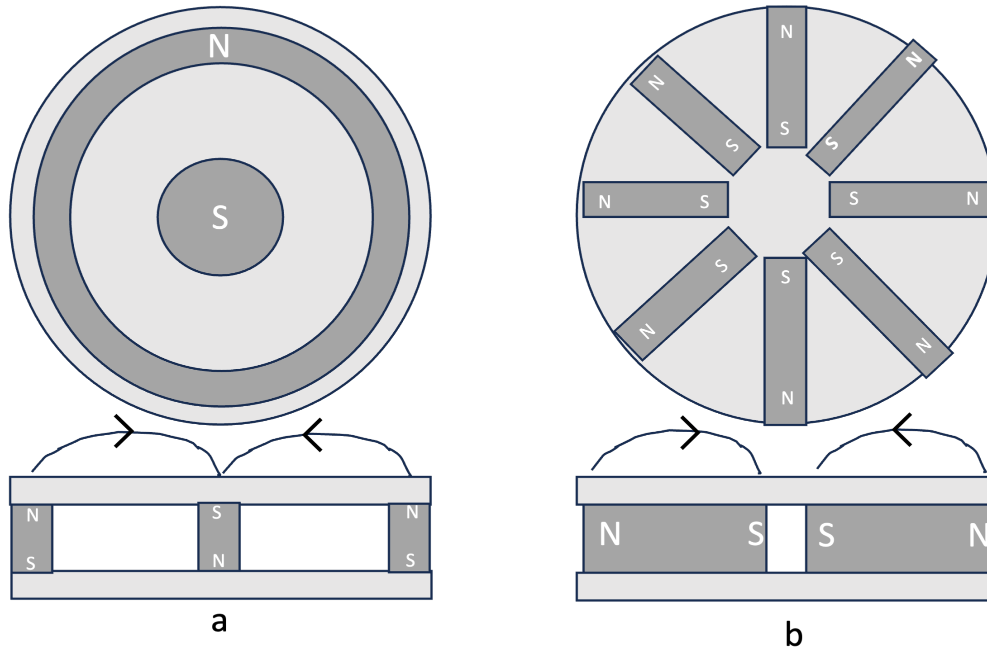

Figure 2.22: Common planar magnetron magnet arrangements

Magnetron Balance

The magnet configuration in planar and rotating cylindrical magnetrons allow for the entrapment of electrons thus generating a high ion density in the vicinity of the target for a given pressure. With an optimum design of system geometry and operating pressure, Electrons are lost from the target area when their energy drops below the ionisation threshold; thus there is a presence low energy electrons in the bulk of the plasma near the substrate. Whilst advantageous to the glow discharge process, in some instances delivering more energy to the substrate also has its benefits. By using an unbalanced magnetron, it has been reported that ion bombardment of the growing films could be increased, which makes the films denser and preferentially orients the crystallites in the growing films. Changing the magnetic field strength of the inner compared to the outer magnet i.e. unbalancing the magnetic configuration, allows for the electrons to escape the magnetic trap and follow the magnetic field lines towards the substrate. This yields a strong electron flux in the vicinity of the substrate. The electron flux and subsequent ion flux can be tuned by adjusting the magnetic field strength balance between the inner and outer magnets. Quantifying the 'K' ratio between the magnetic flux inner and outer magnets is one way to characterise the balance:

$$K = \frac{\phi_{out}}{\phi_{in}} = \frac{\int_{S_{out}} B_{\perp out} dS_{out}}{\int_{S_{in}} B_{\perp in} dS_{in}} \tag{2.13}$$

$B_{\perp}$ represents the magnetic field strength perpendicular to the magnet, and S is the area of the magnet [70].

Shifting the position of the inner and outer magnets with respect to the surface of the target result reduces the discharge voltage which modifies the sputter rate of the target at constant current. The ion-to-atom ratio at the substrate, an important parameter during thin film growth, is modified through the combination of changing position of both magnets. A simpler approach to unbalance the circuitry of the magnetron that's highly tuneable is to implement a external Helmholtz coil which increases the field strength pf the outer magnetic. [71]. This drastically increases the incident ion/atom ratio at the substrate by opening a leak in the plasma trap. Furthermore, the high ion/atom ratios can be attained by using very low ion energies (<10-20) which for the most part do not surpass the film damage threshold. Just as significantly, the substrate bias and the external magnetic field independently control the ion energy and ion flux incident at the substrate respectively. This means that the advantages of an ion beam deposition system can be obtained via high rate magnetron sputtering.

Figure 2.24 illustrate the two types of unbalanced magnetron configurations can be achieved. Type 1 possess a stronger central magnet whereby the ion and electron fluxes to the substrate is reduced. Type II has stronger outer magnets increasing the ion and electron fluxes to the substrate which as discussed yields higher densities and subsequently promotes beneficial ion bombardment effects [72]. Ion currents in the range of 3 to 10 mA/cm^2 have been reported [72,73].

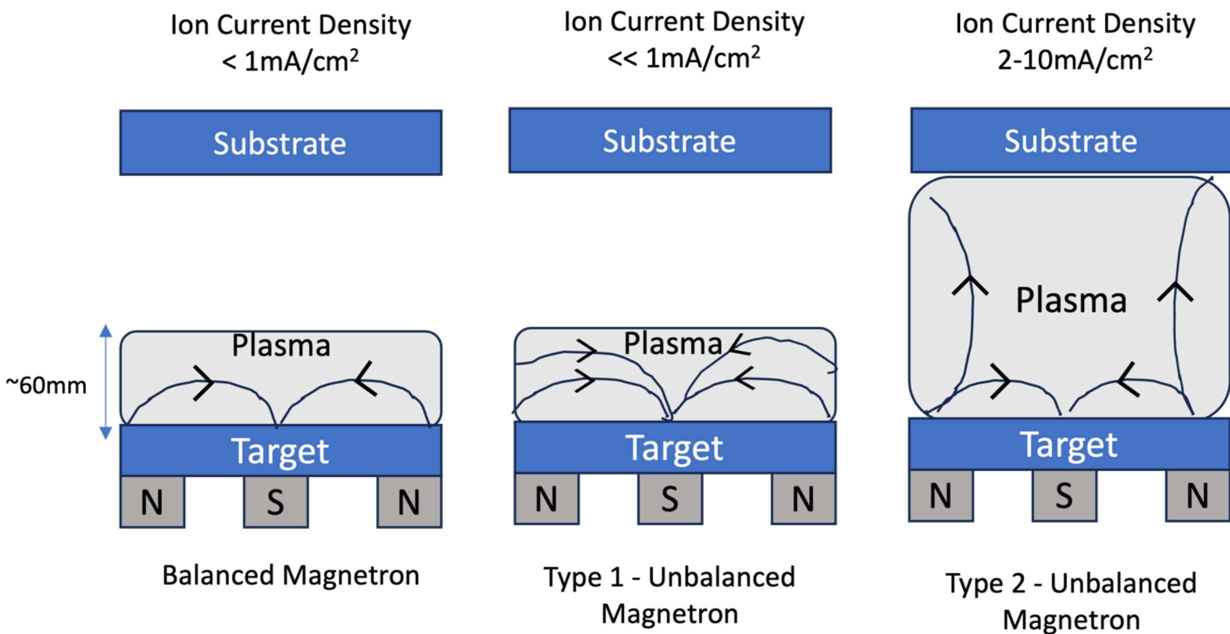

Figure 2.24: a) Balanced magnetron b) Unbalanced Magnetron type I c) type II

2.2.6 Sputtering Efficiency

Numerous variables have an effect on the outcome of the sputtering process e.g. the RF power, gas pressure, deposition time, substrate-to-target height, angle of the target with respect to substrate,

substrate temperature, type of substrate. All of these factors influence the properties of the resulting thin film [74]. Sputter yield and energy of the bombarding ions are of high importance and are primarily dictated by the plasma power [75].

The sputter yield is defined as the rate of deposition and is a measure of the ratio of atoms ejected from the target to high-energy ions incident on the target which is expressed by **equation 1.3.8** [76,77]

$$\Upsilon = \frac{(number\ of\ ejected\ particles)}{(number\ of\ incident\ particles)} \tag{2.14}$$

The sputter efficiency is usually measured in Y per watt of power applied. The binding energy of the target is threshold that must be met or surpassed for the ejection of an atom to occur from its surface. This threshold is dependant upon the effect mass of the target atoms and bombarding ions.; It has been reported that lower binding energies result in more efficient sputtering [76] Ions must possess enough energy upon collision with the target for sputtering to take place which is approximately 25eV. If ions fail to possess this level of energy, sputtering cannot take place irrespective of the incident number of ions. At high energy levels, a reduction in sputtering rates may also be seen as a result of the ions penetrating into the target to deep. The energetic incident electrons on the target do not affect the sputtering process because its energy levels are too small to stimulate the collision cascade [78].

The momentum collision cascade is the process by the energetic ion incident on the surface of the targets causes a sequency of interatomic collisions to occur and subsequently resulting in an atom being ejected from the target which is illustrated in **figure 2.25**.

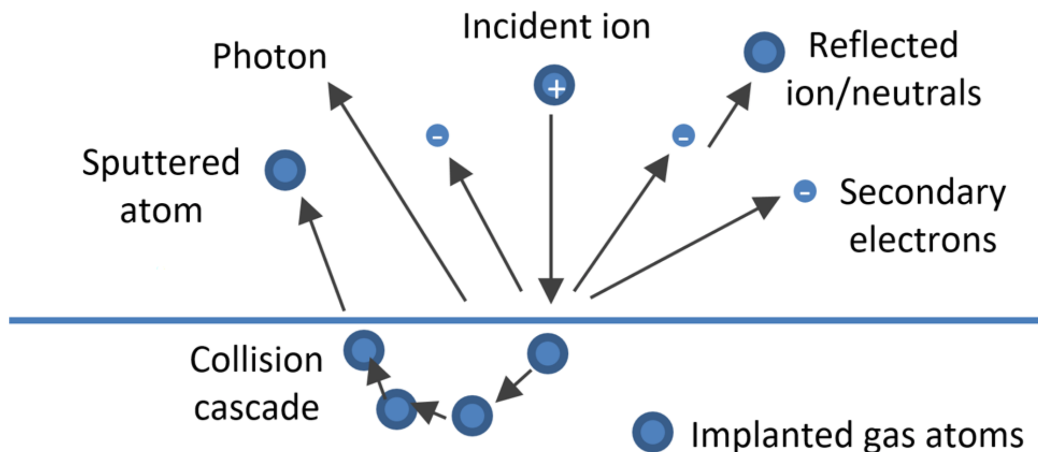

Figure 2.25 Schematic diagram of momentum collision cascade [79]

At the fundamental level, sputtering is a momentum transfer process and therefore sputter yield depends on the transfer of momentum between the high energy ions and the target. It has been reported that there is a correlation between the rate of sputtering and the atomic masses of the target material relative to the bombarding ions; highest rates of sputtering occur when the atomic assess are similar. Conversely the greater the difference in atomic mass, the sputtering is not as efficient. Using the noble gas that has the closest atomic mass to the sputter target ensures maximum efficiency in this regard [76].

Powell et al [76] made the observation of four different physical outcomes of the collision cascade depending on the energy of the incident particles. Between 0 and 50 eV, sputtering only takes place in highly dense plasma whereby the yield is very poor [80-81]. Commercial PVD sputter systems utilise an energy within the moderate range of 50-1000eV. An ion incident upon the target with energies from 1000 and 50, 000 eV results in dense target-atom cascade whereby the atom-to-atom bonds are ruptured. Energy levels greater than 50,000 eV causes a deep implantation of the ions into the target leading to few atoms being sputtered and a subsequent poot sputter yield [76].

The angle of incident of the bombarding ions also has been reported to have an effect on the sputter yield [82-86]. Particles bombarding the target at 90° emit less sputtered atoms compared to ions incident at shallower angles [85]. Shallow angles of the collision cascade take place near the surface of the target which leads to higher change of the sputtering of an atom. By the same token, if the angle is too shallow, the ion will simply deflect of the target surface and thus no sputtering will take place. The ideal sputtering angle is between 45° and 50° [84-86]. In RF sputtering, the inclination of the target does not improve the angle of the incidence of the ions because the plasma sheath is parallel to the target and the ion impact on the target surface is always normal.

Powell et all identify two types of transparent that take place with varying chamber pressure i.e. ballistic transport and diffusive transport. Ballistic pressure is observed at low pressures (1.33 to 1.33×10^{-5} mbar). The sputtered atoms traverse the chamber directly to the substrates with minimal collision to decelerate them. As a results, these atoms arrive at the substrates with high energies [82-86] and implant themselves into the substrate, leading to a thin film that's finely grained with sufficient adhesion to the substrate. At pressures of tens of millibars or above, diffusive transport occurs whereby the collision between the sputtered atoms cause a loss in energy which in turn increases the electrostatic forces. The implications of this include deposition that's more likely to be inhomogeneous and a thin film that consists of large grain sizes.

Other factors, such as target positioning, can alter the properties of the plasma and thin films produced [87]. This occurs when other gasses, apart from the main working gas, are present in the chamber, or when any object within the chamber emits atoms in the form of gas. The presence of such gases in the system should alter the property of the plasma emission.

2.2.7 Summary

The electric glow discharge is formed by passing current through a noble gas such as Ar at a currents ranging from 100 V to several kV. Electrons gain sufficient amount of energy to generate visible light by excitations collisions; a phenomenon which is most easily attained by the Interaction between the anode and cathode generating a complex circuit current that produces the glow. The striking of glow discharges involves formation of restricted electric fields and plasma sheaths at each of the electrodes. Ionisation is

a critical part of a glow discharge under equilibrium conduction. DC power is source that could be used to power the glow discharge which is frequently used to deposit electrically conductive target materials. However, its limitations when it comes to depositing dielectric materials i.e. non conducting insulating target materials that can take on polarised charge. RF sputtering is employed to deposit such materials as it alternates the electrical potential of the current neutralising the charge build-up. Magnets have been widely implemented to confine the plasma near the target allowing for high ionisation efficiencies, better sputter yield and more uniform deposition. Commercial PVD sputter systems utilise an energy within the moderate range of 50-1000eV for satisfactory sputter yield. Microwave power sources can also be used to strike the plasma whereby a resonant condition is created for the electrons which leads to highly efficient ionisation. The next chapter will discuss look into what sort of work has been done with respect to characterising and modelling of the plasma and the need for a simple evaluation of the glow discharge.

2.3 Characterisation and Modelling of Plasma

2.3.1 Introduction

In this chapter, a brief overview of the various methods that are used to characterise and model the glow discharge is presented; it will also present need for simplified evaluation of the discharge such that applied/materials scientist can get a 'snapshot' of the state of plasma and how it correlates with specific process parameters rather than delving into complex theoretical physics.

As discussed in the previous chapter, the plasma in the sputtering procedure is the core of the reaction and is fundamental to the deposition of the thin film coatings such as TCOs that are used in wide range of applications [88]. By evaluating the plasma, A set standard for deposition procedures can be defined, regardless of the machine being used. By considering the sputtering target surface and the plasma as a light source, this concept can be explored However, characterising plasma through optical spectroscopy is nothing new. Currently, plasma physicists study and investigate plasma by means of Emission spectroscopic techniques [89–95]. The diagnosis of laboratory plasma is usually carried out by optical emission spectroscopy (OES), through which numerous analytical techniques are established to determine the plasma properties, such as electron density, plasma temperature, elements recognition, and quantification of elements that are present in the plasma.

The radiative behavior of the atomic constituents of any plasma can only be predicted if the expected populations of possible states are known and the atoms obey the Boltzmann distribution for every possible state and radiation energy density. Subsequently, it can be assumed that a thermal equilibrium condition is present [91–96]. However, creating such a condition in the laboratory would be almost impossible, and hence the concept of local thermal equilibrium (LTE) condition is considered. LTE can be described as a state where the Boltzmann and Saha equation, which governs the distribution of energy level excitation and ionization temperature, are equal to the Maxwell–Boltzmann distribution of free electron velocities [95–97]. Achieving the LTE condition depends on defining the plasma by a common temperature T and the existence of sufficient large electron density. McWhirter proposed a criterion where there is a need for a critical amount of electron density for LTE conditions to exist. This criterion is demonstrated by Equation 2.16 where N_e is the electron density, T is the plasma temperature, and ΔE is the energy gap [98–101].

$$N_e \geq 1.6 \times 10^{12} T^{\frac{1}{2}} (\Delta E)^3 \text{ cm}^3 \tag{2.16}$$

The temperatures of ions and electrons are directly proportional to their random average kinetic energy, and the distribution of velocities for each particle is governed by the Maxwell distribution when thermal equilibrium conditions apply. Under the LTE conditions, the same temperature is assumed for electrons, ions, and atoms in the plasma and the plasma temperature is referred to as the temperature of the electron [91]. Various methods of plasma temperature determination exist, however, the simplest method by far is the Ratio method, which utilises the intensity of two spectral lines for calculating the temperature of the plasma. The intensity of a spectral line associated with a transition is expressed by Equation 2.17. In this equation, I_{ij} is the intensity of transition from state *i* to state *j*, A_{ij} is the transition probability between the two states, *c* is the speed of light, *N* is the number density of electrons, *h* is the plank constant, g_j is the statistical weight of the upper level (*j*) and λ_{ij} is the wavelength corresponding to the transition, E_j is the energy of level (*j*), *T* is the excitation temperature and k is the Boltzmann constant, and the *U(T)* is referred to as the partition coefficient, which accounts for the probability and degeneracy of the two states (*i and j*).

$$I_{ij} = \frac{hcA_{ij}g_jN}{\lambda_{ij}U(T)} e^{-\frac{E_j}{\mathrm{k}T}} \tag{2.17}$$

From the spectral data obtained, two spectral lines can be chosen from the same species and their ionization stages, e.g., Ar *I*, where there is a large difference in the upper energy level. By taking a ratio (I_1)/(I_2) of the intensities of the two selected lines, the constants cancel each other out which yields Equation 2.18, where I_1 and I_2 are the intensity of comparative peaks due to their respective *ij* transition [102].

$$\frac{I_1}{I_2} = \frac{g_1}{g_2}\frac{A_1}{A_2}\frac{\lambda_2}{\lambda_1} e^{[-\left(\frac{E_1-E_2}{\mathrm{k}T}\right)]} \tag{2.18}$$

Solving Equation 2.18 will give the value of *T* in electron volts. This method is the simplest method of calculating the temperature of the plasma, and its accuracy is conditional upon using two lines with a maximum difference in their upper energy states.

As an alternative to the ratio method discussed, a method that is referred to as the Boltzmann method can be applied to calculate the temperature of the electron. This method also utilises Equation 2.17; however, with a rearrangement. The equation is rearranged to give Equation 2.19. Taking the natural logarithm of both sides of Equation 2.19 would lead to Equation 2.20 [91,99–102].

$$\left(\frac{\lambda_{ij}I_{ij}}{hcA_{ij}g_{ij}}\right) = \frac{N}{U(T)} e^{-\frac{E_j}{\mathrm{k}T}} \tag{2.19}$$

$$\ln\left(\frac{\lambda_{ij}I_{ij}}{hcA_{ij}g_{ij}}\right) = -\frac{1}{\mathrm{k}T}\left(E_j\right) + \ln\left(\frac{N}{U(T)}\right) \tag{2.20}$$

By plotting the first term of Equation 2.20 against E_j, the slope of the plot can reveal the value of $1/kT$, from which value of T can be extracted. The electron density can be calculated by using various methods, for example, by applying the Stark broadening relationships. The Stark broadening is caused by the electric field of electrons and ions interfering, which results in the broadening of the spectral line. The interference of the mentioned electric fields causes fluctuations in the field of plasma as the radiating atoms are surrounded by the interfering electrons and ions. The electric field of the electrons or ions causes a perturbation of energy levels that are close to the continuum, while simultaneously affecting the externally applied electric field, which ultimately causes the observed spectral broadening. The magnitude of this broadening in terms of its full width half maximum (FWHM) $\Delta\lambda_{1/2}$ is given by Equation 2.21.

$$\Delta\lambda_{1/2} = 2\omega\left(\frac{N_e}{10^{16}}\right) + 3.5A\left(\frac{N_e}{10^{16}}\right)^{\frac{1}{4}}(1 - 1.2N_D{}^{-\frac{1}{3}})\omega(\frac{N_e}{10^{16}}) \tag{2.21}$$

In this equation, ω is the electron impact parameter, A is ionic impact broadening parameter, N_e is the electron density, and N_D is the Debye shielding parameter. The first term in this equation is associated with broadening that is caused by electrons and the second term is associated with the broadening that is caused by ions [103]. As the emissions from argon species is considered for the measurements, eliminate the second term of the equation that relates to the other ions can be eliminated to obtain Equation 2.22 [102–104]. Hence, rearranging the equation and obtaining the $\Delta\lambda_{1/2}$ value can calculate the N_e.

$$\Delta\lambda_{1/2} = 2\omega(\frac{N_e}{10^{16}}) \tag{2.22}$$

All of the methods mentioned so far are some of the OES methods of measuring the electron density and electron temperature in a plasma. These methods are familiar among plasma physicists; however, when it comes to the application of sputtering plasma and thin film analysis, using the above-mentioned techniques will require the necessary expertise and precision spectroscopy and data interpretation. Many scientists or operators who use plasma deposition for the preparation of thin film coatings would ultimately require a machine that would be easy to use and produce consistent thin film coatings. The objective is to simplify the operation of the sputtering technique for the users and possibly propose a simpler monitoring diagnostic methodology for the plasma deposition process.

2.3.2 Novel approach to characterising the plasma

This work reports on a novel strategy of the in-situ characterization of plasma in a sputtering process by translating the emission spectra into a colour indexing (chromaticity) pattern that is able to quickly monitor any changes in the plasma character with a change in the operating parameter conditions during the course of the process, which in turn provides a better handle to reflect the instabilities of the tool and its optimizing parameters. This is a radical conceptual proposition that can potentially simplify the evaluation of the sputtering plasma for applied scientists by theorising a unique characterisation parameter for particular plasma deposition conditions, just like a fingerprint. As an analogy can be drawn between this work and the human genome that defines each individual person based on the composition

and arrangement of billions of complex genetic coding embedded within each person's DNA, complex laboratory procedures can be used to sequence and encode the genetic makeup of individuals; however, a simpler approach to distinguish people from one another is to check their fingerprint or iris patterns, rather than conducting the complex genetic complexity that defines the individual. Indeed, that is the objective of this communication. By considering the plasma as a light source, the focus on its most apparent character; its colour; in doing so, patterns can potentially be identified that may relate its colour to certain fundamental parameters that are involved in generating the plasma, such as the driving power, the working gas, and its pressure. Plans are underway to further investigate the relationship between the thin film coatings that are deposited via this technique and the plasma colour with reports in due time. The colour of any light source can be mathematically described through what is known as colour spaces. A colour space is a completely-specified scheme for describing the colour of light, ordinarily using three numerical values (called coordinates). An important colour space, defined by the International Commission on Illumination (CIE, the initials of its French name), is the CIE XYZ colour space [105]. However, it is wholly defined in terms of human's perception of light through their eyes. If two instances of light appear to a viewer to be the same colour, they are the same colour. Colour is usually recognized by the viewer as having two aspects:

- Luminance, as an indication of the "brightness" of the light.
- Chromaticity, the property that distinguishes colours.

Colour is not a primary physical property, like the temperature or pressure of a gas. Colour is related to the energy of photons that make up the light. Plotting the intensity of the photon energies (power) that are associated with the relevant wavelength will produce a spectral plot. The intensity and distribution of the emitted wavelengths that ultimately shape the plot determine the chromaticity of the light; its overall "vertical scale" determines its luminance [105]. In fact, there can be several instances of light with different spectrums, which nevertheless have the same colour. This situation is called metamerism. Through mathematics, the XYZ colour spaces are used to construct the *x*,*y* colour function, which is presented in **figure 2.28A**, where the specified area under the defined emission spectrums are used to calculate the coordinates in **figure 2.28B**.

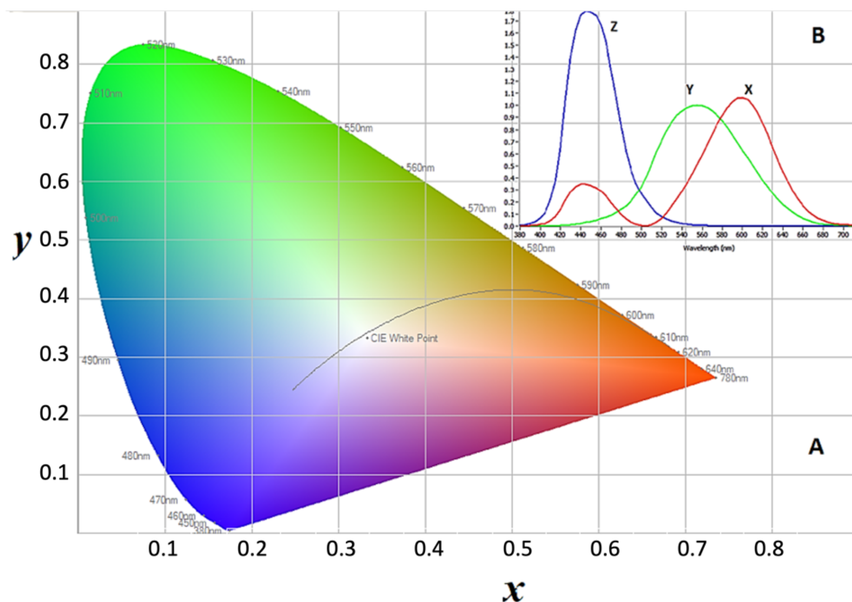

Figure 2.28 (**A**) The *x*,*y* International Commission on Illumination (CIE) chromaticity index. (**B**) The CIE XYZ colour function diagram.

A luminance-chromaticity space (**figure 2.28B**) is then constructed by defining two values; *x* and *y,* as follows:

$$x = \frac{X}{Z + Y + X} \tag{2.23}$$

$$y = \frac{Y}{Z + Y + X} \tag{2.24}$$

In these equations 2.23 and 2.24 , the *X*, *Y*, and *Z* represent the area under emission peaks in the regions. By plotting the *x* against *y,* the CIE *x, y* chromaticity diagram is constructed and is used to give a specific sense to a particular colour (**figure 2.28B**). These peaks represent the emission wavelengths from the light source at the specific wavelengths.

Another photometric parameter is the radiance and spectral radiance of the plasma light. The radiance indicates how much radiant flux is emitted by a surface when it is received by an optical system looking at that surface. The radiance value is calculated by measuring the Radiant flux of an emission source, which is the radiant energy emitted per unit time. Spectral radiance expresses radiance as a function of frequency or wavelength and the spectral plot of the emission is based on the radiance value as a magnitude of intensity [105].

Within a sputtering plasma, a significant number of energy transitions are occurring, leading to a complex emission spectrum. These emissions ultimately define and construct the spectral plot of the plasma as a light source that is observed in plasma. The efficiency and characteristics of the sputtering process depend on the characteristics of the plasma, which in turn depend on the density of the particles and energies within the plasma [106]. Through complex procedures, some of which have already discussed, the electron temperature and electron density, meta-stable atoms, and ions can be deduced and estimated from the spectral plot [107–110]. If the colour parameters can be identified and linked to the existing plasma analysis techniques, it can benefit applied scientists to perform and conduct thin film depositions and can have an easier method of assessing the specifics of the plasma being used.

Due to the extensive optoelectronic applications, high interest in transparent conductive oxides, such as ITO, AZO, and IZO, and their deposition characteristics via plasma sputtering exists and there is plenty of literature available from various research groups [111,112]. These materials are of high interest to many photovoltaic researchers, and hence this study focussed on evaluating the light from a sputtering magnetron plasma source that was fitted with an IZO target and the objective here is to take a radical diversion from the complexity of the conventional plasma characterisation techniques and observe the colour of the plasma and explore the feasibility of exploiting the colour characteristics of the plasma as an indicator of the coating process. A significant number of energy transitions occur in the UV and IR region of the spectrum that are not accounted for when constructing a conventional chromaticity diagram; however, this work is an initial focus on clarifying the feasibility of such a radical approach, after which further efforts can be invested on to modelling a plasma colour analysis system that can provide a shortcut into the characterisation of a sputtering plasma.

2.3.3 Modelling Background

As mentioned above, characterising a plasma via optical spectroscopy has been conducted, typically by optical emission spectroscopy by which numerous analytical techniques are implemented to determine certain properties such as electron density, plasma temperature, elemental recognition and qualification of elements present in the plasma. Investigating such complexities requires in depth knowledge and understanding of plasma physics not to mention time and effort. With the work carried out on characterising the plasma by its light, it serves a steppingstone for the simplified evaluation of the plasma discharge. As such, a deeper study on the modelling of a plasma was carried out to investigate whether alternative methods could be employed in diagnosing the plasma that further reduces the barrier between a materials/applied scientists' understanding and operation of plasma-based systems.

It is important to know that modelling of the magnetron sputtering discharge has been reported on multiple occasions since the 1980s which can be categorised as either purely mathematical models or analytical models. Theoretical models can be subclassified into kinetic models, fluid models or one that is based on plasma physics. Regardless, these models need to integrate calculations of the electric field based on the applied external voltage as well as the distribution of the charged plasma species. Fundamentally, the sputtering process involves the ejection of particles from the target, particle transport and the condensation onto the surface of the substrate. So the complete model of the process would need to discharge physics, plasma physics and interactions at the material surface. Below is a summary of some of the models that have been employed:

1. Analytical models operate via a simple analytical formula that describes the behaviours of the glow discharge parameter e.g. current and voltage. Whilst they are simple and easy to calculate, their accuracy is quite poor and can only be applied to specific ranges of deposition conditions [113]
2. Pathway models was originally developed to determine the ionized fraction of the material arriving at the substrate and provide an explanation for the low deposition rate in some discharges. It is based on monitoring the sputtered material & working gas species within the discharge for a better understanding of process in pulsed magnetron sputtering [114]
3. Fluid models are based on continuity and transport equations for the wide array of discharge species as well as Poisson equation so that a self-consistent electric field distribution is obtained. It defines the plasma as a continuum. Whilst it is computationally simple, its validity to describe a magnetron sputtering discharge has been scrutinised [115]
4. Ionisation region models are volume-averaged and time dependant. This region is defined as the bright glowing plasma near the surface of the target. This time evolution of neutral & charged species as well as the electron temperature in a pulsed magnetron sputter discharge can be determined based on this model. There are some constraints to this model associated with certain experimental parameters and reaction system setup. The model needs to be adapted to an existing discharge and then fitted to reproduce the measured discharge current and voltage waveforms [116,117].
5. Hybrid models makes use of the precision of kinetics models whilst taking advantage of the computational simplicity of fluid models. The secondary electrons are emitted from the surface of the cathode target and are subjected to high energy acceleration within the cathode sheath. The electrons can be classified as either 'fast' electrons whereby their energy exceeds the threshold for inelastic collisions, or slower electrons. These two groups of electrons are treated with a kinetic Monte Carlo model and a fluid model respectively. In the hybrid method, ions &

bulk electrons and fast electrons are treated by the fluid description and particle model respectively [118] though this approached has been critiqued by Kolev and Bogaerts [119]

6. Simulations pertaining to Direct Monte Carlo involve following many plasma species which are represented by test particles. The movement of these particles is impacted by applied forces and collides with other particles. These simulations have been used to prediction the spatial distribution of the ionisation [120] and ion trajectories [121] in a planar magnetron sputtering.
7. Boltzmann solver is a numerical model based on solving the Boltzmann equation to obtain the electron energy distribution within the discharge. While this is a well established model with a high degree of accuracy the Boltzmann equation takes into account the Lorentz force term resulting in complex mathematical calculations. Thus, this method has only been use to successfully model a cylindrical magnetron sputtering discharge with a coaxial inner cathode and an outer anode [122-125].
8. Monte Carlo collisional simulations is a variation of the Monte Carlo simulation. Newton's law is applied to calculate the trajectories of various species and their collisions are characterised by assigning random numbers [126]. In addition, Poisson's equation is used to calculate the electric field distribution self consistently from the displacement of the charged species. This method provides spatial distribution of the charged species that's mapped onto a grid, the electric field across the discharge showing the distribution of the charge density which can be used to determine the electric field distribution. This approach a powerful numerical method pertaining to the analysis of the sputtering discharge. However it is heavily dependant upon immense computational power as it tries to dissect the behaviour of the charged species in great detail along with solving the Poisson equation [127].

The modelling methods mentioned all require a deep understanding and extensive knowledge in the field of theoretical plasma physics and statistical mechanics. However, implementing such detailed knowledge and complex mathematical models is not feasible at operational levels and industrial scale deposition. Moreover, the distribution of the ionisation processes in magnetron sputtering discharges does not appear to be uniform along the racetrack. Such processes commonly exhibit Inhomogeneous plasma with distinct regions of increased intensity of light that seem to float along the racetrack. The presence of rotating dense plasma known as spokes has been reported over the span of a few decades. [128-130].

The plasma may seem inhomogeneous as the spokes are independent of the configuration of the magnetrons i.e. the phenomena has been observed with rectangular, linear & circular magnetron targets [131-134]. At higher discharge currents, where power densities are above 3kW, the inhomogeneities observed become smoother to yield a homogenous plasma azimuthally [135,136]. This reason for this is because of increased electron heating which is a result of a combination of secondary electrons acceleration and pure ohmic heating [137].

The incorporation of reactive gas yields the formation of compounds on the surface of the target which is known as surface poisoning; this detrimentally affects other sputtering discharge parameters like secondary electron emission yields, sputter yield and the plasma composition close to the target. In some instances, it can lead to a change in the shape of the spoke [138] and subsequent reduction in discharge voltage upon the introduction of reactive gas; this has a correlation with a rise in the secondary electron emission [139,140]

In addition to the presence of spokes, the plasma may also show signs of other instabilities. More specifically, the plasma may oscillate in a direction such that it is normal to the target surface which is

known as breathing instability [141,142]. It is common for spokes and the breathing instability to superimpose on each other [141].

Electrons can cause localised excitation and ionization as a result of reaching higher potential and subsequently becoming energized. This implies that images of spokes reflect that of the potential distribution [143]. Held et recently reported that the spokes had a high plasma density, electron temperature and plasma potential that the surrounding plasma [144]

2.3.4 Modelling plasma with artificial neural networks.

A new & comparatively simplified method for modelling the plasma with the intention to impose all the associated complexities and calculations to an artificial neural network has been studied . With the assistance of modern computational and graphical power and artificial intelligence based methodologies pertaining to data assessment, This work investigates on implementing a novel approach in the evaluation of a plasma during the sputter deposition process to assess the qualitative parameters of thin film materials as deposition was taking place. There is strong reason to believe that artificial intelligence and deep learning methods have the potential and power to fully automate and create a digital shadow for the sputtering deposition process on an industrial scale.

A digital shadow is a historical or retrospective representation of a physical entity, process or system while a digital twin is a virtual representation which has the potential to formulate solutions for problems that cannot be resolved with the physical system alone. A shadow is created by aggregating and analysing historical data collected from the physical asset or system over time. Unlike a digital twin, a digital shadow does not provide real-time simulation or monitoring capabilities. Instead, it serves as a repository of past performance data and insights. Digital shadows are often used for post-analysis, trend analysis, historical data comparison, and decision-making based on past experiences. They can help identify patterns, anomalies, and trends in historical data, facilitating informed decision-making and future planning. In summary, while both digital twins and digital shadows involve digital representations of physical entities or processes, digital twins focus on real-time simulation and monitoring for predictive analysis and optimization, whereas digital shadows are retrospective representations used for historical analysis and decision-making based on past data.

Artificial Neural Networks (ANN) are powerful, scalable, versatile and highly complex which serve as the core of deep learning methods. The introduction of high level application programming interfaces (APIs) such as KERAS and TENSORFLOW in python programming language has made it convenient to implement ANNs. The origins of ANNs go as far back as the 1940s but due to their complexity and need for significant computational power, their application was heavily limited. With the rise of modern computing power and business entities like Google and Facebook alongside the accessibility of large banks of digital data, there is an emergence of ANNs which are outperforming existing machine learning models like support vector machines (SVM) which were once market leader as far as popularity and application goes. Historical theoretical limitations pertaining to ANNS like the model getting trapped in local minima function can be circumvented. Ironically, Multidimensional data possessing sophisticated function gradients are least affected by the local minima restriction.

The units that are part of the construction of ANNs hypothetically mimic the behaviour of biological neurons and their interactive connections. However, biological neurons are mysterious and complex by nature which is yet to be fully comprehended by neurologists. Thus, the term neuron in this AI context is

only used for description purposes and not to mistaken as being equivalent to an actual neuron in terms of design and status. The term perceptron was invented to describe the constituents in ANNs in 1957 by Frank Rosenblatt. The perceptron calculates a weighted sum of its inputs and applies a function to that weighted sum. **Figure 2.29** displays how a single perceptron operates in basic mathematical terms. A Detailed review of artificial neural networks and deep learning can be found in [145,146]

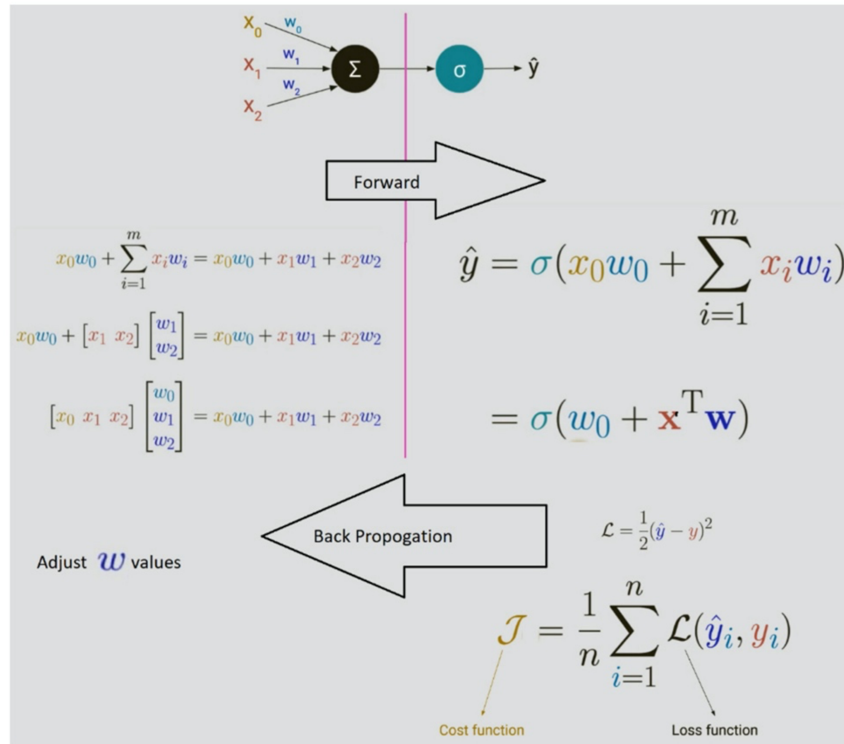

Figure 2.29. A simple representation of the operation of single perceptron fed with three data (X_0,X_1,X_2) inputs to give an output (yˆ)which need to be close to a known (y) value.

ANNs essentially are based on a collection of connected perceptrons and comprise of input layers, hidden layers and output layers. Each perceptron has a weight and threshold associated with it. When an ANN consists of deep stack of hidden layers it is known as deep neural network.

The process involves feeding multidimensional data (vector) to the ANN/DNN via input neurons and gets passed through the hidden layers leading to an outcome/value from the output layers. The model will compare the output value to known experimental outputs and train itself by shifting the weights (**figure 2.30)** associated with the perceptron each layer. The model learns by a process known as back propagation which was first introduced by David Rumelhart [146] which at its core incorporates gradient descent for the calculation of gradient of the networks error. The perceptron will apply weights to the inputs, sum up and apply a function (σ) on the outcome, and will adjust the weights through a forward and backward loop by implementing a loss function (error factor) until the selected weights result in yˆ being as close as possible to y value. A basic understanding of the principles of deep learning method was provided. As this is an exponentially developing field in artificial intelligence and computer science, detailed discussion of the complex theories and mechanism of deep learning is beyond the scope of this

work. This project explores the feasibility of applying deep learning models to sputter depositions process as with the objective of making it more digital.

$$\sigma(\mathbf{x}^{\mathrm{T}}\mathbf{w}) \longrightarrow \hat{y}$$

$$\frac{\partial \mathcal{L}(\hat{y}, y)}{\partial \mathbf{w}} = \frac{\partial \mathcal{L}(\sigma(\mathbf{x}^{\mathrm{T}}\mathbf{w}), y)}{\partial \mathbf{w}}$$

$$\mathcal{L}(\hat{y}, y) = \frac{1}{2}(\sigma(\mathbf{x}^{\mathrm{T}}\mathbf{w}) - y)^2$$

$$u = \sigma(\mathbf{x}^{\mathrm{T}}\mathbf{w}) - y$$

$$\frac{\partial \mathcal{L}(u)}{\partial \mathbf{w}} = \frac{\partial \mathcal{L}(u)}{\partial u}\frac{\partial u}{\partial \mathbf{w}}$$

$$= \frac{\partial \mathcal{L}(u)}{\partial u}\frac{\partial(\sigma(\mathbf{x}^{\mathrm{T}}\mathbf{w}) - y)}{\partial \mathbf{w}}$$

*New (W) = Old (W) - Learning Rate * $\partial \mathcal{L}$*

Figure 2.30. A simplified illustration of the backpropagation process and adjustment of weights by a perceptron.

The objective of this work was to push all the mentioned complexities into the black box of an artificial neural network. With modern computing powers and artificial intelligence (AI)-based data assessment methodologies. The aim was to explore implementing an alternative approach in plasma diagnostics during the sputter deposition process to assess the qualitative parameters of thin films as they were deposited. Artificial intelligence and deep learning can potentially be the answer, if the objective is to fully automate and digitise the industrial-scale sputtering process.

2.3.5 Summary

Conventional methods of plasma evaluation and diagnosis involve complex plasma physics and determination of certain properties such as electron density, plasma temperature, type (and quantity) of elements via numerous analytical techniques. A proposal was put forward that plasma can be characterized by its light which can provide a general overview for the everyday applied/materials scientist. The results of colour characterization of the plasma will be discussed in the next chapter. Following on from this work the modelling history of the plasma was detailed. Various methods exist, however all require a deep understanding and extensive knowledge in the field of theoretical plasma physics and statistical mechanics. Implementing such complex mathematical models is not feasible at operational levels and industrial scale deposition. An relatively simplified method for modelling the plasma involving Artificial Intelligence has been postulated whereby all the associated complexities & calculations are subjected to an artificial neural network. This work paves the way for the digitization and automation of the sputter deposition process.

Chapter 3 Experimental Methods and Characterisation Techniques

This chapter provides a detailed description of the experimental set-up employed for the wide array of experiments conducted during this project. Though the same set-up was used, each set of experiments differed from one another and will be detailed in this chapter. In addition, the array of techniques used to characterise the thin film samples will be discussed.

3.1 Experimental set-up

The sputtering machine used for these experiments was a V6000 unit that was manufactured by scientific vacuum systems limited (SVS Ltd., Wokingham, UK) with a vacuum chamber of ~40 cm × 40 cm × 40 cm. The magnetron of the V6000 unit was fitted with a six-inch 99.99% pure, Zinc Oxde & Indium Zinc Oxide (IZO) target material (of varying compositions) with copper indium back bond for efficient thermal dissipation. The working gas used in the experiments was a 95% argon and 5% hydrogen (Ar + H) single-source mixed-gas cylinder. Spectral data from the plasma was obtained by placing an in-vacuum collimator optic probe that was made by Plasus GmbH (Mering, Germany). The probe was installed on the magnetron, so that it horizontally collected light from ~1.5 cm away from the surface of the target and at a distance of 4 cm from the edge of the target (**Figure 3.1** A). The unique feature of the optic collimator is the honeycomb structure of the photon inlet, which traps the sputtering particle and prevents gradual coating of the collimators quartz window. This is highly important, as any coating of the inlet quartz window will undermine the reliability of the data obtained. Thus, A test was carried out on the quartz lens for any possible coating by running a continuous 5 hours deposition experiment followed by dismantling the collimators (Plasus GmbH, Mering, Germany) and using UV/VIS spectroscopy (Bibby Scientific Ltd, Staffs, UK) to check the inlet quartz window for any coatings formed to ensure the data were not undermined (**Figure** 3.1A). The Plasus Emicon Spectrometer (Mering, Germany) that generates a detail spectral plot of the emission was used for detailed spectral analysis. The software coupled to the Emicon spectrometer was programmed to calculate the area under the peak of the spectral range based on predesignated segments of the spectrum. In addition to this, the light collected from the plasma was also guided to a 2nd spectrometer; a Jeti Specbos 1201 spectrometer (Jena, Germany) that calculates the chromaticity index of the light, the Jeti was programmed, so that, for each measurement, it took 20 readings and inputted the average.

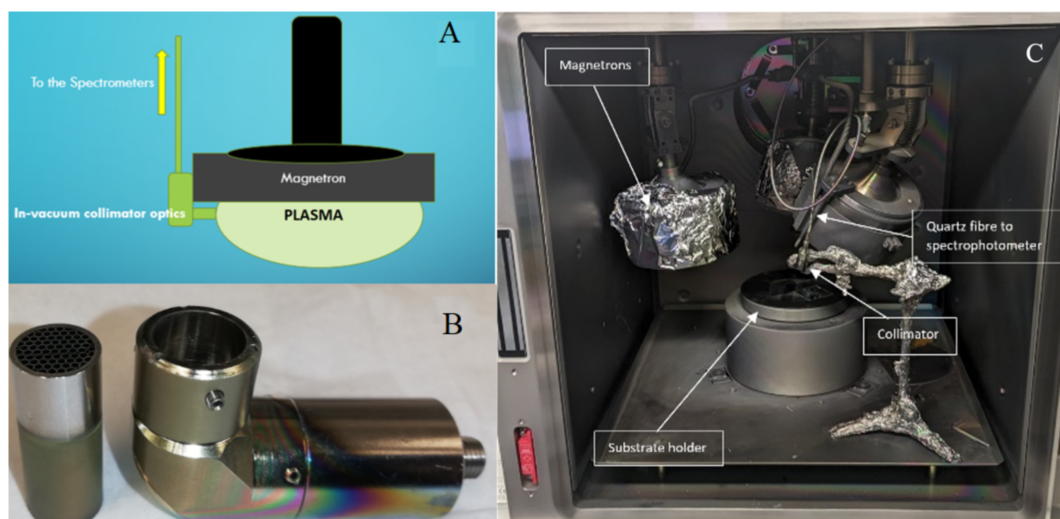

Figure 3.1 (**A**) In-vacuum collimator optics was placed adjacent to the magnetron and the emission data were transferred to the spectrometers via quartz fiber, the distance between the collimator and target edge was 4 cm. (**B**) The Collimator. (**C**) Magnetron with the in-vacuum collimator from the V6000 tool

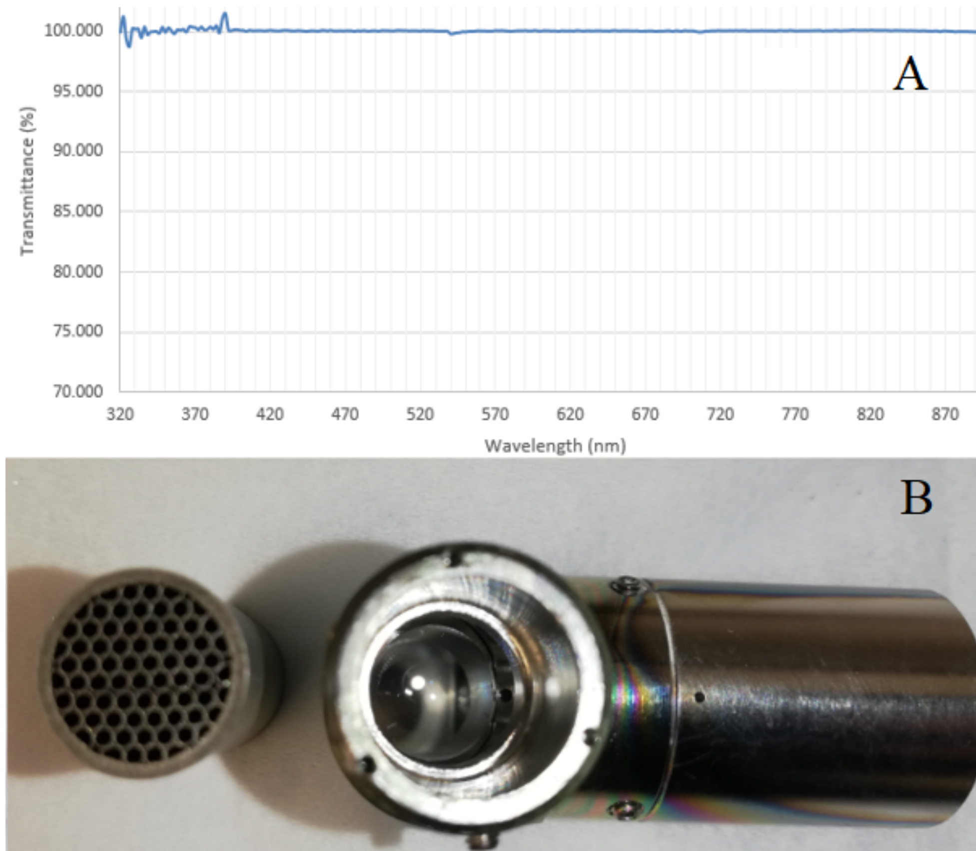

Figure 3.2. (**A**) UV/VIS transmission spectroscopy (320 to 900 nm) to ensure the lens was not coated during the experiments. (**B**) Optic collimator with a honeycomb structure

During each deposition, soda-lime glass slide substrates were thoroughly cleaned and were placed in the chamber, with the substrate stage rotating at a speed of 20 rpm. Prior to loading, all substrates were washed and sonicated with soap water, acetone and ethanol separately to ensure a clean surface before the thin film deposition.

A wide range of spectral data was collected by fitting an array of targets in the magnetron and depositing with varying plasma power and gas flows which will be further outlined subsequently. The 1st set of experiments involved the colour characterization of the plasma during the sputter deposition of a range of TCO targets to not only diagnose the plasma but also to attempt to investigate the relationship between the plasma and the resultant thin film material.

3.1.1 Experiments for the optical analysis of the Glow Discharge via colour characterisation

Using the IZO target fitted onto the magnetron, a series of tests were carried out by igniting and running the plasma under various conditions. The working gas, working gas pressure, and radio frequency (RF) plasma power were varied and data were collected. Two types of working gases were used viz. pure Argon (Gas Ar) and 95% Argon: 5% Hydrogen (Gas ArH). **Table 3.1** defines the experimental regime undertaken. Test 1: where the stability of the plasma was monitored at 100 W under 1.9×10^{-3} mbar of

working gas pressure, under Ar and ArH gas; Test 2: The spectral emission of the plasma was monitored while increasing the power of stabilized plasma from 100 to 300 W under 1.9×10^{-3} mbar of Ar at a rate of 100W per minute; Test 3: The spectral emission of an stabilized plasma was monitored at 100 W plasma power under various Ar and ArH gas pressures at a rate of 5×10^{-4} per minute. (Note: separate spectral analysis of the plasma power was carried out up to 350 W).

Table 3.1. The experimental regime conducted to obtain the spectral results from the plasma light source under various conditions in 3 separate test groups.

Test Regime	Variable Parameter	Power (RF)	Working Gas	Pressure (mbar)
Test 1	Time	100 W	Ar, ArH	1.9×10^{-3}
Test 2	Plasma power	100 W → 300 W	Ar	1.9×10^{-3}
Test 3	Gas pressure	100 W	Ar, ArH	$1.2 \times 10^{-3} \rightarrow 7 \times 10^{-3}$

3.1.2 Experiments for the synthesis of Highly conductive Zinc Oxide films

A range of IZO and ZnO samples were prepared for this experiment. For the IZO samples (S series): The magnetron of the V6000 unit was fitted with a six-inch diameter 99.99% pure indium zinc oxide (IZO) target (In60-Zn40 at %) material with copper indium back bond. Using this target, 'seven' IZO thin film depositions were carried out. The growth conditions of these samples can be found in table 3.2. All the experiments were carried out at ambient temperature for two hours under a 100W RF plasma power and a chamber pressure of 2.3×10^{-3} mbar.

Table 3.2 outlines the range of deposition conditions used to synthesise the 7 IZO samples

Sample ID	Ar+H (sccm)	Working Gas	Prior exposure to Ar+H Plasma (hr)	Prior exposure to Ar Plasma (hr)
S1	9	ArH	0	0
S2	9	ArH	2	0
S3	9	ArH	4	0
S4	9	ArH	6	0
S5	7	ArH then switched to Ar	8	0
S6	7	Ar	0	2
S7	7	Ar	0	4

For ZnO samples (H series): The magnetron was fitted with a six-inch diameter 99.99% pure zinc oxide (ZnO) target material with copper indium back bond. Using this target, 'three' ZnO thin film depositions

were prepared using 150 W RF plasma power with a working gas pressure of 2.3×10^{-3} mbar for exactly 3 hours under the protocol outlined in table 3.3

Table 3.3. outlines the range of deposition conditions used to synthesise the array of H:ZnO samples

Sample ID	Ar+H (sccm)	Working Gas	Prior exposure to Ar+H Plasma (hr)	Prior exposure to Ar Plasma (hr)
H0	9	ArH	0	0
H3	9	ArH	3	0
H6	9	ArH	6	0

3.1.3 Experiments for investigating the effect of substrate position relative to plasma

The focus of this experiment was to present the observations made during the deposition highly conductive zinc oxide films via RF sputtering with varying positions relative to the discharge. For this experiment, a set of chamber pressures were used to deposit films associated with 13.9, 10 and 6 sccm Ar + H flow rates resulting in working chamber pressures of 0.3, 0.23 and 0.15 Pa. The depositions were carried out under 100, 150 and 200 watts of RF (radio frequency) plasma power under each flow rate.

The substrates were placed on the substrate holder of the machine, as depicted in **figure 3.3**, with position E indicating a substrate on the edge of the substrate holder, and C indicating the centre of the substrate holder position. The substrate was rotating at a speed of 10 rpm in all experiments. Using this configuration of substrate positions, thin films of ZnO were deposited under various amounts of plasma power and Ar + H flow rates. **Table 3.2** presents the regime by which samples were prepared and named, where each deposition was carried out for a period of 3 hours. In practice, glass samples were placed in between the C and E positions; however, here the focus was primarily on detailed observations associated with the E and C positions. The gas flow raw is represented as: high(H) flow rate (13.9 sccm), medium(M) flow rate (10 sccm) and low (L) flow rate (6 sccm). For this experiment, 2 collimator probes were used to collect the spectral emission data; one was positioned in the centre of the substrate holder and the 2nd one was placed at the edge of the holder as depicted in **figure 3.4**.

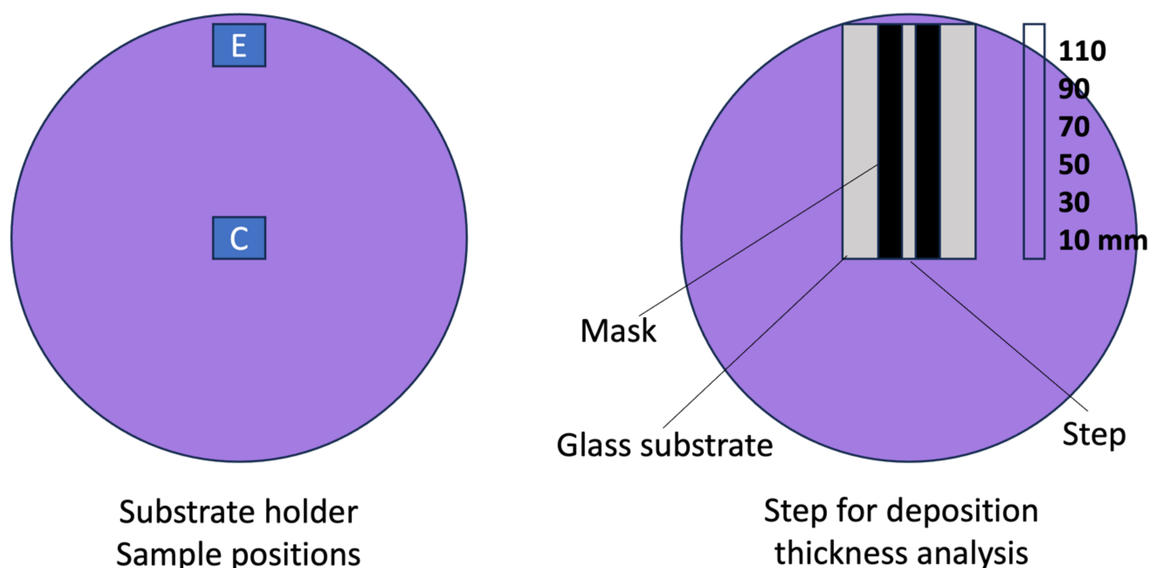

Figure 3.3. During each of the nine deposition trials, two soda lime glass samples were placed on the substrate holder (220 mm diameter), one in the centre and one on the edge (**left**). To measure the thickness gradient from the centre to the edge, a bridge between two masks was designated on an intact glass substrate for profilometric measurements; thickness of the samples was measured at the (10–110 mm) distance from centre, as depicted in this figure (**right**).

Table 3.4. Nine depositions were carried out under various plasma power and gas flow rates:

Sample ID	Position on Substrate Holder	Plasma Power (W)	Gas flow rate (sccm)
E100H	E	100	13.9(H)
E100M	E	100	10(M)
E100L	E	100	6(L)
E150H	E	150	13.9(H)
E150M	E	150	10(M)
E150L	E	150	6 (L)
E200H	E	200	13.9(H)
E200M	E	200	10(M)
E200L	E	200	13.9(L)
C100H	C	100	13.9(H)
C100M	C	100	10(M)
C100L	C	100	6(L)
C150H	C	150	13.9(H)

C150M	C	150	10(M)
C150L	C	150	6(L)
C200H	C	200	13.9(H)
C200M	C	200	10(M)
C200L	C	200	10(L)

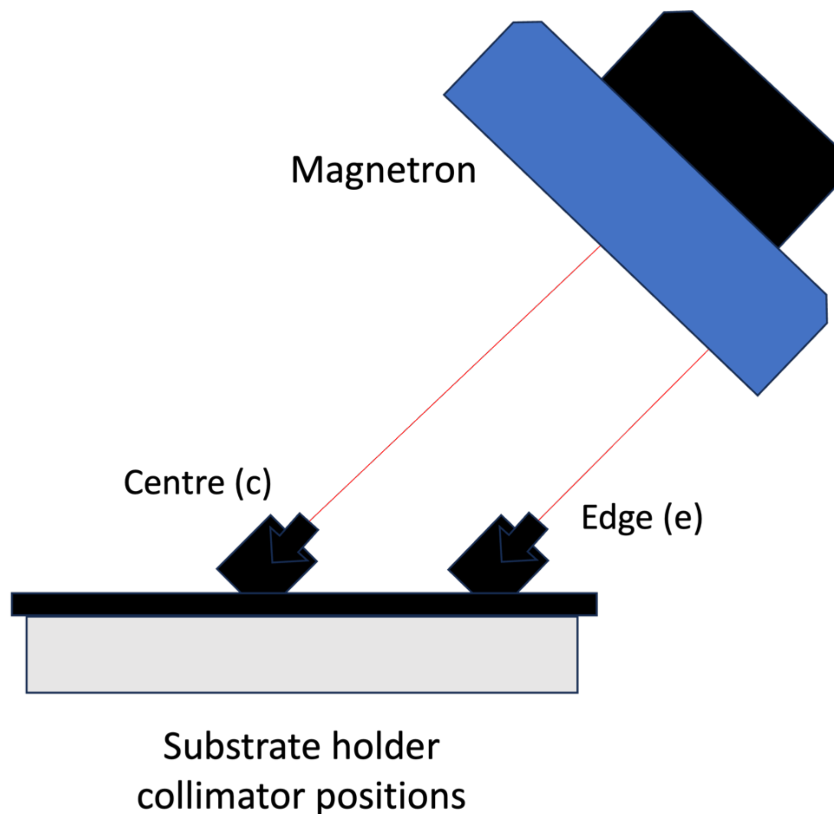

Figure 3.4. Schematic diagram illustrating positions of 2 collimators

3.1.4 Experiments for implementing Machine Learning concepts to the sputter deposition process

At this stage of the research, a transitioned was made from using the colour characterisation method to utilising Machine Learning/deep learning algorithms for the diagnosis and monitoring of the plasma. The experiments conducted generated a substantial volume of data, comprising emission data across a broad wavelength spectrum at specific intervals. Each individual reading comprised a numerical array representing emission peaks at particular wavelengths. To facilitate the management of the overall dataset, random spectra were selected for training the neural network model for each sample. As elucidated in Chapter 2, computer vision-based deep learning techniques were utilized to transform the

1D array linked to the spectral data into a 2D tensor. Further elaboration on the processing of the acquired raw data will be provided in the subsequent subsections.

3.1.4a Artificial Neural Network to predict the sheet resistance of IZO thin films deposited via Plasma deposition

Figure 3.5 presents the experimental stages of this trial where the spectral data emitted from the plasma was captured via a collimator and optical fibre during the sputter deposition of the thin films of Indium doped zinc oxide (IZO). The sheet resistance value was obtained using the 4-point probe measurement system post synthesis.

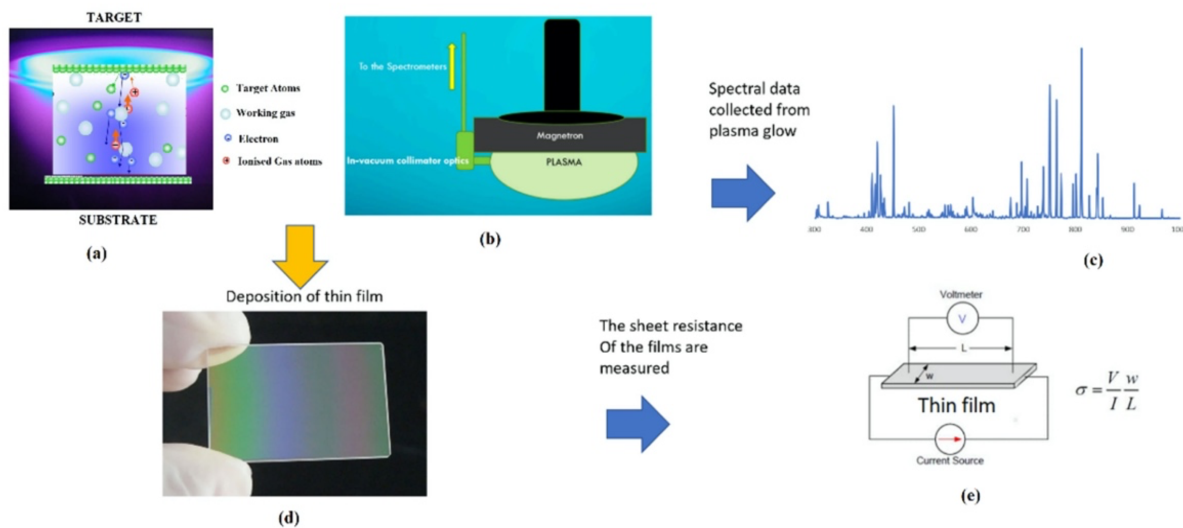

Figure 3.5. Illustration of the sputtering process and the experimental concept. (**a**) Plasma deposition; (**b**) Method of collection of spectral data; (**c**) emission spectrum; (**d**) Thin film coating; and (**e**) Characterisation of sheet resistance

Overall, 114 thin film samples were fabricated. The deposition time and RF power for each run was 1 hour and 300W respectively at room temperature. The substrate was rotating at 10 rpm. The working gas was an Argon/Hydrogen mix (Argon 95%, Hydrogen 5%) from a single cylinder source. The parameter that was varied during the coating of the samples was the chamber working pressure which, as mentioned earlier, can significantly alter the micro-environment of the plasma and sputtered atoms. Thin film depositions were carried out under the following working pressures: 1×10^{-3}, 1.5×10^{-3}, 1.9×10^{-3}, 2.1×10^{-3}, 2.7×10^{-3}, 3.3×10^{-3} and 4.1×10^{-3} mbar.

The data obtained from the spectral map and 4-point probe measurements were plugged into equation described in **3.5** which will be described in further detail in this chapter. The 'x' values represented the emissions at each 0.2nm step of the spectral data and the y value represented the sheet resistance of the film.

ANN Modelling

Figure 3.6 provides a visual representation of the concepts underlying direct artificial neural network (ANN) models. In one approach, the spectral data were transformed into vectors, each containing the area under peaks spaced 100nm apart. Alternatively, the emission intensity at 0.2nm

intervals within segments of the plasma spectrum was formatted. Subsequently, the formatted data was inputted into a deep network of perceptrons. Additionally, the sheet resistance value of the TCO, specifically IZO under examination, was associated with each spectral data vector and incorporated into the neural network to initiate the learning process.

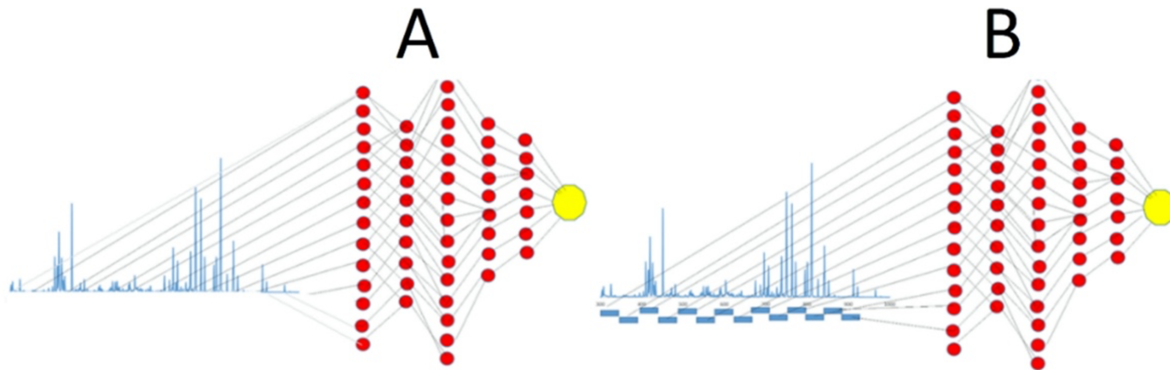

Figure 3.6. Illustration of the theoretical concept. (**A**) In this approach, spectral data of the plasma in form of point-by-point spectral intensity values (**B**) in this approach, spectral data of the plasma in the form of area under the peaks at certain intervals

The model is also fed with the sheet resistance values of IZO, physically measured to enable the model to learn from the spectral data to predict the sheet resistance value. Once the model was fed with enough data with known sheet resistance values and sufficiently trained, it was then exposed to spectral data without the known outcome to predict the thin film conductivity. This was entirely based on emission spectrum of the plasma during the deposition process of the film.

CNN Modelling

In a separate set of experiments, the spectral emission of the plasma was converted into an image by translating the vectors associated with the emission intensity into a matrix. The matrix was then rendered into an image whereby each of the spectral points represented a pixel of the image. These images were then fed into convolutional neural network (CNN) so that the learning process could take place and subsequently predict the sheet resistance values of the films with respect to its specific deposition conditions. CNNs derive their names from the type of hidden layers it consists of i.e. its convolutional and pooling layers to function as opposed to the use of activation functions in conventional feed-forward neural networks. CNN is a technique that allows for the extraction of visual features from a two dimensional (2d) array in small chunks. Each perceptron in a convolutional layer is responsible for a small cluster of layers in the preceding layer and the bounding filter that extracts features and determines the cluster of neurons/perceptrons from the initial signal called a kernel. In the experiments that were conducted, the plasma emission spectrum was converted into an image and certain type of features were extracted from this image using an array of random kernels in a CNN model at which point these were converted into a flat single vector and subsequently used for regression analysis (**figure 3.7).** The kernels were selected randomly during the model training and were learned via gradient descent process. Ultimately, the convolutional method was designed to downsize the dataset and pick out specific features. Mathematical operation and structure of these models was beyond the scope of this work, but further discussion can be found in [147-150].

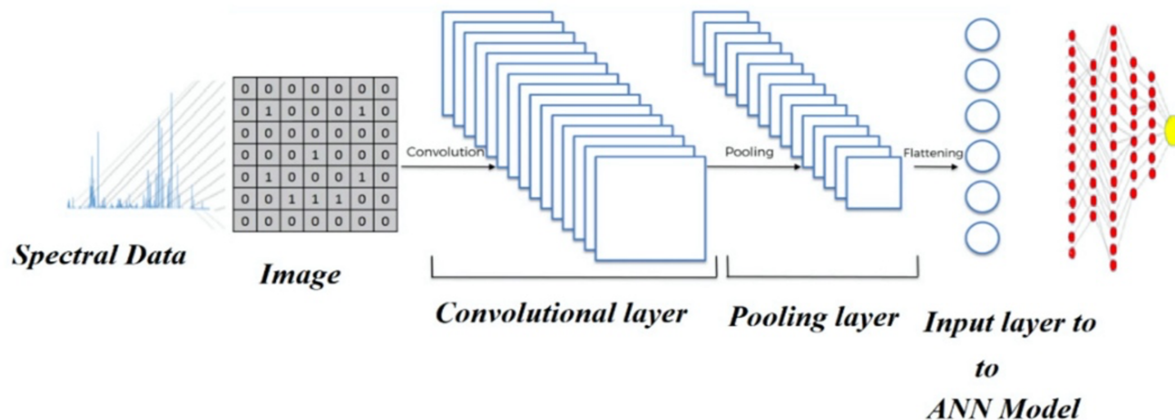

Figure 3.7. Illustration of implementation of a convolutional neural network linked to a regression multilayer ANN model for predicting the sheet resistance of the thin films from an image generated from the spectral emission of the plasma.

Several samples were prepared under the above pressures and the spectral data from the plasma were gathered. After each deposition, the sheet resistance of the films was measured using a Jandel RM3000 four-point probe system, the operating principle of which will be described later on.

The data were tabulated such that each row represented a sample, The last column denoted the calculated sheet resistance, while the other columns, arranged from start to end, represented the signal intensity calculated by the spectrometer at each emission wavelength point with a precision of 0.2 nm.

Figure 3.8 illustrates the spectral peaks of the plasma under four different pressures in a comparative manner. It visually presents the emission peak spectra and their corresponding intensities, comparing 2.1 mbar against 3.7 mbar and 1 mbar against 4.1 mbar. The goal is for the model to assimilate the spectral characteristics of the plasma and forecast the sheet resistance of the indium-doped zinc oxide thin films solely based on these spectral features, thereby obviating the need for complex plasma physics models.

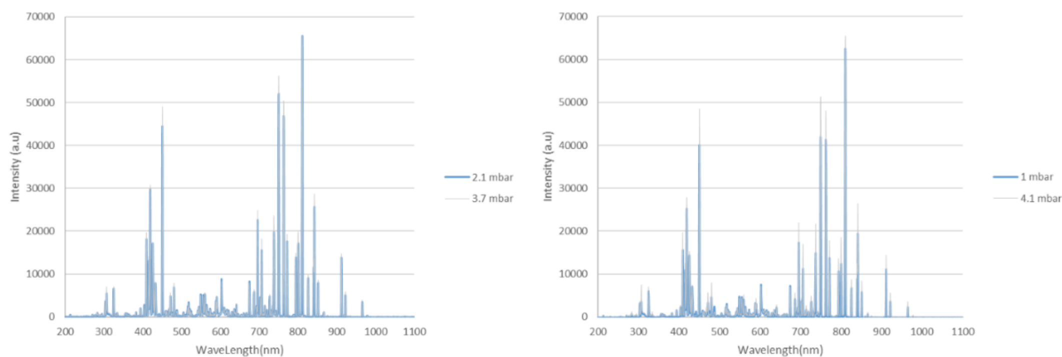

Figure 3.8. Spectral emission from the sputtering plasma under various chamber pressures. Comparing chamber pressures of 2.1 mbar and 3.7 mbar (**left**) and comparing 1 mbar and 4.1 mbar chamber pressures (**right**).

The direct image generated from the spectra was initially utilised to train various convolutional neural network (CNN) models. However, none of these models could effectively learn from the image in its raw form, as CNN models operate more efficiently with standardized values. Subsequently, the pixel values of the image were normalized using two different methods: min-max scaling and standard scaling.

$$x\ (\min\max scaled) = \frac{x - \min(x)}{\max(x) - \min(x)} \tag{3.1}$$

$$x(standard\ scale) = \frac{x - \mu}{\sigma} \tag{3.2}$$

Therefore, the following approaches for preparing and applying the data to train the neural network models were pursued: (a) an ANN-based integral approach with 50 nm spectral windows, (b) an ANN-based spectral approach and (c) a CNN-ANN-based spectral approach that deviated into computer vision and image recognition. In this approached, the spectral data was transformed into two-dimensional scaled images, incorporating an advanced computer vision techniques with deep learning convolutional neural network architecture for image recognition model. This was coupled to a neural network model for regression analysis (**Figure 3.9).**

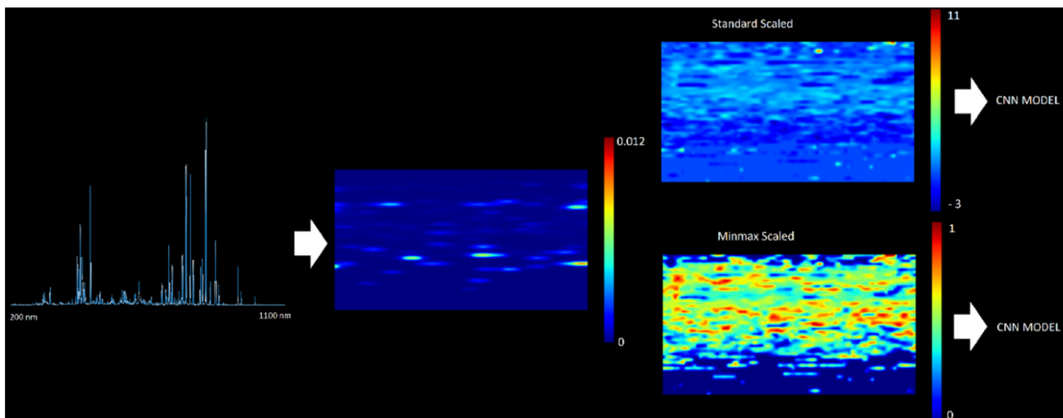

Figure 3.9. Conversion of the spectral plot of the plasma into 2D images formed from scaling the spectral values. (**a**) the original spectra, (**b**) image directly formed from original spectra, (**c**) image formed from the standard scaling of the original spectra, (**d**) an image formed from the min max scaling of the original spectra.

In the preceding step, as each image was technically a matrix of size (50, 90), singular value decomposition (SVD) to every single image was applied. The SVD decomposed the image matrix into three matrices: a U matrix, which spanned the column space of the image; a V matrix, which spanned the row space of the image; and a diagonal matrix holding singular values that were scalers associated with consecutive columns of U and V. The whole image was able to be reconstructed from the out product of U and V scaled by the diagonal singular value matrix. This is illustrated in **figure 3.10**.

$$\begin{bmatrix} | & | & & | \\ X_1 & X_2 & \cdots & X_n \\ | & | & & | \end{bmatrix} = \begin{bmatrix} | & | & & | \\ u_1 & u_2 & \cdots & u_n \\ | & | & & | \end{bmatrix} \begin{bmatrix} \sigma_1 & & \\ & \sigma_2 & \\ & & \sigma_n \end{bmatrix} \begin{bmatrix} — v_1 — \\ — v_2 — \\ \vdots \\ — v_n — \end{bmatrix}$$

$$= \sigma_1 u_1 v_1 + \sigma_2 u_2 v_2 + \cdots \sigma_n u_n v_n$$

$$X = \sum \sigma_1 u_1 v_1, \; \sigma_2 u_2 v_2, \; \sigma_n u_n v_n$$

Figure 3.10. The singular value decomposition and reconstruction of a matrix.

The vectors within U and V were unit vectors. The corresponding singular value served as a scalar, providing magnitude to the outer product of these vectors. The condition number of a matrix reflects the dispersion of information within it and can be computed by dividing the highest singular value of the matrix by its lowest singular value.

Deep learning necessitates vast datasets. Large quantities of data, comprising feature columns and corresponding output columns, are essential for training these models. Therefore, the primary objective of this research was to accumulate a sufficiently large dataset by continuously operating a sputtering deposition system, capturing spectral data, and measuring an output value associated with the experimentally prepared samples—in this instance, the sheet resistance of the thin films. The data utilized in this chapter were obtained through continuous operation of the machine over a one-year period. The substantial progress made in deep learning models owes much to the extensive ongoing research efforts of data science researchers, which have made these models powerful and straightforward to implement. Nevertheless, the foundational requirement for their implementation remains large datasets, underscoring the centrality of data acquisition in this research endeavour.

3.1.4b Experiments for Implementing unsupervised deep learning methods to predict sputtering plasma features

The next set of experiments conducted is a follow-up of initial research work carried out on applying deep learning concepts to the sputter deposition process. Unsupervised learning; a more intricate and multifaceted machine learning concept is explored whereby the spectral data collected from the plasma is used to trained models without any well-labelled data or known outcomes. Once the model was trained,

attempts were made to use it for accurately predicting the growth conditions of the plasma depositions associated with a particular emission spectrum.

The spectral emission data from the plasma glow of various sputtering targets containing indium oxide, zinc oxide, and tin oxide were obtained as detailed in section. The plasma was generated at various power and chamber pressures. These spectral data were then converted into two-dimensional arrays by implementing a basic array-reshaping technique and a more complex procedure utilizing an unsupervised deep-learning technique, known as the self-organizing-maps method. The two-dimensional images obtained from each single-emission spectrum of the plasma mimic an image that can then be used to train a convolutional neural network model capable of predicting certain plasma features, such as impurity levels in the sputtering target, working gas composition, plasma power, and chamber pressure during the machine operation.

In these experiments, seven different targets were fitted:

1. Pure zinc oxide,
2. Pure indium oxide
3. IZO (indium oxide, zinc oxide) 70:30 ratio
4. IZO (indium oxide, zinc oxide) 60:40 ratio
5. IZO (indium oxide, zinc oxide) 50:50 ratio
6. IZO (indium oxide, zinc oxide) 40:60 ratio
7. ITO (indium oxide, tin oxide) 90:10 ratio

With each of these targets fitted into the magnetron, a plasma was generated under various operating conditions, whereby power, gas-flow rate, and working gas purity (using either pure argon or argon with 5% hydrogen content) were altered. With each experiment, collected the spectral data associated with plasma glow was collected.

The primary objective was to investigate how accurately a deep-learning model (convolutional neural network models) trained with the spectral data would predict the following parameters using only the spectra of a sputtering plasma:

1. Generation power;
2. Gas-flow rate;
3. Level of indium and zinc content in the target;
4. Presence of hydrogen in the chamber;

The spectral data from the plasma were collected by fitting seven different targets in the magnetron and collecting spectral data under varying plasma powers and gas-flow rates, as depicted in **Table 3.5.** Similar to the 1st deep learning experimental method, the spectral data were collected via a collimator fitted next to the magnetron. At each single point, spectral data were collected, to have a collection of spectral data associated with plasma operating conditions. Overall, a total of 588 spectral data plots were selected for deep-learning studies.

Table 3.5 Different Plasmas generated using a combination of a different deposition parameters.

Material	ITO, IZO, ZnO & InO

Working gas	Ar & Ar/H
Plasma power (W)	100, 150 200
Gas flow (sccm)	3, 5, 6, 7, 8, 9 & 10

Data collection

These experiments generate a large quantity of numerical data. The spectral emissions were collected from 204 nm to 1104 nm at 0.2 nm intervals, which means each single reading was an array of 4500 numbers representing emission peaks at particular wavelengths. For each sample, 2 random spectra were selected for training the neural network model. Therefore, the overall data set was a matrix of 588 rows and 4500 columns.

As the intent was to use computer-vision-based deep learning to create the model, there was a need to convert the 1-dimensional array associated with the spectral data into a 2dimensional tensor.

Two approaches were taken to convert the 1-dimensional array into 2D:

1. Basic cut and stacking. As illustrated in **3.11a**, the 4500 long array associated with the spectra was cut into 50 segments and stacked to form a matrix of 50 × 90 pixels, as illustrated in **3.11b**.
2. By implementing an unsupervised machine-learning technique called self-organizing map (SOM), forming a 2-dimensional array of 90 × 90 pixels. The SOM illustrated in **figure 3.12** is an algorithm that was introduced by Teuvo Kohonen, acting as a non-supervised clustering algorithm capable of presenting multidimensional feature data into a two-dimensional map of clusters [151].

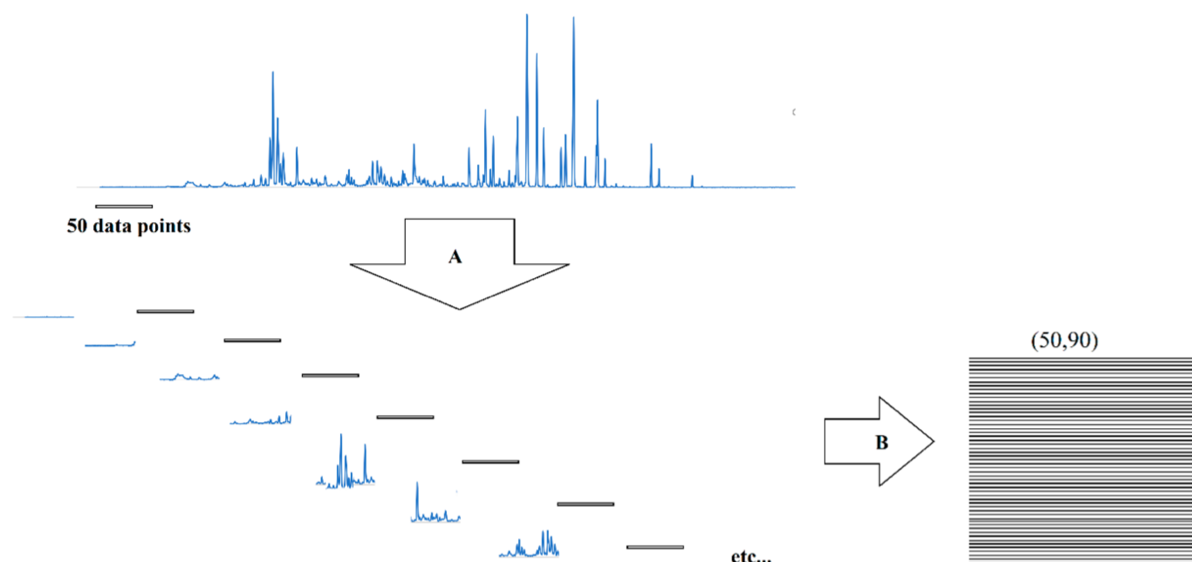

Figure 3.11 (a)The basic cut-and-stack method of converting a 1-dimensional array to a 2-dimensional array. (b)The spectral data were converted into a 2-dimensional matrix.

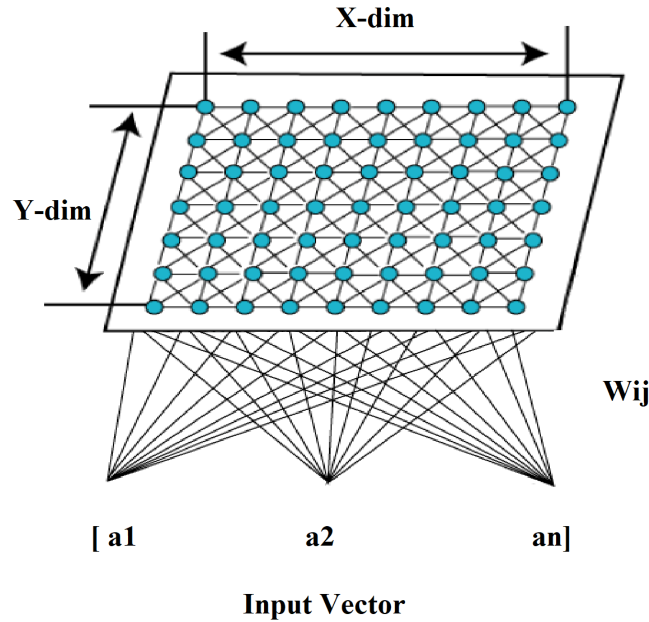

Figure 3.12 Using the SOM unsupervised deep-learning model to generate a 2-dimensional array from the spectral data. The 1-dimensional spectral data array was fed to SOM model and projected onto a 2-dimensional feature map.

It is important to highlight the fact that prior to forming the 2-dimensional matrices from the spectral data, they were scaled via min-max scaling method as per **equation 3.1**.

Once the 2-dimensional images were formed, a singular value decomposition (SVD) on the 2-dimensional matrices was carried out and then reconstructed the matrix by first layer of the SVD model as discussed previously.

Therefore, every spectral datum that related to a particular target at particular RF plasma power and gas-flow rate and specific working gas was converted into four separate images. This family of images was then used to train a convolutional neural network (CNN) model. **Figure 3.12** illustrates the formation of four separate images from every spectral datum. Given that there were 588 spectral data, it quadrupled as there were 4 image groups (588X4), which were used separately to train a CNN.

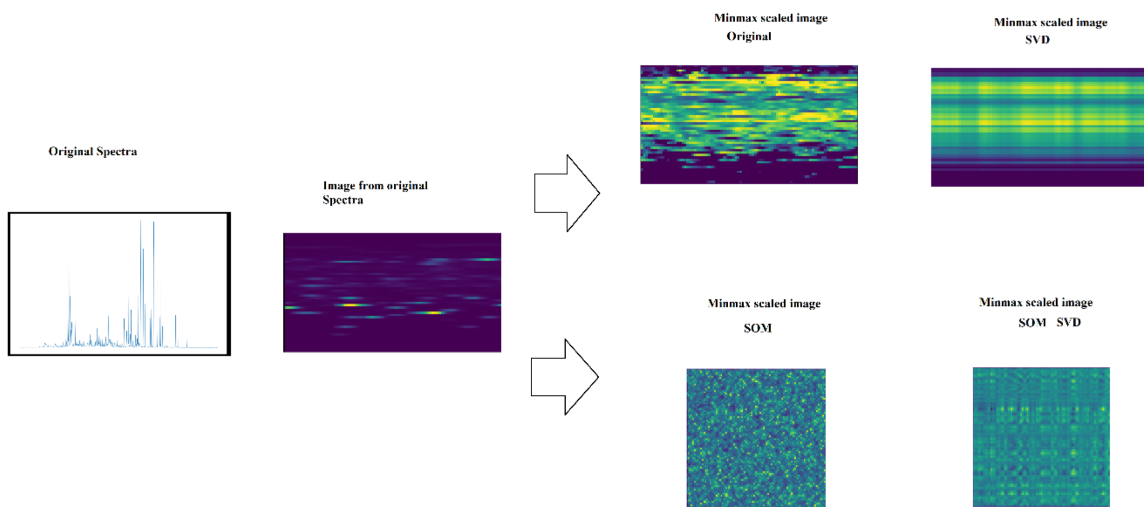

Figure 3.12 Each spectral datum was converted into four images; a min-max-scaled 2-dimensional array and its SVD reconstruction of first layer and a SOM-generated 2-dimensional array and its SVD reconstruction of the first layer. The arrows represent the routes to the methods of conversion (original and SOM).

To appreciate how difficult it was to distinguish the glow of the plasma under various conditions, some plots of the plasma spectrum are presented in the following figures: **Figure 3.13** presents the emission spectrum associated with 9-, 7-, and 3-standard-cubic-centimeter-per-minute argon flow rates overlayed (A) and also in a segregated format (B). In **figure 3.14,** the effect of the presence of 5% hydrogen in the argon gas in overlay and segregated form is presented. In **figure 3.15**, the emission spectrum associated with the four different target materials is presented. These spectra reveal some differences if precise attention is paid. However, these examples are presented here to illustrate the complexity and precision of the spectra in detail.

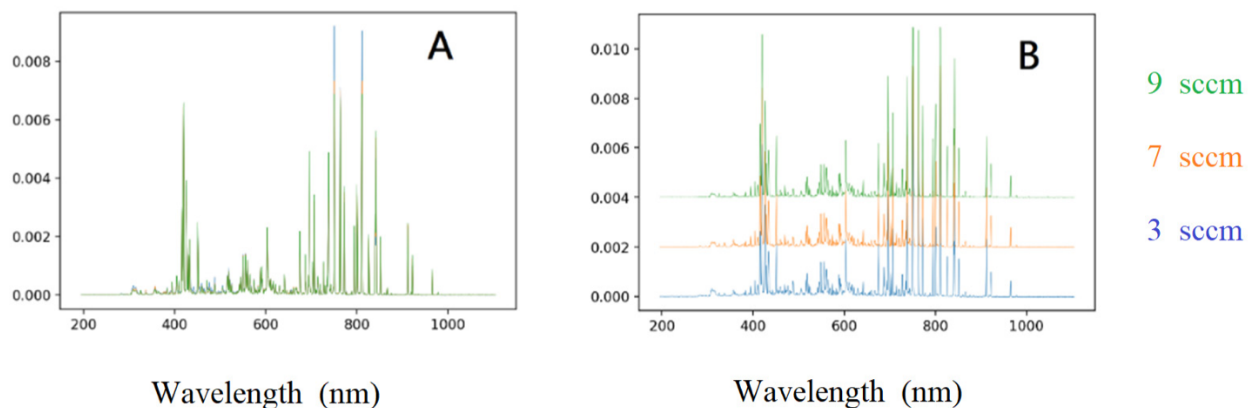

Figure 3.13. (A) Overlay of spectral data at 9, 7, and 3 sccm. (B) Segregation of the spectra.

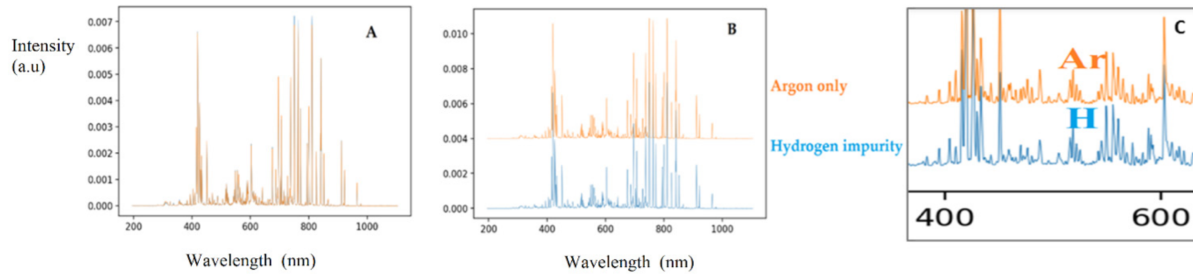

Figure 3.14. (A) Overlay of spectral data relating to pure argon and argon with 5% hydrogen impurity. (B) Segregation of the same spectra. (C) Section of the spectra magnified to illustrate the miniscule variation in the spectral data.

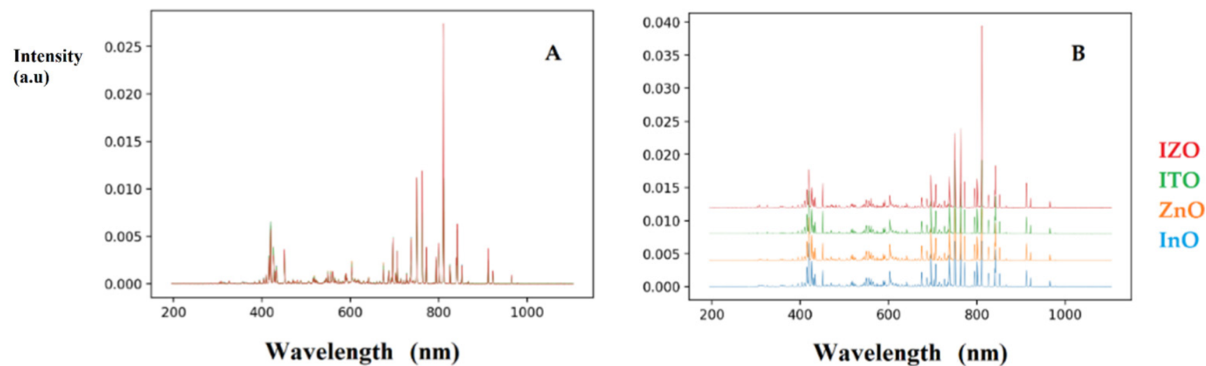

Figure 3.15. (A) Overlay of spectral data associated with four example target materials. (B) Segregation of the spectra.

The objective was for the CNN model to be able to calculate certain parameters, such as the gas-flow rate, plasma power, and presence of hydrogen, through computer vision assessment of these spectra. This is further illustrated in figure 7.9, where a section between 400 and 600 nm is magnified to illustrate the difference between spectra of the same target material at same plasma power and pressure, but with 5% hydrogen impurity in one.

The CNN Model

The four classes of image forms were used separately to train the CNN model. The structures of the CNN model for regression analysis and classification analysis were the same except for the final layer. The structure of the CNN model is presented in **figure 3.16**. The image data were submitted to two steps of convolution and max pooling, consecutively, prior to being flattened into a single vector. The vector was then used to train an artificial neural network model with four dense layers containing 5000, 5000, 100, and 20 neurons each, all bearing a rectified linear-unit function.

For regression analysis, a final dense layer with a single neuron was used for predicting the gas-flow rates and plasma power. The loss function used for the model training was mean squared error.

For classification analysis, the final dense layer with a single neuron was set up with a sigmoid activation function. The loss function used for model training was binary cross entropy.

Both the regression and the classification models utilised an Adam optimiser with a learning rate of 0.001.

Layer (type)	Output Shape	Param #
conv2d_6 (Conv2D)	(None, 46, 86, 20)	520
max_pooling2d_6 (MaxPooling2D)	(None, 23, 43, 20)	0
conv2d_7 (Conv2D)	(None, 21, 41, 32)	5792
max_pooling2d_7 (MaxPooling2D)	(None, 10, 20, 32)	0
flatten_3 (Flatten)	(None, 6400)	0
dense_15 (Dense)	(None, 5000)	32,005,000
dense_16 (Dense)	(None, 5000)	25,005,000
dense_17 (Dense)	(None, 100)	500,100
dense_18 (Dense)	(None, 20)	2020
dense_19 (Dense)	(None, 1)	21

Figure 3.16. The structure of the CNN model.

A vital part of this study was its focus on the treatment of the numerical data prior to model training. It is a well-known fact that for all deep-learning models, the data need to be scaled or standardised.

However, a secondary step in scaling the data was carried out. For each emission spectrum, the peak intensities were summed, and every intensity to the resolution of 0.2 nm was divided by the total sum. The importance of this step is vital to the performance of the models. This operation was performed specifically because the temperature of ions and electrons in the plasma are directly proportional to their random average kinetic energy, while Maxwell distribution governs the distribution of velocities for each particle when thermal equilibrium conditions apply. This has been well detailed in chapter 2.2.

This method is the simplest approach to calculate the temperature of the plasma, and its accuracy is conditional on using two lines, with a maximum difference in their upper energy states. Therefore, there are hidden patterns associated with each individual plasma when ratio of peak intensities is considered. Therefore, by implementing the operation of representing each 0.2-nanometer peak intensity as a fraction of the total intensities, it provides the neural network model with hidden features related to the microenvironment of the plasma for the model training.

The glow from the plasma is a representation of the plasma ingredients, its constituents, and their states. It can be assumed that a vast amount of information is embedded in the plasma glow. The objective

conducting the experiments associated with deep learning is to extract and exploit this information and correlate it with the parameters that are implemented during plasma formation. As these parameters ultimately govern the quality and properties of the thin films produced via this method, this is a step toward defining a digital shadow for the sputter-deposition system.

3.2 Characterisation Techniques

3.2.1 Four point probe

The 4-point probe is a simple apparatus is used to quickly determine the sheet resistance of a sample. As the name suggests, it consists of 4 probes which are aligned with one another (and 1mm spacing in between) and it measures the resistivity of semiconductor samples by applying a fixed current (I) through the two outer probes and measuring the voltage (V) through the two inner probes [152]. This is illustrated in **figure 3.17.**

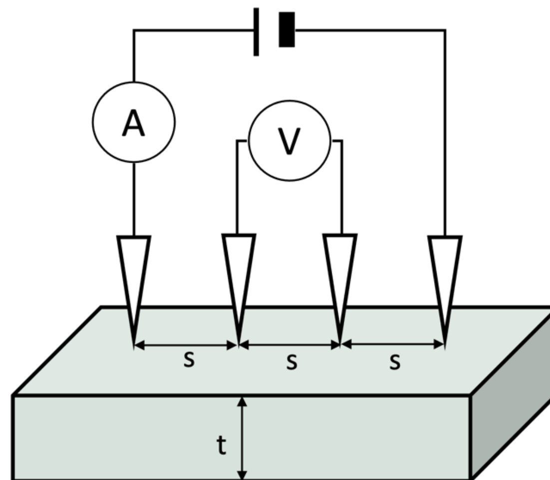

Figure 3.17. Schematic diagram of four-point probe setup

The measurement is taken in both forward and reverse mode, where the direction of the current is altered allowing an accurate reading. This allows the measurement of the samples' sheet resistance which can then be used to determine resistivity. Resistivity (ρ) (Ω.cm) for a semi-infinite volume is given by eq. 2.1 [153].

$$\rho = 2\pi s \left(\frac{V}{I}\right) \tag{3.3}$$

Where 's' is the spacing in between the probes and 't' is the thickness of the sample. This applies for bulk samples where the sample thickness is greater than the probe spacing in which case the current spreading from the outer probe is modelled as a sphere.

There are a number of factors that can affect the accuracy of the measurements. The probes must make ohmic contact with the material; if the material has a very low resistance and it is significantly thick, it will be immeasurable for the instrument due to the limited range of current source. Thus, for conducting materials, only accurate readings can be taken off of thin film samples. In addition to the thickness, the shape of the material can also contribute towards measurement errors. It is important to implement a correction factor to the samples sheet resistance to take into account the ratio of probe spacing to film

thickness/sample diameter. This factor can be determined via a thickness correction factor plot found elsewhere [154].

In the most cases, thickness will be significantly less than that of the probe spacing (thickness, t<<s) in which case the correction factor is applied as the current will spread out in rings rather than in sphere:

$$\rho = 4.53t\left(\frac{V}{I}\right), \left(\frac{t}{s}\right) \geq 0.5 \quad (3.4)$$

For this project, the Jandel Model RM3 4-point probe system was employed to measure the sheet resistance.

3.2.2 Hall Effect

The principle of operation of the Hall effect is based on the van der Pauw method. It is a measurement technique that accurately measures the resistivity of an arbitrarily shaped thin film with 4 small ohmic contacts placed on the corners of the sample.

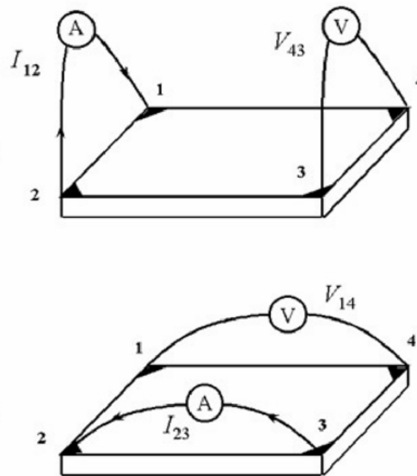

Figure 3.18. Schematic diagram of a van der Pauw configuration used to determine characteristic resistances R_A and R_B [154]

Van der Pauw method demonstrates that there are two characteristic resistances R_A and R_B corresponding to the terminals as shown in **figure 3.18**. The characteristics resistances are determined by passing current through 1 set of contacts and measuring the voltage from the other two. As per the van der Pauw configuration, R_A and R_B are calculated via the following expressions [154].

$$R_A = \frac{V_{43}}{I_{12}} \quad (3.5)$$

$$R_B = \frac{V_{14}}{I_{23}} \quad (3.6)$$

R_A and R_B are related to the sheet resistance via the following equation:

$$exp\left(-\frac{\pi R_A}{R_S}\right) + exp\left(-\frac{\pi R_B}{R_S}\right) = 1 \quad (3.7)$$

From this, the bulk resistivity ρ can be determined via:

$$\rho = R_s t \quad (3.8)$$

To perform the van der Pauw method, the following requirements have to be fulfilled:

- Sample is flat and uniformly thick
- Sample is homogenous and isotropic
- Contacts placed at circumference/edge of sample
- Area of contact should be at least an order of magnitude smaller than that of sample
- Surface does not contain any pinholes.

The Hall effect describes the behaviour of the free carriers in a semiconductor material upon the application of not only an electric but also a magnetic field. The objective of the hall effect is to determine the sheet carrier density n_s, by measuring the Hall voltage. If a constant electric current flows through a conductor in the presence of a magnetic field perpendicular to the plane of the sample, there is a transverse force exerted onto the moving charge carriers by the magnetic field which pushes them to one side of the conductor. This leads to a build-up of charge at both sides of the conductor which balances the magnetic influence, producing a measurable voltage between the two sides of the semiconductor [152]. This measurable transverse voltage is known as the Hall voltage. In addition to the carrier density, the measurement of this Hall voltage is also used to determine the nature of conductivity and the carrier mobility.

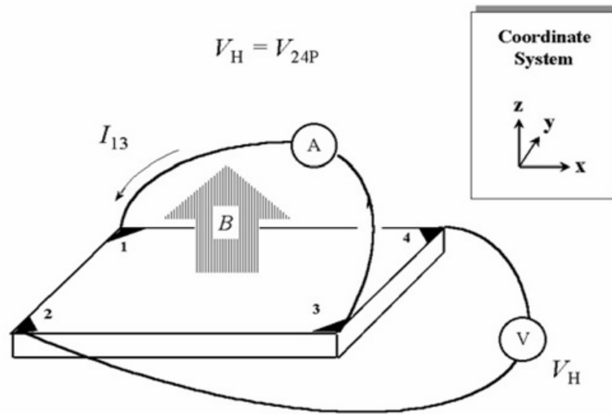

Figure 3.19. Schematic diagram of van der Pauw configuration used in the determination of the hall voltage V_H [155]

Figure 3.19 provides a visual representation of the Hall effect. To measure the Hall voltage, V_H, a current, I_{13}, is passed through opposing pair of contacts i.e. 1 and 3 and the Hall voltage (V_{24}) is measured across the other pair contacts i.e. 2 and 4 as the sample is subjected to a perpendicular magnetic field. Once the V_H is determined, the sheet carrier density/concentration can be calculated via the following formula:

$$n_s = \frac{IB}{q|V_H|} \tag{3.10}$$

from the known values of I, B, and q where I is current, B is magnetic field strength q is the elementary charge.

The Hall effect system at LSBU consist of discrete hardware of bespoke design allowing for accurate measurements. Whilst the majority of the hardware is commercially available, the configuration of the system was designed and custom-built consisting of the following components:

- An Oxford instruments, water cooled variable pole geometry electromagnet (Model N100) which was responsible for generating the magnetic field. This was powered by a PC controlled power supply (Sorenson XG-100-15) and is capable of achieving a peak field strength of 1 tesla.
- A custom PC controlled switching unit (developed in-house) to allow for automated reversal of the magnet polarity.
- Keithley measurement system which provided current sourcing, monitoring and voltage measurements which were PC controlled via a GPIB cable. This consisted of:
  -A model 7065 Hall effect matrix switching card, housed in a model 7001 switch mainframe which automates the multiple source and measuring configurations applied to samples under examination

- A model 6220 current source capable of supplying current ranging from 100fA to 100mA allowing for measurements of samples with wide resistivity ranges.

-A model 2182A nano-voltmeter capable of measuring voltages in the range of 1nV to 100V with a high degree of accuracy.

- Control of the various hardware components and data logging were achieved via a bespoke software solution by Semimetrics Ltd allowing for almost complete automation of the Hall effect measurement process upon configuring the initial conditions.

3.2.3 Spectrophotometry

Spectrophotometry is the quantitative measurement of the reflection and transmission properties of a material as a function of wavelength. A spectrophotometer is an instrument that is used to measure the intensity of wavelengths in a spectrum (UV-VIS-NIR) of light compared with the intensity of light from a standard source. This beam is chopped and diffracted to discreet wavelengths. The light beam is passed through a sample and the intensity of light that reaching the detector is measured [156].

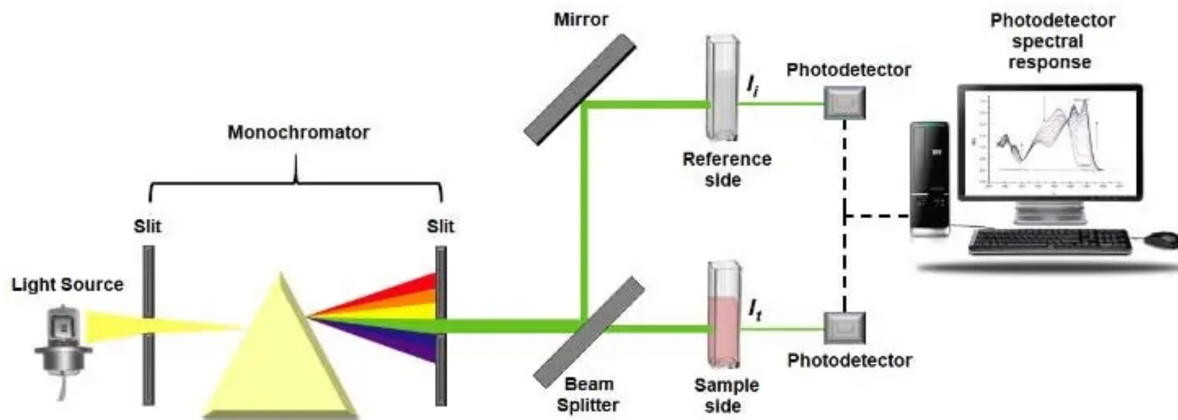

Figure 3.20. Working principle of double beam spectrophotometry [157]

A typical spectrophotometer such as the Varian Cary 500 is capable of producing and detecting light from the UV range, through the visible and into the short-wave IR regions (175-3300nm). It makes use of a pair lamps i.e., tungsten and deuterium and a series of shutters and grating to generate the monochromatic light in nm steps. A double beam UV visible spectrophotometer is typically used to determine the transmission and reflection properties of the samples as seen in **figure 3.20**. The light source strikes the monochromator which selects the light beam with specific analytical wavelengths from the source. This is achieved by allowing the polychromatic light to enter the slit of the monochromatic instrument and only allowing light with a single wavelength (consisting of a small region of the electromagnetic spectrum) to pass through via the exit slit. As mentioned, light is passed through the system with one beam being fed directly to a detector as a reference measurement and then the second being directed to the measurement area. This beam is then navigated through an array of fixtures depending on the requirement of the measurement before it returns to a 2nd detector. The detector converts the arrival of photons in the light rays into an electrical signal which allows for the measurement of transmission and reflection and subsequent calculation of absorption [158].

Optical properties of the thin films were carried out via a UV-VIS spectrometer (Bibby Scientific Ltd, Staffs, UK) by using the absorption data. Tauc plots were made to measure the optical bandgap of the material. The plot was made by plotting the hv(a-axis) against the $(\alpha\text{-hv})^{1/2}$ (y-axis), where the α is the absorption coefficient of the material.

3.2.4 Stylus Profilometer

A surface profilometer was employed to measure the thickness of the samples. The mechanically based profilometer possesses a stylus which detects the surface and traverses along it whilst maintaining contact in order to acquire changes in the surfaces' height. A feedback loop monitors the mechanical force from the sample that is exerted onto the probe as it scans along the system. The profilometer uses a feedback system to keep the arm at a fixed setpoint (i.e. torque) and adjustments in the z-position of the arm holder to maintain the setpoint can be used to reconstruct the surface [159] which can be seen in in **figure 3.21**.

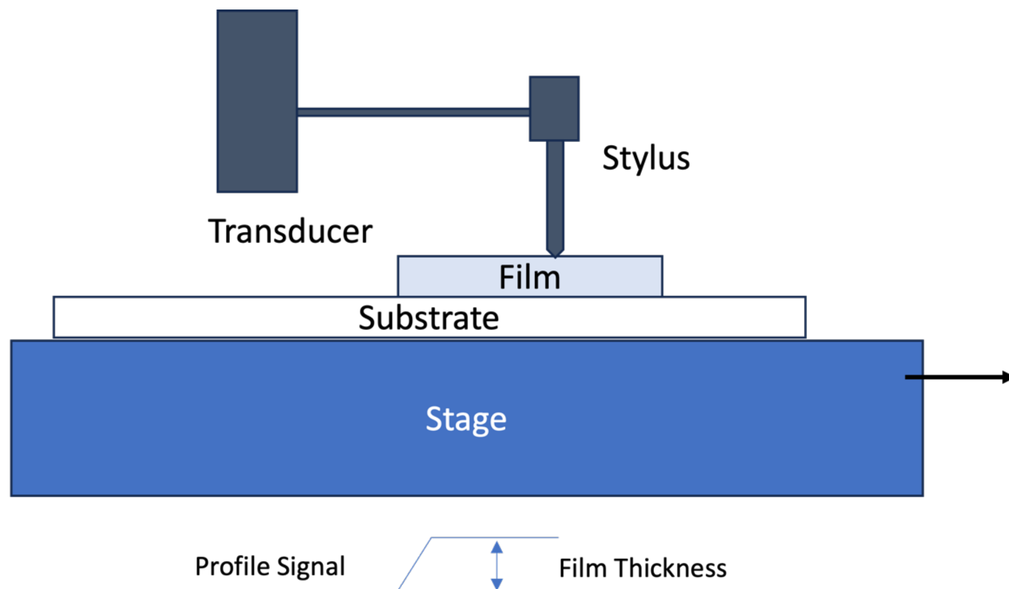

Figure 3.21. Schematic diagram of a basic stylus profiler

The samples were tested for film thickness via a profilometer (Veeco, NY, USA); this was carried out by scanning the stylus of the profilometer over a one mm strip of deposited films on a soda-lime glass substrate. A removable strip of Kapton tape was used to shield a particular area of the sample from film deposition creating a step which the stylus profilometer scanned over for the measurement of film thickness.

3.2.5 Scanning Electron Microscopy (SEM)

A scanning electron microscopy is a powerful instrument used to direct an electron beam from the cathode at the surface of a sample (mounted onto an anode) which raster scans the surface to form an image. The SEM provides information about the surface morphology of the sample [160]. The interaction between the electrons in the beam and the surface of the samples results various being produced which can be used to obtain in-depth information about the surface topography and composition.

The SEM works by producing highly energised electrons at the top of the column and accelerating them down which then pass through a series of magnetic lenses and apertures to yield a focused beam of electrons until it finally reaches the surface of the sample. The stage that the sample is mounted on is situated in the chamber area and in most cases both the column and the chamber are operated in a vacuum; the level of vacuum depends on the design of the microscope.

The position of the electron beam is controlled by a pair of scan coils which sits above the objective lens; these coils allow the beam to scan the surface of the sample in a raster fashion revealing information about a defined area on the sample and depending on the signal produced from the sample-electron interaction, the information is collected by appropriate detectors [161, 162].

These primary electrons, upon impacting the surface, transfer their energy into the surface in a tear drop shaped area of interaction. As the electrons in the beam interact with the sample, various signals are ejected from the sample i.e. secondary electrons, backscattered electrons and characteristic X-rays as shown in **figure 3.22**. These signals are collected by several detectors to produce an image displayed on the computer screen. The sample is penetrated by the electron beam by a few microns which varies with the accelerating voltage and density of the sample.

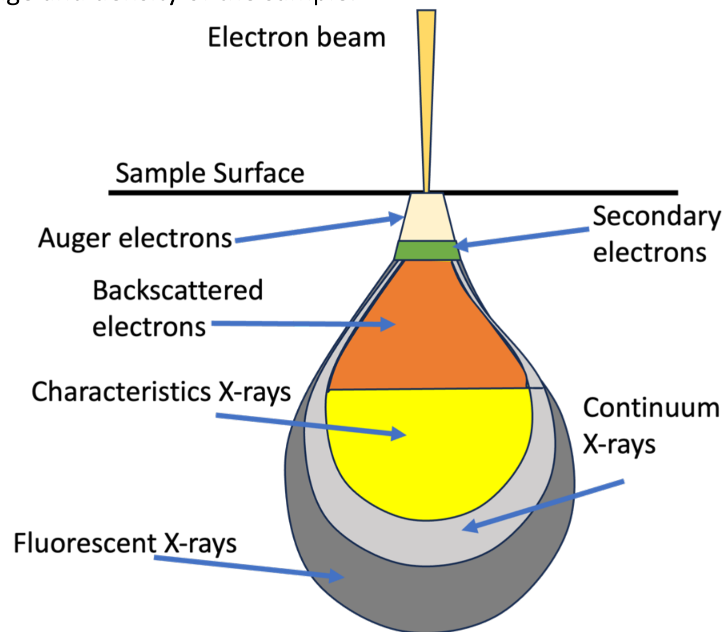

Figure 3.22. Schematic diagram of the sample-electron interaction ejecting various signals

Since the SEM relies on a beam of electrons to image, it is essential that the samples being investigate are charge free as it can result in distortion and/or image drift during high resolution image capture, which is take at a slower raster scan rate. If the sample is of a non-conductive nature then it is usually sputter-coated with thin film of gold (<5nm) beforehand to ensure a conductive path is created without comprising surface features [163].

3.2.6 EDS

Energy-dispersive X-ray spectroscopy (EDS) is a powerful tool that allows the analysis of the elemental composition of the desired thin film sample. The principle of operation is the capacity of high

energy electromagnetic radiation (i.e. X-rays) to eject core electrons (i.e. inner shell electrons) from an atom in the sample. This principle is known as Mosley's Law which states that there is a direct correlation between the frequency of light release and the atomic number of the atom.

Ejecting these inner shell electrons from the atom will results in a vacant site or a hole which can be occupied by a higher energy electron; it will release energy as it relaxes into the hole. The energy that is released during the relaxation process is unique to each element found on the periodic table and the bombardment of a thin film sample with X-rays permits the identification of elements and to which degree these are present.

A schematic diagram illustrates the principle of operation of EDS (**figure 3.23**). The letters K, L and M signify the 'n' value that electrons in that shell occupy. For K electrons, which occupy the innermost shell, n=1 while α and β denote the size of the transition. For example, relaxation of an electron from L to K is described as Kα while going from M to K would be defined as Kβ transition. This method used to describe the process as a whole is known as Siegbahn notation.

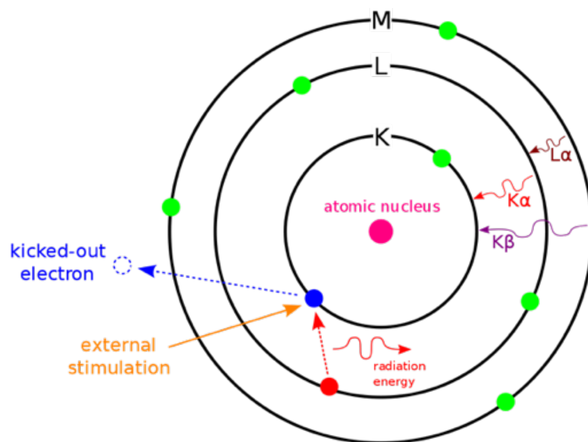

Figure 3.23. Schematic diagram illustrating the ejection and relaxation of electrons in an atom [164]

The films prepared via the experiments outlined in 3.1.2 were consequently characterised using a Zeiss Supra VP35 Field Emission Gun Scanning Electron Microscope equipped with an EDAX Octane Super Energy Dispersive Spectrometer (Ametek, Darmstadt, Germany) (Energy-dispersive X-Ray spectroscopy, EDS) to evaluate the homogeneity and morphology of the film and gather indication on the film chemical composition, in particular the In/Zn ratio (samples S1 to S7) or level of contaminants in the pure ZnO films (samples H0, H3 and H6). The films were also investigated using diffraction techniques, both electron backscatter diffraction (within the Zeiss Supra FEG-SEM equipped with an EDAX DigiView EBSD camera, Darmstadt, Germany).

3.3 Summary

An array of thin film IZO and hydrogen doped ZnO samples with varying growth conditions were deposited via RF magnetron sputtering. For experiments involving the analysis of the plasma via the colour characterisation method, the glow discharge during deposition was exposed to two different spectrometers as discussed in section 2.1, one to calculate the chromaticity of light and the other to

acquire the emission spectrum. For experiments pertaining to machine learning, the spectral emission of the plasma was converted into a format that was interpretable for a number machine learning/ deep learning models. The well-trained models were given the task to predict certain features of the resultant thin film samples and growth conditions associated with a particular emission spectrum. The thin film samples were subjected to surface, opto-electronic and electrical characterisation.

Chapter 4 Optical Analysis of RF Sputtering Plasma through Colour Characterization

In this chapter, as mentioned in the literature review (Chapter 2.3), a novel strategy of the in-situ characterisation of plasma in a sputtering process has been reported by translating the emission spectra into a colour indexing (chromaticity) pattern that is able to quickly monitor any changes in the plasma character with a change in the operating parameter conditions during the course of the process, which in turn provides a better handle to reflect the instabilities of the tool and its optimising parameters. The materials and methods employed for this experiment can be found in 3.1.1.

4.1 Results

4.1.1 Chromaticity of the Plasma Emissions

The emission characteristics in terms of the whole spectral plot and the chromaticity index were obtained for each test group.

Test 1, from the moment that the plasma is ignited, the spectral data can be obtained from it. However, by plotting the chromaticity *x, y* values of the plasma light from a cold start, these values will keep varying for up to 2 h. After 2 h, the variance in the *x* and *y* values that were obtained will significantly reduce; this is the point the plasma can be considered to be stabilized or more stable. **figure 4.1** presents this observation. The *x* and *y* data obtained from the plasma during the first hour of ignition at 100 W for a magnetron fitted with Indium Zinc Oxide (IZO) target under gas Ar (**A**,**B**) and gas ArH (**C**,**D**) along with data obtained 2 h after ignition. During this 1 h interval the plots remain relatively stable. The stabilized data were gathered over an additional thirty minutes period. As it can be seen (**A**,**C**) prior to stabilisation the *x,y* coordinates are scattered across the plot area until the plasma is stabilized at which point the plots fall within close proximity (**B**,**D**).

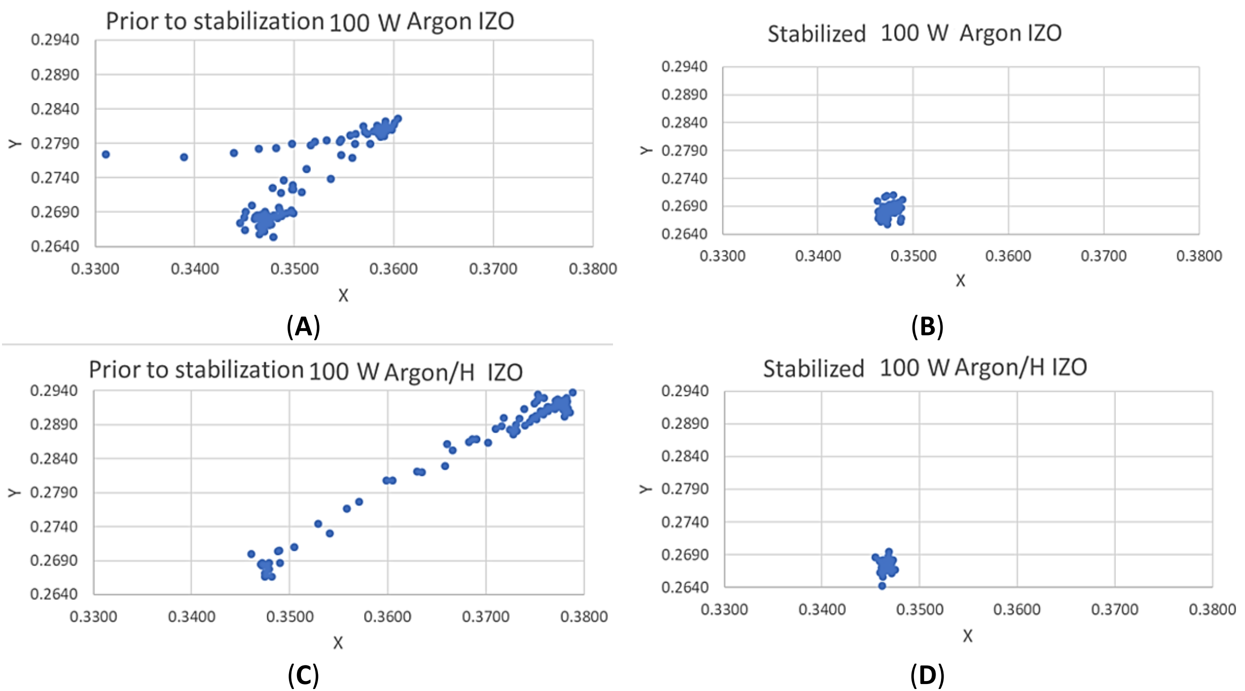

Figure 4.1. The *x* and *y* data obtained from the plasma during the first hour of ignition at 100 W for a magnetron fitted with Indium Zinc Oxide (IZO) target under gas Ar (**A**,**B**) and gas ArH (**C**,**D**).

To demonstrate the complexity of relying on the conventional methods, such as the peak intensity ratio method, to monitor the progress of the plasma toward stability, the spectral plot of the 100 W Argon plasma over a period of one hundred and thirty minutes post-plasma ignition are presented in **figure 4.2**. As an example, particular transitions that were previously evaluated by other authors for measuring electron temperature and density were chosen to measure these data [165]. The ratio plot that is presented in **figure 4.2**A is related to the intensity ratio of 404.44 nm (Ar-I) transition 3*s*23*p*5(2P°1/2)5*p* 2[3/2] 2 to 3*s*23*p*5(2P°3/2)4*s* 2[3/2]° 1 and 426.62 nm (Ar-I) transition 3*s*23*p*5(2P°3/2)5*p* 2[3/2] 2 to 3*s*23*p*5(2P°3/2)4*s* 2[3/2]° 1. The ratio plot presented in **figure 4.2**B is related to the intensity ratio of 480.60 nm (Ar-II) transition 3*s*23*p*4(3P)4*p* 4P° [5/2] to 3*s*23*p*4(3P)4*s* 4P [5/2] and the 470.23 nm (Ar-I) transition 3*s*23*p*5(2P°3/2)5*p* 2[1/2] 1 to 3*s*23*p*5(2P°1/2)4*s* 2[1/2]° 1. It can be seen that it will be challenging to apply the peak intensity method as an instant real time monitoring technique. This highlights the novelty of using colour function as a mean to monitor the plasma stability as the chromaticity plot of the *x* and *y* values clearly demonstrates a linear path toward the stable *x, y* chromaticity values.

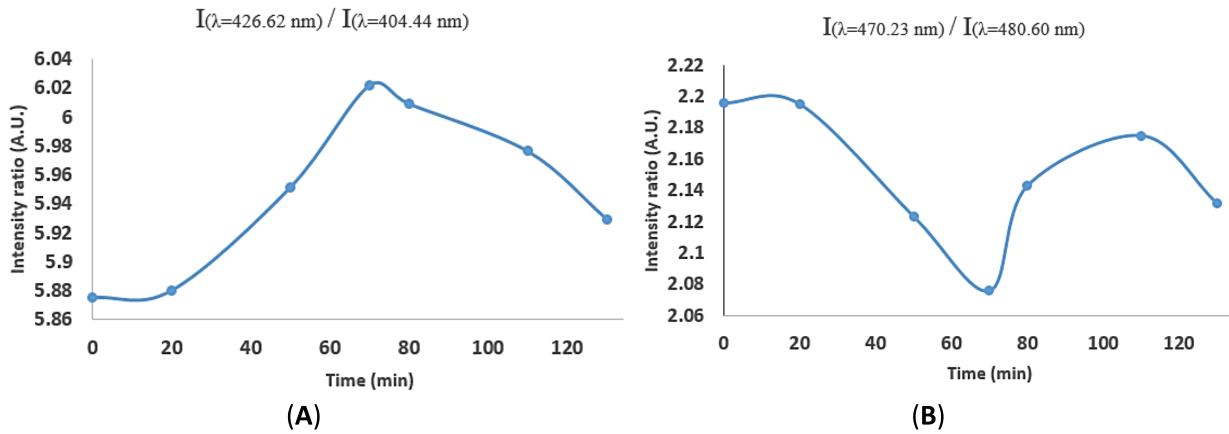

Figure 4.2. The intensity ration of four peaks are presented over 130 min. (**A**) The intensity ratio of the (Ar I) 404.44 nm and the (Ar I) 426.62 nm emission peaks. (**B**) The intensity ratio of the (Ar I) 470.4 nm and the 480.60 nm emission peaks.

Test 2, the RF power that was used to ignite and run the plasma is the source of energy for ionising the working gas and driving the sputtering process. Higher energy will result in more excited and metastable atoms to be created, and consequently will increase the bombardment of the target surface. During this part of the investigation, after stabilising the plasma at 100 W, the power was increased up to 300 W (at a rate of 100W per minute) and data was collected at ~9 s intervals under argon. A clear linear relationship can be observed between the chromaticity value and the plasma power, as presented in **figure 4.3**. The values of *x* and *y* decrease with increasing the RF power and a shift toward blue in a linear manner is also observed.

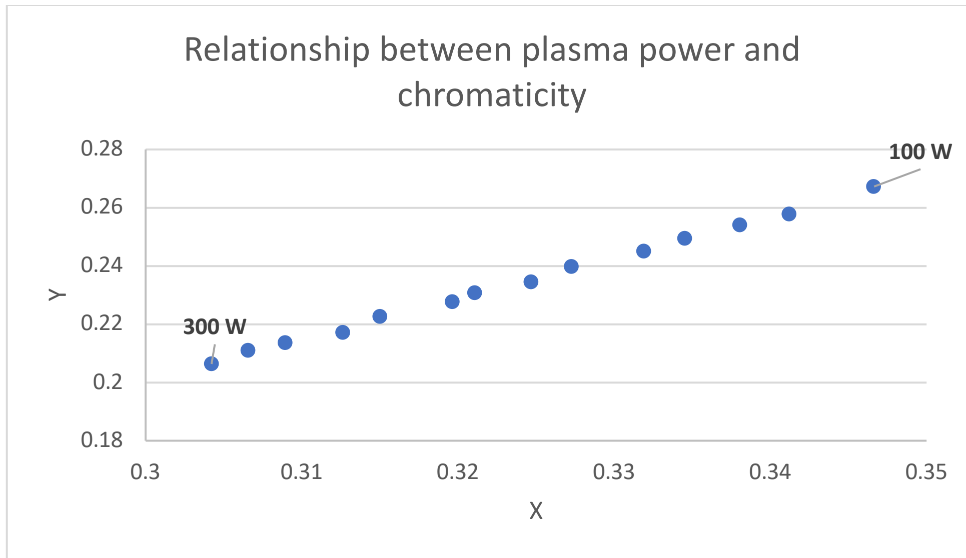

Figure 4.3. The relationship between the power of plasma (radio frequency (RF)) and the *x* and *y* values.

In Test 3, an interesting pattern is observed by increasing the pressure of the chamber under each Gas (Ar or ArH), after the plasma has been stabilized, which is highlighted in **figures 4.4 and 4.5**. The test was started with the lowest pressure achievable based on the mass flow controller of the machine (1.2×10^{-3} mbar) and then the pressure was increased. With increasing the pressure, the *x* and *y* values start to increase, but, at a certain point, a loop is made (a U-turn shape) and it starts to decrease with higher pressure indicating that the colour is initially shifting toward white and then reverting toward blue.

Table 4.1. The *x* and *y* data obtained by Jeti spectrometer from the plasma at 100 W, and 2 h after stabilization for a magnetron fitted with IZO target under gas Ar at various pressures

Pressure ($x10^{-3}$ mbar)	x	y
1.20	0.3396	0.2634
1.50	0.3439	0.3668
2.00	0.3481	0.2678
2.50	0.3498	0.2691
3.00	0.3500	0.2677
3.50	0.3505	0.2665
4.00	0.3505	0.2648
4.50	0.3500	0.2640
5.00	0.3487	0.2625
5.50	0.3485	0.2614

6.00	0.3479	0.2606

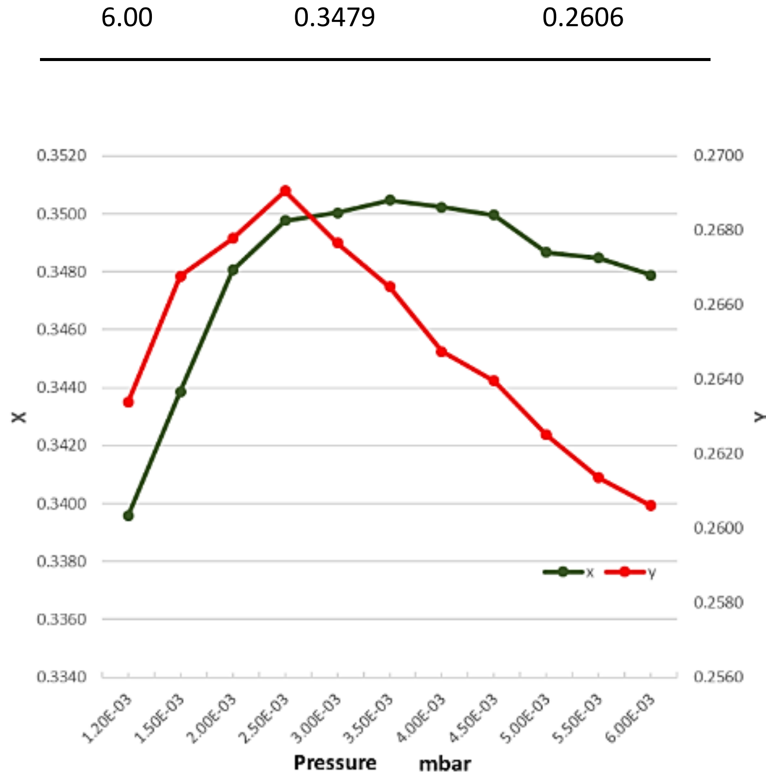

(A)

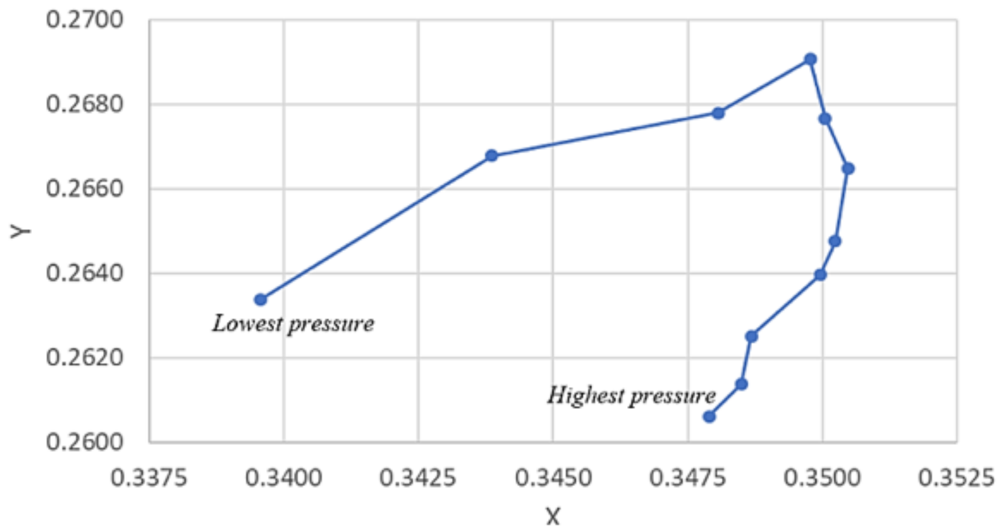

(B)

Figure 4.4. (**A**). As the Argon pressure is increased, the *x* and *y* values increase until about 2.5×10^{-3} mbar and then start to decrease. (**B**) The *x* and *y* plot demonstrates a U-turn formation.

Table 4.2. The *x* and *y* data obtained by Jeti spectrometer from the plasma at 100 W, and 2 h after stabilization for a magnetron fitted with IZO target under gas ArH at various pressures

Pressure	x	y

(x10^{-3} mbar)		
1.20	0.3361	0.2609
1.50	0.3429	0.2663
2.00	0.3480	0.2689
2.50	0.3497	0.2691
3.00	0.3502	0.2677
3.50	0.3506	0.2672
4.00	0.3512	0.2670
4.50	0.3495	0.2646
5.00	0.3489	0.2642
5.50	0.3490	0.2624
6.00	0.3488	0.2615
6.50	0.3482	0.2612
7.00	0.3470	0.2590

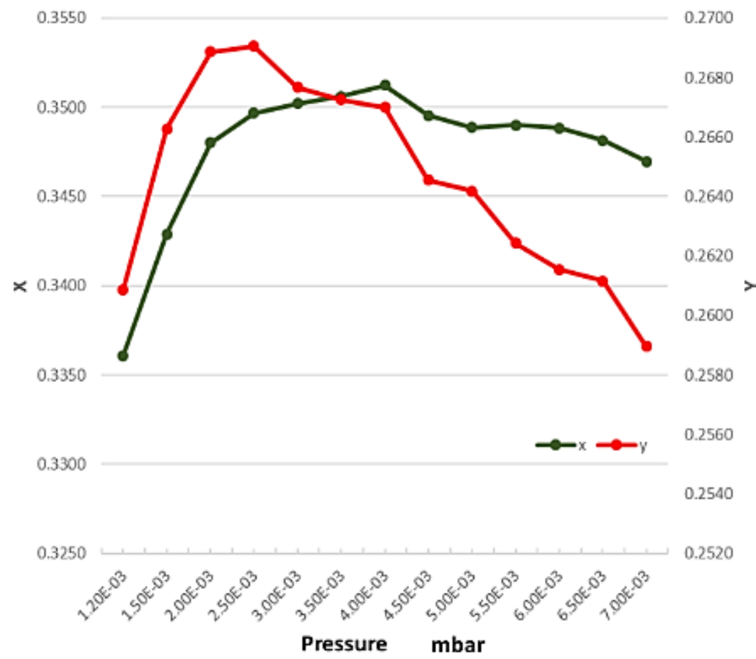

(A)

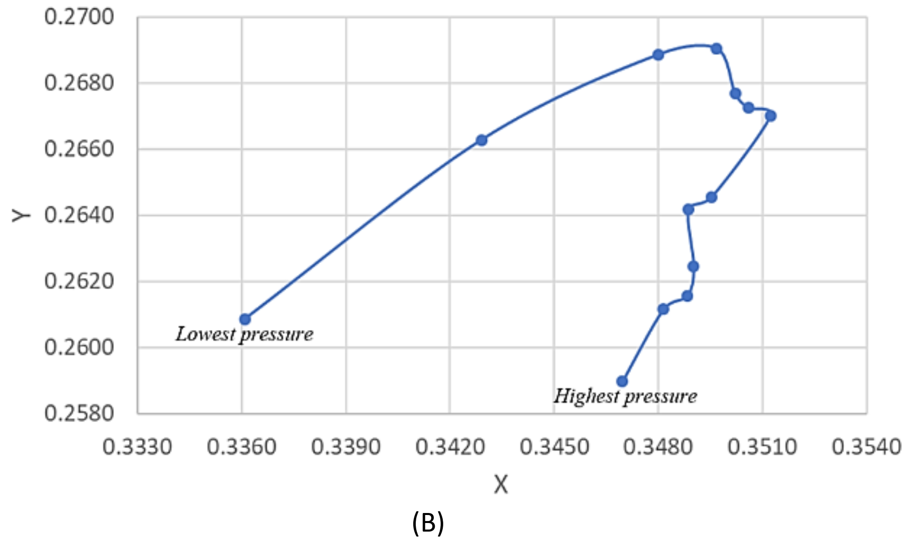

(B)

Figure 4.5. (A). As the Argon Hydrogen mix pressure is increased, the *x* and *y* values increase until about 2.5×10^{-3} mbar and then start to decrease. (B). The *x* and *y* plot demonstrates a U-turn formation, indicating that the colour is initially shifting toward white and then reverting toward blue .

The spectral plot of the plasma emission under various pressures clearly shows an increase in the intensity of some of the transition lines with increasing the pressure, which ultimately affects the *x* and *y* reading (for example, the data obtained from IZO target and Argon gas at various pressures is presented in **figure 4.6**).

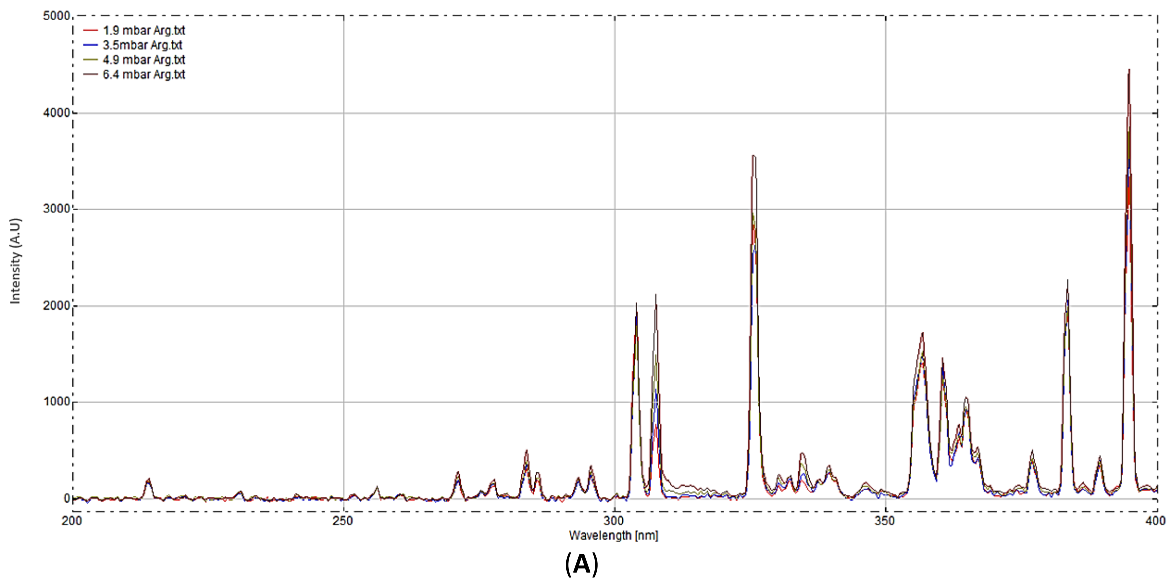

(**A**)

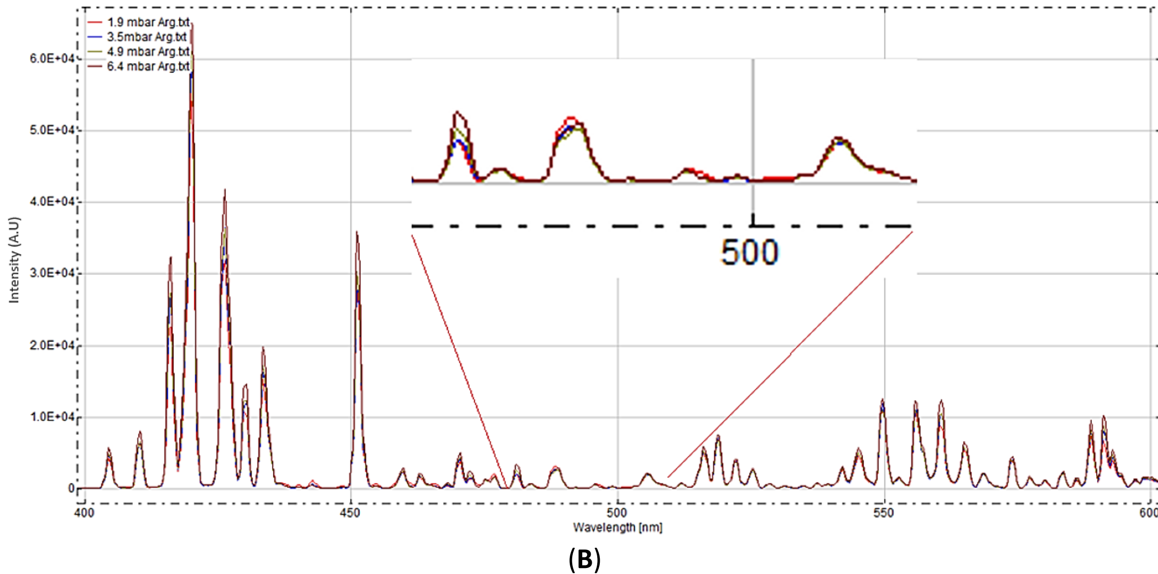

(**B**)

Figure 4.6. The effect of working gas pressure observed on the spectral plot (200 to 600 nm) of the plasma with IZO target and Argon gas only at various working gas pressures.

When compared to the *x* and *y* plots in **figures 4.4** and **4.5**, it can be observed from the spectra that there is an increase in the intensity of certain peaks which makes the assessment of the data complex with further evaluation. All of these increases in intensity can be summarised as presented in **figures 4.4 and 4.5** by evaluating the colour of the plasma discharge. The inset in the second section of the plot demonstrates the complexity of analysing every single peak for the amount of slight increase in one of the peaks. (A): spectral plot 200 to 400nm; (B): spectral plot from 400 to 600nm.

The rise in the intensity of all the peaks is simply due to the larger number of excited atoms and well known, however, the exact mechanism by which the *x*, *y* values make such a U-turn pattern is possibly related to complex switching of the electronic transitions, and hence it is related to the area under emission peaks of certain transitions across the spectrum and these peak areas are related to the microenvironment of the plasma and the interaction of the plasma constituents, distribution of energy, electron temperature, and charge densities involved, but the exact mechanism needs further attention and research, this suggests that there is a possibility of correlating the colour to the plasma's physical state.

This is currently being investigated by the authors through the monitoring of the above-mentioned factors affecting the plasma constituents and will be reported separately. Here, the core of the current communication is a focus on the currently observed data in terms of colour indications.

Finally, another particular observation was made; once the IZO target material is exposed to gas ArH and under a stable plasma, switching from ArH to Ar does not lead into a direct swift stable reading, rather for a period up to ~1 h, the values of *x* and *y* fluctuate. The fluctuation is only observed when going from gas ArH to Ar, and not from Ar to ArH under the same protocol, which indicates the possible incorporation of hydrogen into the target material similar to the target poisoning process, however this cannot be verified prior to close investigation of the target material. **figure 4.7** presents this observation.

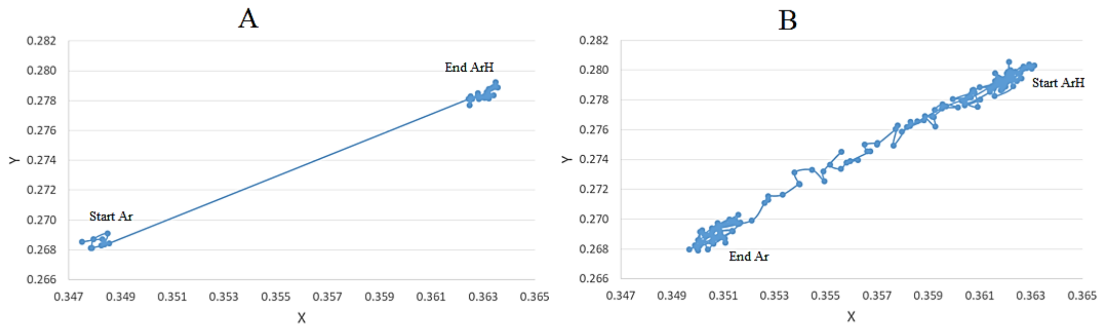

Figure 4.7. Chromaticity (x, y) diagram of:. (**A**) Switching from Ar to ArH occurs swiftly. (**B**) Switching from ArH to Ar,

The plasma colour demonstrates a colour change as the *x,y* values change over the course of ~1 h prior to stabilisation in a linear fashion after the target has been exposed to Argon/Hydrogen mixture. This observation can be interpreted as either the rate by which hydrogen is disappearing from the chamber and/or possible formation of target hydrogen compounds at the surface of the target (target poisoning by hydrogen) and the time that is required for the target to revert back its original state while switching from Ar to ArH does not demonstrate any pattern, rather a swift instant jump is observed.

4.1.2 Optical Emission Spectroscopy of the Plasma Emissions

In the previous section, The focus was on the chromaticity (colour) of the emission, parallel to these studies Results from optical emission spectroscopy of the plasma was obtained, which are associated with the experiments involving only the Argon gas as a comparative guide to enable to discuss the observations seen through chromaticity analysis.

During **Test 1**, the stability of the plasma was monitored through the colour functions, at the same time, the optical emission data of the spectra was obtained and divided the spectrum to seven sections: a, b, c, d, e, f, and the UV. **Figure 4.8** presents these sections; the UV covered emissions from 300–400 nm, a: 400–430, b: 431–449, c: 450–500, d: 500–600, e: 600–700, and f: 700–800 nm. The area under each region was calculated and monitored. The area via integral under each peak region was then used for further analysis of the data to monitor the variations of the area as a dependent of various experimental parameters that was already discussed; duration of emission stability, RF power applied to the magnetron, and the various operating Argon pressures.

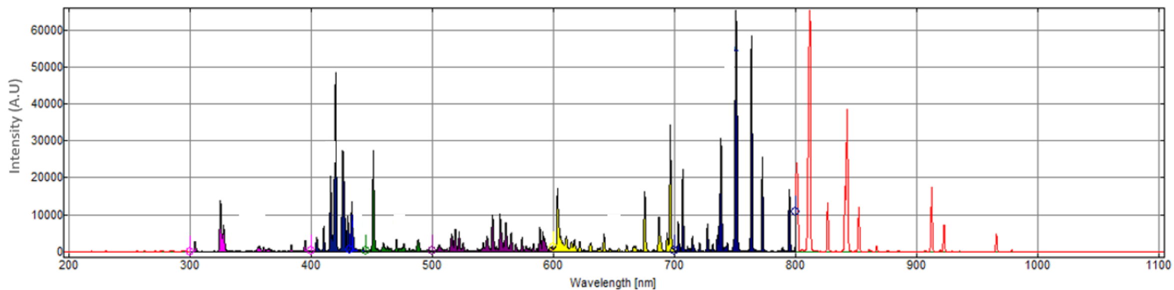

Figure 4.8. The emission spectra of the plasma were segmented into seven sections. The area under each region was calculated and monitored.

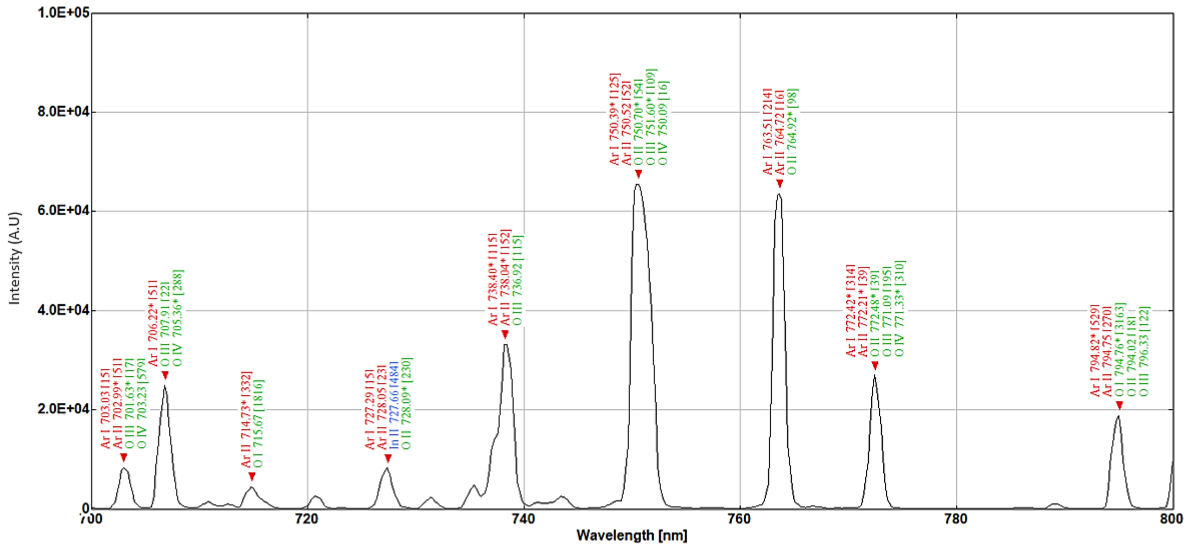

(A)

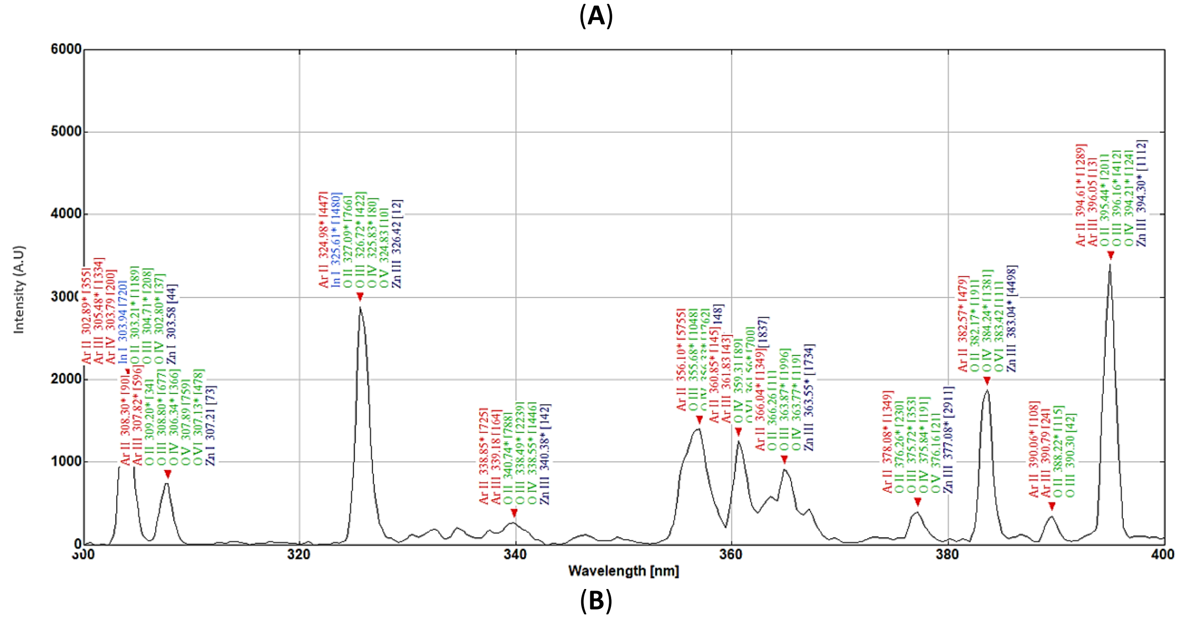

(B)

Figure 4.9. The emission spectrum and the associated Argon, Indium, Zinc and Oxygen states within far infra-red (**A**) and the UV section (**B**) of the spectrum obtained from the sputtering plasma.

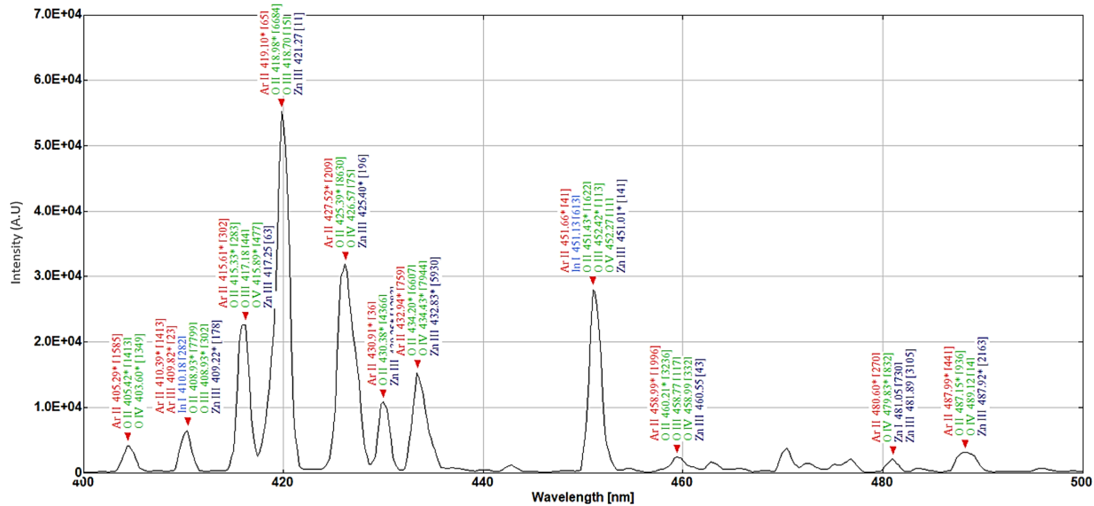

(A)

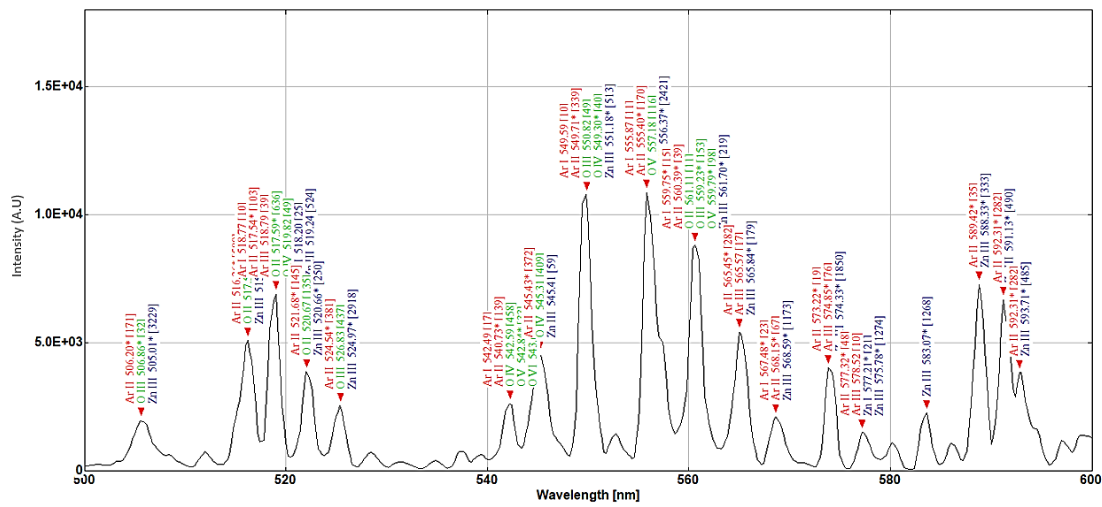

(B)

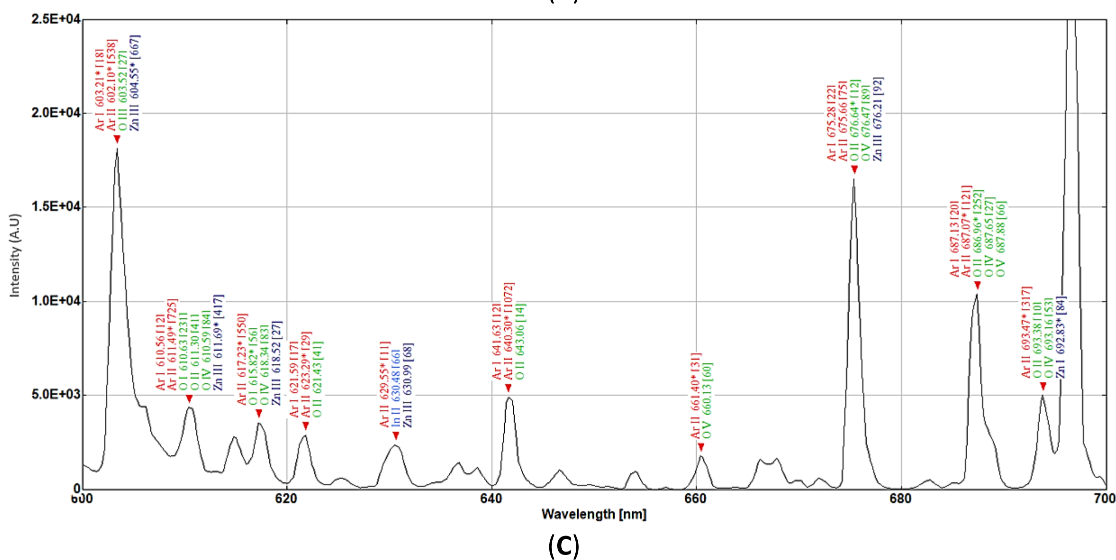

(C)

Figure 4.10. The emission spectrum and the associated Argon, Indium, Zinc, and Oxygen states within the 400–700 nm section of the spectrum obtained from the sputtering plasma. Spectral range, (A):400-500nm, (B)500-600nm, (C):600-700nm.

The area under all of the regions was summed, and then the ratio of the area under each section of the study was calculated as a percentage of the total area under the peaks to visualise how the emissions from the associated transition changed during plasma stabilisation and when the parameters, i.e., power and Argon pressure, were changed. In **figure 4.11**, the stability of the plasma over time is monitored over a total period of 5000 s at intervals 1000 s, e.g., T1: 0 to 1000 s, T2: 1000–2000 s, etc.

It can be seen that some of these regions demonstrate a progressive increase in their emission ratio when compared to the overall ratio, while some demonstrate a reduced ratio of emission to the whole emission intensity. Ultimately, the area under the peak readings tend to move toward stabilisation, and is this very much in agreement with mentioned observation associated with the chromaticity data.

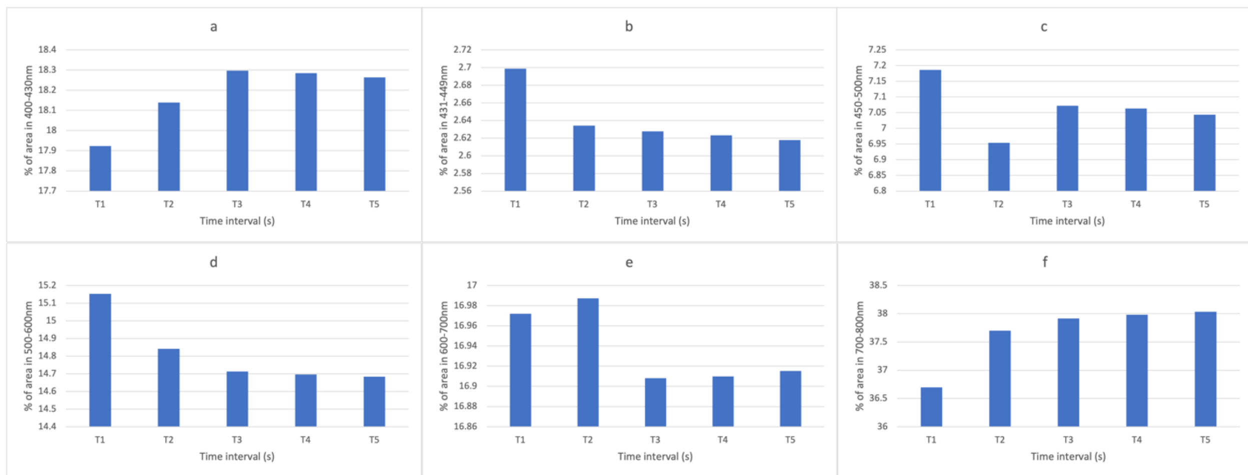

Figure 4.11. Plot demonstrating the ratio of peak in (**a**) 400-430nm (**b**) 431-449nm (**c**) 450-500nm (**d**) 500-600nm (**e**) 600-700nm (**f**) 700-800nm wavelength range to the total spectral area under the peak during the first 5000 s from the ignition of the plasma. The time series is divided into five sections of 1000 s.

Figure 4.12 presents the effect of the RF power applied to the magnetron on the emission peak areas of the spectral segments, where it is clearly noticeable that an increase in the emission ratio is observed in sections **a**, **b**, and **c**, while **d**, **e**, and **f** demonstrate a reduction. There seems to be a linear trend in both cases. This is interesting and it matches the observation of the chromaticity indices, which also demonstrated a linear relationship with plasma generating power.

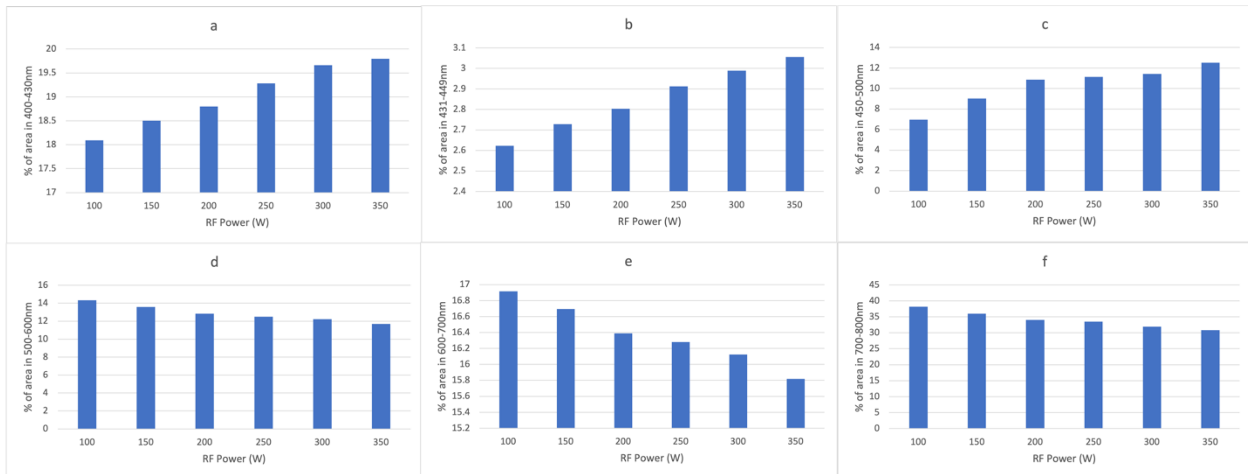

Figure 4.12. Plot demonstrating the ratio (to the total spectral cover from 300 to 800 nm) of the area under the peak in each of the segments with RF plasma power for the IZO deposition.

Figure 4.13 presents the effect of the chamber pressure on the regions of the emission spectrum and the ratio of the peak areas to the overall area covered. Just like the previous cases, it can be seen that the different sections of the spectrum demonstrate different trends in terms of increase or decrease of the peak areas. Once again, each section is demonstrating either an increasing or decreasing ratio of emission areas to the overall spectral emission area under the peaks. Although the UV emission region (300–400 nm) and the f section of the spectrum (700 to 800 nm) are not used for calculating the chromaticity indicates, the data were presented here to demonstrate the spectral property of the plasma at those regions. The results for the UV section of the spectrum are separately presented in **figure 4.14**. Where the UV emissions peak area demonstrate an increasing trend over the 5000s period and demonstrate a linearly increasing relationship with the plasma power, the higher chamber pressure seems to reduce the ratio of the UV emissions to the overall emission within the spectrum.

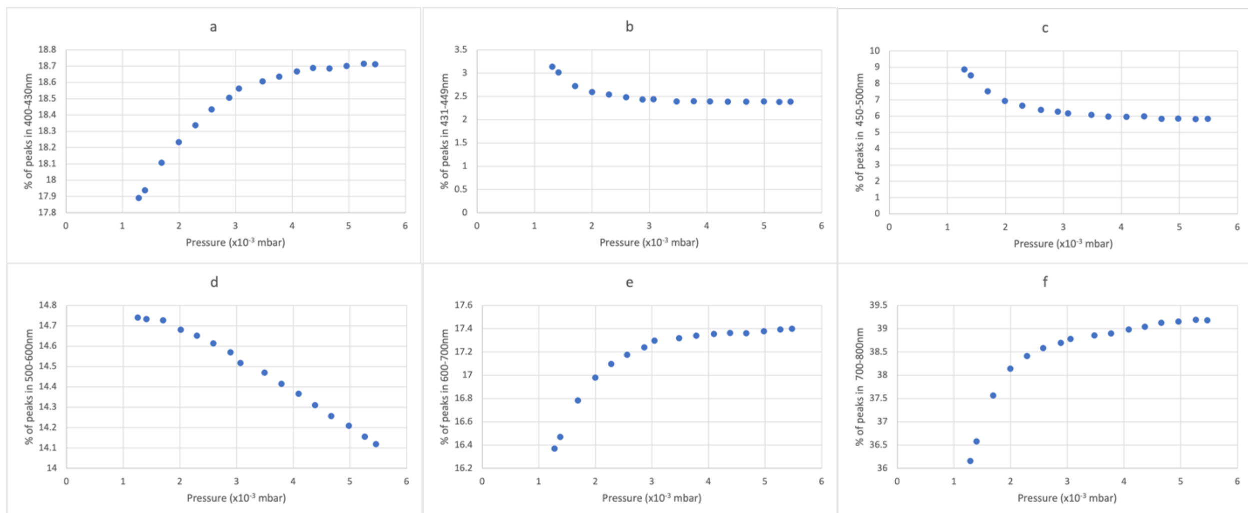

Figure 4.13. These data demonstrate the ratio (to the total spectral cover from 300 to 800 nm) of the area under the peak in each of the segments in response to varying the chamber pressure for fabrication of IZO.

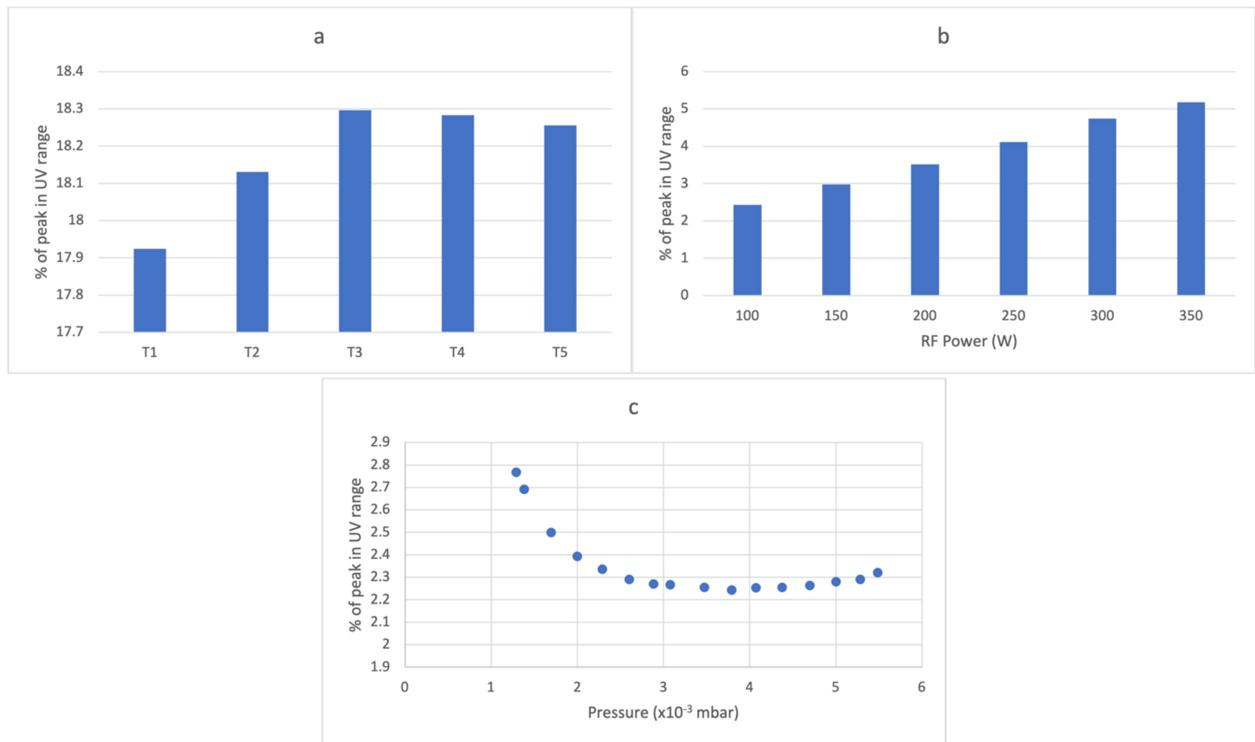

Figure 4.14. (a): Plot stability test over 5000 seconds period, (b): Effect of plasma power on UV emission ratio, (c): Effect of pressure on UV emission ratio.

Figure 4.14 demonstrates the ratio (to the total spectral cover from 300 to 800 nm) of the area under the peak in the UV section (300–400 nm) of the spectrum. The UV emissions demonstrate an increasing trend over the 5000 s period, followed by a slight decline and they demonstrate a linearly increasing relationship with the plasma power. The higher chamber pressure seems to be reducing the ratio of the UV emissions to the overall emission within the spectrum.

4.2 Discussion

This study demonstrated how the complex analysis of the emission spectrum can be summarised by applying the colour coordinates of the plasma light. The calculation of the colour functions is extracted through the area that is covered under the emission peaks of the plasma light that are affected by various parameters. Higher plasma power simply provides more energy toward the ionization of the working gas atoms. A higher density of ionized atoms, in turn, give a higher flux of emission and, as such, increase the intensity of the spectra. By increasing the power of the plasma, the number and momentum of the argon ions and sputtering particles are both increased, which results in higher bombardment rate of the target surface and higher mobility of the atoms at the deposited thin film surface. The higher mobility of the atoms will reduce the stress at the thin film surface, and hence facilitates further crystallisation [166].

The discharge current linearly increases with increasing the plasma power, irrespective of the chamber pressure. The energy of the sputtered atoms arriving at the surface of the substrate increases with increasing the plasma power. Parallel to this, the effect of high energy bombardment of the substrate surface is also increased, providing thermal energy at the surface atoms to become more mobile. Overall, the higher plasma power should lead to more crystalline deposition of thin films. However, excessive power can have an adverse effect by causing degradation of the thin film surface, resulting in high defect

density [167]. Based on the colour functions of the plasma, a linear relationship with the plasma power has been demonstrated, hence giving this technique the potential of defining a relationship between the film properties and the *x* and *y* colour coordinates, which will be potentially be explored this further in future work.

If all of the peaks would increase at the same rate with increasing the power, the chromaticity parameters should not change, but in **figure 4.3** There is a linear trend in how the *x* and *y* values are plotted against each other. This indicates that as the plasma power is increased and different energy bands tend to respond to the higher magnitude of the power. This is currently under investigation and the reason that section 400 to 500 nm section of the spectrum divided into three sections to progress one's understanding of this observation; however, as yet, the findings are not conclusive and hence no further explanation or claims can be made at present. However, from an applied scientist or an operator of a plasma deposition system, the relationship observed in **figure 4.3** is a simple observational method if in depth an operator does not require theoretical knowledge. The broadening of the spectral lines, as discussed in the introduction, are ultimately related to the electron density via the stark broadening process.

The colour functions are calculated from the area under the emission peaks, hence this broadening is taken into consideration during the colour coordinate measurements and present a simplified form of data for the operator, who may be only interested in basic monitoring protocols and not necessarily wish to indulge in to the complex statistical mechanics of the plasma. A similar argument can be applied for the emission line shapes which are strongly influenced by the interaction of the radiating atoms or ions with surrounding particles. All of the spectral data that were obtained during these experiments were carried out using the same distance between the collimator head and the plasma. It is important to acknowledge that this distance is highly important and it can influence the spectra of the plasma and it is part of the ongoing research objectives to investigate various distances of the collimator and the plasma.

Through the data presented in **figure 4.2**, it has also been demonstrated that, when trying to identify the stability of the plasma through the line ratio method, there may be confusion as certain peaks may increase or decrease, irrespective of their initial magnitude and ratio, while the proposed colour index values can provide a simple route to follow. **Figure 4.10** presents some of the possible transitions that need assessment when using the conventional line intensity techniques, while, through colour coordinate calculations, the overall area of the peaks is considered, hence simplifying the monitoring process for a user with limited need of extensive plasma physics knowledge. However, the colour coordinates do not take into consideration the emissions in the UV and far-red part of the spectrum. Hence, an alternative colour function for this application can be envisaged. If this method is matured in the future, then it can be beneficial for applied scientists and those who utilise plasma sputtering for thin film coatings and depositions. The colour of the plasma is derived by the quantity and state of various meta-stable atoms and ions that constitute it. In an analogical overview, a simplified shortcut can be established to characterise the plasma by being able to identify the relationship between the colour of the plasma and physical events within the plasma, just as the fingerprint pattern is used to characterise people rather than their individual genome sequence.

Higher chamber pressure lowers the voltage at which the plasma can be ignited and maintained. This is because higher chamber pressure increases the probability of the ionisation process of argon. Higher chamber pressure on the other hand means that more argon atoms are available to be energised to bombard the target surface; however, a higher concentration of argon atoms means that there will be more collision between the sputtered atoms or ions and argon atoms. These collisions can lead to lesser

energetic atoms arriving at the surface of the substrate [168]. A correlation can clearly be seen between the *x* and *y* coordinates of the chromaticity index of the plasma light and certain parameters, such as plasma stability, the working gas and the associated chamber pressure and the plasma power that affect the *x* and *y* values. This highlights a clear potential of pursuing and investigating the proposed concept and, if successful for a given target material to be sputtered, regardless of the manufacturer of the sputtering deposition machine, matching the colour parameters can indicate exact similar plasma operating conditions. Meanwhile, theoretically, there is a possibility of operating a plasma under two different conditions and getting similar colour values, which has been partially investigated, where, by altering the chamber pressure and plasma power, similar *x* or *y* values can be mimicked, but having an identical *x* and *y* values at the same time so far has not been observed, this itself will be a future experimental protocol.

The *x* and *y* coordinates can give an excellent, easy indication of the point at which the plasma is stable when compared to more complex calculation methods. The stabilisation process itself is an interesting concept to consider, slight variation in parameters that are required for driving plasma can create unstable conditions, and the colour factor can be an excellent indicator of this.

4.3 Conclusion

This work demonstrated that, under unique chamber pressure and plasma power, there can be a distinct *x* and *y* value that can be utilised by the operators of the machine to create a library of the thin film property relevant to particular *x* and *y* coordinate values, making the process of monitoring the thin film quality significantly easy. However, what has been reported here is just the beginning of a concept that bears potential. The colour coordinates that are driven from the plasma here do not take into consideration the UV and IR emissions. The work presented in this chapter has also been peer-reviewed and published [169].

Additionally, in future efforts, the relationship between the coating properties and the plasma photometric need to be established. Future efforts on further investigation of this concept require establishing the relationship between the chromaticity parameters and the plasma's inner parameters, such as electron temperature and charge density, which enables formulating a reliable relationship between the mentioned factors. Thereby, the first step in any future development of this concept is to prepare and create an alternative colour coding that will take the UV and IR emissions into account and will create a colour index beyond one's vision.

Chapter 5 Highly Conductive Zinc Oxide Films Prepared Using RF Plasma Sputtering Under Reducing Atmosphere

The previous chapter presented relationships between the plasma operating parameters such as plasma power and chamber pressure can be established with the colour functions of the plasma was demonstrated. The colour functions are driven from the area under the peaks of the emission spectrum of any light source, and by treating the plasma as a light source A proposal was put forward that it can be evaluated based on its colour. A significant observation has been demonstrated regarding the effect of hydrogen on shifting of the colour functions and how these functions behaved once the sputtering target was exposed to hydrogen. This study takes a closer look at this methodology with an emphasis on detailed monitoring of the sputtering plasma during IZO preparation with argon (Ar) and argon/hydrogen (5%) gas mix (Ar + H) as the working gas. An investigation on the effect of consecutive exposure of pure ZnO target to (Ar + H) on the electrical properties of ZnO films without any target material doping as a precursor was carried out. The sample preparation and experimental methods have been outlined in 3.1.2.

5.1 Results and Discussion

Evaluation of the EDS system accuracy and best practice for the chemical analyses of the films was performed using InAs of MAC reference sample #3601. The analyses of the standards were performed at 20 and 10 kV to evaluate the differences in the quantitative analyses (table 4.1) and select the optimal conditions. Only atomic percent was under scrutiny because the analyses aimed to identify the ratio of In/Zn in the IZO films following the different deposition conditions. Columns highlighted in grey are the columns indicating the ratio between the In/Zn cations in the films and In/As cation in the reference material used for the evaluation of the analytical best practice.

It can be observed in **table 5.1** that the system used tends to overestimate the lighter elements both at 20 and 10 kV. When the carbon build-up is considered in the quantification, the atomic % calculation seems to show better agreement with the certified values. The correlation of the quantification at 10 and 20 kV seems to be consistent, however, further overestimation of the lighter elements can be observed at 10 kV.

If this is applied to the films it can be inferred that the measurement at 20 kV is closer to the composition of the films, however, potential underestimation of indium could be applied. In the reference material at 20 kV, a wider scatter of results can be seen, however, the results are constantly closer to the certified results (ratio 1, atomic % 50/50) while the results are more constant at 10 kV, however they are further from the certified values overall.

Theoretically, the results at 10 kV might be more representative of the ratio of In/Zn in the films since the volume of the interaction of the beam is more limited to the surface of the samples, hence, the final spectrum includes only a very limited amount of the elements present in the glass slide which forms the substrate of the film. However, the indication obtained by the presence of carbon build-up in the analysis indicates that an overall evaluation of all elements present in the volume of interaction might be closer to the truthful composition of the material, hence, the data obtained at 20 kV will be used as a characteristic of the films under analyses.

Table 5.1. Energy-dispersive X-ray spectroscopy (EDS) investigation of the films (S1 to S7) at 10 and 20 kV

Sample ID	*20kV*		*Ratio*	*10kV*		*ratio*
	In	Zn		In	Zn	
1	8.04	3.1	2.6	28.7	8.1	3.5
2	14.1	5.2	2.7	40.2	8.4	4.8
3	17.8	5.7	3.1	40	8.4	4.7
4	15	5.3	2.8	37	8	4.6
5	12.4	5.3	2.3	37	9.6	3.9
6	13	5.6	2.3	38	9.5	4
7	14	5.5	2.5	38	8.7	4.4
InAs MAC reference material						
	20kV		*ratio*	*10kV*		*ratio*
	In	*As*		*In*	*As*	
Area 1	47.8	52.2	0.9	46	54	0.9
Area 2	49.4	50.6	1	44	56	0.9
Area 3	47.9	52.1	0.9	46	54	0.9
Area 4	48	52	0.9	46	54	0.9
Area 2 with Carbon build-up				8.1	9.1	0.9
Area 250*250μm				46	54	0.9

5.1.1 Film Morphology, Composition and Crystallinity Characteristics

Secondary electron images of samples S1 to S7 showed a high homogeneity of the film surface (**figure 5.1** A & B). Some samples show oriented linear marks (samples S6 and S7). All samples (using both Ar + H gas and Ar only) show areas with flower-like structures, identifiable as formation islands (**figure 5.2** C & D) with dimensions varying between 1 and 10 microns.

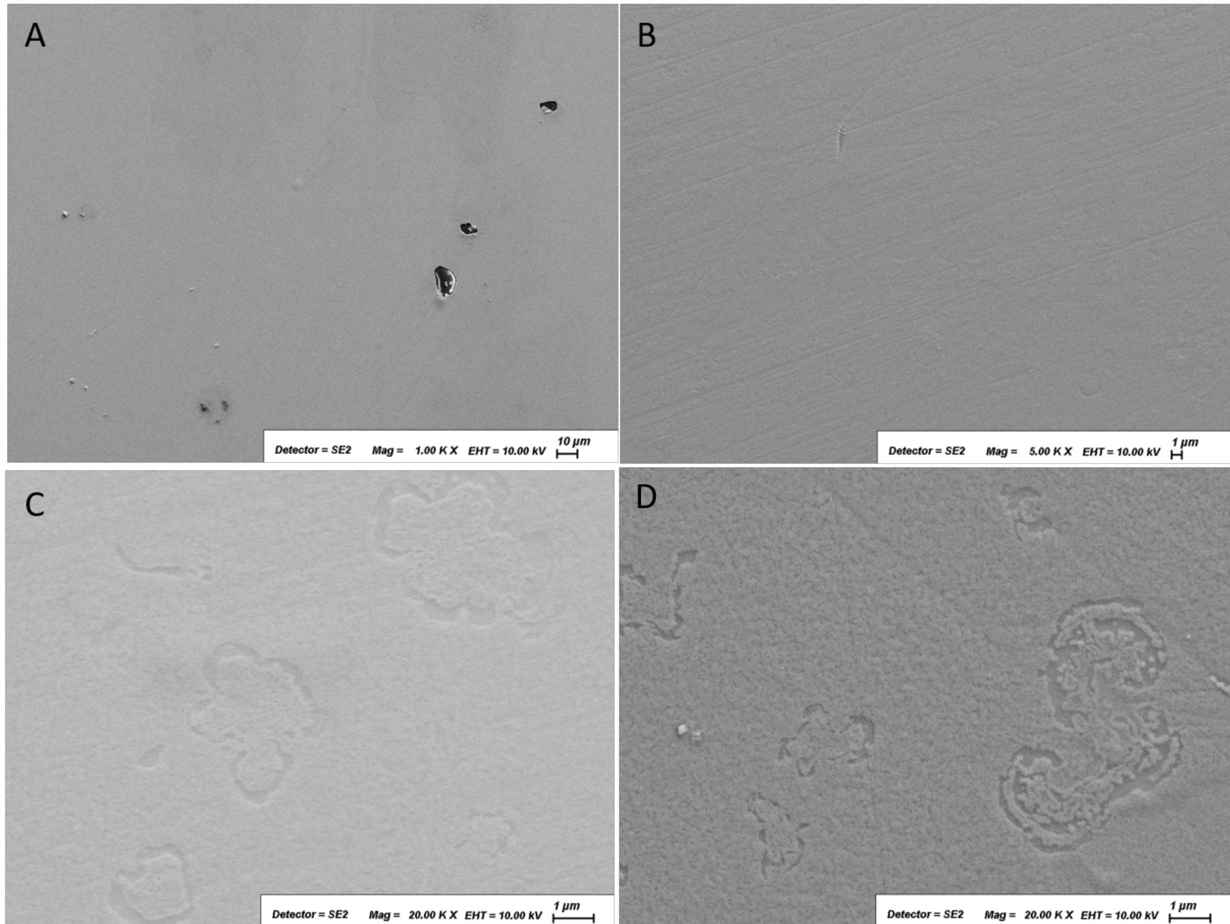

Figure 5.1. (**A**) The smooth homogenous surface of S6; (**B**) homogenous distribution of the film in sample S7 (**C**) secondary electron image of sample S2 (**D**) secondary electron image of sample S5

The compositions of the thin films obtained at 20 kV (as discussed above, the validity of the results obtained at different kV was assessed using a reference material to identify which one is most representative, and 20 kV was deemed to be so) show an indium/zinc ratio of 2.3 to 1 to 3.1 to 1, different (higher) from the In2O3/ZnO composition obtained by Sheng et al. However, a closer investigation of the results indicates that the presence of the indium ratio in samples deposited with hydrogen is higher than in those deposited with Ar gas alone and sample S5, which represented the switch from Ar + H to Ar gas, shows the lowest In/Zn ratio. Investigation of the crystallinity of the thin films, both using X-ray and electron backscatter diffraction showed that the IZO thin film is amorphous, in agreement with the above-mentioned work of Sheng et al. [170].

Pure ZnO samples (H0, H3 and H6) show an even more distinct granularity (**figure 5.2** A–C) with grains of approximately 100 nm size and heterogenous shape; however, sample H0 shows some defects and a larger less compact grain distribution (**figure 5.2**B) and no "flower-like" structure is visible in any of the ZnO films.

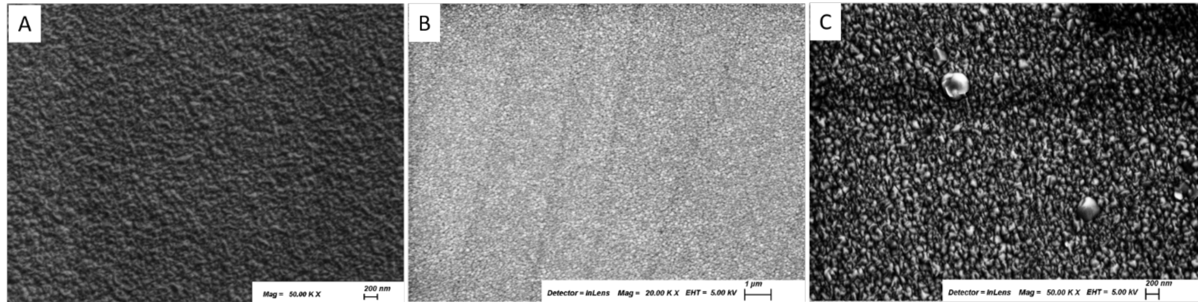

Figure 5.2 (**A**). In lens image of H6; (**B**) in lens image of H3; (**C**) in lens image of H0 showing larger less homogenous grains and fast carbon build-up during the SEM investigation.

Investigation of the composition of the ZnO films using EDS analyses shows a low concentration of nickel and copper, aside from the zinc and oxygen and from the elements deriving from the substrate glass (Ca, K, Si, Al, Mg).

The nickel is constantly detected at 0.2 wt % in H0 and H3, while iron varies from not detected to 0.2 wt % in these two samples. In H6, nickel is still detected from 0.2 to 0.3 wt %, while iron varies from not detected in the majority of the areas analysed to below 0.2 wt %. Overall, the composition does not show dramatic differences between the three samples, while morphologically, H0 shows larger grains and a less uniform deposition compared to the other two samples, and the distribution of the grains improves also from H3 to H6, which shows the most uniform aspect (**figure 5.2**A–C).

The ZnO films are fully crystalline, showing the hexagonal ZnO zincite phase (PDF 01-075-1533) with a (101) preferential orientation.

5.1.2 Electrical Properties

The IZO and ZnO coated substrates were tested for their electrical properties via a four-point probe and Hall effect measurement equipment. The Hall effect samples were 10 mm by 10 mm with contact pads connecting at ~1 mm into the sample from the corners. **Figure 5.3** demonstrates the average sheet resistance of the four substrates belonging to the S1–S7 (IZO) and H0, H3, H6 (ZnO) samples along with the standard deviation of the data. The conductivity of the samples S1–S4 clearly shows improvement with each consecutive coating under the Ar + H gas. Sample S5 was prepared by switching the gas from Ar + H to Ar gas from the beginning of the process and a very poor electrical conductivity in this sample was observed, while the consistency of the results among the four substrates in the S5 group is significantly poorer than in the other. As for the samples S6 and S7, which were prepared under Ar gas following the processing of S5, there is an improvement in conductivity, but this does not reach the performance of the samples prepared under Ar + H gas (S1–S4). It can be seen that each consecutive deposition process under Ar + H gas gradually improves the sheet resistance of the deposited thin films from S1 to S4. Sample S5 is the sample that was deposited by reverting to Ar gas only. Sample S5 has very poor conductivity. From the standard deviation of the obtained sheet resistance data, it can be seen that during the transition period (S5) even the samples from the same batch demonstrate poor continuity of the property (**Figure 3a**). The sheet resistance of the three ZnO samples demonstrates the improvement in sheet resistance of the films due to prolonged exposure to Ar + H gas (**Figure 5.3b**).

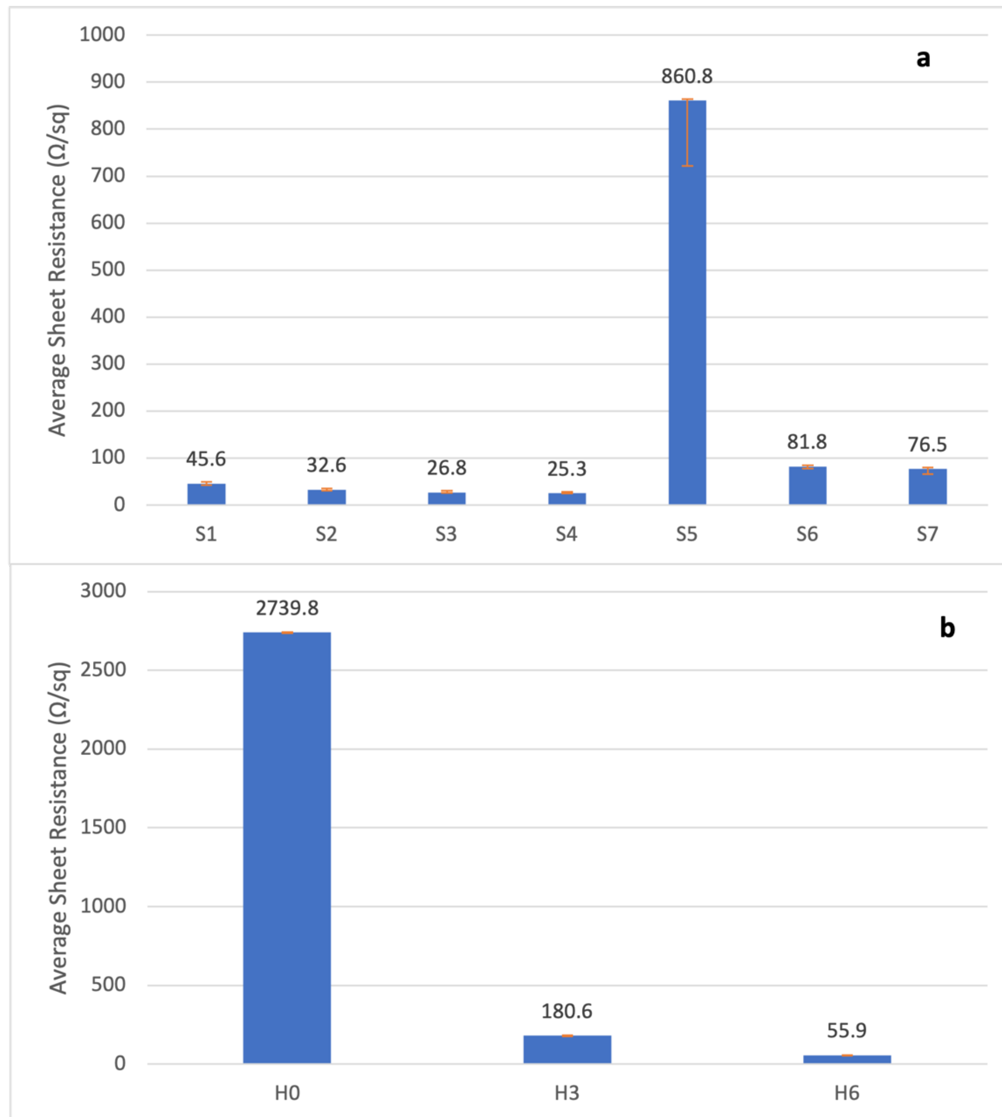

Figure 5.3. (**a**) The average sheet resistance of the S series samples and (**b**) H series samples

The ZnO only samples (H0, H3, H6) also clearly demonstrate the effect of consecutive exposure of the target material to the Ar + H gas. These samples, as discussed, were all prepared with Ar + H gas. Sample H0 was prepared with a fresh target, while H3 and H6 were prepared when the target was exposed to 3 and 6 h of Ar + H exposure, respectively. It can be seen that the electrical conductivity of the samples prepared improves concerning the prior exposure of the gas to Ar + H gas. The H6 sample, which was prepared with longer period of prior exposure to Ar + H gas, was superior to H0 and H3 in terms of electrical properties.

The resistivity of the samples and the thickness of the films are demonstrated in **figure 5.4**. Apart from the sample S1, the rest of the films demonstrate a similar trend in terms of film thickness; however, the resistivity of the samples highlights what has already been observed and discussed in **figure 5.3**. (**a**) The resistivity of the films obtained using the Hall-effect measurement technique demonstrates that each consecutive deposition process under Ar + H gas gradually improves the electrical conductivity of the films, while the S5 sample, deposited during the transition from Ar + H to Ar gas, shows poor results. (**b**) The

thickness of the films does not show a significant difference, however, the first sample deposition, where the target was first exposed to hydrogen, demonstrates a lower yield. (**c**) Prolonged exposure to Ar + H gas in improving the resistivity of ZnO based samples. (**d**) All ZnO samples demonstrate similar film thickness.

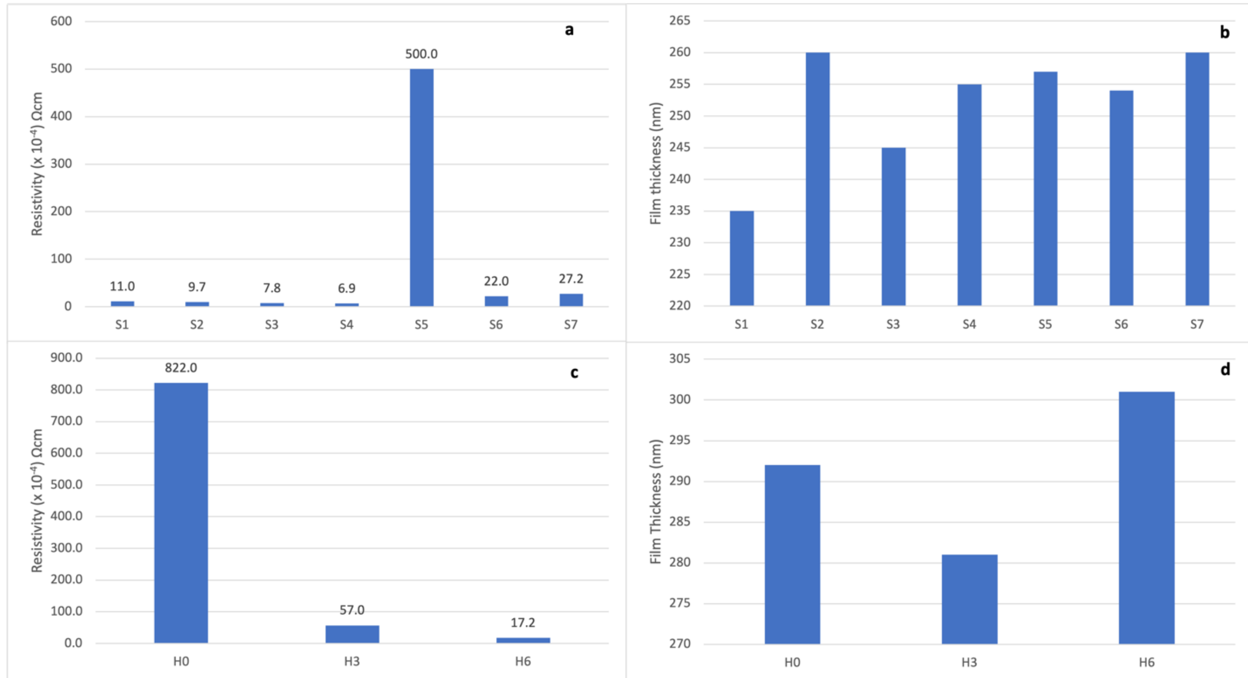

Figure 5.4. (**a**) Resistivity of S series samples (**b**) Film thickness of S series samples (**c**) Resistivity of H series samples (**d**) Film thickness of H series samples.

In **figure 5.5**, One can see that the S1–S4 samples have similar mobility values, while the S5 is the poorest, and S6 and S7 are close to the samples coated under Ar + H gas. However, the carrier concentration data suggest that consecutive coating under Ar + H gas further improves the carrier concentration. The carrier concentration in the S4 sample is 5 times higher than the S6 and S7 samples; the S5 transition sample demonstrates the poorest results. The standard deviation values of the average sheet resistance give an indication of the error associated with electrical properties, considering the error associated with mobility and carrier concentration; the 'S' series samples show standard deviation values in the range of (0.33–0.48) for mobility values, with the exception of S5 sample having a standard deviation of 2.8 from the four samples prepared for each series. The standard deviation of carrier concentration in these samples was in the range of 3.9×10^{18} for S1–S5 and ~3.2×10^{17} for S6 and S7. The H series samples show standard deviation values of (0.25–0.33) for mobility and ($3.1–3.9 \times 10^{18}$) for the carrier concentration error in these samples.

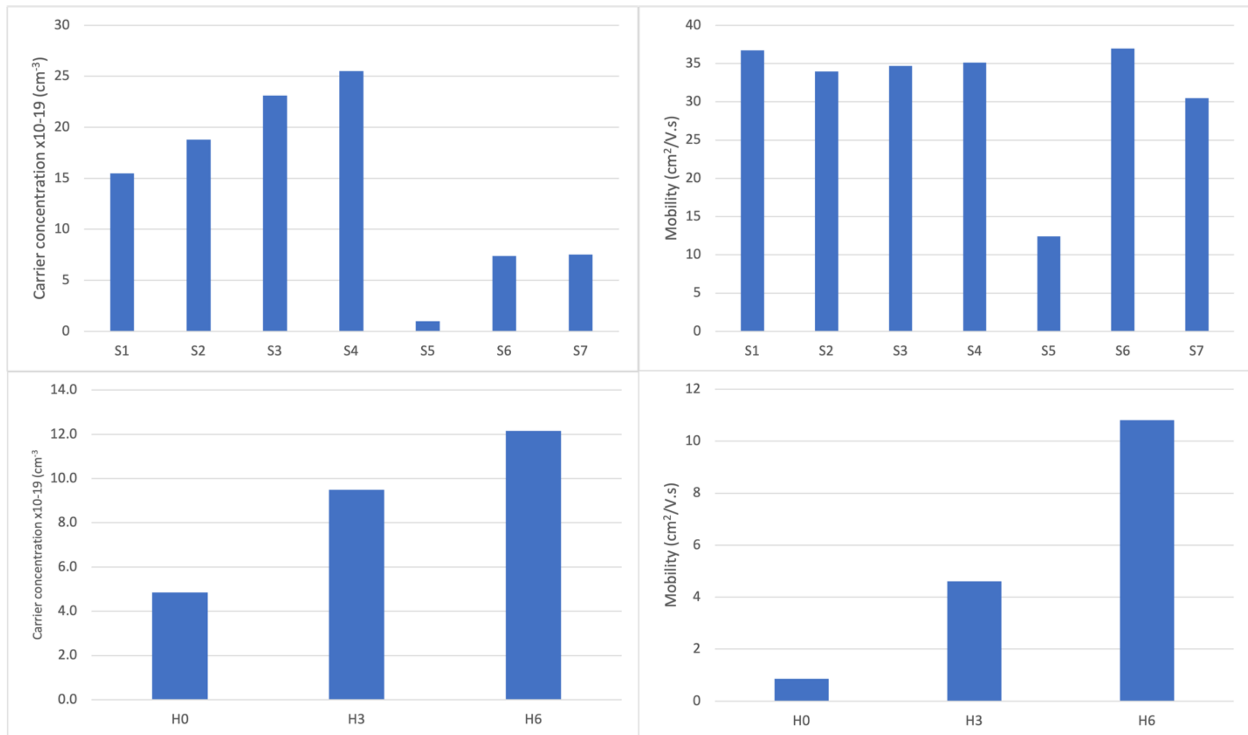

Figure 5.5. (**a**) Carrier Concentration of S series samples. (**b**) Mobility of S series samples. (**c**) Carrier Concentration of H series samples and (**d**) Mobility of H series samples

Charge carrier mobility and the carrier concentration are important in determining the electrical conductivity of a material. The mobility of the carriers is a function of carrier recombination time within the material, while the carrier concentration is related to the carrier density. The carrier density in turn is a product of density of states and probability of occupancy.

Both IZO and ZnO samples demonstrate electrical conductivity improvement with consecutive exposure of the target material to Ar + H gas. However, it can be seen that in the case of the IZO sample, the improvement can be traced to enhancement of the carrier concentration values as the mobility values are not significantly affected. This indicates that Ar + H gas processing does not impact the carrier recombination time significantly; however, the increase in carrier concentration indicates the density of states at band level or probability of occupancy of these levels is altered.

In contrast, ZnO samples demonstrate an increase in both mobility and carrier concentration values. It is important to mention that there is a trade-off between increasing carrier concentration and carrier mobility; as carrier concentration increases the probability of charge carrier scattering increases, and as such, overall conductivity would be affected, hence, as is indicated from the results shown, there is potentially room for further improvement on the ZnO sample until this trade-off is observed. This observation can be further explored to determine the maximum achievable conductivity.

When electrons are traveling through a periodic solid, their movement will be affected by the local forces within the crystal. Thus, a term is used to define the mass of the electrons under that environment, which is referred to as the effective mass. The effective mass, in turn, will be influencing the mobility of the electron (charge carrier). The orbital overlap between the metal cation and the oxygen in the host lattice (e.g., ZnO) is reported to be an important factor in determining the electron mass because metal

oxides with predominant s-character of the cation at the CBM are correlated with lowest effective electron masses [171]. The results indicate that the presence of hydrogen in the sputtering gas enhances the mobility of the electrons. This is possibly achieved by hydrogen influencing the oxygen content of the lattice and enhancing the s-characteristic of the indium and zinc. The hydrogen radicals generated in plasma are a strong reducing species [172], and they can withdraw oxygen from the crystal during the deposition. Oxygen vacancy has been believed to play the role of doubly charged donor in In_2O_3 [173,174].

On the other hand, hydrogen atoms can be incorporated in the solid film when they occupy the interstitial site of the crystal. The residing hydrogen forms a hydroxyl bond which may play the role of scattering centre for charge carriers [175] A separate study on ITO (Indium Tin Oxide) has demonstrated that due to the withdrawal of oxygen during the deposition of ITO films, the hydrogen in plasma can be so effective for achieving lower resistivity that the films were prepared without any sintering [176]. As discussed, the samples were prepared without additional sintering, and achieving highly conductive films without the thermal energy requirement of sintering offers significant commercial benefits.

The hydrogen impurity can be either interstitial or substitutional. Theoretical studies reported by van de Walle have demonstrated that hydrogen present in ZnO lattice can exclusively behave as an electron donor [177], and this theoretical study is verified by electron nuclear double resonance and Muon spin spectroscopy [178,179].

Considering interstitial locations, computing for formation energies associated with interstitial hydrogen in ZnO indicates that hydrogen is in H+ state and the H0 and H− are not feasible in the ZnO system [179]. The H+ in the ZnO system will occupy locations within the lattice where it can bind to an oxygen atom and form an O–H bond. This in turn will lead to lattice relaxations resulting in zinc and oxygen experiencing a slight move from their location. Regarding substitutional hydrogen, it is located in the proximity of a nominal oxygen position within the lattice and behaves as a shallow donor [180]. The donor behaviour of the hydrogen impurity in ZnO clearly explains the conductivity observed in ZnO systems and improvement of IZO conductivity.

The electrical conductivity improvements in IZO and ZnO thin films have been observed with the introduction of the hydrogen into the sputtering process are highly important considering the cost of indium metal and its economic impact at industrial scale TCO production. This means that at industrial scale levels, by applying hydrogen in the process, thinner films of IZO can be produced while the desired electrical conductivity is maintained, and in the case of ZnO, further improvements would eliminate the cost of indium. Also, hydrogen doped ZnO films have been developed at room temperature bears some exclusive processing advantages viz. polymer substrates, unlike aluminium doped ZnO films of desired conductivity which are generally optimised at around 300 ^{o}C.

For a TCO material to be suitable for most electrode applications, the electrical resistivity (ρ) should be low (10^{-4} to 10^{-5} ohm·cm), the charge carrier mobility (μ) maximized to ~60 $cm^2\ V^{-1}\ s^{-1}$ and the carrier concentrations be kept at about $2 \times 10^{21}\ cm^{-3}$ to minimize optical absorption [181]. The charge mobility presented in the results does not match these expectations yet, however, the improvement with using hydrogen could be exploited further by altering the amount of hydrogen, plasma power and chamber pressure, which will be pursued in future work.

The addition of the hydrogen during the sputtering procedure has been reported to cause a drop in the ionization discharge and Ar ion densities [182-185]. Some have also reported yield reduction with

introducing hydrogen [186,187] due to the low mass of hydrogen, but this was not observed in this study; this can be explained by the formation of ArH + ions. Within the plasma, ArH + ions are formed which possess high kinetic energy during target bombardment compared to Ar ions [187]. The film thickness analysis shows that the presence of hydrogen in the plasma has not affected the yield, and the bombardment of the target surface by the ArH + heavy ions could be an explanation for this.

5.1.3 UV-Vis Spectroscopy

The optical transparency of the films was examined using UV-Vis spectroscopy, and the results are presented in **figure 5.6**. As the four samples within each deposition procedure (S1, S2, H6) demonstrated a similar result, only 'one' sample from each set was used for these measurements (the results do not represent average values). Samples coated under Ar + H demonstrate very similar results with a clear indication of a wider bandgap allowing more light in the 320–430 nm region, and the samples coated under Ar are also very similar within their group. The S5 sample, which so far has been demonstrating poor performance in electrical properties, is no different than the S6 and S7 samples, which were also coated under Ar gas. The ZnO based samples (H series) demonstrate a wider transmission spectrum covering the shorter wavelengths, however, their band gap value is smaller than the IZO samples.

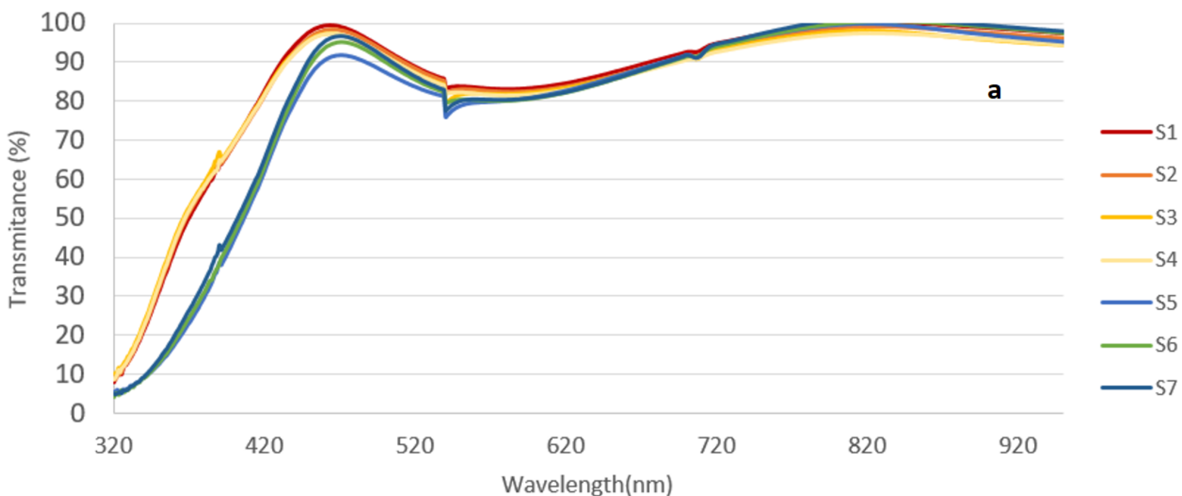

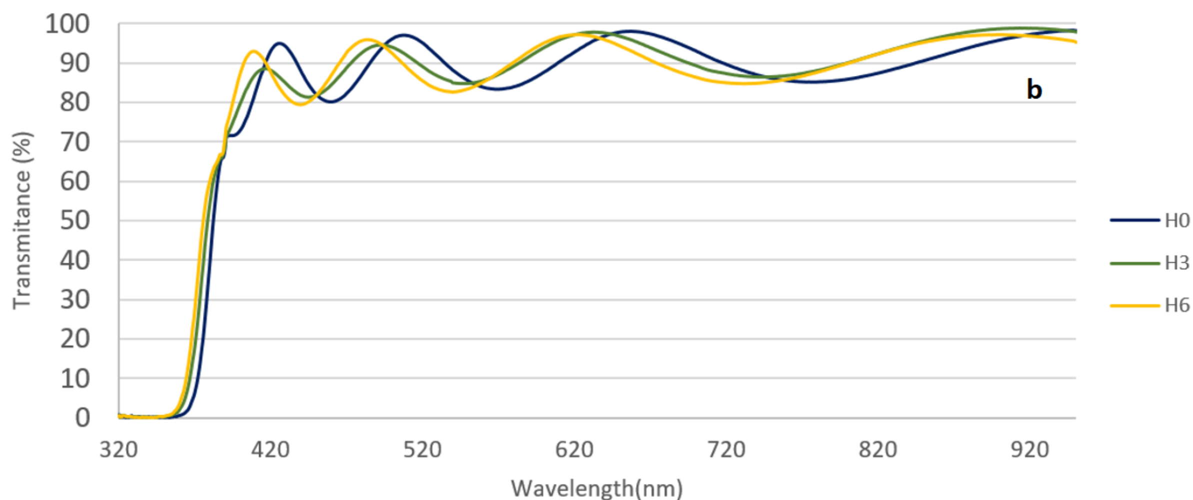

Figure 5.6. The UV-Vis spectral analysis of the samples in % transmittance is presented for; (**a**) IZO samples; (**b**) ZnO samples.

Through the absorption data obtained, by applying a Tauc plot, the optical bandgap of the films was calculated, and the data are presented in **figure 5.7**. The samples S1–S4, which were prepared under Ar + H, demonstrate a wider optical band gap, while the samples S5–S7 demonstrated a smaller optical bandgap. Here, the S5 sample again demonstrates smaller optical wavelength. The H series samples (ZnO) demonstrate an increase in optical band gap values as a result of prolonged exposure of the target to ArH gas.

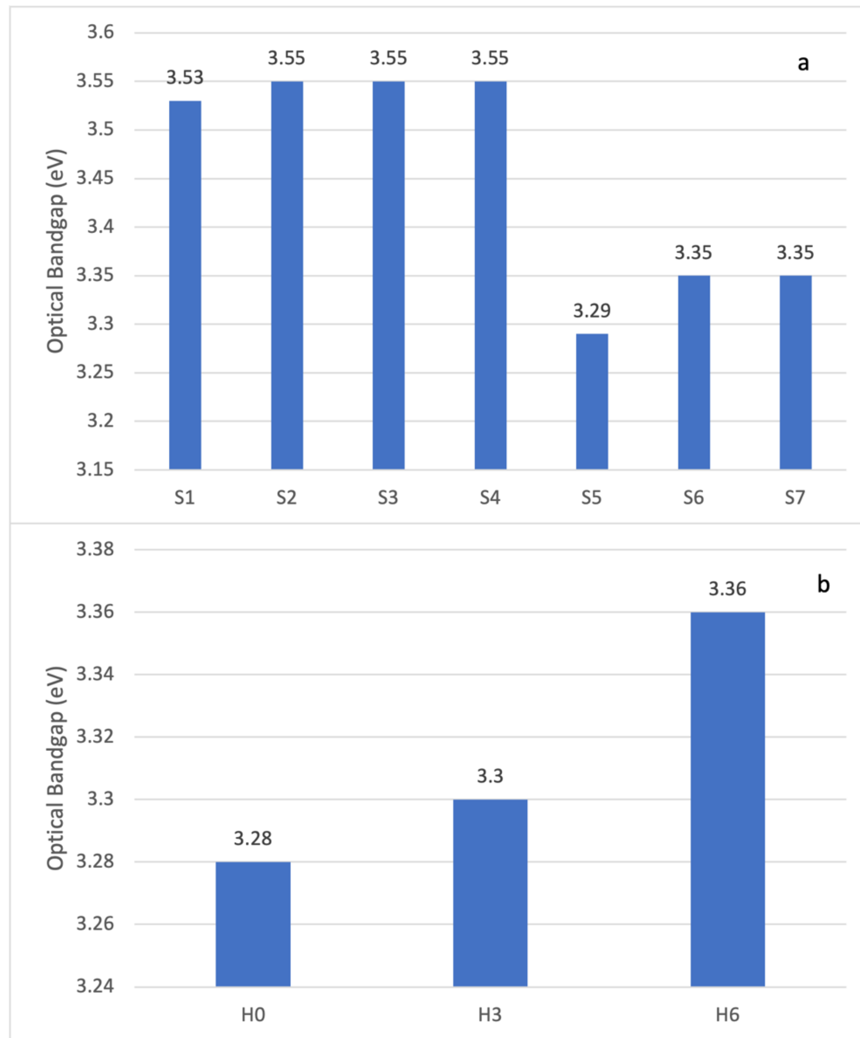

Figure 5.7. The optical band gap of; (**a**) the deposited IZO films. (**b**) ZnO samples.

5.1.4 Spectral and Colour Function Analysis of the Plasma

The emission characteristics in terms of the whole spectral plot and the chromaticity index were obtained for each test group over two hours. **Figure 5.8** represents the x and y coordinate values of the plasma colour during the transition from Ar gas to Ar + H and vice versa. As previously reported, the shifting of the *x* and *y* coordinates during Ar to Ar + H gas are swift compared to the data obtained when switching from Ar + H to Ar, as was the case during the preparation of the S5 sample. One can see that it takes more than one hour for the x and y coordinates to reach their initial value. This indicates that the plasma during this transition period is not stable and is changing.

The colour function approach, although still immature, bears the potential of becoming an ideal industrial-scale real-time monitoring system of the process control due to its simplicity of understanding for the operators. Although the colour function method of monitoring the plasma as a diagnostic tool is demonstrating useful applications, from the presented results significant variations in the 300–400 nm of

the spectrum obtained from the plasma was observed, which is not accounted for in the constructing of the x and y chromaticity coordinates.

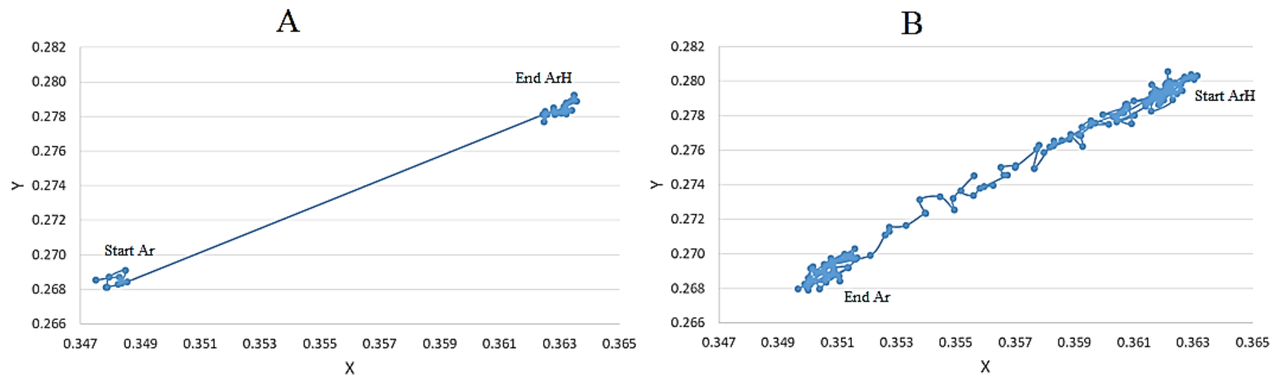

Figure 5.8. (A) The chromaticity colour functions, *x* and *y*, are plotted during the transition from Ar to ArH as the deposition of the S1 samples is undertaken. (B) The switch to the Ar gas from the ArH during the S5 sample deposition

This indicates that the introduction of hydrogen not only affects the plasma and the specifics of the deposited IZO and ZnO thin film, rather one can conclude that hydrogen is altering the target material itself and possibly forms surface compositions on the target or adsorption at the surface of the target that tend to affect the coating procedure. This can only be confirmed by surface analysis of the target post deposition, which will be investigated by the authors in the future.

Given the specific characteristics of the S5 sample and the shifting of the colour functions during the transition from Ar + H to Ar, the focus shifted to presenting and examining the plasma emissions during the S5 deposition process. The spectral data of the S5 sample at every 100 nm interval from 300 to 900 nm at various stages (from 1 s after the deposition process to 100, 1000, 3000 and 6000 s) of the process of the samples were examined. For simplicity, the 300 to 400 nm segment of the emission spectra is presented in **figure 5.9** as an example, and the rest of the spectral segments are discussed. From the spectral data it is observed that some emission peaks demonstrate an increase, decrease or no change through the deposition process.

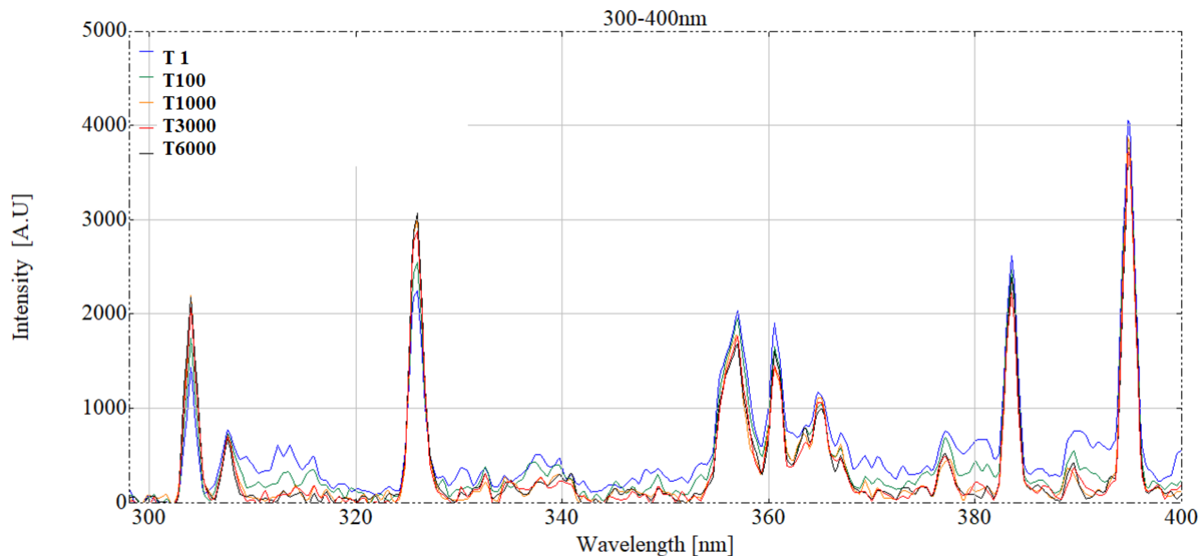

Figure 5.9. The detailed emission spectra of the plasma between 300 and 400 nm during the deposition of the S5 sample are presented.

The NIST database (National Institute of Standards and Technology, Gaithersburg, MD, USA) can be used to identify and refer to some of these peaks. **Figure 5.9** represents the 300–400 nm segment of the emission spectra of the plasma. Here, for example, One can see that the emission at 303.94 nm belonging to oxygen (II) in association with the transition 2s22p2(3P)3d 4D 5/2 to 2s22p2(3P)5f D 2[3]° 7/2 is gradually increasing along with the emission at 326.09 nm belonging to oxygen (III) in association with the transition 2s22p(2P°)3p 3D 2 to 2s22p(2P°)3d 3F° 3. In **figure 5.9**, a decrease in the 357.07 nm emission peak belonging to argon (II) in association with the transition 3s23p4 (1D) 4p 2D° 3/2 to 3s23p4(3P) 5d 4P 3/2 was also observed. There is also an increase in the 360.58 nm belonging to argon (II) in association with the 3s23p4(3P)3d 2P 3/2 to 3s23p4(1D)4p 2D° 5/2 transition.

In the 400–500 nm segment of the emission spectra of the plasma, there is an increase at 410.2 nm which is typically associated with an oxygen (II) transition with the2s22p2(3P)3p 4P° 1/2 to 2s22p2(3P)3d 4D 1/2 transition. There is also another peak at 451.07 nm, which is associated with Ar (I) 3s23p5(2P°1/2)4s 2[1/2]° 1 to 3s23p5(2P°3/2)5p 2[1/2] 0 transition, which also demonstrates a gradual increase.

In the 500–600 nm range, a decrease at 560.6 nm belonging to argon (I) in association with the 3s23p5(2P°3/2)4p 2[1/2] 1 to 3s23p5(2P°3/2)5d 2[1/2]° 1 transition was found. There are many other peaks which can also be seen increasing during the preparation of the S5 sample in this region.

In the 600–900 nm range, results indicate that variations in peak intensity or the area covered under the spectrum are not significantly affected.

There have been some reports on the emission line intensity variations when hydrogen is introduced into an argon discharge along with ionization variations with hydrogen introduction [188,189]. However, all these studies require time-consuming efforts and data analysis at micro levels in terms of interpreting the data, which may not be easy to apply during the deposition process.

As hydrogen is added to the Ar magnetron discharge, the plasma parameters in the discharge begin to change. Studies on plasma behaviour during the preparation of TiO_2 films have shown that the addition of hydrogen to oxygen-containing argon discharge leads to a continuous decrease of electron density and a corresponding increase of electron temperature from 6.30 to 6.74 eV [190]. The increase in electron temperature can be accounted for by the reduction of the value of electron density in the discharge.

For a good approximation in low-pressure discharge, the emission intensity of a particular line of an element is considered to be proportional to the density of that particular species [191,192]. Comparing the line intensity ratio of selected transitions, one can estimate the degree of dissociation and ionization of particular species present in the discharge. The line intensity ratios of I_H/I_{Ar} can be used to determine the degree of dissociation in hydrogen plasma using the following relation [193]:

$$N_H = k \frac{I_H}{I_{Ar}} \quad (4.1)$$

where N_H and N_{Ar} are the degrees of dissociation of hydrogen and argon, and *k* is a parameter related to the rate coefficients for direct excitation of the corresponding Ar and H atoms and the radiation transition probabilities and lifetimes of the corresponding excited states respectively.

As discussed earlier, an increase in the intensities associated with certain argon and oxygen transitions during the Ar + H gas switch to Ar only can be seen. The detailed study of the plasma is beyond the scope of this research; however, from these results, it can be seen that that once the target material is exposed to the Ar + H gas, the process of reverting the plasma condition to a prior state is time dependent. The sample S5, which was prepared during such a process, is the result of a continuously changing plasma condition, and as such, the properties of the film are directly affected. The colour function approach, as demonstrated in **figure 4.8**, also verifies this. Hence, the colour function approach can be considered a simpler approach toward monitoring the status of the plasma when significant details are not required.

5.2 Conclusion

It has been demonstrated that the deposition of IZO and ZnO film under a reducing atmosphere can enhance the electrical property of these thin films by enhancing the carrier concentration of IZO films and increasing the carrier concentration and mobility in ZnO films. The key findings of the work carried out are as follows:

1. Most importantly, there is clear evidence that consecutive exposure of the target material to Ar+H gas will to some extent add further improvements to the electrical properties. A target that has been previously exposed to Ar+H gas seems to be altered at the surface, as reverting to Ar gas only for deposition will initially produce a thin film with inconsistent electrical properties.
2. The improvements obtained with introducing hydrogen during the sputter deposition of IZO can minimise the consumption of indium, as thinner films with identical electrical properties can be deposited. In the case of further improvements with the electrical properties of pure ZnO thin films, introduction of hydrogen can potentially lead to the elimination of indium. As such, there can be significant commercial benefits in depositing the ZnO based family of TCOs under Ar+H gas mix, if the need for indium and high-temperature sintering is avoided; however, further improvement and assessment are required.

3. One can visualize the status of the plasma stability via the application of the colour function analysis. During the sputter deposition of IZO under argon, when the target has been previously exposed to hydrogen, An unstable plasma yields an IZO film with very poor performance, resulting also in the lowest concentration of indium. The fact that the chromaticity index values (x and y) do not swiftly fall back to the values expected for argon indicates that for the surface modifications caused by hydrogen to revert to the original state, a layer from the target has to be removed, leading to a film with poor charge carrier and density properties.

The colour function evaluation of the plasma can be a beneficial observational tool for monitoring the plasma during system operations. However, further work is required to mature this method of plasma monitoring and assessment. Hence, the next task will be to investigate the plasma emissions and, if necessary, formulate a new colour function that takes into account the emissions in the 300–400 nm region. This will lead to constructing a new colour coordinate system that will specifically define the colour of plasma, similar to how the colours in the visible spectrum are defined by the x and y index values. The research work and findings presented in this chapter have also been published as a journal publication [194].

Chapter 6 Investigation on substrate position relative to Plasma during the sputter deposition of Hydrogen Doped Zinc Oxide

Following on from the previous chapter where the enhancement of the electrical properties of IZO and ZnO systems by repeated exposure of the sputtering target to an argon/hydrogen mixture as the working gas was investigated. In this set of experiments as detailed in chapter 3.1.3, interesting complexities associated with reactive hydrogen/argon sputtering of un-doped ZnO targets have been identifited, which is believed to be associated with the reported magnetic properties of hydrogenated ZnO particles, and this report outlines these observations.

As described in chapter 3, the recently reported on implementing a novel approach through which the sputtering plasma can be given a unique fingerprint based on the colour of the plasma, which is identical to the method by which colour functions of a light source are expressed in a “x” and “y” coordinate system to define the unique colour of the light source. This technique was applied for monitoring the plasma during these experiments and attempted to explain the effects observed by evaluating the colour parameters of the plasma in association with the electrical properties of the ZnO thin films deposited via reactive hydrogen/argon sputtering.

6.1 Results and Discussion

6.1.1 Electrical Properties

The ZnO coated substrates were tested for their electrical properties via a four-point probe and Hall effect measurement equipment. Although no study was carried out on the crystal structure of the deposited thin films; in the previous report/chapter, where samples of zinc oxide thin films deposited in the presence of hydrogen were examined, the ZnO films were fully crystalline, showing the hexagonal ZnO zincite phase (PDF 01-075-1533) with a (101) preferential orientation.

The results indicated that the presence of hydrogen in the sputtering gas induces n-type conductivity by enhancing the concentration and mobility of the charge carriers (electrons). However, It can be seen that there is significant variation when comparing results between the samples positioned at the edge and centre of the substrate holder, as indicated in **figure 6.1**.

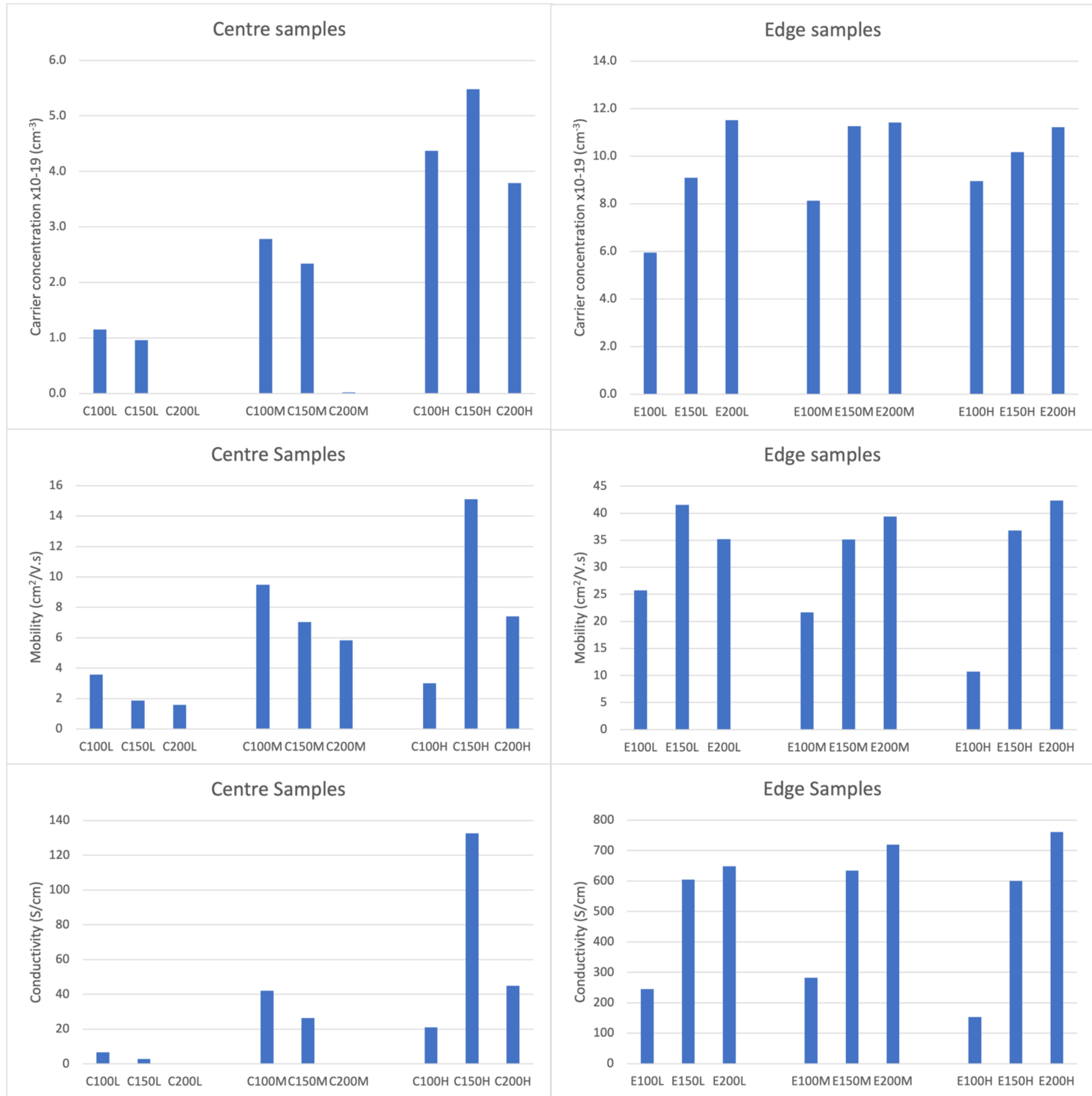

Figure 6.1. Carrier concentration and mobility were measured for ZnO samples deposited in the centre (**left**) and the edge (**right**) of the substrate holder under various plasma power and chamber pressures.

Charge carrier mobility and the carrier concentration are important in determining the electrical conductivity of a material, and it can be seen that high carrier concentration and mobility values are associated with the samples at the edge of substrate holder, while depositions at the centre demonstrate smaller values, and as such the overall conductivity of the edge samples are much higher. The mobility of the carriers is a function of carrier recombination time within the material while the carrier concentration is related to the carrier density. The carrier density in turn is the product of density of states and probability of occupancy. As previously discussed, the hydrogen impurity behaves as a donor in these

samples. Associating higher conductivity to hydrogen integration into the lattice based on the discussed literature, the results can possibly indicate lower hydrogen content in the films prepared at the centre of the substrate holder, although this hydrogen content needs to be measured in future work to be perfectly conclusive. As discussed, substrates were placed between the edge and centre regions. These samples were tested via a four-point probe measurement and a conductivity gradient was found when moving from the edge to the centre of the sample holder, the electrical property of the thin films became smaller. Based on the mentioned ongoing studies comparing IZO and ZnO, this is only observed in ZnO samples. To demonstrate a comparison for this report, the experiment with an IZO target fitted on the magnetron was repeated, and only the sheet resistance of the films was measured for presentation in this report. These results, presented in **6.2**, indicated that IZO does not behave like ZnO.

Figure 6.2. Plot of Sheet resistance vs distance away from centre for IZO and ZnO samples

As can be seen from the results presented in **figure 6.2**, the electrical properties of the deposited films significantly varied for ZnO, depending on the position for the substrate, while for IZO the variation was significantly less elaborated (comparing the associated edge and centre samples). Results presented in chapter 5 demonstrated the enhanced electrical properties of the IZO when deposited under the argon–hydrogen mix. These results combined with the observations presented in **6.2** suggest that one way to explain this is to assume that more hydrogen doping is occurring at the edge of the substrate compared to the centre, unless the thickness of the coating was causing this observation. However, that thickness is not a relevant explanation for this observation as justified in the following section.

The mobility of electrons through a solid is affected by local forces within the crystal structure. This mobility is then interpreted as the mass of the electrons within that crystal environment. In a ZnO crystal structure, the orbital overlap between the Zn cation and the oxygen anions can be an important factor in

determining the above-mentioned electron mass due to the s-character of the cation at the conduction band [195]. It can be hypothesized that when hydrogen is present as a sputtering gas, it may interact with the oxygen content of the lattice and result in localised lower oxygen contents, which will consecutively lead to predominant s-characteristics. This hypothesis is based on previously reported studies demonstrating the hydrogen to be a strong reducing gas in a plasma [196], while withdrawing oxygen from the In_2O_3 crystals during the deposition process has been reported to play a role of a doubly charged donor [197,198]. However, this cannot clearly explain the variation observed in edge and centre samples. Sheet resistance of edge and centre prepared ZnO samples are presented in **figure 6.3.**

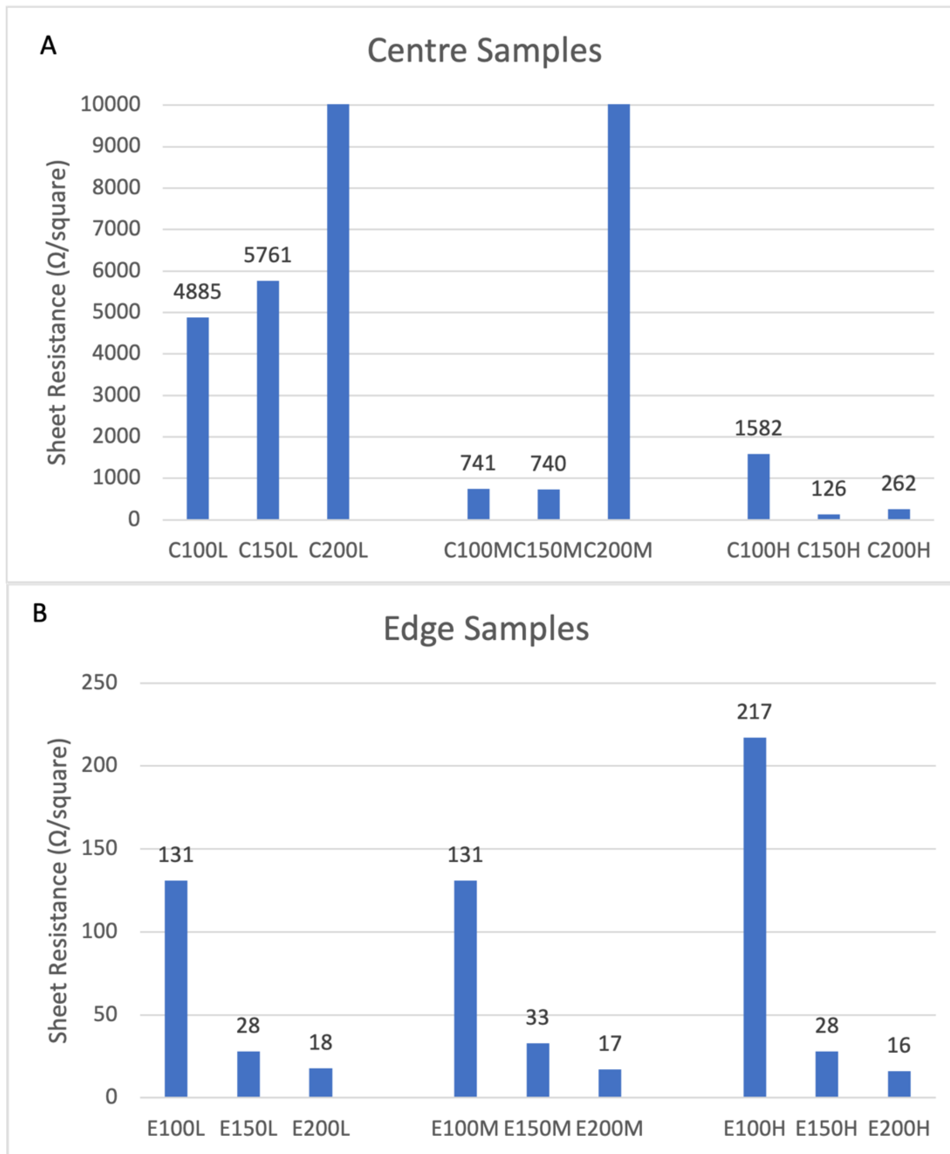

Figure 6.3. (A)The sheet resistance (Ω square) of the ZnO samples deposited on the Centre and (B) Edge part of the substrate holder under various deposition conditions.

6.1.2 Film Thickness and Optical Properties

The thickness of the coatings obtained via the profilometer in line with the sample preparation described in chapter 3 are presented in **figure 6.4** for all the ZnO samples.

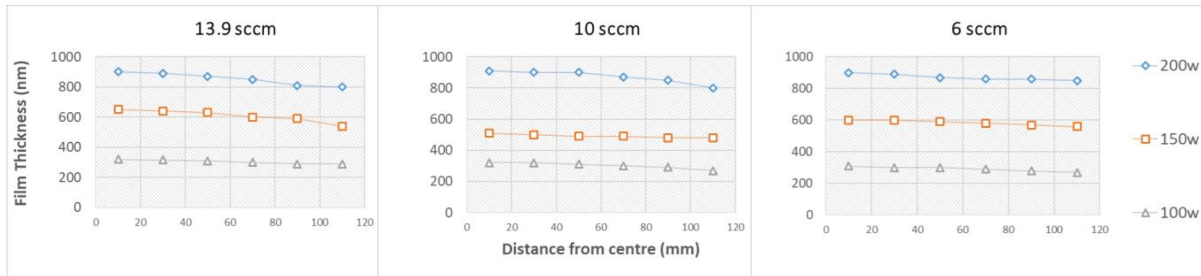

Figure 6.4. The coating thickness associated with the position of the substrate on the substrate holder (at a distance from the centre) under the varying deposition parameters, power and gas flow rate.

From **figure 6.4** One can see that the films are actually slightly thinner with the position of samples closer to the edge of the substrate holder.

The addition of the hydrogen during the sputtering procedure has been reported to cause a drop in the ionization discharge and Ar^+ ion densities [199-201]. Some have also reported yield reduction with the introduction of hydrogen [202-204] due to the low mass of hydrogen, and this may explain why there was a slightly thinner coating on the edge region if hydrogen bombardment of the target and its consecutive incorporation into the lattice behaved selectively, depending on the position of the sample.

Hence, the original assumption can be considered where it was stated that more hydrogen atoms are doped into ZnO lattice at the edge of the substrate holder and oxygen vacancy alone is not a determining factor.

For a TCO material to be suitable for most electrode applications, as well as the electrical resistivity (ρ), the optical absorption should be minimised [205]. The overall sheet resistance of the ZnO samples based on their position on the substrate holder is presented in **figure 6.1**.

The evaluation of all the ZnO samples with UV–Vis spectroscopy, and the absorption properties of the films are presented in figure 5.7.

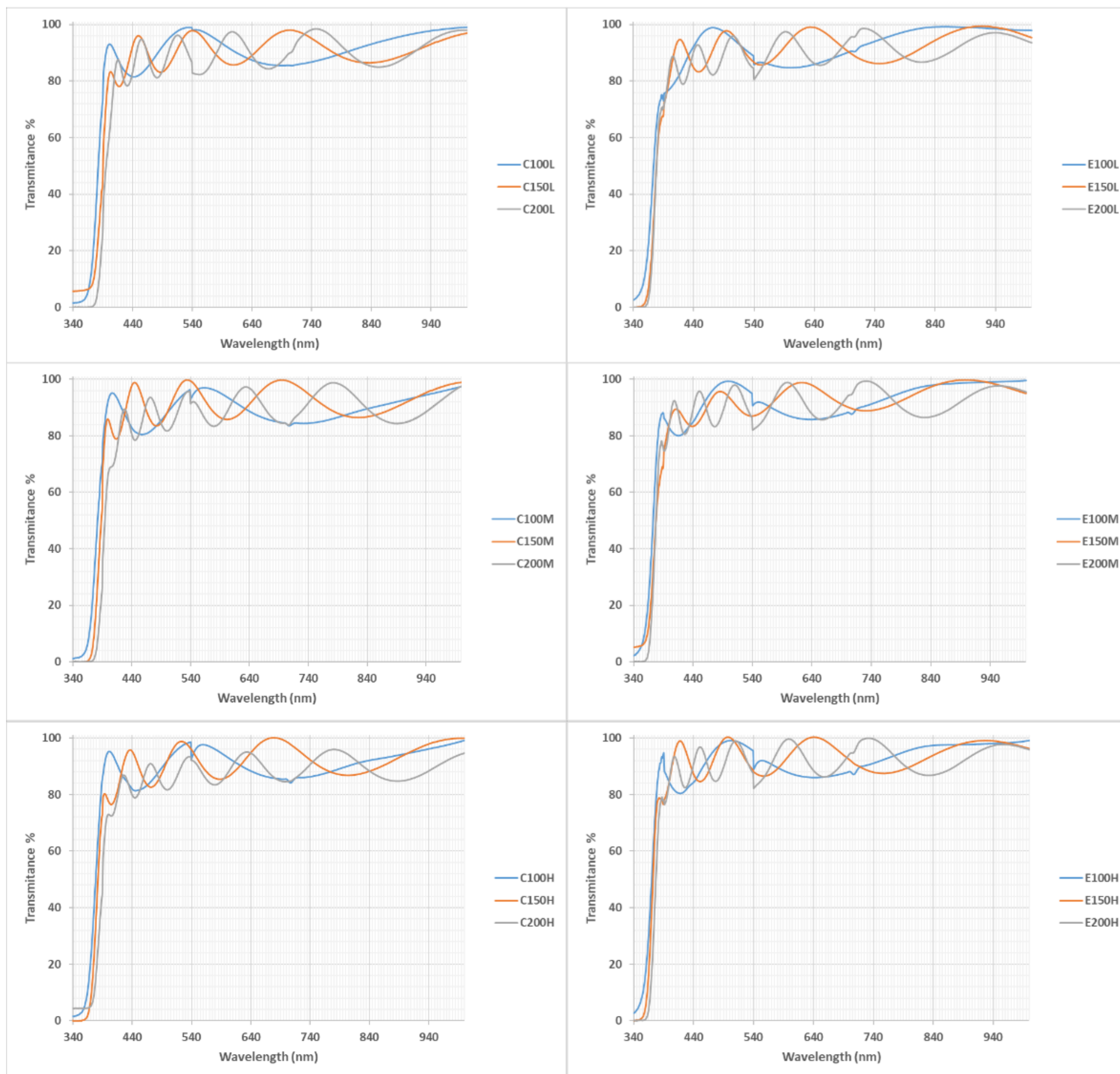

Figure 6.5. The transmittance spectra of the ZnO thin films obtained via UV–Vis spectroscopy. All samples demonstrate above 80% transmittance between 400 nm and 1000 nm.

The data presented in **figure 6.3** and **figure 6.5** clearly demonstrated the potential of ZnO as an alternative TCO without the need for indium or any other metal doping at room temperature, if the position of the substrate with respect to the plasma is considered. The optical band gap of the deposited thin films was obtained via the Tauc plot method, the results are presented in **Table 6.1** for edge- and centre-deposited ZnO thin films. The samples prepared on the edge also demonstrate a slightly higher band gap.

Table 6.1. The optical band gap of the ZnO samples deposited at various conditions, comparing the results obtained from samples positioned on the edge and centre of the substrate holder.

Centre Samples	Optical Band Gap (eV)	Edge Samples	Optical Band Gap (eV)
C100H	3.3	E100H	3.4
C150H	3.30	E150H	3.4
C200H	3.20	E200H	3.37
C100M	3.30	E100M	3.3
C150M	3.29	E150M	3.35
C200M	3.32	E200M	3.39
C100L	3.25	E100L	3.35
C150L	3.20	E150L	3.39
C200L	3.22	E200L	3.35

Centre	Optical band gap (eV)	Edge	Optical band gap (eV)
C100H	3.3	E100H	3.4
C150H	3.300	E150H	3.4
C200H	3.200	E200H	3.38
C100M	3.300	E100M	3.37
C150M	3.290	E150M	3.3
C200M	3.320	E200M	3.39
C100L	3.250	E100L	3.35
C150L	3.200	E150L	3.39
C200L	3.220	E200L	3.35
Average	3.264		3.37
SD	0.047		0.032

6.1.3 Analysis of the Plasma Emissions

The plasma emissions at the surface of the target were examined as described in the experimental section. A comparative study with an IZO target fitted on the magnetron to evaluate the variation in plasma emissions comparing the two targets (IZO and ZnO) was carried out, considering that with the IZO sample, a drastic variation of electrical properties associated with sample position was not observed(**figure 6.2**).

The emissions from the plasma generate numerous emission peaks, and the ratio of these peaks is classically associated with plasma conditions. However, although peak intensities varied from centre to edge, observations purely based on the spectral plot did not indicate an easily identifiable variation between the two materials. To illustrate this, the data representing the emission of the plasma at 100 watts under a 10 sccm flow rate for the ZnO and IZO targets are presented in **figure 6.6.**

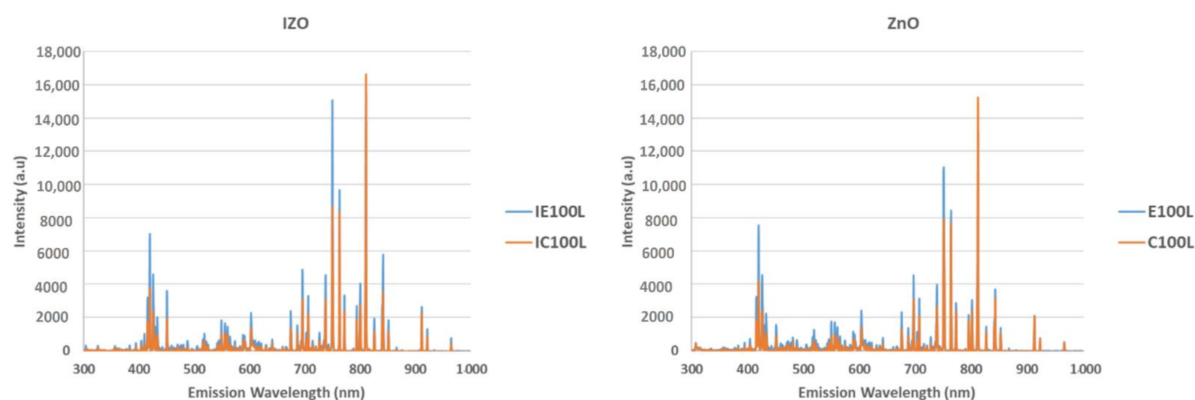

Figure 6.6. The spectral emission of the plasma at 100 watts of power under a 6 sccm flow rate at the edge (blue) and centre (orange) of the target for the IZO (**left**) and ZnO (**right**) targets.

In **figure 6.6** One can see that the intensity of various peaks is higher at the edge of the target surface compared to the centre region. These emissions are associated with various atomic transition in the plasma. The increase in intensity at the edge is due to the way that the magnetron operates, given the magnets installed in it, leading to an area with higher ion bombardment rate [206]. It is possible to analyse every peak intensity and to obtain certain parameters such as the electron temperature from the data, which is a time intensive approach and beyond the scope of this report. Instead, A simpler assessment was applied which was based on the colour function parameters of the plasma at the centre and edge region of the target based on the previous work. This simple approach was applied to evaluate an overall change in the plasma condition. The colour functions of the plasma light at the centre and edge regions were calculated and are presented in **figure 6.7**. Using this approach, the difference in plasma conditions became more apparent to the naked eye. The colour functions could represent the overall macro environment of the plasma constituents without indulging in deep physics and statistical mechanics associated with evaluating a plasma.

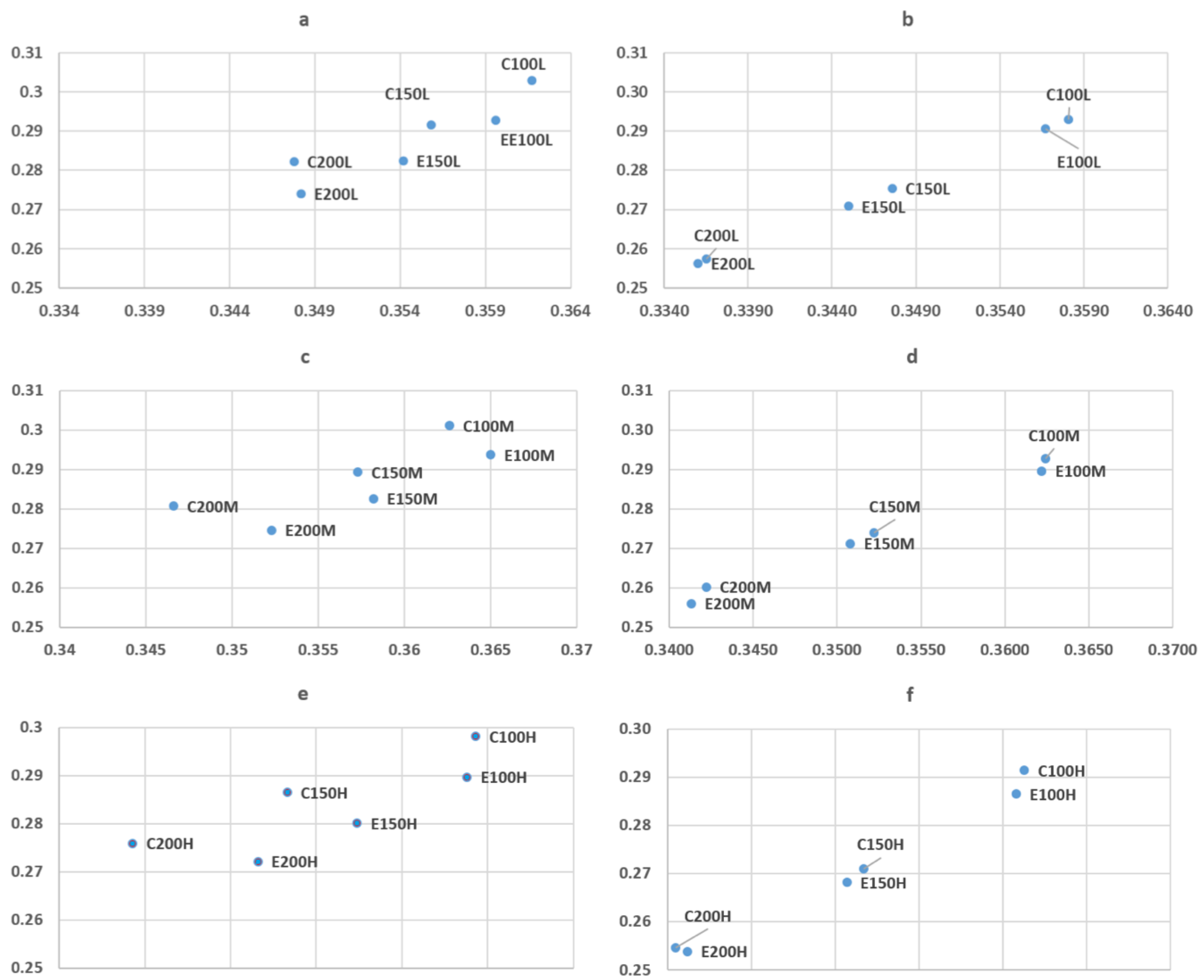

Figure 6.7. The x and y chromaticity index of the plasma light associated with the array of deposition conditions

From the results presented so far, although one can see certain variation between the emission patterns associated with ZnO and IZO targets, the variations are interesting but do not seem to be conclusive for explaining the observed variation in electrical conductivity of ZnO and IZO as presented

in figure 5.4. An in-depth peak ratio analysis can be performed to gain insights into the physical parameters of the plasma, such as electron temperature; however, in the current report the focus was just on describing the observations and such studies require a separate dedicated study report.

Up to this point, It can be assumed that the hydrogen impurity incorporation within a ZnO or IZO lattice follows a certain reduced gradient from the edge to the centre. The hydrogen impurity can be either interstitial or substitutional. The H+ in the ZnO system will occupy locations within the lattice, where it can bind to an oxygen atom and form an O–H bond. Considering substitutional hydrogen, it is located in the proximity of a nominal oxygen position within the lattice and behaves as a shallow donor. The donor behaviour of the hydrogen impurity in ZnO clearly explains the conductivity observed in ZnO systems and improvement of IZO conductivity.

This implies that there is a need to consider the state of the materials during their transport from the target surface to the substrate. From these results, and reported studies discussed, one can assume that the ZnO particles that form on the substrate surface have more hydrogen content at the edge location compared to the centre region of the substrate holder. This observation can possibly be explained considering the following concepts and assumptions:

- Firstly, hydrogen ions (along with argon ions) bombard the surface of the target material, resulting in ejection of surface atoms from the surface of the target, while some of these ions will also integrate into the target material.
- Secondly, the integration of the hydrogen into the surface of the target material as discussed and based on referenced literature may lead to formation of regions at the target surface possessing complex magnetic behaviour.

One way of explaining the observations reported in this study is to consider previously reported studies where angular dependency of thin films depositions via the sputtering process were investigated. During the sputtering deposition process it has been shown that geometrical shadowing of an incident beam by the existing protruding parts of the growing surface profoundly affect the deposition's morphology [207]. This is referred to as competitive shadowing, which can affect the properties of the thin films, in particular step coverage and microelectronic properties [208]. In a more recent study, Hippler et al. [209] carried out a study on the angular dependence of plasma parameters and thin film properties focusing on titanium and titanium oxide layers deposited via HIPIMS. They performed separate reactive (argon/oxygen) and non-reactive depositions regimes using a Langmuir probe and substrates at various angular positions (0°, 30°, 60° and 80°) with respect to the target [209]. In their study, significant variations in electron density were reported depending on the reactive or non-reactive experimental regime, with the non-reactive regime showing up to five times larger electron density values. They also measured the mean electron energy (pulse time dependent), which demonstrated similar values between the two regimes. However, most interesting are the values they demonstrated depending on the substrate position with respect to the target, which finds significant relevance with the observations found in this work. Both electron density and mean electron energy values are reduced at wider incident angles on the target surface. It should be noted that the work in this study needs to be repeated mimicking the experimental protocols carried out by Hippler et al., something that appears very interesting and will be pursued in the future. Considering the observations reported here, such studies will give a significant perspective in understanding the formation of the conductive zinc oxide films in presence of hydrogen during the sputtering process. However, at this stage, based on the above reported research, if

incorporation of the hydrogen into the target material leads to the formation of surfaces at the target with complex magnetic behaviours, then it may result in the target material itself interfering with the magnetron's magnetic fields and as such creating electron density and electron energy values dependent on angular incidence on the target surface. The time dependency studies on plasma potential reported by Hippler et al. at various angular positions can also be influenced by the target surface gaining magnetic properties as well as due to the overall interaction of electron and ions in such a complex magnetic environment.

Parallel to the above discussion, it has been reported that the sputtered flux from an ion bombarded target surface is composed of atoms, polyatomic molecules and clusters [210-212], and various models have been proposed to describe the sputtering of small clusters and molecules [213-219]. If one was to assume that during the sputtering process, molecular ejection from the target surface occurs, there will be a flux of both pure ZnO and hydrogen doped ZnO leaving the target surface with various speeds and randomly dispersed direction vectors. As discussed, hydrogenated ZnO nanoparticles have been shown to demonstrate ferromagnetism.

Hypothetically, the hydrogen doped ZnO particles possessing ferromagnetic properties are affected by the magnetic field of the magnetron's magnets. This effect creates additional vector forces that ultimately promote the ferromagnetic hydrogen doped ZnO to the edge of the target, while the non-ferromagnetic pure ZnO particles are condensed randomly across the substrate holder. This model is illustrated in **figure 6.8**, where a very simple approach can be followed which considers a certain number of small particles with a magnetic moment along a magnetic field between the N and S poles of the magnetron's magnet. Upon surface bombardment of the target with Ar/H ions, the target atoms acquire kinetic energy for travel to the surface of the substrate. If these particles possess ferromagnetic properties as hypothesized in this report, then there is dipole–dipole interaction that needs to be considered in this model; an attractive and repulsive force vector will exist as these magnetic particles interact with the field and their geometrical orientation within space. This vector either will combine with the initial vector or will counter it depending on the particles' positions, according to **equations 6.1–6.4.**

$$U = -MBcos\theta \tag{6.1}$$

$$B = \frac{\mu}{4\pi} x \frac{nM}{R^3} \tag{6.2}$$

$$T = -MBsin\theta \tag{6.3}$$

$$Force = -\frac{dU}{dR} \tag{6.4}$$

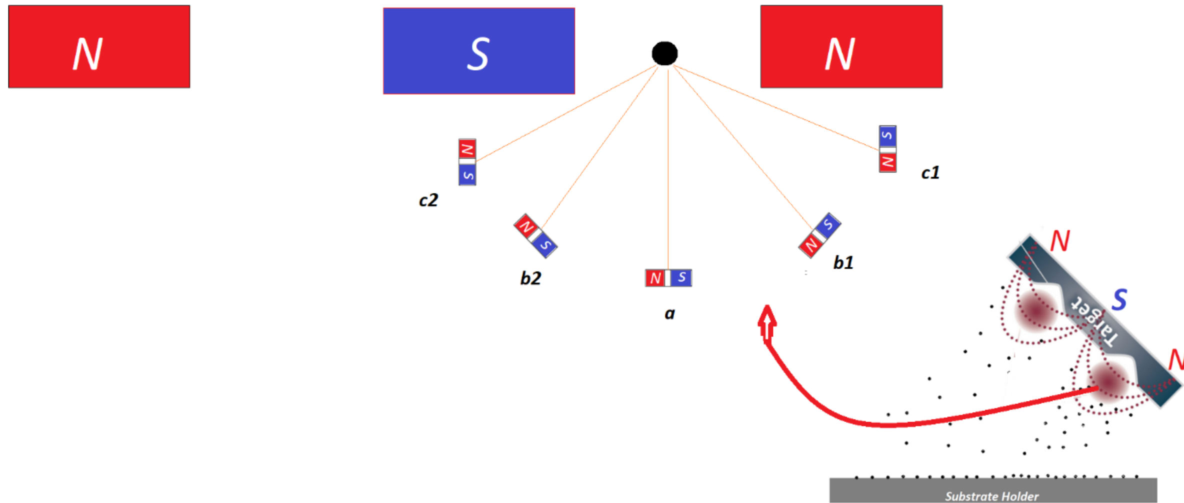

Figure 6.8. A simple approach of considering a certain number of small particles with a magnetic moment along a magnetic field between the N and S poles of the magnetron's magnet. The angle between the centres of the magnets and their position defines how the larger magnet affects them.

Considering the interaction of two hypothetical magnets alfa and beta, in these equations, U is the potential energy of a magnet "alpha" exposed to the magnetic field of magnet "beta". B is the magnetic field of the magnet alpha, M is the magnetic momentum, θ is the angle between the axial angle of the magnetic moment of a magnetic dipole and the magnetic field generated by the magnetron magnet, R is the distance between the centres of the two magnets and F is force imposed on alpha. Considering these equations, It can be seen that the angular geometry of one magnet to another as well as its location in space can lead to positive to negative values of force. Considering this and assuming the hypothetical magnetic particles depicted in **figure 6.8**, the difference between the point c1/b1 and c2/b2 is the magnetic field gradient. In the central position, the magnetic field gradient is higher than in the edge positions. Then, the attractive magnetic force will be higher in the centre than in the edges. Particles at points b2 and c2 will experience a more complex magnetic environment countering their velocity away from the target surface. The gas flow rate, which technically translates to the working chamber pressure and the plasma power, which translates to the kinetic energy of the sputtered particles, will affect the process such that at higher chamber pressures, the probability of particle collisions increases, while higher plasma power leads to higher energy particles, which will be less influenced by the magnetic complexity described. The effect of higher kinetic energy overcoming the magnetic complexity can be seen in **figure 6.3,** where higher plasma power results in deposition of more conductive films at the edge region of the substrate holder. Higher chamber pressure would also result in more particles interacting with the magnetrons magnetic field, and as such may reduce the effect of the field with respect to sputtered particles; however, such conclusions require extensive analysis of the magnetic fields during the experiment, which is beyond the scope of this report.

The following hypothesis to explain the experimental observations can be proposed: during the sputtering process, due to complex magnetic dipole interactions, hydrogen doped ZnO particles leaving the target surface tend to accumulate on the edges of the substrate holder region. This results in thin films with better electrical conductivity, while at the centre, ZnO particles that do not possess magnetic

properties are more predominant, and as such, samples prepared in the centre location of the substrate holder are less conductive.

This process occurs both in IZO and ZnO targets, hence the samples prepared at the edge of the substrate demonstrate higher conductivity due to the higher hydrogen doping. In IZO samples, however, since the presence of indium already acts as a carrier concentration enhancer, a slight improvement in conductivity can be seen; however, in ZnO samples, because only hydrogen acts as the electron donor in the lattice, the large variation of conductivity gradient from the edge to the centre was noticed.

However, this work needs to be followed up with simulation studies and more in depth experimental work to verify the hypothesis proposed here, and the authors are planning explore this study further accordingly. The magnetron in this study had a balanced magnetic set up; the plan for future studies will be to carry out the experiments with unbalanced magnetic and no magnet set up magnetron systems.

6.2 Conclusion

This study primarily is a report of observations associated with deposition of zinc oxide films in the presence of hydrogen along with argon and will require further studies to validate the assumptions and hypothetical statements in this report, particularly similar experiments to that described by Hippler et al. it was demonstrated that it is possible to produce highly conductive ZnO thin films doped with hydrogen at room temperature. The films possess acceptable optical band gap and as such demonstrate above 80% transmittance and best sheet resistance of ~18 Ω square and an average thickness of 850nm (E200 samples). However, the procedure requires certain precisions in terms of substrate positioning and its trajectory with the magnetron. The work carried out and subsequent findings presented in this chapter has been published in a journal [220].

The potential of assessing the sputtering plasma via colour function analysis was also demonstrated, based on evaluating the specific ratios of area under emission peaks as a tool for monitoring the status of plasma during sputtering procedures. This method does not require precise plasma analysis and complex calculations when detailed study of the plasma is not required and instead provides the operator with an easy to understand observing parameter as an indicator of sputtering plasma status.

The hypothesis proposed on the ferromagnetic properties of the sputtered ZnO particles requires further examination and will require detailed analysis of the hydrogen doping variations with balanced and unbalanced magnetron configurations to validate this conjecture. The integration of hydrogen into the target is an area that should be explored further to assess this hypothesis in future attempts. It is an interesting topic to explore by other researchers interested in the field.

Chapter 7 Implementation of Machine Learning/Deep learning concepts: A step towards the digitisation of the sputter deposition process

Moving away from characterisation of the plasma through its colour in the previous chapters, this chapter focuses on the modelling of the plasma discharge by applying Artificial Intelligence as a monitoring and predictive tool. There is reason to believe that artificial intelligence and deep learning can be the answer if the objective is to fully automate and digitise the industrial-scale sputtering process. A brief introduction on AI/Machine learning has been provided in in Chapter 2.3. A more detailed explanation on how specific deep learning technique was applied to the sputter deposition process as well the materials involved can be found in chapter 3.1.4.

7.1 Results and Discussion

7.1.1 Artificial Neural Networks to predict sheet resistance of IZO thin films deposited via Plasma deposition

The objective of this research carried out was to push all the mentioned complexities into the black box of an artificial neural network (ANN) and a convolutional neural network (CNN). With modern computing powers and artificial intelligence (AI) based data assessment methodologies, it was aimed to explore implementing an alternative approach in plasma diagnostics during the sputter deposition process to assess the qualitative parameters of thin films as they were deposited.

The Integral Approach

The area under the spectral peaks from 300nm to 900nm in 50nm intervals was calculated yielding a data frame with 12 columns linked to these areas. This resulted in a data frame with 517 rows and 12 columns associated with peak area values, a vector of thin film sheet resistance values represented the 13th column. **Figure 6.6** presents the structure of the neural network model for the integral approach to model construction; it also shows the predictions made by the model for sheet resistance of 24 samples that were randomly chosen. The model is consisted of five dense layers. Layers 1 to 5 have 30, 20, 8, 4 and 1 neuron/s, respectively, generating a total of 1219 parameters requiring computation. The model's R^2 value is 0.795. The Adam optimizer was used in this model [221], with a learning rate of 0.01 and Huber loss function [222].

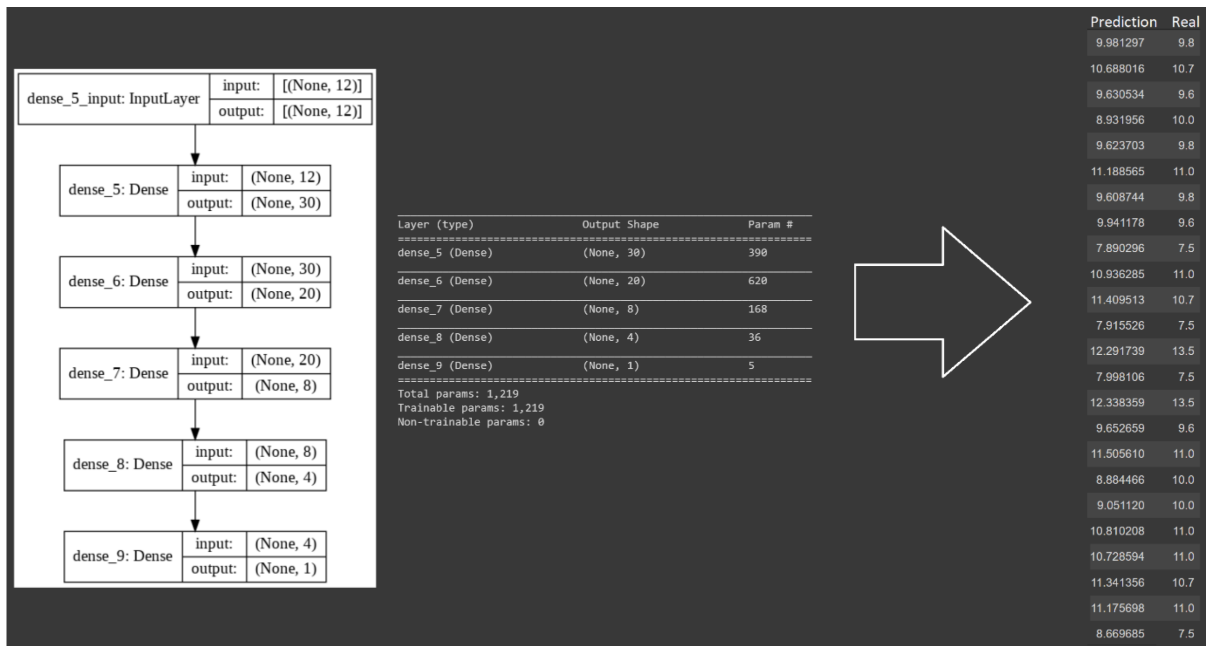

Figure 7.1. The structure of the neural network model designed for training with the integral approach.

The model was given the task to predict the sheet resistance for of 24 samples which was compared with the actual value calculated via the four-point probe system. The R^2 value for the models' predictions was 0.795 with a mean squared error of 0.7.

When attempts were made to re-run the samples, the model demonstrated signs of instability; this could be as a result of the size of the data frame being too small. Large datasets are required to train neural networks and the dataset used was relatively smaller, although sizeable from a practical material engineering point of view, than the standard datasets employed in machine learning and dataset.

The Spectral Approach

The goal of the spectral approach was to utilized the peak intensity values in the 195nm-1104nm spectrum range with a 0.2nm resolution. This yielded a data frame consisting of 113 rows and 4552 columns. Any negative values from the spectrometer signal were deemed as noise and thus set to 0. The columns of the data frame depcited the ratio of the intensity of the spectral signal at each wavelength over the total sum of the intensity. The structure of the model and its predictions are illustrated in **figure 7.2**. The model consisted of eight dense layers. Layers 1 to 8 have 4551, 2000, 500, 300, 50, 8, 4 and 1 neuron/s, respectively, generating a total of over 30 million parameters requiring computation. The model's R^2 value is 0.153.

Layer (type)	Output Shape	Param #
dense_106 (Dense)	(None, 4551)	20716152
dense_107 (Dense)	(None, 2000)	9104000
dense_108 (Dense)	(None, 500)	1000500
dense_109 (Dense)	(None, 300)	150300
dense_110 (Dense)	(None, 50)	15050
dense_111 (Dense)	(None, 8)	408
dense_112 (Dense)	(None, 4)	36
dense_113 (Dense)	(None, 1)	5

Total params: 30,986,451
Trainable params: 30,986,451
Non-trainable params: 0

Prediction	Real
11.716638	11.0
7.242265	9.6
10.095633	11.4
8.587937	10.0
7.953916	9.6
6.134621	9.6
9.904041	10.7
14.390054	13.5
15.105602	13.5
6.924340	9.6
10.712859	11.0
7.827822	9.6
7.944081	9.8
6.307054	7.5
7.642253	9.8
12.122385	11.0
10.446682	10.7
11.522214	10.7
6.534186	7.5
8.289657	9.8
8.393852	9.6
9.558954	10.0
8.455545	9.6

Figure 7.2. The structure of the neural network model designed for training with the spectral approach.

From the results presented in **figure 6.7**, One can see that the model was significantly bigger and more complex than the previous model managing the integral data frame. The model was given the task to handle over 30 million parameters compared to the 1219 parameters of the previous model, which was computationally very demanding. Despite this, the model's statistical performance with R^2 value of 0.15 was significantly better than the 0.795 R^2 value of the previous model.

A number of neural network models were created to manage the spectral data frame. Since the data frame was composed of large dimensions, a technique known as Principal Component analysis (PCA) was utilized in efforts to reduce this [223]. PCA, a form of feature engineering, reduced the number of features columns from 4552 to a mere 12; it was able to retain hidden factors from the dataset and defined data using less components, which is explained the discrepancy in the data. Thus, it resulted in the reduction of computational complexity. These 12 principal components were fed in the neural model as input features. The model structure and the predictions made on physically measured samples are shown in **figure 7.3**. The model is consisted of seven dense layers. Layers 1 to 7 have 10, 10, 10, 10, 8, 4 and 1 neuron/s, generating a total of 349 parameters demanding computation; the model's R^2 value is 0.883. The model reported here displayed a dominant performance when compared to the previous models.

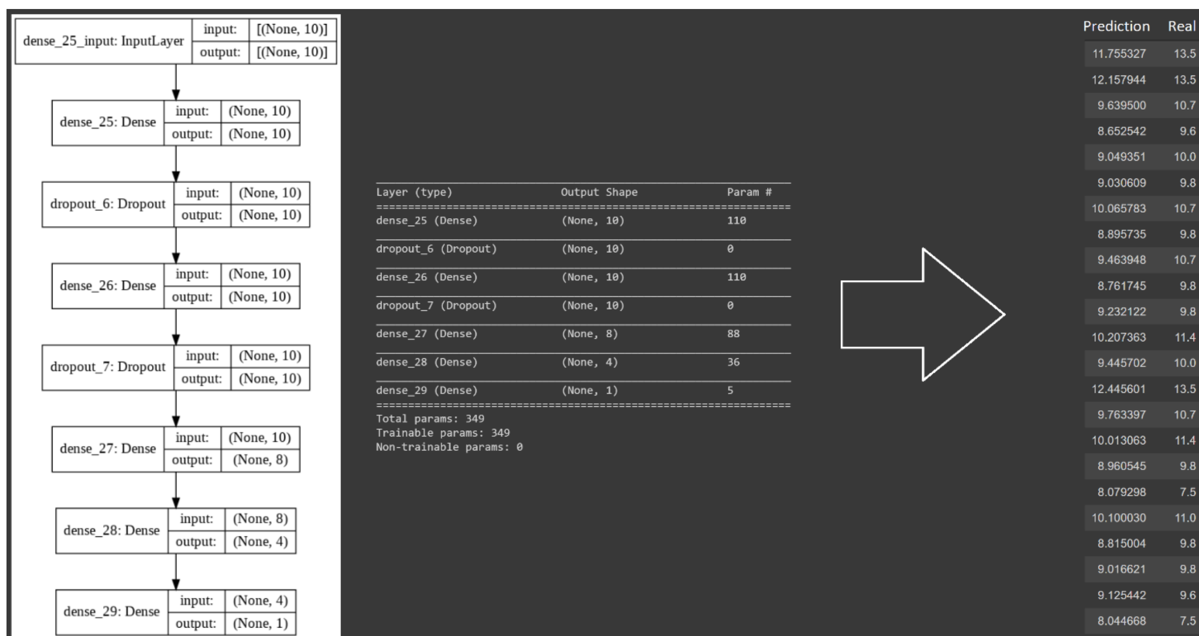

Figure 7.3. The structure of the neural network model designed for training with the combined principal component analysis and spectral approach.

As depicted in **figure 7.3**, in the PCA/spectral data frame integration approach, the model exhibited superior performance compared to the integral approach experiment, achieving an R^2 value of 0.883, notably surpassing the performance of prior models.

The Image Recognition Approach

The spectral data, spanning from 200 to 1100 nm with a resolution of 0.2 nm, resulted in an array comprising 4500 data points. This array underwent transformation into a matrix with shape of (50, 90). Subsequently, this matrix was translated into an image format, where each value of the matrix corresponded to a pixel value within a 50-pixel x 90-pixel image. This process is depicted in **figure 7.4**.

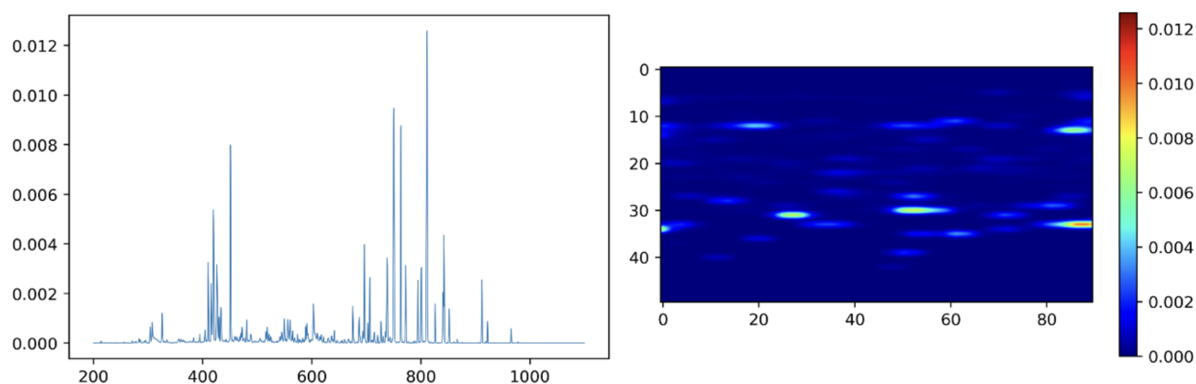

Figure 7.4. Converting a spectral plot (**a**) into an image (**b**). The spectral data are initially summed up and each peak value is calculated by dividing the original peak value over the sum. It is then converted into a matrix of (50, 90) shape.

The image derived directly from the spectra was initially employed to train several convolutional neural network models. However, none of these models could effectively learn from the image in its original format, as CNN models typically operate more efficiently with standardized values. Subsequently, the pixel values of the image were scaled using two distinct normalization methods: min-max scaling and standard scaling, as outlined in Chapter 3.1.4. New images were then generated based on the normalized pixel values of the original image. Two examples of these normalized images are illustrated in **Figure 7.5**.

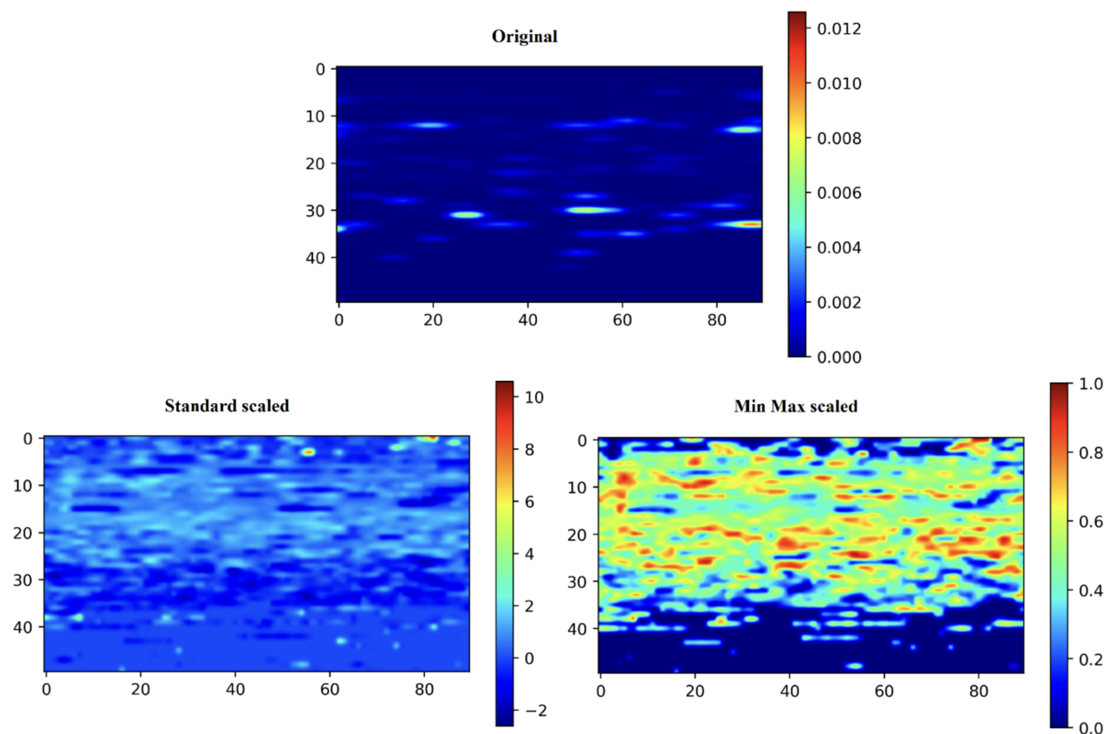

Figure 7.5. The original image (**top**) is converted to an image from normalised values via standard scaling (**bottom left**) and min-max scaling methods (**bottom right**).

Subsequently, the normalized images were utilized to train the model for predicting the sheet resistances of the IZO films deposited through the corresponding plasma process. Following training, the normalized images were subjected to similar convolutional models for testing purposes. The outcomes of these tests are showcased in **Figures 7.6 and 7.7**. Interestingly, the min-max scaled data yielded the most accurate predictions of sheet resistance, as evidenced by the results and corresponding R^2 values. Specifically, the standard scaled images displayed R^2 values of 0.642, whereas the min-max scaled images exhibited significantly higher R^2 values of 0.897.

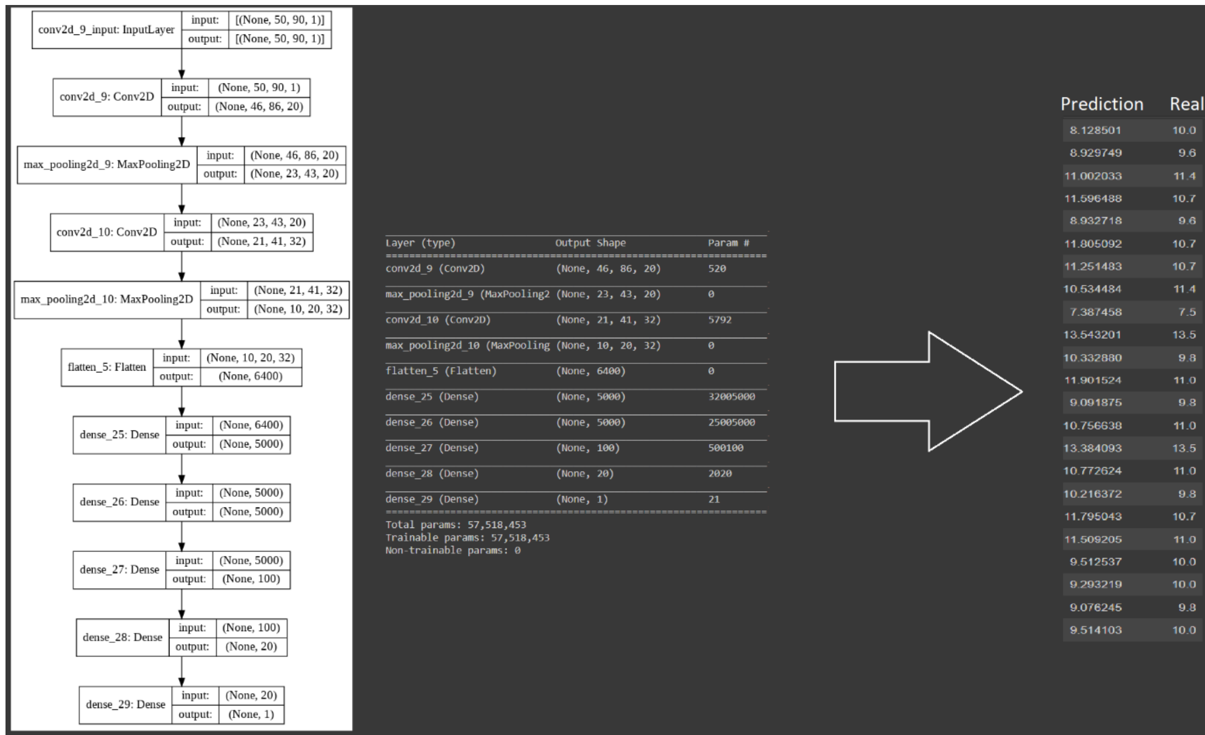

Figure 7.6. The structure of the convolutional neural network model designed for training with standard scaled values of the pixels in image of the spectra.

The model in **figure 7.6** is consisted of two convolutional layers and two max-pooling layers which are then flattened and fed to a deep network with five dense layers. Where layers 1 to 5 had 5000, 5000, 100, 20, and 1 neuron/s, generating a total of 57,518,453 parameters requiring computation, the model's R^2 value was 0.642.

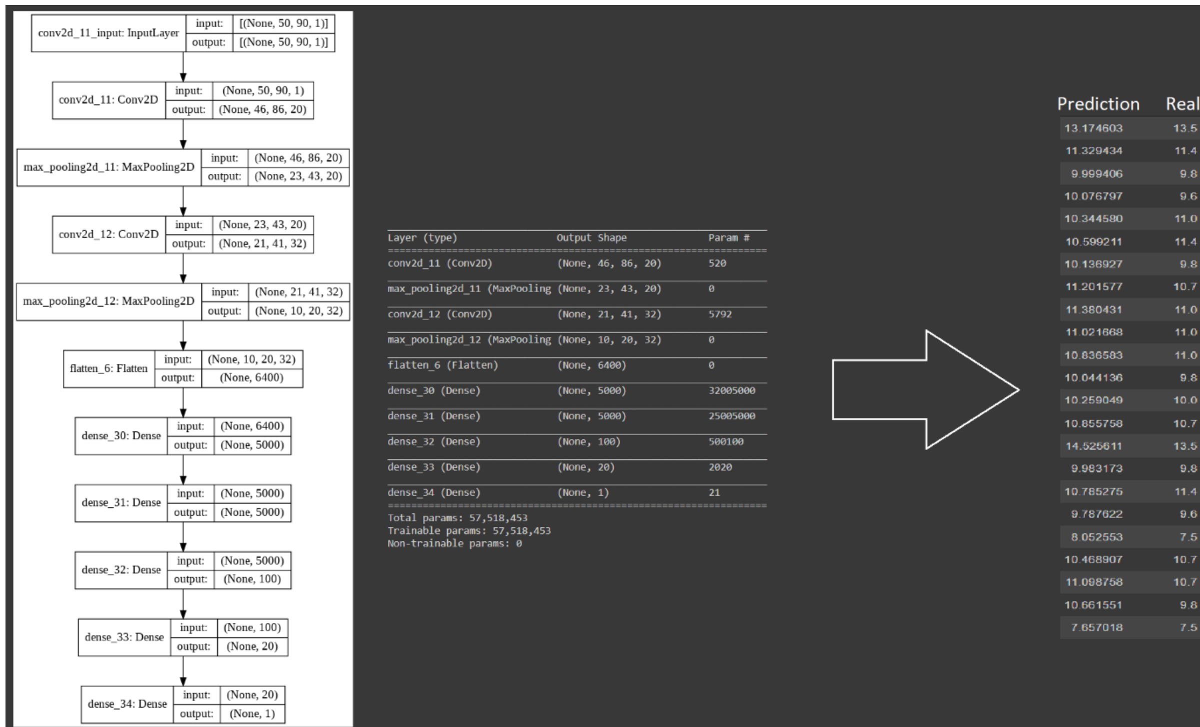

Figure 7.7. The structure of the convolutional neural network model designed for training with the min-max scaled values of the pixels in images of the spectra.

The model in **figure 7.7** is consisted of two convolutional layers and two max-pooling layers which are then flattened and fed to a deep network with five dense layers. Where layers 1 to 5 had 5000, 5000, 100, 20, and 1 neuron/s, generating a total of 57,518,453 parameters requiring computation, the model's R^2 value was 0.897.

The findings thus far suggest that employing min-max scaling on the data enhances the CNN model's ability to accurately discern patterns and hidden features within the images. At this stage, each image, characterized by a matrix of shape (50, 90), underwent the Singular Value Decomposition (SVD) process, as detailed in Chapter 3.1.4. Despite both standard scaled and min-max scaled image matrices exhibiting similar condition numbers, there were discrepancies in the distribution of information across singular values when SVD was applied to the images. **Figure 7.8** illustrates the typical distribution of singular values, known as the "scree plot," for each layer of decomposed standard scaled and min-max scaled matrices. In a min-max scaled matrix, the first singular value (representing the maximum value) encapsulated a higher percentage of the total sum of values compared to the standard scaled decomposed matrices.

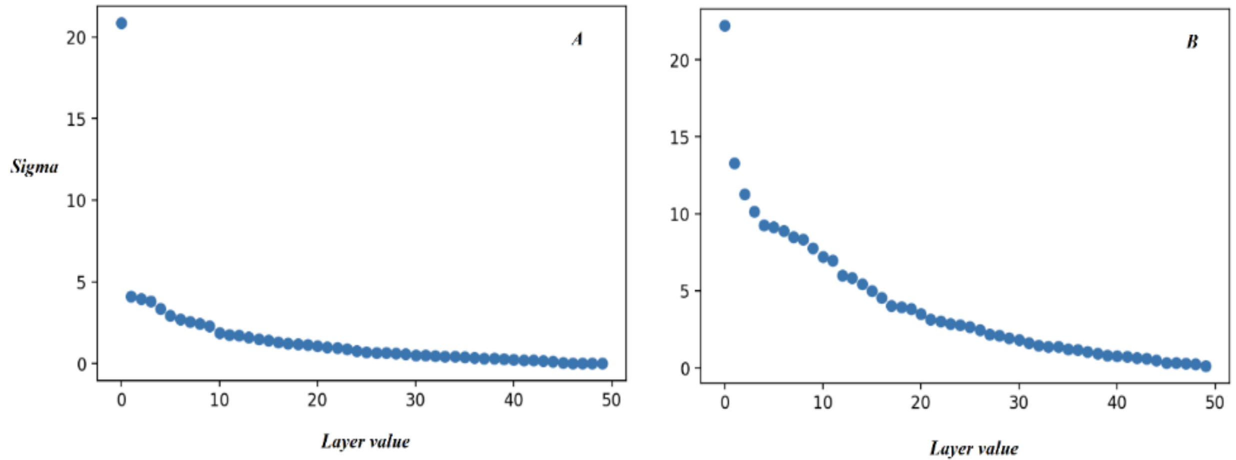

Figure 7.8. The scree plot of singular values for (**A**) min-max scaled images and (**B**) standard scaled images.

In the subsequent phase aimed at enhancing the CNN model's accuracy, the spectral image matrices were systematically decomposed layer by layer (a total of 50 layers for each image). Subsequently, the CNN model was trained using images reconstructed from smaller layers—or even individual layers—derived from the SVD process. Given the underperformance of standard-scaled whole images in previous trials (refer to **figure 7.6**, R^2 value 0.642), efforts were directed towards achieving improved performance with min-max scaled values. However, contrary to expectations, an image reconstructed from the first single layer of standard-scaled images decomposed by SVD surpassed all other CNN training endeavours, yielding an impressive R^2 value of 0.935. Notably, this model demonstrated exceptional stability across repeated training sessions. Conversely, reconstructing an image from the first single layer of a min-max scaled image yielded poor results in training the CNN model, with an R^2 value of 0.74.

This discovery proved highly intriguing: while the original standard-scaled images performed inadequately in training the CNN model, the min-max scaled originals exhibited notable success. Moreover, the reconstruction of an image from the first single layer of standard-scaled images outperformed all models in terms of both accuracy and stability. Consequently, given that these experiments were conducted across various chamber pressures, the reconstructed images from the first layer of the singular value decomposed original images were converted into a spectral format. These findings are illustrated in **figures 7.9** and **7.10**, where each column represents four randomly selected spectral reconstructions of plasma emissions from the first layer of SVD of the original image at specific chamber pressures.

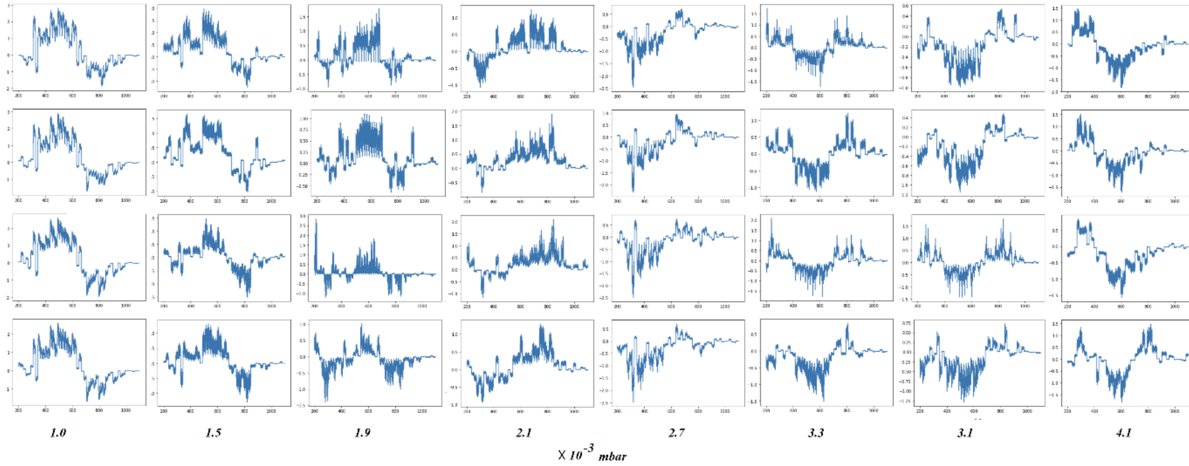

Figure 7.9. Four randomly selected conversions of the first layer of the image decomposition via SVD, associated with process chamber pressures into a spectral format. For standard scaled images. *x*-axis represents emission wavelengths and *y*-axis is emission intensity.

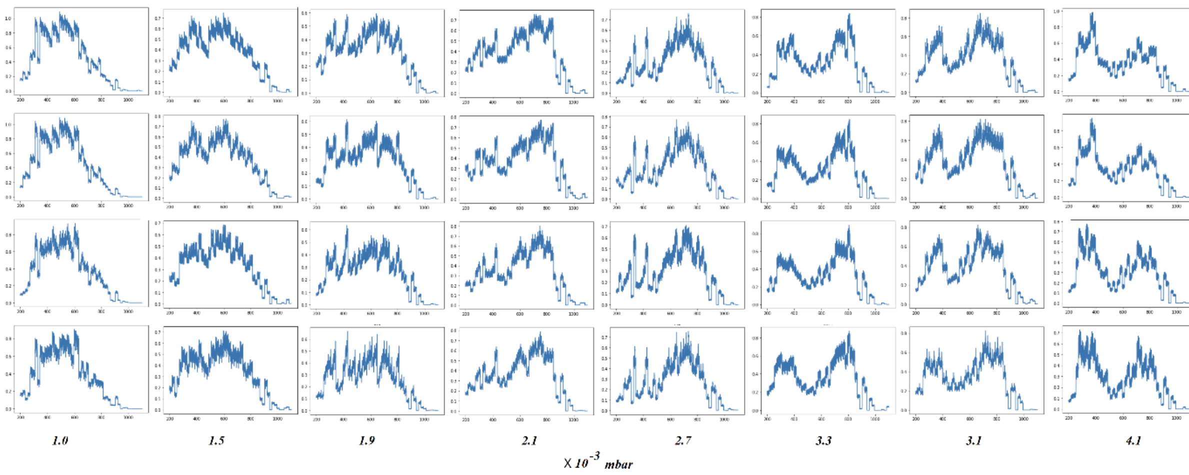

Figure 7.10. Four randomly selected conversions of the first layer of the image decomposition via SVD associated with process chamber pressures into a spectral format. For min-max scaled images, *x*-axis represents emission wavelengths and *y*-axis is emission intensity.

Table 7.1. Prediction of the thin film sheet resistance from a CNN model learning from the first layer of a singular value decomposed image of a plasma spectra (standard scaled).

Predicted	Real	Relative Error
7.598	7.5	1.31
13.955	13.5	3.37
7.360	7.5	1.87

10.832	11.4	4.98
9,967	9.6	3.82
7.487	7.5	0.18
10.893	11	0.97
10.255	9.6	2.32
9.377	9.6	2.77
10.996	10.7	2.77
10.518	10.7	1.71
10.457	10.7	2.27
7.467	7.5	0.45
13.073	13.5	3.16
11.098	11.4	2.65
9.937	10	0.63
7.329	7.5	2.27
10.551	11.4	7.44
10.290	10.7	3.83
10.045	9.8	2.50
11.811	10.7	10.38
11.457	11	4.32
10.474	10	4.74

Table 7.1 showcases the predictions derived from the standard scaled image data by the CNN model. An explanation can be made for the observed training performance associated with the standard scaled first layers images when looking at **figures 7.9** and **7.10** in comparison. Detecting specific features in a particular image is the basis of the operation of CNNs. These features (and their detection with the black box of a DNN) lack intuition and can sometimes be mysterious. As a result, standard scaling of images, derived from the original plasma spectrum, resulted in feature consolidation within specific column and row spaces of the image. Conversely, min-max scaling led to a distribution of features across alternative row and column vector spaces. Nonetheless, considering the long-term objective of investigating the applicability of deep learning models in transitioning toward digitized sputtering processes, the model's performance was deemed satisfactory. Nevertheless, this presents an intriguing avenue for further exploration, particularly by researchers with a primary focus on the practical engineering aspects of deep learning models.

Table 7.2 encapsulates the overall performance of all experiments conducted in this study, in terms of their predictive accuracy. Notably, the CNN model approach achieved the highest R^2 value. The stability metric reflects the repeatability of consecutive R^2 values produced by the model, indicating the degree of deviation from the maximum R^2 obtained. A deviation of 0.15 points is categorized as poor stability, 0.1 as moderate, and 0.05 as good, when the models were repeated ten times.

Table 7.2. The overall performance of the models and the data approach employed in experiments.

Modelling Approach and Data	R^2	Stability
ANN model, Integral approach	0.795	Poor
ANN model, Spectral approach	0.153	poor
ANN model, Spectral approach with PCA dimensionality reduction	0.883	Moderate
CNN model, Standard Scaled	0.642	Moderate
CNN model, Min Max scaled	0.897	Moderate
CNN model, Standard Scaled, SVD first layer	0.934	Good
CNN model, Min Max Scaled, SVD first layer	0.741	Good

7.1.2 Implementing Supervised and Unsupervised Deep-Learning Methods to Predict Sputtering Plasma Features

As detailed in chapter 3.1.4. This set of experiments reports the follow up of the previous set of experiments whereby supervised and unsupervised deep-learning methods were implemented i.e. CNN to predict the sputtering growth parameters by feeding the spectral data of the plasma to it.

Overall, 2352 images were used (588 images per method of 2-dimensional matrix formation) which is associated with various targets—working gas pressures, plasma power, and hydrogen impurity—that were present in the argon gas. 80% of the data was randomly selected for training the models and used the remaining 20% to evaluate the prediction of the models and their accuracy.

Regression models

A very interesting initial observation made was that the models were trained best on the data sets for which the peak-intensity ratio operations were carried out. In fact, without this step, standard scaling alone was insufficient to train the models, as extremely poor results and prediction were observed. However, the min-max scaling resulted in desirable accuracies, as in a sense it converts the data points to a minimum–maximum range of 0 to 1. However, once the peak-intensity ratio operation was carried out, standard scaling and min-max scaling were equally good for training the models for desirable accuracy. However, all the results presented in this report are associated with data that were min-max scaled. The results for each set of samples and experiments were investigated separately.

When presenting the results (**figures 7.11-7.14**), 'Original' refers to the min-max-scaled stack-overlay-formed images turned into a 2d matrix. 'Original_SVD' refers to the first-layer reconstruction of the original image after SVD decomposition. 'SOM' refers to images generated from the spectra via the self-organizing map method and 'SOM_SVD' refers to the first-layer reconstruction of the SOM image after SVD decomposition. The R-squared (R2) and mean squared error (MSE) of the models predictions

are also presented. The results of predicting the zinc concentration in the target are presented in **figure 7.10**. It can be seen that SVD reconstructions of the SOM-formed images performed less effectively.

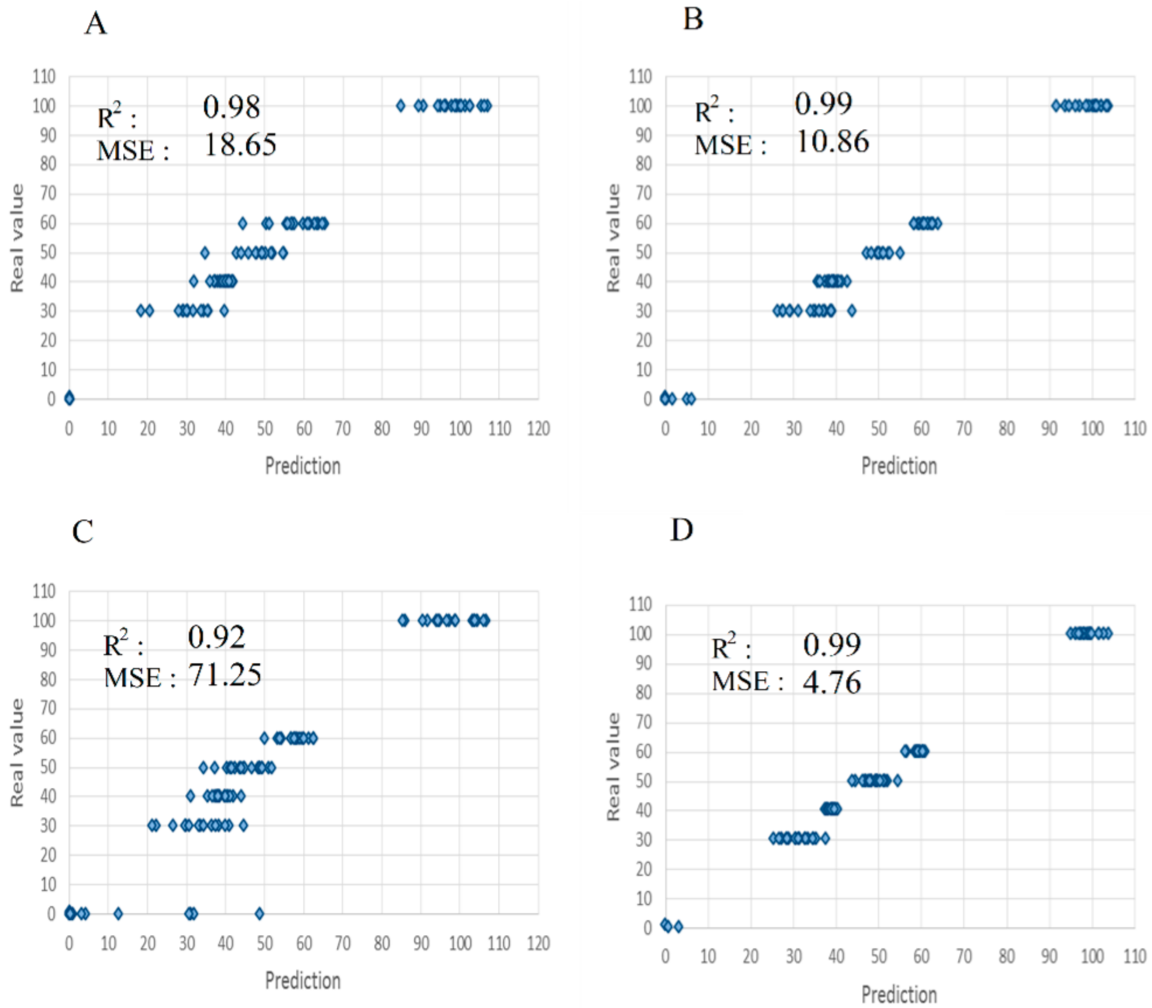

Figure 7.11. The real value of the zinc content in the target (wt%) on the 'y' axis and the prediction of the zinc content (wt%) of the target composition in the 'x' axis (**A**) Original, (**B**) SOM image, (**C**) SOM_SVD, (**D**) Original_SVD images

The results of predicting the indium concentration in the target are presented in **figure 7.12**. Once again, One can see that the SVD reconstruction of the SOM-formed images performed less effectively. **Figure 7.13** and **figure 7.14**, respectively, demonstrate the predictions of the gas-flow rate and plasma power.

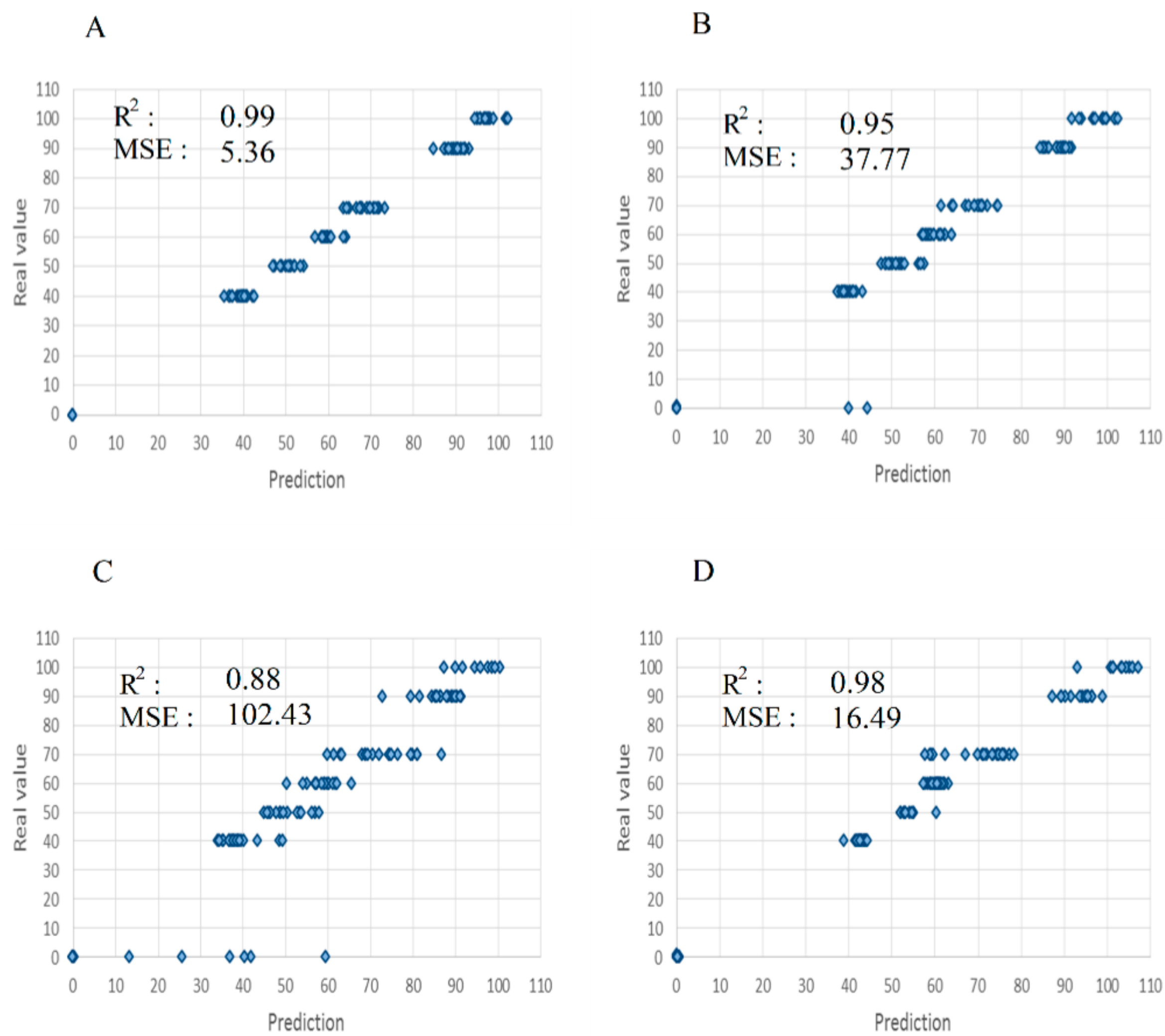

Figure 7.12. The real value of the indium content in the target (wt%) on the 'y' axis and the prediction of the indium content (wt%) of the target composition in the 'x' axis. (**A**) Original, (**B**) SOM, (**C**) SOM_SVD image, (**D**) Original_SVD images.

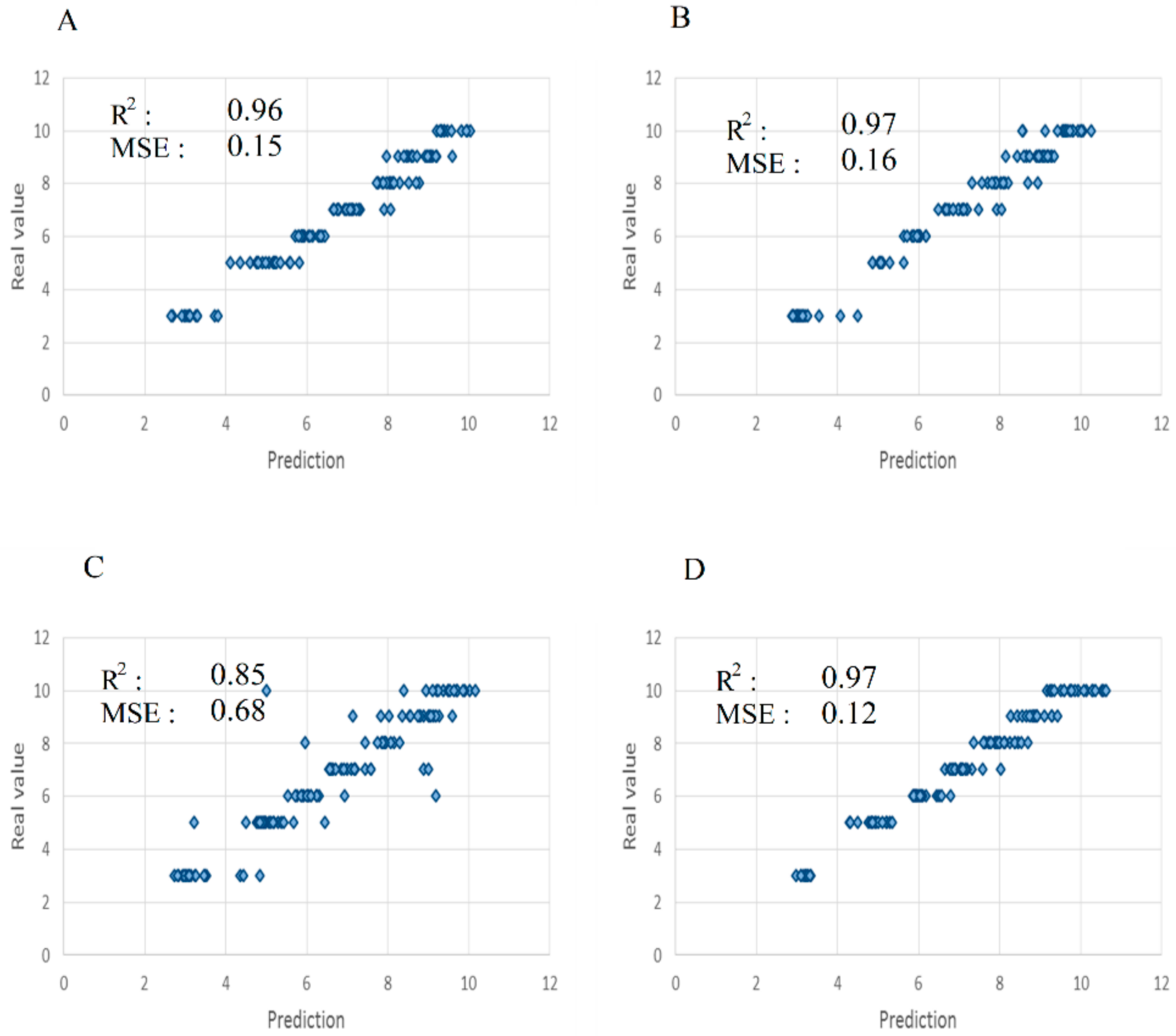

Figure 7.13. The real values of gas-flow rate (sccm) during the sputtering process are presented in 'y axis and the predicted values in 'x axis. (**A**) Original, (**B**) SOM, (**C**) SOM_SVD, (**D**): Original_SVD

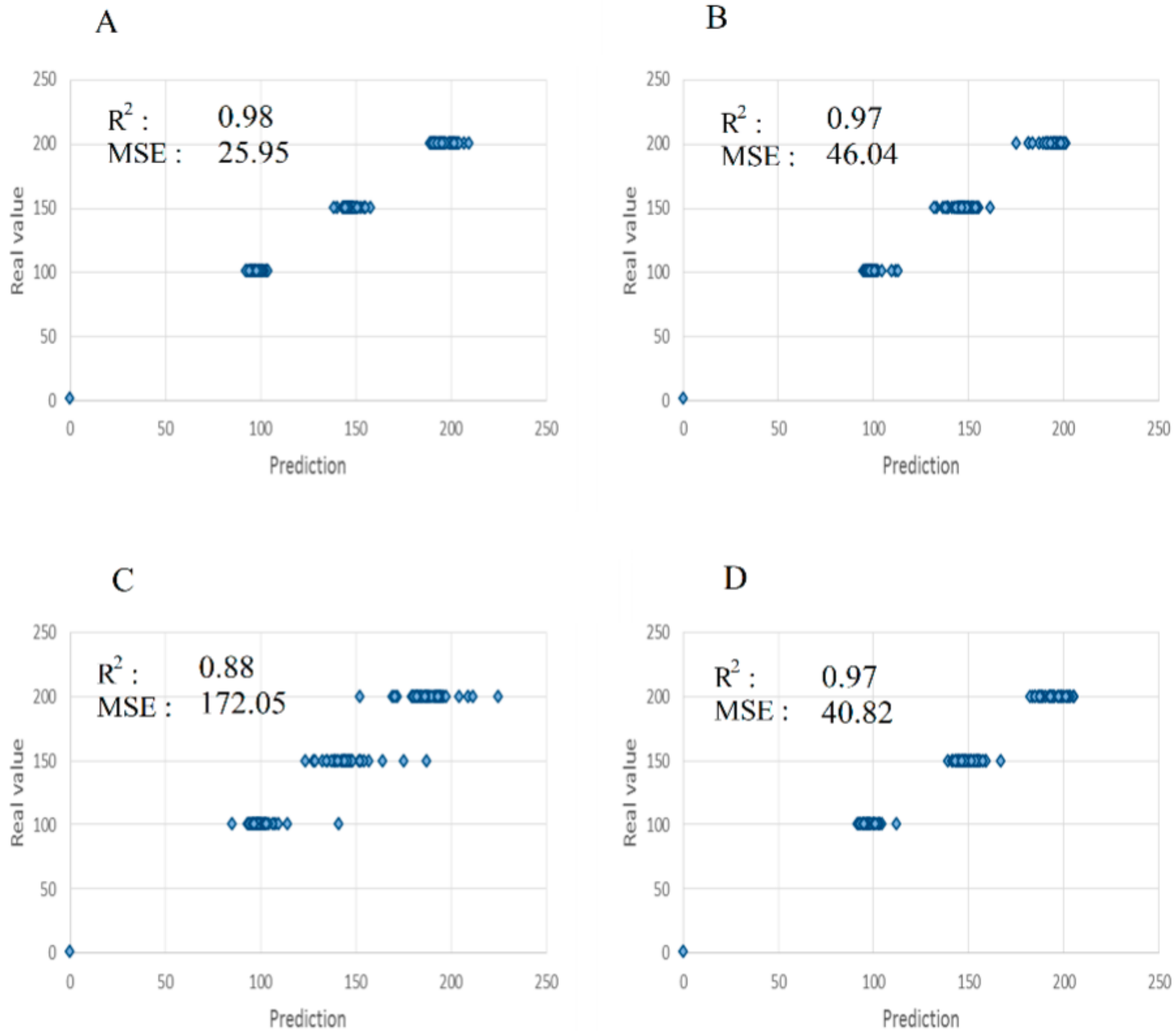

Figure 7.14. The real values of plasma RF power (Watts) during the sputtering process are presented in 'y axis and the predicted values in 'x axis. (**A**) Original, (**B**) SOM image, (**C**): SOM_SVD, (**D**) Original_SVD

Out of all the results, it can be seen that the SVD reconstruction of the SOM model (SVDS) produced the least accurate predictions. The original stack-overlay method of reconstructing a two-dimensional array from the one-dimensional array of the spectra seems to be sufficient for training the CNN model for accurate predictions.

Classification model

When the model was used as a classifier rather than a regressor to predict the presence of hydrogen impurity and impurity in the indium-oxide-based target, excellent results with all forms of two-dimensional conversion techniques were obtained, as presented in **figure 7.15** and **figure 7.16**. In both cases, The SVD reconstruction of the SOM method demonstrated one inaccurate classification, while all other models performed with 100% accuracy. The accuracy metrics associated with the hydrogen presence and indium-oxide target purity are presented in Table 1, Presenting the accuracy metrics of the CNN model's performance trained with images formed from the four methods of two-dimensional image formation; presence of hydrogen in the working gas and impurity in the indium-oxide target.

Hydrogen presence

Original

Actual \ Predicted	False	True
False	64	0
True	0	54

SOM

Actual \ Predicted	False	True
False	57	0
True	0	61

SVDZ

Actual \ Predicted	False	True
False	61	0
True	0	57

SVDS

Actual \ Predicted	False	True
False	56	1
True	0	61

Figure 7.15. Confusion matrices demonstrating the accuracy of the two-dimensional images to generate images for training ANN model for classification, on presence of hydrogen impurity in the sputtering working gas.

Indium Oxide target purity

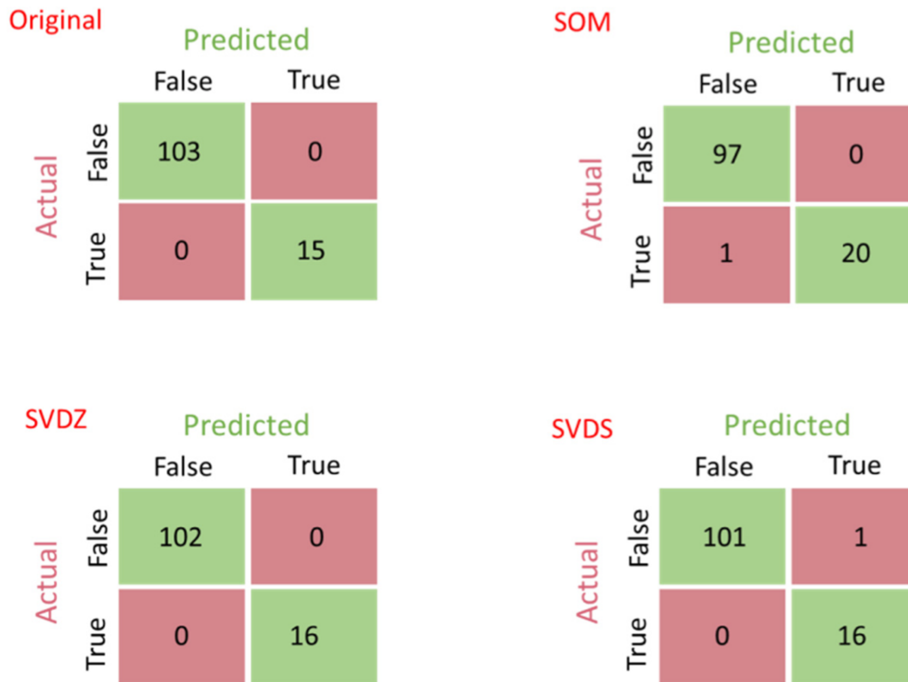

Figure 7.16. Confusion matrices demonstrating the accuracy of the two-dimensional generated images for training CNN model for classification of 100% purity of indium-oxide sputtering target.

Table 7.3. Confusion matrix of model classification associated with Hydrogen presence and impurity in the indium oxide target.

Hydrogen Presence			
Model	**Accuracy**	**Recal**	**Precision**
SOM_SVD	0.99	1	0.98
ORIG_SVD	1	1	1
SOM	1	1	1
ORIG	1	1	1
Impurity presence in InO Target			
Model	**Accuracy**	**Recal**	**Precision**
SOM_SVD	0.99	1	0.94
ORIG_SVD	1	1	1
SOM	0.99	0.95	1
ORIG	1	1	1

7.2 Conclusion

The integration of deep learning models into spectral analyses of sputtering plasma offers the potential to digitize the sputtering process. This implies that during deposition, specific film properties could be estimated solely by observing the characteristics of the plasma. Through various modelling approaches, as outlined in **Table 7.2**, the CNN model approach yielded the highest R^2 value with commendable stability. The study highlighted that result accuracy depended on both the quantity of data points and the number of process parameters considered. Additionally, the modelling approach adopted played a crucial role, particularly when focusing on specific electrical properties such as sheet resistance of the TCO. Undoubtedly, future endeavours will encompass exploration of additional sample features, including charge carrier concentration, mobility, crystal structure parameters, and optical band gap, aiming for enhanced optimization and control. Future research will also entail adjusting other experimental parameters, such as sample rotation speed, incident angle of the magnetron to the substrate, and their relative distance, to achieve highly accurate predictions of the functionality of the deposited films.

The results presented in this chapter (**figures 7.11-16**) clearly demonstrate the potential of deep learning and, in particular, computer-vision-based CNN models as the tool of choice to be utilised in associating the spectra emissions of plasma to the operating conditions of sputtering units. Plasma power and gas-flow rates do indeed affect plasma glow and its spectral characteristics. Higher plasma power can lead to higher energy ions and higher rates of excitation, which also affect the property of the thin film deposited while demonstrating a unique glow feature in the plasma emission. Higher gas-flow rates increase the chamber pressure, resulting in a greater flux of atomic collisions and variation in the ion distribution. This, in turn, affects the property of the thin film deposited. The models presented were shown to be successful at predicting various features associated with the process, such as (wt%) content of the target ingredients in **figure 7.11** and **figure 7.12** and the gas-flow rate and plasma power, as presented in **figure 7.13** and **figure 7.14**. The model also demonstrated the ability to predict the presence of an additional gas (hydrogen) as a 5% impurity in the argon working gas and to assess the purity of the target itself, as presented in **figure 7.15** and **figure 7.16**. In the experiments carried out, a static CNN construction was trained with the images that were formed from the four described two-dimensional images. By further adjusting the CNN model, higher accuracies are achievable. It was shown that the spectral data can be easily used to form an image that can benefit from the power of modern computer-vision deep-learning models. This simple approach even outperformed the more complex SOM method of two-dimensional array formation.

All these parameters are critical in defining the properties of the thin films produced via this form of plasma sputtering. When neural networks can associate the spectral features of the plasma with a numerical assessment of these critical operating features, they can also be implemented to predict the properties of thin films. This was demonstrated by focusing on a single sputtering target (indium zinc oxide) and assessing the electrical property of the produced thin films. The range of the target materials was extended to further validate the observations seen in section 7.1.

It was acknowledged that further improvements in model construction could be achieved with access to additional data, particularly from other sputter systems, which unfortunately were not available. Nonetheless, the work conducted within these constraints represents a significant step towards

establishing correlations between digital datasets and the desired functionality of TCO films with a reasonable level of accuracy. Consequently, this research holds significance for optoelectronic industries employing physical vapor deposition techniques , to produce high-yield products.

In conclusion, the presented results emphasise the need for the establishment of a global repository where data generated at various research levels by diverse research groups, including material engineers and scientists, can be shared for analysis and model training. In the long run, this initiative will reduce research and development costs and expedite the advancement of novel materials and technologies, ultimately benefiting industries as they transition towards efficient and cost-effective scaling-up of their production processes.

Chapter 7.1 demonstrated how these models can be used to predict the physical properties of thin films, with a focus on a single material. In Chapter 7.2, it has been shown that these models are capable of predicting the nature of plasma at a high level of precision and, therefore, one can conclude that these can be instrumental in predicting various other material properties associated with thin films produced via sputtering. The deep learning trial studies carried out and subsequent findings in this chapter have also been presented in the format of publications [224,225].

Proficient researchers specializing in data science, artificial intelligence (AI), and machine learning are continuously refining algorithms, loss functions, backpropagation models, and optimizations to advance this field as a universal tool for various scientific domains. Consequently, the models showcased in this study have the potential for further refinement to attain greater accuracy. Therefore, integrating AI processes, as demonstrated in this investigation and its correlation to functional properties, could greatly enhance the digitized manufacturing process in the realm of thin film depositions.

Chapter 8 Summary, Highlights and Future Work

8.1 Summary

The thesis is an attempt to bring together the research work that has explored and demonstrated two novel and simple approaches viz. the colour characterisation method and the application of Artificial Intelligence/Machine Learning to the diagnosis and evaluation of the glow discharge during RF magnetron sputtering. The key findings of the work are summarized below:

In chapter 4, the photometric properties of a radio frequency (RF)-based sputtering plasma source were monitored through optical spectroscopy. The colour of the plasma source was deduced based on conventional chromaticity index analysis and it was compared to the direct spectral data plots of the emission peaks to investigate the possibility of characterising the plasma based on its specific colour and exploring the potential of defining a new method by which the plasma sputtering process can be addressed based on the plasma colour parameters. The intention of this investigation is to evaluate the possibility of simplifying the monitoring and assessment of the sputtering process for applied scientists operating plasma sputter deposition systems. a viable potential for this technique was demonstrated in terms of providing information regarding the stability of the plasma, chamber pressure, and plasma power; however, further work is underway to verify and assess a relationship between the quality of the thin film coating and the colour characteristics of the deposition plasma. Here, the focus was solely on the feasibility of such an approach and demonstrate interesting observations. There was a clear linear relationship between the colour functions and the plasma power, while the stability of the sputtering plasma can be assessed based on the plasma colour functions. The colour functions also follow a unique pattern when the working gas pressure is increased.

Chapter 5, showcases the spectral properties and colour functions of a radio frequency (RF)-based sputtering plasma source was monitored during consecutive sputter deposition of zinc doped indium oxide (IZO) thin films under argon and argon/hydrogen mix. The effect of target exposure to the hydrogen gas on charge density/mobility and spectral transmittance of the deposited films was investigated. It was demonstrated that consecutive exposure to the hydrogen gas during the deposition process progressively affects the properties of thin films with a certain degree of continuous improvement in electrical conductivity while demonstrating that reverting to only argon from argon/ hydrogen mix follows a complex pathway, which has not been reported previously in such detail to one's knowledge. It was then demonstrate that this effect can be used to prepare highly conductive zinc oxide thin films without indium presence and as such eliminating the need for the expensive indium addition. As demonstrated, the complexity observed in emission spectra can be simply identified by monitoring the colour of the plasma through its colour functions, making this technique a simple real-time monitoring method for the deposition process.

Chapter 6 investigates the complexity of the reactive sputtering of highly conductive zinc oxide thin films in the presence of hydrogen at room temperature. The importance of precise geometric positioning of the substrate with respect to the magnetron to achieve maximum conductivity was studied. The results were examined which entailed studying the electrical properties of the deposited thins films based on their position on the substrate holder relative to the magnetron. By considering early reports by other researchers on the angular dependency of plasma parameters and the effect of hydrogen doping on electric and magnetic properties of hydrogen-doped zinc oxide, a hypothesis was put forward regarding

the hydrogenated ZnO compounds exhibiting ferromagnetic properties near the edge; further tests are required to be carried out to verify this hypothesis. Overall, this report presents the preparation highly conductive zinc oxide thin film coatings via RF sputtering with hydrogen presence along with argon as the sputtering gas.

Moving away from evaluation of the plasma via colour characterisation, the feasibility of applying artificial intelligence for the modelling of the glow discharge in chapter 7 was explored. Deep learning models were implemented to examine the accuracy of predicting a single feature (sheet resistance) of thin films of indium-doped zinc oxide deposited via plasma sputter deposition by feeding the spectral data of the plasma to the deep learning models. It was demonstrated that artificial neural networks could be implemented as a model that could predict the sheet resistance of the thin films as they were deposited, taking in only the spectral emission of the plasma as an input with the objective of taking a step toward digital manufacturing in this area of material engineering. This research work is concluded in by presenting the spectral emission data from the plasma glow of various sputtering targets containing indium oxide, zinc oxide, and tin oxide were obtained. The plasma was generated at various power and chamber pressures. These spectral data were then converted into two-dimensional arrays by implementing a basic array-reshaping technique and a more complex procedure utilizing an unsupervised deep-learning technique, known as the self-organizing-maps method. The two-dimensional images obtained from each single-emission spectrum of the plasma mimic an image that can then be used to train a convolutional neural network model capable of predicting certain plasma features, such as impurity levels in the sputtering target, working gas composition, plasma power, and chamber pressure during the machine operation. The single-array-to-2D-array conversion technique, coupled with deep-learning techniques and computer vision, was shown to achieve high predictive accuracy and can, therefore, be fundamental to the construction of a sputtering system's digital shadow.

8.2 Highlights of the Research

The research work conducted has evolved from the studies conducted for the basic understanding of the plasma characteristics in a sputtering chamber and its relationship with the vacuum processing parameters using advanced spectroscopy and predictive modelling tools. The optimisation of the sputtering process in pinpointing a process condition in vacuum process industry has always been a holy grail and is limited to finding recipes for each vacuum instrument, the research work was conducted with a motivation to find these limiting factors drawing its origins from the plasma source itself. Whilst each chapter registers the conclusion of the studies conducted along with the summary of the work in the preceding section, the highlights of the results can be presented as following.

- The characteristic colour of RF plasma has been successfully linked with the chromaticity index and was demonstrated for the first time a linear relationship between the colour functions and the plasma power, whilst a defined unique patterns for the stability of the plasma and the effect of variations of chamber gas pressure, thus making this technique a simple real-time monitoring method for the deposition process.
- A highly conductive (18 ohms/sq) and transparent (>80% transmission in the visible range) ZnO films have been obtained at room temperature using hydrogen doping, making it one of the useful TCOs for low temperature processing required for perovskite and organic solar cells.
- A correlation has been established for the first time of extensive set of electrical sheet resistance of IZO thin films data and the RF plasma glow characteristics, which has also been validated by

modelling tools involving artificial intelligence viz. deep learning and computer vision methods. These have achieved high predictive accuracy and thus can be applied to construction of sputtering system's digital shadow for high value and high yield manufacturing.

8.3 Future work

Extensive work on incorporating deep learning methods in the sputter deposition process to further establish the design of a digital shadow is underway. This includes feeding the spectral emission data of the glow discharge into a CNN deep learning model to predict an array of electrical properties (such as carrier concentration & mobility) of a range of thin film TCOs. Plasma sputtering is a highly complex process which involves deep theoretical physics to explain which is a limiting factor for applied/materials scientist who want further to explore this type of deposition technique; This gap in knowledge can by addressed by incorporating AI to establish a relationship between the plasma sputtering process and the properties of thin films. The application of AI does not have to be limited to the deposition of TCOs only but can also be applied to a wide variety of thin film semiconducting materials; one such example would be photoactive materials. The implementation of AI i.e. Machine Learning and Deep learning methods in the manufacture of thin films materials (and the semiconductor industry as a whole) can bring forth great prospects leading to enhanced productivity, efficiency and performance whilst reducing costs.

Since Frank Rosenblatt proposed the concept of the perceptron in the 1960s [226], followed by the ground-breaking contributions of Hinto, LeCun, and Bengio in the 1980s [227], the field of computer science has witnessed continuous advancements. Presently, with leading companies like Google and Facebook actively leveraging its capabilities, there's a surge in the development of increasingly intricate deep-learning models, expanding the horizons of numerical analysis. Consequently, there's a growing necessity for researchers in traditional domains such as material science to embrace and apply this technology in their work.

Integrating deep learning models into plasma-assisted thin-film deposition processes could result in the creation of a digital replica for sputter-deposition, a critical step in producing numerous thin films used in various everyday products. The primary challenge lies in acquiring the vital data. Deep learning models exhibit enhanced accuracy and efficiency when trained on substantial datasets. Incorporating these models into established engineering or materials-engineering domains will necessitate strategies for accessing or compiling structured data. Therefore, efforts aimed at generating an extensive repository of spectral emissions linked to the sputtering of diverse materials will play a pivotal role in establishing a digital counterpart for plasma-sputtering processes.

References

1. Gonzalez Vazquez, I.; Milasi, S.; Carretero Gomez, S.; Napierala, J.; Robledo Bottcher, N.; Jonkers, K.; Goenaga, X. The Changing Nature of Work and Skills in the Digital Age (EUR 29823 EN); 2019.
2. Ginley, D.S.; Hosono, H.; Paine, D.C. Handbook of Transparent Conductors; Springer: Berlin, Germany, 2011; pp. 353–425.
3. Ginley, D.S.; Bright, C. Transparent Conducting Oxides. MRS Bull. 2000, 25, 15–18.
4. Hosono, H. Recent progress in transparent oxide semiconductors: Materials and device application. Thin Solid Films 2007, 515, 6000–6014.
5. Ellmer, K. Past achievements and future challenges in the development of optically transparent electrodes. Nat. Photonics 2012, 6, 809–817.
6. Granqvist, C.G. Transparent conductors as solar energy materials: A panoramic review. Sol. Energy Mater. Sol. Cells 2007, 91, 1529–1598.
7. King, P.; Veal, T.D. Conductivity in transparent oxide semiconductors. J. Phys. Condens. Matter 2011, 23, 334214.
8. Calnan, S.; Tiwari, A.N. High mobility transparent conducting oxides for thin film solar cells. Thin Solid Films 2010, 518, 1839–1849.
9. Morales-Masis, M.; Nicolas, S.M.D.; Holovsky, J.; Wolf, S.D.; Ballif, C. Low temperature high-mobility amorphous IZO for silicon heterojunction solar cells. IEEE J. Photovolt. 2015, 5, 1340–1347.
10. Khachatryan, H.; Kim, D.J.; Kim, M.; Kim, H.-K. Roll-to-Roll fabrication of ITO thin film for flexible optoelectronics appli-cations: The role of post-annealing. Mater. Sci. Semicond. Process 2018, 88, 51–56.
11. Morales-Masis, M.; De Nicolas, S.M.; Holovsky, J.; De Wolf, S.; Ballif, C. Low-Temperature High-Mobility Amorphous IZO for Silicon Heterojunction Solar Cells. IEEE J. Photovoltaics 2015, 5, 1340–1347.
12. Martins, R.; Almeida, P.; Barquinha, P.; Pereira, L.; Pimentel, A.; Ferreira, I.; Fortunato, E. Electron transport and optical characterization amorphous indium zinc oxide films. J. Non Cryst. Solids 2006, 352, 1471–1474.
13. Taylor, M.P.; Readey, D.W.; Van Hest, M.F.A.M.; Teplin, C.W.; Alleman, J.L.; Dabney, M.S.; Gedvilas, L.M.; Keyes, B.M.; To, B.; Perkins, J.D.; et al. The remarkable thermal stability of amorphous In-Zn-O transparent conductors. Adv. Funct. Mater. 2008, 18, 3169–3178.
14. Park, Y.R.; Nam, E.-K.; Boo, J.-H.; Jung, D.-G.; Suh, S.-J.; Kim, Y.-S. Hydrogenated In-doped ZnO thin films for the new anode material of organic light-emitting devices: Synthesis and application test. Bull. Korean Chem. Soc. 2007, 28, 2396–2400.
15. Park, Y.R.; Kim, J.; Kim, Y.S. Growth and characteristics of hydrogenated In-doped ZnO thin films by pulsed DC magnetron sputtering. Appl. Surf. Sci. 2009, 256, 1589–1594.
16. Hosono, H.; Ueda, K. Transparent Conductive Oxides Springer Handbook of Electronic and Photonic Materials; 2017; pp 1391–1404.
17. Blakemore, J. S. Semiconducting and Other Major Properties of Gallium Arsenide. J.Appl. Phys. 1982, 53.
18. Dixit, R.; Gupta, S.; Kumar, P.; Sikarwar, S.; Yadav, B. C. Preparation and Properties of Transparent Conducting Oxide (TCOs) Thin Films : A Review. Int. J. Innov. Res. Sci. 2017, 6(2).
19. https://physics.stackexchange.com/questions/497212/why-is-the-carrier-distribution-density-of-states different-in-doped-semicondu
20. Sze, S. M. Physics of Semiconductor Devices, 2nd Edition.; John Wiley and Sons: New York,1981.
21. Fan, J. C. C.; Goodenough, J. B. X-ray Photoemission Spectroscopy Studies of Sn-doped Indium-oxide Films. J. Appl. Phys. 1977, 48 (8), 3524–3531.
22. Giusti, G. Deposition and Characterisation of Functional ITO Thin Films, University of Birmingham, 2011.
23. Ma, Z.; Li, Z.; Liu, K.; Ye, C.; Sorger, V. J. Indium-Tin-Oxide for High-Performance Electro-Optic Modulation. Nanophotonics 2015, 4 (1), 198–213.
24. Kasap, S.; Koughia, C.; Ruda, H. E. Springer Handbook of Electronic and PhotonicMaterials; Capper, P., Safa, K., Eds.; 2017.
25. Bellingham, J. R.; Phillips, W. A.; Adkins, C. J. Electrical and Optical Properties of Amorphous Indium Oxide. J. Phys. Condens. Matter 1990, 2 (28), 6207–6221.

26. Dixit, R.; Gupta, S.; Kumar, P.; Sikarwar, S.; Yadav, B. C. Preparation and Properties of Transparent Conducting Oxide (TCOs) Thin Films : A Review. Int. J. Innov. Res.Sci. 2017, 6 (2)
27. Kittel, C.; McEuen, P.; Sons, J. W. &. Introduction to Solid State Physics; John Wiley & Sons, 2019.
28. Hass, G.; Hunter, W. R.; Tousey, R. Influence of Purity, Substrate Temperature, and Aging Conditions on the Extreme Ultraviolet Reflectance of Evaporated Aluminum. J. Opt. Soc. Am. 1957, 47 (12), 1070–1073.
29. Dixon, S. C.; Scanlon, D. O.; Carmalt, C. J.; Parkin, I. P. N-Type Doped Transparent Conducting Binary Oxides: An Overview. J. Mater. Chem. C 2016, 4 (29), 6946–6961.
30. Kahn, A. Fermi level, work function, and vacuum level. Mater. Horiz. 2016, 3, 7–10
31. Braunstein, G.; Muraviev, A.; Saxena, H.; Dhere, N.; Richter, V.; Kalish, R. P Type Doping of Zinc Oxide by Arsenic Ion Implantation. Appl. Phys. Lett. 87 (19), 192103–1921033.
32. Yoshimura, R. Proceedings of the 35th Annual Technical Conference of the Society of Vacuum Coaters. 1992, 362.
33. Zeigler, Y.; Fischer, D. 49th Annual Technical Conference Proceedings. In Roll-to-roll Production of Thin Film Silicon Solar Cells on PET Film Substrate: A Smart Energy Option of the Future; Society of Vacuum Coaters: Washington, D.C., 2006; pp 609–613.
34. Menezes, C. Fourth E.C. Photovoltaic Solar Energy Conference : Proceedings of the International Conference; D. Reidel Pub. Co. ; Distributed in the U.S. by Kluwer Boston: Stresa, 1982.
35. Mollwo, E. The effect of hydrogen on the conductivity and luminescence of zinc oxide crystals. Z. Phys. 1954, 138, 478–488.
36. Thomas, D.G.; Lander, J.J. Hydrogen as a Donor in Zinc Oxide. J. Chem. Phys. 1956, 25, 1136–1142.
37. Van de Walle, C.G. Hydrogen as a Cause of Doping in Zinc Oxide. Phys. Rev. Lett. 2000, 85, 1012–1015.
38. Kohan, F.; Ceder, G.; Morgan, D.; Van de Walle, C.G. First-principles study of native point defects in ZnO. Phys. Rev. B 2000, 61, 15019. [Google Scholar] [CrossRef][Green Version]
39. Hofmann, D.M.; Hofstaetter, A.; Leiter, F.; Zhou, H.; Henecker, F.; Meyer, B.K.; Orlinskii, S.B.; Schmidt, J.; Baranov, P.G. Hydrogen: A Relevant Shallow Donor in Zinc Oxide. Phys. Rev. Lett. 2002, 88, 045504.
40. Cox, S.F.J.; Davis, E.A.; Cottrell, S.P.; King, P.J.C.; Lord, J.S.; Gil, J.M.; Alberto, H.V.; Vilão, R.C.; Duarte, J.P.; De Campos, N.A.; et al. Experimental Confirmation of the Predicted Shallow Donor Hydrogen State in Zinc Oxide. Phys. Rev. Lett. 2001, 86, 2601–2604.
41. Van de Walle, C.G. Hydrogen as a shallow centre in semiconductors and oxides. Phys. Status Solidi b 2003, 235, 89–95.
42. Hosono, H.; Ueda, K. Transparent Conductive Oxides. In Springer Handbook of Electronic and Photonic Materials; Springer: Berlin, Germany, 2017.
43. Yan, X.; Tian, L.; Tan, X.; Zhou, M.; Liu, L.; Chen, X. Modifying oxide nanomaterials' properties by hydrogenation. MRS Commun. 2016, 6, 192–203.
44. Li, T.; Ong, C.S.; Herng, T.S.; Yi, J.; Bao, N.; Xue, J.M.; Feng, Y.P.; Ding, J. Surface ferromagnetism in hydrogenated-ZnO film. Appl. Phys. Lett. 2011, 98.
45. Park, J.K.; Kwon, H.-J.; Lee, C.E. NMR Observation of Mobile Protons in Proton-Implanted ZnO Nanorods. Sci. Rep. 2016, 6, 23378.
46. Robaina, O.V.; Cabrera, A.F.; Meyer, M.; Romano, R.M.; Cruz, A.F.; Torres, C.E.R. Room-Temperature Ferromagnetism Induced by High-Pressure Hydrogenation of ZnO. J. Phys. Chem. C 2019, 123, 19851–19861.
47. Esquinazi, P.; Hergert, W.; Spemann, D.; Setzer, A.; Ernst, A. Defect-Induced Magnetism in Solids. IEEE Trans. Magn. 2013, 49, 4668–4674.
48. Salimian, A.; Hasnath, A.; Anguilano, L.; Onwukwe, U.; Aminishahsavarani, A.; Sachez, C.; Upadhyaya, H. Highly Conductive Zinc Oxide Based Transparent Conductive Oxide Films Prepared Using RF Plasma Sputtering Under Reducing Atmosphere. Coatings 2020, 10, 472.
49. Song, S.; Yang, T.; Liu, J.; Xin, Y.; Li, Y.; Han, S. Rapid Thermal Annealing of ITO Films. Appl. Surf. Sci. 2011, 257 (16), 7061–7064.
50. Vatakketath, R. K. Investigation on the Transparent Conducting Oxide (TCO) Material Used in CIGS Thin Film Solar Cell in Midsummer AB, Uppsala University, 2020.
51. Shigesato, Y.; Takaki, S.; Haranoh, T. Electrical and Structural Properties of Low Resistivity Tin-Doped Indium Oxide Films. J. Appl. Phys. 1992, 71 (7), 3356–3364.

52. Suzuki, A.; Matsushita, T.; Aoki, T.; Yoneyama, Y.; Okuda, M. Pulsed Laser Deposition of Transparent Conducting Indium Tin Oxide Films in Magnetic Field Perpendicular to Plume. Jpn. J. Appl. Phys. 2001, 40 (Part 2, No. 4B), L401–L403.
53. Gondoni, P. Nanostructured Transparent Conductive Oxides for Photovoltaic Applications, Politecnico di Milano, 2014.
54. Langmuir, I. Oscillations in Ionized Gases. *Proc. Natl. Acad. Sci.* **1928**, *14*, 627–637.
55. Roth, J. R. *Industrial Plasma Engineering Volume 1: Principles*; Institute of Physics Publishing: Knoxville, 1995; Vol. 1.
56. Budtz-jørgensen, C. V. Studies of Electrical Plasma Discharges, Aarhus University, 2001.
57. Llewellyn-Jones, F. The Glow Discharge and an Introduction to Plasma Physics. *Am. J. Phys.* **1967**, *35* (5), 453.
58. https://www.plasma-universe.com/electric-glow-discharge/
59. Chen, F. F. *Erratum to: Introduction to Plasma Physics and Controlled Fusion*; 2018.
60. Jeon, M.; Kamisako, K. Synthesis and Characterization of Silicon Nanowires Using Tin Catalyst for Solar Cells Application. *Mater. Lett.* **2009**, *63* (9), 777–779. ??
61. Depla, D.; Mahieu, S.; Greene, J. E. Sputter Deposition Processes. In *Handbook of deposition technologies for films and coatings : science, applications and technology*; Martin, P. M., Ed.; Elsevier: Oxford, 2010; pp 253–296.
62. Lieberman, M. A.; Lichtenberg, A. J. *Principles of Plasma Discharges and Materials Processing*, 2nd Ed.; Wiley, 1994.
63. http://www.glow-discharge.com/rf_vs_dc.htm 91
64. Chapman, B. *Glow Discharge Processes: Sputtering and Plasma Etching*; Wiley, 1980.
65. Waite, M. M.; Chester, W.; Glocker, D. a; Incorporated, I.; York, N. Sputtering Sources. *Soc. Vac. Coaters* **2010**, 42–50.
66. [(Greene, J. E. Review Article: Tracing the Recorded History of Thin-Film Sputter Deposition: From the 1800s to 2017. *J. Vac. Sci. Technol. A Vacuum, Surfaces, Film.* **2017**, *35* (5), 05C204.
67. Parsons, R. II-4 - Sputter Deposition Processes; Vossen, J. L., Kern, W. B. T.-T. F. P., Eds.; Academic Press: San Diego, 1991; pp 177–208.
68. Glocker, D. A.; Shah, S. I. *Handbook of Thin Film Process Technology*; Handbook of Thin Film Process Technology; Institute of Physics Pub., 2002.
69. Maurya, D.; Sardarinejad, A.; Alameh, K. Recent Developments in R.F. Magnetron Sputtered Thin Films for PH Sensing Applications—An Overview. *Coatings* **2014**, *4* (4), 756–771.
70. Svadkovski, I. V.; Golosov, D. A.; Zavatskiy, S. M. Characterisation Parameters for Unbalanced Magnetron Sputtering Systems. *Vacuum* **2002**, *68* (4), 283–290.
71. Petrov, I.; Adibi, F.; Greene, J. E.; Sproul, W. D.; Münz, W. -D. Use of an Externally Applied Axial Magnetic Field to Control Ion/Neutral Flux Ratios Incident at the Substrate during Magnetron Sputter Deposition. *J. Vac. Sci. Technol. A* **1992**, *10* (5), 3283–3287.
72. Window, B.; Savvides, N. Unbalanced Dc Magnetrons as Sources of High Ion Fluxes. *J. Vac. Sci. Technol. A* **1986**, *4* (3), 453–456.
73. Kelly, P. J.; Arnell, R. D. Magnetron Sputtering: A Review of Recent Developments and Applications. *Vacuum* **2000**, *56* (3), 159–172.
74. Tchenka, A.; Agdad, A.; Vall, M.C.S.; Hnawi, S.K.; Narjis, A.; Nkhaili, L.; Ibnouelghazi, E.; Ech-Chamikh, E. Effect of RF Sputtering Power and Deposition Time on Optical and Electrical Properties of Indium Tin Oxide Thin Film. *Adv. Mater. Sci. Eng.* **2021**, *2021*, e5556305.
75. Abdulameer, M. Simulation of plasma properties in magnetron sputtering with Kr gas. *Int. J. Appl. Or Innov. Eng. Manag.* **2013**, *2*, 290–296.
76. Powell, R.A.; Rossnagel, S.M. (Eds.) Chapter 2 Physics of sputtering. In *Thin Films*; Elsevier: Amsterdam, The Netherlands, 1999; Volume 26, pp. 23–49
77. [Oechsner, H. Sputtering—A review of some recent experimental and theoretical aspects. *Appl. Phys.* **1975**, *8*, 185–198.
78. Fridman, A. *Plasma Chemistry*; Cambridge University Press: Cambridge, UK, 2008.
79. 'The Technology - Plasma Quest'. https://www.plasmaquest.co.uk/the-technology/ (accessed Apr. 06, 2022).

80. Kenmotsu, T.; Wada, M.; Hyakutake, T.; Muramoto, T.; Nishida, M. Enhanced sputtering yields of carbon due to accumulation of low-energy Xe ions. *Nucl. Instrum. Methods Phys. Res. Sect. B Beam Interact. Mater. At.* **2009**, *267*, 1717–1720.
81. Yagisawa, T.; Makabe, T. Modeling of dc magnetron plasma for sputtering: Transport of sputtered copper atoms. *J. Vac. Sci. Technol. Int. J. Devoted Vac. Surf. Film* **2006**, *24*, 908.
82. Wehner, G. Influence of the Angle of Incidence on Sputtering Yields. *J. Appl. Phys.* **1959**, *30*, 1762–1765.
83. van Hattum, E.D.; Palmero, A.; Arnoldbik, W.M.; Rudolph, H.; Habraken, F.H.P.M. On the ion and neutral atom bombardment of the growth surface in magnetron plasma sputter deposition. *Appl. Phys. Lett.* **2007**, *91*, 171501.
84. Stamate, E. Spatially Resolved Optoelectronic Properties of Al-Doped Zinc Oxide Thin Films Deposited by Radio-Frequency Magnetron Plasma Sputtering Without Substrate Heating. *Nanomaterials* **2019**, *10*, 14.
85. Bairagi, S.; Järrendahl, K.; Eriksson, F.; Hultman, L.; Birch, J.; Hsiao, C.-L. Glancing Angle Deposition and Growth Mechanism of Inclined AlN Nanostructures Using Reactive Magnetron Sputtering. *Coatings* **2020**, *10*, 768.
86. Güttler, D.; Abendroth, B.; Grötzschel, R.; Möller, W.; Depla, D. Mechanisms of target poisoning during magnetron sputtering as investigated by real-time in situ analysis and collisional computer simulation. *Appl. Phys. Lett.* **2004**, *85*, 6134–6136.
87. Tian-Ye, N.; Jin-Xiang, C.; Lei, L.; Jin-Ying, L.; Yan, W.; Liang, W.; You, L. A comparison among optical emission spectroscopic methods of determining electron temperature in low pressure argon plasmas. *Chin. Phys.* **2007**, *16*, 2757–2763.
88. Lewis, B.G.; Paine, D.C. Applications and processing of transparent conducting oxides. *MRS Bull*. **2000**, *25*, 22–27.
89. Crintea, D.L.; Czarnetzki, U.; Iordanova, S.; Koleva, I.; Luggenhölscher, D. Plasma diagnostics by optical emission spectroscopy on argon and comparison with Thomson scattering. *J. Phys. D* **2009**, *42*, 045208.
90. Zhu, X.; Pu, Y. Optical emission spectroscopy in low-temperature plasmas containing argon and nitrogen: Determination of the electron temperature and density by the line-ratio method. *J. Phys. D* **2010**, *43*, 403001.
91. Trevizan, L.C.; Santos, D., Jr.; Samad, R.E.; Vieira, N.D., Jr.; Nunes, L.C.; Rufini, I.A.; Krug, F.J. Evaluation of laser induced breakdown spectroscopy for the determination of micronutrients in plant materials. *Spectrochim. Acta Part B Atomic Spectrosc.* **2009**, *64*, 369–377.
92. Unnikrishnan, V.K.; Alti, K.; Nayak, R.; Bernard, R.; Khetarpal, N.; Kartha, V.B.; Santhosh, C.; Gupta, G.P.; Suri, B.M. Optimized LIBS setup with echelle spectrograph-ICCD system for multi-elemental analysis. *J. Instrum.* **2010**, *5*, P04005.
93. Bastiaans, G.J.; Mangold, R.A. The calculation of electron density and temperature in Ar spectroscopic plasmas from continuum and line spectra. *Spectrochim. Acta Part B Atomic Spectrosc.* **1985**, *40*, 885–892.
94. Iordanova, S.; Koleva, I. Optical emission spectroscopy diagnostics of inductively-driven plasmas in argon gas at low pressures. *Spectrochim. Acta Part B Atomic Spectrosc.* **2007**, *62*, 344–356.
95. Gurnett, D.A.; Bhattacharjee, A. *Introduction to Plasma Physics: With Space and Laboratory Applications*; Cambridge University press: Cambridge, UK, 2005.
96. Bellan, P.M. *Fundamentals of Plasma Physics*; Cambridge University Press: Cambridge, UK, 2008.
97. Unnikrishnan, V.K.; Alti, K.; Kartha, V.B.; Santhosh, C.; Gupta, G.P.; Suri, B.M. Measurements of plasma temperature and electron density in laser-induced copper plasma by time-resolved spectroscopy of neutral atom and ion emissions. *Pramana* **2010**, *74*, 983–993.
98. McWhirter, R.W.P. *Plasma Diagnostic Techniques*; Huddlestone, R.H., Leonard, S.L., Eds.; Academic Press: Academic Press, New York, NY, USA, 1965.
99. Diwakar, P.; Hahn, D. Study of early laser-induced plasma dynamics: Transient electron density gradients via Thomson scattering and Stark Broadening, and the implications on laser-induced breakdown spectroscopy measurements. *Spectrochim. Acta Part B Atomic Spectrosc.* **2008**, *63*, 1038–1046.
100. Shaikh, N.M.; Rashid, B.; Hafeez, S.; Jamil, Y.; Baig, M.A. Measurement of electron density and temperature of a laser-induced zinc plasma. *J. Phys. D* **2006**, *39*, 1384.

101. Tawfik, W.; Mohamed, Y.; Askar, A. Study of the matrix effect on the plasma characterization of heavy elements in soil sediments using LIBS with a portable Echelle spectrometer. *Prog. Phys.* **2007**, *1*, 46–52.
102. Hong, Y.J.; Kwon, G.C.; Cho, G.; Shin, H.M.; Choi, E.H. Measurement of electron temperature and density using stark broadening of the coaxial focused plasma for extreme ultraviolet lithography. *IEEE Trans. Plasma Sci.* **2010**, *38*, 1111–1117.
103. Diao, C.Y.; Chen, C.S.; Man, B.Y.; Wang, C.; Fu, H.B. Influence of distances between the lens and the target on the characteristic of laser induced lead plasma. *Eur. Phys. J. D* **2011**, *63*, 123–128.
104. Konjević, N.; Lesage, A.; Fuhr, J.R.; Wiese, W.L. Experimental Stark widths and shifts for spectral lines of neutral and ionized atoms (a critical review of selected data for the period 1989 through 2000). *J. Phys. Chem. Ref. Data* **2002**, *31*, 819–927.
105. Wyszecki, G.; Stiles, W.S. *Color Science Concepts and Methods, Quantative Data and Formulae*, 2nd Ed.; Wiley: New York, NY, USA, 1982.
106. Conrads, H.; Schmidt, M. Plasma generation and plasma sources. *Plasma Sources Sci. Technol*. **2000**, *9*, 441.
107. Alder, J.; Bombelka, R.; Kirkbright, G. Electronic excitation and ionization temperature measurements in a high frequency inductively coupled argon plasma source and the influence of water vapor on plasma parameters. *Spectrochim. Acta Part B Atomic Spectrosc.* **1980**, *35*, 163–175.
108. Bogaerts, A.; Neyts, E.; Gijbels, R.; Van der Mullen, J. Gas discharge plasmas and their applications. *Spectrochim. Acta Part B Atomic Spectrosc.* **2002**, *57*, 609–658.
109. Wagatsuma, K.; Hirokawa, K. Characterization of atomic emission lines from argon, neon, and nitrogen glow discharge plasmas. Anal. Chem. 1985, 57, 2901–2907.
110. Angeli, J.; Bengtson, A.; Bogaerts, A.; Hoffmann, V.; Hodoroaba, V.D.; Steers, E. Glow discharge optical emission spectrometry: Moving towards reliable thin film analysis—A short review. J. Anal. Atomic Spectrom. 2003, 18, 670–679.
111. Ablikim, M.; An, Z.H.; Bai, J.Z.; Berger, N.; Bian, J.M.; Cai, X.; Cao, G.F.; Cao, X.X.; Chang, J.F.; Chen, C.; et al. Design and construction of the BESIII detector. Nucl. Inst. Methods Phys. Res. 2010, 614, 345–399.
112. Wang, F.H.; Yang, C.F.; Liou, J.C.; Chen, I.C. Effects of hydrogen on the optical and electrical characteristics of the sputter-deposited Al_2O_3-doped zno thin films. J. Nanomater. 2014, 2014, 857641.
113. Palmero, A.; van Hattum, E.; Arnoldbik, W.; Habraken, F. Argon plasma modelling in a RF magnetron sputtering system. Surf. Coat. Technol. 2004, 188–189, 392–398.
114. Christie, D.J. Target material pathways model for high power pulsed magnetron sputtering. J. Vac. Sci. Technol. A 2005, 23, 330–335.
115. Kolev, I. Particle-In-Cell-Monte-Carlo Collisions Simulations for a Direct Current Planar Magnetron Discharge. Ph.D. Thesis, University of Antwerp, Antwerp, Belgium, 2007.
116. Brenning, N.; Huo, C.; Lundin, D.; Raadu, M.; Vitelaru, C.; Stancu, G.; Minea, T.; Helmersson, U. Understanding deposition rate loss in high power impulse magnetron sputtering: I. Ionization-driven electric fields. Plasma Sources Sci. Technol. 2012, 21, 025005.
117. Huo, C.; Raadu, M.; Lundin, D.; Gudmundsson, J.; Anders, A.; Brenning, N. Gas rarefaction and the time evolution of long high-power impulse magnetron sputtering pulses. Plasma Sources Sci. Technol. 2012, 21, 045004.
118. Shidoji, E.; Ohtake, H.; Nakano, N.; Makabe, T. Two-Dimensional Self-Consistent Simulation of a DC Magnetron Discharge. Jpn. J. Appl. Phys. 1999, 38, 2131–2136.
119. Kolev, I.; Bogaerts, A. Numerical Models of the Planar Magnetron Glow Discharges. Contrib. Plasma Phys. 2004, 44, 582–588.
120. Sheridan, T.; Goeckner, M.; Goree, J. Pressure dependence of ionization efficiency in sputtering magnetrons. Appl. Phys. Lett. 1990, 57, 2080–2082.
121. Goeckner, M.; Goree, J.; Sheridan, T. Monte Carlo simulation of ions in a magnetron plasma. IEEE Trans. Plasma Sci. 1991, 19, 301–308.

122. Passoth, E.; Behnke, J.; Csambal, C.; Tichý, M.; Kudrna, P.; Golubovskii, Y.; Porokhova, I. Radial behaviour of the electron energy distribution function in the cylindrical magnetron discharge in argon. J. Phys. D Appl. Phys. 1999, 32, 2655–2665.
123. Porokhova, I.; Golubovskii, Y.; Bretagne, J.; Tichy, M.; Behnke, J. Kinetic simulation model of magnetron discharges. Phys. Rev. E 2001, 63, 056408.
124. Porokhova, I.; Golubovskii, Y.; Behnke, J. Anisotropy of the electron component in a cylindrical magnetron discharge. I. Theory of the multiterm analysis. Phys. Rev. E 2005, 71, 066406.
125. Porokhova, I.; Golubovskii, Y.; Behnke, J. Anisotropy of the electron component in a cylindrical magnetron discharge. II. Application to real magnetron discharge. Phys. Rev. E 2005, 71, 066407.
126. Birdsall, C. Particle-in-cell charged-particle simulations, plus Monte Carlo collisions with neutral atoms, PIC-MCC. IEEE Trans. Plasma Sci. 1991, 19, 65–85.
127. Revel, A.; Minea, T.; Costin, C. 2D PIC-MCC simulations of magnetron plasma in HiPIMS regime with external circuit. Plasma Sources Sci. Technol. 2018, 27, 105009.
128. Tozer, B. Rotating plasma. Proc. Inst. Electr. Eng. 1965, 112, 218.
129. Wasa, K.; Hayakawa, S. Formation of Rotating Plasma in Crossed Field. J. Phys. Soc. Jpn. 1966, 21, 738–743.
130. Wilcox, J.; Cooper, W.; DeSilva, A.; Spillman, G.; Boley, F. Swirls Produced in a “Crowbarred” Rotating Plasma. J. Appl. Phys. 1962, 33, 2714–2715.
131. Anders, A. Localized heating of electrons in ionization zones: Going beyond the Penning-Thornton paradigm in magnetron sputtering. Appl. Phys. Lett. 2014, 105, 244104.
132. Panjan, M.; Loquai, S.; Klemberg-Sapieha, J.; Martinu, L. Non-uniform plasma distribution in dc magnetron sputtering: Origin, shape and structuring of spokes. Plasma Sources Sci. Technol. 2015, 24, 065010.
133. Anders, A.; Yang, Y. Direct observation of spoke evolution in magnetron sputtering. Appl. Phys. Lett. 2017, 111, 064103.
134. Anders, A.; Yang, Y. Plasma studies of a linear magnetron operating in the range from DC to HiPIMS. J. Appl. Phys. 2018, 123, 043302.
135. Andersson, J.; Ni, P.; Anders, A. Smoothing of Discharge Inhomogeneities at High Currents in Gasless High Power Impulse Magnetron Sputtering. IEEE Trans. Plasma Sci. 2014, 42, 2856–2857.
136. Arcos, T.; Layes, V.; Gonzalvo, Y.; Gathen, V.; Hecimovic, A.; Winter, J. Current–voltage characteristics and fast imaging of HPPMS plasmas: Transition from self-organized to homogeneous plasma regimes. J. Phys. D Appl. Phys. 2013, 46, 335201.
137. Šlapanská, M.; Hecimovic, A.; Gudmundsson, J.; Hnilica, J.; Breilmann, W.; Vašina, P.; von Keudell, A. Study of the transition from self-organised to homogeneous plasma distribution in chromium HiPIMS discharge. J. Phys. D Appl. Phys. 2020, 53, 155201.
138. Hecimovic, A.; Corbella, C.; Maszl, C.; Breilmann, W.; von Keudell, A. Investigation of plasma spokes in reactive high power impulse magnetron sputtering discharge. J. Appl. Phys. 2017, 121, 171915.
139. Depla, D.; Mahieu, S. Reactive Sputter Deposition; Springer Series in Materials Science; Springer: Berlin/Heidelberg, Germany, 2008; Volume 109.
140. Marcak, A.; Corbella, C.; de los Arcos, T.; von Keudell, A. Note: Ion-induced secondary electron emission from oxidized metal surfaces measured in a particle beam reactor. Rev. Sci. Instrum. 2015, 86, 106102.
141. Yang, Y.; Zhou, X.; Liu, J.; Anders, A. Evidence for breathing modes in direct current, pulsed, and high power impulse magnetron sputtering plasmas. Appl. Phys. Lett. 2016, 108, 034101.
142. Yang, Y.; Tanaka, K.; Liu, J.; Anders, A. Ion energies in high power impulse magnetron sputtering with and without localized ionization zones. Appl. Phys. Lett. 2015, 106, 124102.
143. Anders, A.; Ni, P.; Andersson, J. Drifting Ionization Zone in DC Magnetron Sputtering Discharges at Very Low Currents. IEEE Trans. Plasma Sci. 2014, 42, 2578–2579.
144. Held, J.; Maaß, P.; Gathen, V.; Keudell, A. Electron density, temperature and the potential structure of spokes in HiPIMS. Plasma Sources Sci. Technol. 2020, 29, 025006.
145. Schmidhuber, J. Deep learning in neural networks: An overview. Neural Netw. 2015, 61, 85–117.

146. Hinton, G.; Rumelhart, D. Neural Network Architectures for Artificial Intelligence; American Society for Artificial Intelligence: San Mateo, CA, USA, 1988.
147. Introduction to Convolutional Neural Networks. 2017. Available online: **https://cs.nju.edu.cn/wujx/paper/CNN.pdf**
148. Lecun, Y. Gradient Based Learning for Document Recognition. 1998. Available online: **http://yann.lecun.com/exdb/publis/pdf/lecun-01a.pdf**
149. He, K.; Zhang, X.; Ren, S.; Sun, J. Spatial Pyramid Pooling in Deep Convolutional Networks for Visual Recognition. *IEEE Trans. Pattern Anal. Mach. Intell.* **2015**, *37*, 1904–1916.
150. Suárez-Paniagua, V.; Segura-Bedmar, I. Evaluation of pooling operations in convolutional architectures for drug-drug interaction extraction. *BMC Bioinform.* **2018**, *19*, 39–47.
151. Cottrell, M.; Olteanu, M.; Rossi1, F.; Villa-Vialaneix, N. Self-organizing maps, theory and applications. *Rev. Investig. Oper.* **2018**, *39*, 1–22.
152. Fridman. Measurements with the Model 4200-SCS. Appl. Note 2007, No. 2475, 2005 2007.
153. Valdes, L. B. Resistivity Measurements on Germanium for Transistors. Proc. IRE 1954, 42 (2), 420–427
154. Illinois, E. GT2 - Four Point Probe Correction Factor a (thickness),” Theory and Fabrication of Integrated Circuits. http://fabweb.ece.illinois.edu/gt/gt/gt2.aspx (accessed 2022-08-19).
155. Gutiérrez, M. P.; Li, H.; Patton, J. Thin Film Surface Resistivity. 2002, 0–24.
156. Vo,K.Spectrophotometry. https://chem.libretexts.org/Core/Physical_and_Theoretical_Chemistry/Kinetics/Reaction _Rates/Experimental_Determination_of_Kinetcs/Spectrophotometry (accessed 2022-08-19).
157. Multispectral Colorimetric system (diagram)
158. Tkachenko, N. V. Chapter 3 - Lasers for Spectroscopy Applications; TKACHENKO, N. V. B. T.-O. S., Ed.; Elsevier Science: Amsterdam, 2006; pp 39–59.
159. Instruments, N. How A Profilometer Works. http://www.nanoscience.com/technology/optical-profiler-technology/how-profilometer- works (accessed 2017-05-01).
160. Reimer, L. Introduction. In Scanning Electron Microscopy; Springer Berlin Heidelberg: Berlin, 1998; pp 1–12.
161. Sandeman, K.; Coombe, P. Raman Spectroscopy and Scanning Electron Microscopy. https://doitpoms.admin.cam.ac.uk/ (accessed 2017-05-05).
162. Everhart, T. E.; Thornley, R. F. M. Wide-Band Detector for Micro-Microampere Low-Energy Electron Currents. J. Sci. Instrum. 1960, 37 (7), 246–248.
163. Echlin, P. Handbook of Sample Preparation for Scanning Electron Microscopy and X-Ray Microanalysis, 1st Ed.; Springer New York, N, 2009.
164. https://en.wikipedia.org/wiki/Energy-dispersive_X-ray_spectroscopy#/media/File:EDX-scheme.svg
165. Qayyum, A.; Ikram, M.; Zakaullah, M.; Waheed, A.; Murtaza, G.; Ahmad, R.; Majeed, A.; Khattak, N.A.D.; Mansoor, K.; Chaudhary, K.A. Characterization of argon plasma by use of optical emission spectroscopy and Langmuir probe measurements. *Int. J. Mod. Phys. B* **2003**, *17*, 2749–2759.
166. Kwak, D.; Park, M.; Sung, Y. Discharge power dependence of structural and electrical properties of Al-doped ZnO conducting film by magnetron sputtering (for PDP). *Vacuum* **2008**, *83*, 113–118.
167. Yan, L.; Rath, J.; Schropp, R. Electrical properties of vacuum-annealed titanium-doped indium oxide films. *Appl. Surf. Sci.* **2011**, *257*, 9461–9465.
168. Sultan, M.S. Effect of gas pressure and flow rate on the plasma power and deposition rate in magnetron sputtering system. *Res. J. Nanosci. Eng.* **2018**, *2*, 1–8.
169. Salimian, A.; Haghpanahan, R.; Hasnath, A.; Upadhyaya, H. Optical Analysis of RF Sputtering Plasma through Colour Characterization. *Coatings* **2019**, *9*, 315
170. Sheng, J.; Lee, H.-J.; Oh, S.; and Park, J.S. Flexible and high-performance amorphous indium Zinc oxide thin-film transistor using low-temperature atomic layer deposition. *ACS Appl. Mater. Interfaces* **2016**, *8*, 33821–33828
171. Hautier, G.; Miglio, A.; Waroquiers, D.; Rignanese, G.-M.; Gonze, X. How does chemistry influence electron effective mass in oxides? A high-throughput computational analysis. *Chem. Mater.* **2014**, *26*, 5447–5458.

172. Wallinga, J.; Arnold Bik, W.M.; Vredenberg, A.M.; Schropp, R.E.I.; van der Weg, W.F. Reduction of Tin Oxide by Hydrogen Radicals. *J. Phys. Chem. B* **1998**, *102*, 6219.
173. De Wit, J.H.W. Electrical properties of In2O3. *J. Solid State Chem.* **1973**, *8*, 2, 142.
174. Dewit, J.H.W.; Vanunen, G.; Lahey, M. Electron concentration and mobility in In2O3. *J. Phys. Chem. Solids* **1997**, *38*, 819–824.
175. Luo, S.; Kohiki, S.; Okada, K.; Kohno, A.; Tajiri, T.; Arai, M.; Shoji, F. Effects of Hydrogen in Working Gas on Valence States of Oxygen in Sputter-Deposited Indium Tin Oxide Thin Films. *Acs Appl. Mater. Interfaces* **2010**, *2*, 663–668.
176. Dixon, S.C.; Scanlon, D.O.; Carmalt, C.J.; Parkin**,** I.P. *n*-Typed doped transparent conductive binary oxides: An overview. *J. Mater. Chem. C* **2016**, *4*, 6946–6961.
177. Van de Walle, C.G. Hydrogen as a Cause of Doping in Zinc Oxide. *Phys. Rev. Lett.* **2000**, *85*, 1012–1015.
178. Hofmann, D.M.; Hofstaetter, A.; Leiter, F.; Zhou, H.; Henecker, F.; Meyer, B.K.; Baranov, P.G. Hydrogen: A Relevant Shallow Donor in Zinc Oxide. Physical Review Letters, **2002**, *88*, 045504.
179. Cox, S.F.J.; Davis, E.A.; Cottrell, S.P.; King, P.J.C.; Lord, J.S.; Gil, J.M.; Alberto, H.V.; Vilo, R.C.; Piroto Duarte, J.; Ayres de Campos, N.; et al. Experimental Confirmation of the Predicted Shallow Donor Hydrogen State in Zinc Oxide. *Phys. Rev. Lett.* **2001**, *86*, 2601–2604.
180. Van de Walle, C.G. Hydrogen as a shallow center in semiconductors and oxides. *Phys. Status Solidi* **2003**, *235*, 89–95.
181. Knewstubb, P.F.; Tickner, A.W. Mass spectrometry of ions in glow discharges. I. apparatus and its application to the positive column in rare gases. *J. Chem. Phys.* **1962**, *36*, 674.
182. Gordon, M.H.; Kruger, C.H. Non-equilibrium effects of diluent addition in a recombining argon plasma. *Phys. Fluids B: Plasma Phys.* **1993**, *5*, 1014.
183. Meulenbroeks, R.F.G.; van Beek, A.J.; van Helvoort, A.J.G.; van de Sanden, M.C.M.; Schram, D.C. Argon-hydrogen plasma jet investigated by active and passive spectroscopic means. *Phys. Rev. E* **1994**, *49*, 4397– 4406.
184. Mason, R.S.; Miller, P.D.; Mortimer, I.P. Anomalous loss of ionization in argon-hydrogen plasma studied by fast flow glow discharge mass spectrometry. *Phys. Rev. E* **1997**, *55*, 7462–7472.
185. Tabares, F.L.; Tafalla, D. Sputtering of metallic walls in Ar/H2 direct current glow discharges at room temperature. *J. Vac. Sci. Technol. A* **1996**, *14*, 3087–3091.
186. Budtz-Jorgensen, C.V.; Kringhoj, P.; Bottiger, J. The critical role of hydrogen for physical sputtering with Ar–H2 glow discharges. *Surf. Coat. Technol.* **1999**, *116*, 938–943.
187. Smithwick, R.W., III; Lynch, D.W.; Franklin, J.C. Relative ion yields measured with a high-resolution glow discharge mass spectrometer operated with an argon/hydrogen mixture. *J. Am. Soc. Mass Spectrom.* **1993**, *4*, 278–285.
188. Saito, M. The relationship between relative sensitivity factors and ionization potential in dc glow discharge mass spectrometry using Ar/0.2 vol.% H2 mixture. *Anal. Chim. Acta.* **1997**, *355*, 129–134.
189. Saikia, P.; Saikia, B.K.; Bhuyan, H. Study on the effect of hydrogen addition on the variation of plasma parameters of argon-oxygen magnetron glow discharge for synthesis of TiO2 films. *Aip Adv.* **2016**, *6*, 045206(1–9).
190. Kakati, H.; Pal, A.R.; Bailung, H.; Chutiya, J. Effect of oxygen on the characteristics of radio frequency planar magnetron sputtering plasma used for aluminum oxide depositionJ. *Appl. Phys.* **2007**, *101*, 083304(1– 7).
191. Coburn, J.W.; Chen, M. Optical emission spectroscopy of reactive plasmas: A method for correlating emission intensities to reactive particle density. *J. Appl. Phys.* **1980**, *51*, 3134–3136.
192. Lavrov, B.P.; Pipa, A.V.; Röpcke, J. On determination of the degree of dissociation of hydrogen in non-equilibrium plasmas by means of emission spectroscopy: I. The collision-radiative model and numerical experiments. *Plasma Sources Sci. Technol.* **2006**, *15*, 135–146.
193. Clay, K.J.; Speakman, S.P.; Amaratunga, G.A.J.; Silva, S.R.P. Characterization of a-C: H: N deposition from CH4/N2 rf plasmas u
194. Salimian, A.; Hasnath, A.; Anguilano, L.; Onwukwe, U.; Aminishahsavarani, A.; Sachez, C.; Upadhyaya, H. Highly Conductive Zinc Oxide Based Transparent Conductive Oxide Films Prepared Using RF Plasma Sputtering Under Reducing Atmosphere. Coatings **2020**, 10, 472.

195. Hautier, G.; Miglio, A.; Waroquiers, D.; Rignanese, G.-M.; Gonze, X. How Does Chemistry Influence Electron Effective Mass in Oxides? A High-Throughput Computational Analysis. Chem. Mater. **2014**, 26, 5447–5458.
196. Wallinga, J.; Arnoldbik, W.M.; Vredenberg, A.M.; Schropp, R.E.I.; Van Der Weg, W.F. Reduction of Tin Oxide by Hydrogen Radicals. J. Phys. Chem. B **1998**, 102, 6219–6224.
197. De Wit, J. Electrical properties of In_2O_3. J. Solid State Chem. **1973**, 8, 142–149.
198. Dewit, J.H.W.; Vanunen, G.; Lahey, M. Electron concentration and mobility in In_2O_3. J. Phys. Chem. Solids **1997**, 38, 819–824.
199. Gordon, M.H.; Kruger, C.H. Non-equilibrium effects of diluent addition in recombining argon plasma. Phys. Fluids B Plasma Phys. **1993**, 5, 1014.
200. Meulenbroeks, R.F.G.; Van Beek, A.J.; Van Helvoort, A.J.G.; Van De Sanden, M.C.M.; Schram, D.C. Argon-hydrogen plasma jet investigated by active and passive spectroscopic means. Phys. Rev. E **1994**, 49, 4397–4406.
201. Mason, R.S.; Miller, P.D.; Mortimer, I.P. Anomalous loss of ionization in argon-hydrogen plasma studied by fast flow glow discharge mass spectrometry. Phys. Rev. E **1997**, 55, 7462–7472.
202. Tabares, F.L.; Tafalla, D. Sputtering of metallic walls in Ar/H2 direct current glow discharges at room temperature. J. Vac. Sci. Technol. A **1996**, 14, 3087–3091.
203. Budtz-Jorgensen, C.V.; Kringhoj, P.; Bottiger, J. The critical role of hydrogen for physical sputtering with Ar–H2 glow dis-charges. Surf. Coat. Technol. **1999**, 116, 938–943.
204. Smithwick, R.W., III; Lynch, D.W.; Franklin, J.C. Relative ion yields measured with a high-resolution glow discharge mass spectrometer operated with an argon/hydrogen mixture. J. Am. Soc. Mass Spectrom. **1993**, 4, 278–285.
205. Knewstubb, P.F.; Tickner, A.W. Mass Spectrometry of Ions in Glow Discharges. I. Apparatus and Its Application to the Positive Column in Rare Gases. J. Chem. Phys. **1962**, 36, 674–683.
206. Luo, S.; Kohiki, S.; Okada, K.; Kohno, A.; Tajiri, T.; Arai, M.; Ishii, S.; Sekiba, D.; Mitome, M.; Shoji, F. Effects of Hydrogen in Working Gas on Valence States of Oxygen in Sputter-Deposited Indium Tin Oxide Thin Films. ACS Appl. Mater. Interfaces **2010**, 2, 663–668.
207. Bales, G.S.; Bruinsma, R.; Eklund, E.A.; Karunasiri, R.P.U.; Rudnick, J.; Zangwill, A. Growth and Erosion of Thin Solid Films. Science **1990**, 249, 264–268.
208. Horkel, M.; van Aeken, K.; Eisenmenger-Sittner, C.; Depla, D.; Mahieu, S.; Leroy, W.P. Experimental determination and simulation of the angular disruption of the metal flux during magnetron sputter deposition. J. Phys. D Appl. Phys. **2010**, 43.
209. Hippler, R.; Hubicka, Z.; Cada, M.; Ksirova, P.; Wulff, H.; Helm, C.A.; Stranak, V. Angular dependence of plasma parameters and film properties during high power impulse magnetron sputtering for deposition of Ti and TiO_2 layers. J. Appl. Phys. **2017**, 121, 171906.
210. Hofer, W.O. Angular, energy, and mass distribution of sputtered particles. In Sputtering by Particle Bombardment III; Behrisch, R., Wirrmaack, K., Eds.; Springer: Berlin/Heidelberg, Germany, 1991; Volume 64, p. 15.
211. Urbassek, H.M.; Hofer, W.O. Sputtering of molecules and clusters. Mat. Fys. Medd. **1993**, 43, 97–125.
212. Sundqvist, B.U.R. Desorption of organic molecules from solid and liquid surfaces induced by particle impact. In Sputtering by Particle Bombardment III; Behrisch, R., Wirrmaack, K., Eds.; Springer: Berlin/Heidelberg, Germany, 1991; Volume 64, p. 257.
213. Gerhard, W.; Villalba, V.; Maggiolo, A.R. A model calculation of the neutral molecule emission by sputtering processes. Eur. Phys. J. B **1975**, 22, 31–39.
214. Können, G.P.; Tip, A.; De Vries, A.E. On the energy distribution of sputtered dimers. Radiant. Eff. **1974**, 21, 269–274.
215. Konnen, G.P.; Tip, A.; de Vries, A.E. On the energy distribution of sputtered Clustrs. Radiant. Eff. **1975**, 26, 23–29.
216. Honda, F.; Lancaster, G.M.; Fukuda, Y.; Rabalais, J.W. SIMS study of the mechanism of cluster formation during ion bombardment of alkali halides. J. Chem. Phys. **1978**, 69, 4931–4937.
217. Galera, R.; Blais, J.; Bolbach, G. Molecular sputtering and damage induced by kiloelectron ions in organic monolayer—Metal systems. Int. J. Mass Spectrom. Ion Process. **1991**, 107, 531–543.
218. Haff, P.K.; Watson, C.C.; Yung, Y.L. Sputter ejection of matter from Io. J. Geophys. Res. Space Phys. **1981**, 86, 6933–6938.

219. King, B.V.; Ziv, A.R.; Lin, S.H.; Tsong, I.S.T. Mass distribution of ejected molecules and clusters in nanocascade sputtering processes. J. Chem. Phys. **1985**, 82, 3641–3645.
220. Salimian, A.; Hasnath, A.; Aminishahsavarani, A.; Upadhyaya, H. Hypothesis on the Influence of the Magnetic Behaviour of Hydrogen Doped Zinc Oxide during Its Plasma Sputtering Process. *Coatings* **2021**, *11*, 222
221. Aparnev, A.; Barten'ev, O. Analyzing the Loss Functions in Training Convolutional Neural Networks with the Adam Optimizer for Classification of Imagess. *Vestn. MEI* **2020**, *2*, 90–105.
222. Balasundaram, S.; Prasad, S. Robust twin support vector regression based on Huber loss function. *Neural Comput. Appl.* **2019**, *32*, 11285–11309.
223. Beattie, J.; Esmonde-White, F. Exploration of Principal Component Analysis: Deriving Principal Component Analysis Visually Using Spectra. *Appl. Spectrosc.* **2021**, *75*, 361–375.
224. Salimian, A.; Aminishahsavarani, A.; Upadhyaya, H. Artificial Neural Networks to Predict Sheet Resistance of Indium-Doped Zinc Oxide Thin Films Deposited via Plasma Deposition. *Coatings* **2022**, *12*, 225.
225. Salimian, A.; Haine, E.; Pardo-Sanchez, C.; Hasnath, A.; Upadhyaya, H. Implementing Supervised and Unsupervised Deep-Learning Methods to Predict Sputtering Plasma Features, a Step toward Digitizing Sputter Deposition of Thin Films. *Coatings* **2022**, *12*, 953
226. Rosenblatt, F. Perceptron Simulation Experiments. *Proc. IRE* **1960**, *48*, 301–309.
227. LeCun, Y.; Bengio, Y.; Hinton, G. Deep learning. *Nature* **2015**, *521*, 436–444.